Dynamics and Interaction of Magnons in the two dimensional Heisenberg Antiferromagnet

Dissertation

zur Erlangung des Doktorgrades

der Naturwissenschaften

der Fakultät Physik

der Technischen Universität Dortmund

vorgelegt von

Michael Powalski

aus Laurahütte

Dortmund, 27. Januar 2017

Erster Gutachter:	Prof. Dr. Götz S. Uhrig
Zweiter Gutachter:	Prof. Dr. Kai P. Schmidt
Tag der mündlichen Prüfung:	31. März 2017

Kontakt zum Autor: michael.powalski@tu-dortmund.de

"Problems in science are sometimes made easier by adding complications."

Daniel Dennett

Abstract

In this thesis the elementary excitations of the spin-1/2 Heisenberg antiferromagnet on the square lattice are studied. This fundamental model is a paradigmatic example for long range ordered quantum phases and the spontaneous breaking of a continuous symmetry in condensed matter.

The elementary excitations at long wavelengths are well understood by quantized spin waves, i.e., magnons, which are the gapless Goldstone bosons of the broken SU(2) symmetry. However, recent findings reveal an anomalous energy dip at short wavelengths, which cannot be explained by the conventional spin wave theory. The nature of spin waves at short wavelengths remains unclear to this day.

A central aim of this thesis is the derivation of an effective magnon description for the square lattice antiferromagnet which is quantitatively valid for all length scales. For this purpose, the method of continuous unitary transformations (CUT) is extended to its use for gapless excitations. CUT methods provide a powerful tool for the derivation of effective quasi-particle descriptions by means of flow equations. However, typical approaches are truncated in real space restricting their scope of application to gapped quantum phases.

In order to circumvent these limitations a CUT approach in momentum space is developed. The scaling dimension of operator terms is established as a suitable truncation criterion for gapless quasi-particles. Moreover, a diagrammatic representation of operator terms is introduced which simplifies the derivation and interpretation of flow equations in momentum space.

The developed approach is used to transform the Heisenberg Hamiltonian into an effective Hamiltonian which conserves the number of magnons. In addition, effective observables required for the theoretical description of inelastic neutron scattering are derived.

The initial magnon operators before the transformation are defined by the Dyson-Maleev representation which leads to a superficially non-hermitian Hamiltonian. As a result, the transformation constitutes a continuous similarity transformation (CST). This formalism enables the formulation of spin wave interactions by means of quartic boson operators. A crucial step of the transformation is the proper renormalization of the spin wave interaction which is achieved by a selfsimilar CST for scaling dimension $d = 2$.

The resulting effective magnon description is consistent at all length scales. In particular, the magnon dispersion exhibits an energy dip at short wavelengths which is in quantitative agreement with recent numerical and experimental data. Further analysis of the spectral properties indicates a strong attraction between spin waves giving rise to a resonance in the longitudinal two-magnon channel. This resonance can be interpreted as the amplitude or Higgs mode of the continuously broken SU(2) symmetry with finite lifetime. The origin of the anomalous dispersion is ascribed to a scattering between the Higgs resonance and single magnon states. The theoretical results are directly compared with experimental data obtained by inelastic neutron scattering and various numerical results which support this view.

The quantitative agreement between the effective spin wave approach and numerous numerical and experimental findings shows that magnons are a valid description of the elementary excitations at all length scales. Therefore, this thesis provides a final settlement of the question about the nature of the elementary excitations in the square lattice quantum antiferromagnet.

Kurze Zusammenfassung

In dieser Arbeit werden die elementaren Anregung des antiferromagnetischen spin-1/2 Heisenbergmodells auf dem Quadratgitter untersucht. Dieses fundamentale Modell ist ein paradigmatisches Beispiel für langreichweitig geordnete Quantenphasen und das Auftreten von spontan gebrochenen kontinuierlichen Symmetrien in kondensierter Materie.
Für lange Wellenlängen können seine elementaren Anregungen in Form von quantisierten Spinwellen, auch Magnonen genannt, beschrieben werden. Dabei handelt es sich um die lückenlosen Goldstonebosonen der spontan gebrochenen SU(2) Symmetrie. Aktuelle Untersuchungen deuten auf eine Energieabsenkung bei kurzen Wellenlängen hin, welche mithilfe der konventionellen Spinwellentheorie nicht erfasst werden kann. Bis heute ist die Natur kurzwelliger Magnonen nicht geklärt.
Ein wesentliches Ziel dieser Arbeit ist es die Eigenschaften der Magnonen in einem physikalisch quantitativen Gesamtbild wiederzugeben. Zu diesem Zweck wird die Methode der kontinuierlichen unitären Transformationen (CUT) für die Anwendung auf lückenlose Anregungen in langreichweitig geordneten Quantenphasen erweitert. Die CUT Methode ermöglicht die Herleitung effektiver Quasiteilchenbeschreibungen mithilfe sogenannter Flussgleichungen. Typische Anwendung erfordern jedoch eine Trunkierung im Ortsraum, was ihren Anwendungsbereich auf lückenbehaftete Quantenphasen beschränkt.
Um diese Einschränkungen zu umgehen wird eine CUT Methode für den Einsatz im Imulsraum entwickelt. Die Skalierungsdimension von Operatortermen kann dabei als geeignetes Trunkierungskriterium für lückenlose Quasiteilchen etabliert werden. Des Weiteren wird eine diagrammatische Representation für Operatorterme eingeführt, welche die Herleitung und Interpretation von Flussgleichungen im Impulsraum deutlich vereinfacht.
Die entwickelte Methode wird dann verwendet um den Hamiltonoperator des Heisenbergmodells in einen effektiven Hamiltoperator zu überführen. In der effektiven Darstellung ist die Zahl der Magnonen eine Erhaltungsgröße. Darüberhinaus werden auch die Observablen für die Beschreibung inelastischer Neutronstreuung transformiert.
Vor der Transformation werden die Magnonen im Rahmen des Dyson-Maleev Darstellung behandelt. In dieser Darstellung verliert der Hamiltonoperator seine Hermitizität und muss daher mithilfe einer kontinuierlichen Ähnlichkeitstransformation (CST) überführt werden. Dieser Formalismus ermöglicht es die Wechselwirkung zwischen Spinwellen nur mithilfe von quartischen Bosonoperatoren zu beschreiben. Ein wesentlicher Punkt ist dabei die korrekte Renormierung der Magnonwechselwirkung. Diese wird technisch mithilfe einer selbstähnlichen CST für Skalierungsdimension $d = 2$ umgesetzt.
Das resultierende effektive Modell ergibt ein konsistentes physikalisches Gesamtbild. Insbesondere findet sich eine Energieabsenkung der Magnondispersion für kurze Wellenlängen, welche mit aktuellen numerischen und experimentellen Daten quantitativ übereinstimmt. Weitere Untersuchungen der spektralen Eigenschaften weisen auf eine deutliche Anziehung zwischen Spinwellen hin, welche sich in Form einer Resonanz im longitudinalen Kanal zweier Magnonen manifestiert. Diese Resonanz kann als Amplitudenmode bzw. Higgsmode der spontan gebrochenen SU(2) Symmetrie mit endlicher Lebensdauer gedeutet werden. Die Energieabsenkung kurzwelliger Magnonen lässt sich auf Streuprozesse zwischen einzelnen Magnonen und der Higgsresonanz zurückführen. Ein direkter Vergleich der theoretischen Ergebnisse mit den experimentallen Daten aus inelastischer Neutronstreuung bestätigt diese Interpretation.

Die quantitative Übereinstimmung des effektiven Spinwellenmodells mit einer Vielzahl von numerischen und experimentallen Ergebnissen zeigt, dass die elementaren Anregungung für alle Wellenlängen tatsächlich in Form von Magnonen beschrieben werden können. Die Natur der elementaren Anregungen im Heisenbergantiferromagneten auf dem Quadratgitter ist somit abschließend geklärt.

Contents

Für Kathrin

CHAPTER 1

Introduction

The concept of *many body physics* incorporates the idea that the physical world is composed of simpler building blocks constituted by a finite set of objects and fundamental laws describing their interactions. Although its universal validity is subject of controversial discussion [1–3], the reductionist approach constitutes a major part of our understanding of physical reality. The most relevant part of matter surrounding us can be conceptually decomposed into neutrons, protons and electrons which are interacting by four fundamental forces.[1] So in fact, the set of elementary building blocks is surprisingly small and, yet, the number of objects and phenomena we observe in our physical world is virtually infinite. At first glance, this might seem astonishing but it can be illustrated by a simple analogy comparing our world to a composition of rudimentary Lego bricks. As we know, a large number of Lego bricks can be organized to a complex assembly with properties that differ drastically from the characteristics of its simple building blocks. The interplay between a huge number of bricks provides the potential for novel properties which are accompanied by new types of principles describing the relation and interaction between those compounds. This organizational effect is called *emergence* and it's one of the most -if not the most- fundamental principle in nature, since it is responsible for the vast diversity of phenomena that we observe, from the structure of atoms and molecules, the different properties and phases of matter up to the evolution of life.

In order to develop a profound comprehension of the mechanisms which drive emergent phenomena, we require theories which go beyond pure a phenomenological description. Especially in condensed matter theory the in-depth understanding of how complicated many body systems can be explained by the properties of their underlying constituents is of great interest. Unfortunately, it is the enormous diversity that makes a complete mathematical deduction impossible. Even a general interacting three body system is mathematically not fully tractable without approximations [5], least of all for many body system with a typical number of $N \sim 100\text{-}10^{23}$ particles. In order to obtain qualitative and quantitative descriptions, condensed matter theorists have developed a variety of concepts and approaches many of which are standard tools in many body physics nowadays[6, 7].

A very powerful way to understand complex systems is the derivation of simplified effective models. Ideally, an effective model captures the essential mechanisms of the system and neglects irrelevant properties and processes leading to a considerable reduction of complexity. Typical experiments in condensed matter physics, for example, are performed at temperatures

[1] Striktly speaking, neutrons and protons are composed of quarks. However, quarks do not appear as free particles due to confinement. [4]

which are low compared to the intrinsic energy scales of the system. Therefore, an appropriate theory has to capture the low-energy properties which are governed by the ground state and the corresponding elementary excitations. These states, in fact, constitute only a small part of the physical Hilbert space. The general problem is the identification and quantitative description of the relevant degrees of freedom because one has to integrate out high-energy states in order to reduce the complexity of the system.
A fundamental idea in low-energy descriptions is the concept of quasi-particles. This concept is based on the observation that in many cases the elementary excitations exhibit properties which are reminiscent of particles, in the sense that they are characterized by quantities like momentum, spin, mass, charge etc. Accordingly the ground state is interpreted as quasi-particle vacuum. Originally, this idea was introduced by Landau in his Fermi liquid theory establishing the term *quasi-particle*[8].[2]
Nowadays the quasi-particle concept is a standard notion in condensed matter physics which is applied in a much broader scope [10]. Quasi-particles can be viewed as an emergent phenomenon, where cooperative interactions between constituents of many body systems give rise to excitations which themselves behave like particles.
A crucial advantage of the quasi-particle picture is due to the fact, that one can rely on established mathematical concepts from particle physics. Therefore, one has effective tools to describe the intricate collective motion of many body systems in a simplified and very intuitive way.
The quasi-particle concept appears in many different fields and the list of different quasi-particles is sheer endless. Important examples for quasi-particles are

phonons, the quantized vibrational modes in crystals [11],

excitons, bound electron hole pairs [12] or

triplons, which describe triplet excitations in dimerized quantum magnets [13, 14],

to name only a few. An interesting and general review on the concept of quasi-particles is given in Ref. [10].

Quasi-particle descriptions also play a central role in this thesis. The focus is on *magnons*, the quasi-particles of the two dimensional Heisenberg quantum antiferromagnet, which is one of the most paradigmatic models of quantum magnetism [15, 16]. Despite the lack of an exact solution, numerical and analytical studies establish a very consistent picture of its low-energy properties [17]. There is strong evidence, that the Heisenberg antiferromagnet on the square lattice exhibits long range Néel order giving rise to a finite staggered magnetization which breaks the continuous rotational spin symmetry (SU(2)-symmetry) [18]. Thus, this system provides an important example of broken continuous symmetries in condensed matter [19]. Furthermore, it is of major importance for the understanding of high-T_c superconductivity because it describes undoped parent compounds of high-T_c superconductors [17, 20].
The elementary excitations of the long range Néel order are wavelike deviations in the staggered magnetization which are described by the fundamental theory of spin waves [21, 22]. Spin wave theory establishes magnons as the Goldstone bosons of the spontaneously broken

[2] Landau realized that under certain circumstances the excitations in systems of interacting electrons are adiabatically connected to the excitations of the non-interacting Fermi gas. Thus, they are characterized by the same quantum numbers such as spin, charge and momentum. Due to interactions they exhibit renormalized dynamical properties, e.g. a renomarlized mass, as well as a finite life time giving rise to a broadened quasi-particle peak in the spectral density. For this reason, Landau termed them quasi-particles. The Fermi liquid theory was further developed by Abrikosov and Khalatnikov [9].

SU(2) symmetry which are gapless according to Goldstones theorem [23, 24]. At long wavelengths, i.e, at small energies, magnons are quantitatively well understood by conventional spin wave theory [21, 22].
However, recent numerical and experimental findings revealed an anomalous dispersion at short wavelengths, i.e., at high energies, which cannot be explained by the conventional spin wave approach [25–28]. This seeming failure of spin wave theory has led to a substantial debate about the fate of high-energy magnons [28–30]. A vast amount of effort has been made to resolve these discrepancies [30, 31] but the nature of short wavelength spin waves remains unclear to this day. A further introduction to the Heisenberg antiferromagnet and the problem of short wavelength spin waves is given in chapter 4.

A major part of this thesis is devoted to the question whether high-energy magnons can be described in terms of interacting spin waves. To this end, we want to derive an effective quasi-particle description based on spin wave theory.
A versatile and powerful analytical tool especially suited to such tasks is the continuous unitary transformation (CUT) method which was independently introduced by Wegner [32] as well as Glazek and Wilson [33] in 1994. Combined with the quasi-particle concept, it provides a capable approach for the description of strongly correlated quantum systems [14, 34, 35]. Unfortunately, standard CUT approaches are truncated in real space and, therefore, their application is limited to systems with finite correlation length, i.e with a finite gap [36].
In the presence of criticality or long range order effective field theories and renormalization group approaches provide very adequate tools as they directly exploit the lack of an characteristic energy and length scale [7]. However, such methods fade out microscopic structures of the systems which in turn are important for the understanding of short range processes. Thus, from a methodical point of view, it is difficult to capture both aspects, short range correlations and scale invariance at long wavelengths. The derivation of effective models for gapless quasi-particles is very challenging, especially when processes on very different length scales are relevant, which is the case in the two dimensional quantum antiferromagnet.

In this thesis we want to extend the use of CUT methods to systems with long range order aiming at a quantitative description of their excitations and their mutual interaction. In order to avoid generic problems of real space approaches, we apply the CUT in momentum space. Moreover, we identify a truncation criterion which is particularly suited for gapless systems, namely the scaling dimension of operator terms. By means of these tools we derive an comprehensive and quantitative description of magnons in the two dimensional quantum antiferromagnet.

The thesis is organized as follows.
Chapter 2 gives an introduction to the CUT approach focusing on its use in momentum space.
Chapter 3 deals with technical aspects of CUTs in momentum space and the methods required for the analysis of the two dimensional quantum antiferromagnet.
In chapter 4 the elementary excitations of the two dimensional quantum antiferromagnet are studied. The presented methods are used to derive an effective magnon description which is valid for all length scales. The obtained results are compared with various numerical and experimental data.
Chapter 5 provides a concluding summary.

CHAPTER 2

Continuous Unitary Transformations in Momentum Space

This chapter gives an introduction to the flow equation approach, often referred to as method of continuous unitary transformation (CUT), which constitutes the methodical framework of this thesis. The main focus is on the extension of the CUT approach to its application on physical systems exhibiting gapless excitations. Thereby, the development of new concepts for the use of CUTs in momentum space is a central issue. The presented approach circumvents generic limitations in real space, that are imposed by excitations with infinite spatial extension as they appear for diverging correlation lengths. The major objective is the derivation of an effective description in terms of quasi-particles with arbitrary small energy which is quantitatively valid for any length scale. The resulting effective model provides deeper insight into the dynamics and interactions of the elementary excitations and allows the calculation of experimentally accessible quantities such as dynamic structure factors.

In the first section the motivation and basic idea behind continuous unitary transformations is presented comprising a concise review of the background and of the relevant literature.
Subsequently, the mathematical framework of the method is introduced and a brief overview of varied applications is given. In this context, different truncation schemes are presented with regard to their advantages and limitations.
The second section constitutes the main part of this chapter, discussing the utilization of the CUT method for gapless systems for which the standard real space approach breaks down. The application of the CUT approach in momentum space and the consequent advantages for the description of gapless quasi-particles are described. Moreover, a suitable truncation criterion is introduced, namely the scaling dimension of operator terms, which defines a natural hierarchy arising from the gapless nature of the underlying excitations.
In the third section the generalization of the flow equation approach to similarity transformations is examined. This generalization is of major importance when dealing with non-hermitian or pseudo-hermitian problems.

2.1 Introduction

The method of continuous unitary transformations (CUT), also referred to as flow equation approach, was independently introduced by Wegner [32] and Glazek and Wilson [33] in 1994. It provides a general framework for the systematic derivation of effective low energy models from first principles. Since its introduction, the CUT method was used in a broad scope of applications [13, 14, 35, 37, 38]. An important key step was the combination of CUTs with the concept of quasi-particles, which was first proposed by Stein [39] and established in seminal works by Knetter and Uhrig [40–42]. Considerable effort was made enhancing and refining the concepts of CUTs using perturbative expansions [43, 44], non-perturbative approaches [44–47], as well as using linked cluster expansions and graph theory [34, 48–50] or developing new concepts for the understanding of quasi-particle decay [51–53]. A particular strength of the CUTs turned out to be the description of gapped phases and the identification of their breakdown at critical points providing a reliable tool for the determination of second order phase transitions [35, 54–56]. This strength results from the combination of sophisticated generator schemes which direct the unitary flow, and appropriate truncation schemes in real space which enable a systematic and efficient way to capture physical processes of finite range. However, the common approach breaks down once the excitation gap closes at a second order phase transition due to diverging correlation lengths, thereby complicating the investigation of gapless phases.
There are first attempts extending the CUT approach to long range ordered systems [57, 58] which demonstrate the potential of the CUTs, but a decisive advancement in the description of gapless quasi-particles is still pending. Nevertheless, the huge versatility of the CUT method and the seminal findings in the last decade render the extension of CUTs for the application to gapless phases a feasible task and constitute the fundamental motivation of this thesis. An important aim is the development of a CUT approach which establishes a quantitatively valid quasi-particle picture for gapless magnons in a long range Néel phase. In order to circumvent the problems of a real space approach the CUT is applied in momentum space. Before investigating the characteristics and advantages of CUTs in momentum space a brief introduction to the methodical groundwork of CUTs is given in the following. For a discussion of the method and its applications the reader is referred to Ref. 59.

2.1.1 Basic concept

The concept of CUTs is based on the idea of simplifying the Hamilton operator H of a physical system at hand by finding a convenient basis. Technically, the translation between different sets of orthogonal basis states $\{|\nu\rangle\}$ can be expressed by a unitary mapping $U : |\nu\rangle \rightarrow |U\nu\rangle$ which transforms the Hamilton operator into

$$H' = UHU^\dagger \quad . \tag{2.1}$$

The unitary mapping can be envisioned as a rotation of physical basis states that preserves their orthogonality and their norm. Orthogonality ensures that each basis vector representing a certain physical state $|\nu\rangle$ is uniquely distinguishable from the other states $|k\rangle$ by at least one quantum number, i.e., it has no overlap $\langle\nu|k\rangle = 0$ for $\nu \neq k$. Consequently, any representation (2.1) that is unitarily equivalent to the initial Hamiltonian is a valid description of the

physical system. Ultimately, one is interested in finding a transformation that diagonalizes (or block diagonalizes) the Hamiltonian, which in turn simplifies the computation of experimentally relevant quantities. But for most of the typical many body systems the corresponding Hilbert space is unimaginably huge and, therefore, finding a convenient unitary operator U is highly nontrivial. So instead of trying to find a one-step transformation, the procedure can be systematized by continuously rotating the basis in a controlled way until the optimal basis is reached. For this purpose, a continuous parameter ℓ is defined such that $H(\ell = 0)$ corresponds to the initial Hamiltonian which transforms with increasing ℓ and finally reaches the desired structure for $\ell \to \infty$. The unitary operator $U(\ell)$ is then defined as a sequence of infinitesimal unitary transforms $e^{-\eta(\ell)d\ell}$ determined by the anti-hermitian generator $\eta(\ell)$. Accordingly, the transformation of the Hamiltonian can be expressed by the flow equation

$$\partial_\ell H(\ell) = [\eta(\ell), H(\ell)] \quad . \tag{2.2}$$

Moreover, the unitary transformation may also be defined for observables described by some operator O in the following way

$$\partial_\ell O(\ell) = [\eta(\ell), O(\ell)] \tag{2.3}$$

yielding an effective observable $O_{\text{eff}} = O(\ell \to \infty)$ [42, 60].
In order to obtain a simplified effective model $H_{\text{eff}} = \lim_{\ell\to\infty} H(\ell)$, a suitable generator has to be specified. An adequate choice of the generator certainly depends on the concrete structure of the Hamiltonian during the flow $H(\ell)$. Hence, the generator has to be a function of the Hamiltonian itself $\eta(\ell) = \eta(H(\ell))$. Mathematically, such operator valued functions of operators are usually termed *super operators*. In the context of the CUT method this function is often referred to as a *generator scheme* [44, 61]. The choice of the generator scheme constitutes a crucial part of the method, because it determines the structure of the resulting effective Hamiltonian. In the following, a brief discussion of different generator schemes is given.

2.1.2 Generator schemes

The generator scheme as originally proposed by Wegner [32] has the form

$$\eta^{\text{W}}(H(\ell)) = [\, H_d(\ell), H(\ell)\,] \tag{2.4}$$

where $H_d(\ell)$ denotes the diagonal part of the Hamiltonian $H(\ell)$. It is chosen such that all off-diagonal matrix elements between states $|i\rangle$ and $|j\rangle$ corresponding to non degenerate diagonal elements $h_{i,i}(\ell) \neq h_{j,j}(\ell)$ become arbitrarily small for $\ell \to \infty$. In the limit $\ell \to \infty$ the flow vanishes and $[\, H_d(\infty), H(\infty)\,] = 0$ holds which implies that the resulting Hamiltonian is diagonal or block diagonal in the case of degeneracies. The convergence of the flow equation is proven for finite systems [32], infinite systems bounded from below [45] and also for certain classes of self-similar truncated systems [62].
A drawback of the Wegner generator is, that it introduces new matrix elements $h_{i,j}$ with arbitrary distance $d = |i - j|$ even if these were zero initially. This effect can spoil the simple structure (e.g. band diagonality) of a given initial Hamiltonian. In order to avoid this effect,

Mielke proposes a different generator of the form

$$\eta^{\mathrm{M}}_{i,j}(\ell) = \mathrm{sign}(i-j)h_{i,j}(\ell) \quad , \tag{2.5}$$

which preserves band-diagonality of Hamiltonians [63]. In contrast to the Wegner generator this scheme enforces the Hamiltonian to be completely diagonal for $\ell \to \infty$ even in the case of degeneracies. Moreover, it can be shown that the asymptotic behavior of the off diagonal matrix elements is given by an exponential decrease $h_{i,j}(\ell) \propto \exp\big(-\mathrm{sign}(i-j)(e_i(\ell)-e_j(\ell))\big)$ whereby the diagonal matrix elements $e_i(\ell)$ are sorted in ascending order.

2.1.3 Particle conserving generator

In this thesis the so called quasi-particle (qp) conserving generator η^{qp} [39, 41] is used. This generator scheme is based on the idea of transforming an intricate many body system into a simplified few body problem by a decoupling of subspaces with a different number of excitations. The transformation is realized by the generator scheme

$$\eta^{\mathrm{qp}}(\ell) = H^{+}(\ell) - H^{-}(\ell) \tag{2.6}$$

where H^{+} or H^{-} denote the part of the Hamiltonian that increases (+) or decreases (-) the number of quasi-particles or excitations, respectively. This concept requires a proper definition of a vacuum or reference state and an according notion of a quasi-particle number, e.g. by means of second quantization. The matrix elements of (2.6) in the quasi-particle basis are given by

$$\eta^{\mathrm{qp}}_{i,j}(\ell) = \mathrm{sgn}(q_i - q_j)h_{i,j}(\ell) \quad , \tag{2.7}$$

where q_i denotes the quasi-particle number of state $|i\rangle$. This scheme can be seen as a generalization of the Mielke generator in 2.5. But, instead of decoupling each individual eigenstate, only matrix elements between states with a different quantum number q_i are turned off. Similar to the Mielke generator, the particle conserving scheme enforces an assorting of energies in ascending order [51, 64]. The resulting effective Hamiltonian is block diagonal in the particle number and can be written as a sum of irreducible n-particle operators H_n

$$H_{\mathrm{eff}} = \sum_n H_n \tag{2.8}$$

which act solely on m-particle states with $m \geq n$. More specifically, H_0 comprises the ground state energy, H_1 determines the dynamics of a single particle and H_n with $n > 1$ correspond to n-particle interactions. Hence, the complicated many-body problem is reduced to a system of a few particles describing the low energy regime of the system.
The particle conserving CUT is a powerful approach because it provides a systematic derivation of effective low energy models based on an intuitive quasi-particle interpretation. This concept goes far beyond the sheer determination of eigen values and eigen states, as for example obtained in standard diagonalization procedures. Analyzing the dynamics of elementary excitations and the effects of their mutual interactions in the context of a quasi-particle picture is of significant importance for the understanding of collective phenomena in many body systems.
The advantages of this approach become also apparent in the computation of spectral densities

for observables which describe experimentally relevant quantities such as dynamic and static structure factors. The flow equation (2.3) can be used to derive effective observables which in turn simplify the calculation of correlation functions and spectral densities. A discussion of the computation and interpretation of effective spectral densities in the context quasi-particle conserving CUTs is given in section 2.3.3.

Next, let us discuss the limitations and present extensions of this scheme. It should be stressed, that the mapping to the low energy model is well defined only if the reference state (or quasi-particle vacuum state) is adiabatically connected to the exact ground state of the Hamiltonian.[1] The initial reference state becomes ill-posed once the system undergoes a second order phase transition and, consequently, the quasi-particle description breaks down. Therefore, this method is very well suited for the analysis of gapped quantum phases and the detection of second order phase transitions using perturbative as well as non-perturbative approaches.

From a conceptual point of view, the particle-conserving CUT relies on the existence of stable quasi-particles states in the system at hand. In several cases, however, the stability of quasi-particles is limited to a reduced sector of momenta and quasi-particle decay occurs beyond a certain threshold leading to a breakdown of the quasi-particle picture [51]. In gapped systems this phenomenon is observed when a dispersion branch is merging into a higher quasi-particle continuum giving rise to a resonance of multi-particle states with finite energy width, i.e., finite lifetime [65, 66]. In such scenarios the standard η^{qp} generator categorically tracks the lower edge states of the continuum, which exhibit a vanishing spectral weight and, therefore, provide no substantial information about the systems excitations. In practice, this behavior leads to convergence problems in numerical applications [67] or spurious extrapolations in perturbative realizations [68, 69]. Energetic overlaps between states with different quasi-particle number preclude a well defined description in terms of conserved particles unless there are additional conserved quantum numbers protecting those states. This makes the application of the approach complicated. In order to circumvent these problems, Fischer and Uhrig introduced a generalized generator scheme denoted by $\eta^{\mathrm{m:n}}$ which decouples only sectors up to m particles [51]. As a result, the CUT is not affected by energetic overlaps in higher quasi-particle channels. The first successful extension of CUTs for the description of quasi-particle decay is based on the $\eta^{\mathrm{0:n}}$ scheme [51]. This scheme decouples the ground state from higher quasi-particle states, whereas processes describing the decay of 1-qp states into multi-particle states are retained. The structure of the resulting effective Hamiltonian is depicted in Figure 2.1. The remaining interactions are treated by tridiagonalization in a restricted Hilbert space, which is a valid approximation if the remaining terms are sufficiently small [70].

A recently developed modification of the η^{qp} generator scheme adjusts the flow according to the spectral weight of the states, thereby enabling the treatment of quasi-particle decay even in the case of strong interactions [53].

Furthermore, there are several improvements based on variational generator schemes that enhance the stability of numerical CUT approaches in the case of energetically overlapping qp-subspaces [71].

Besides the use of a suitable generator, the choice of a physically motivated truncation scheme is a crucial part in most practical applications of the CUTs. This aspect is the main topic of the next part.

[1] Here, the ground states of two Hamiltonians H_1 and H_2 are defined to be adiabatically connected, if there is a parameter dependent Hamiltonian $H(x)$ which can be adiabatically transformed from $H_1 = H(x_1)$ to $H_2 = H(x_2)$ without traversing a second order phase transition.

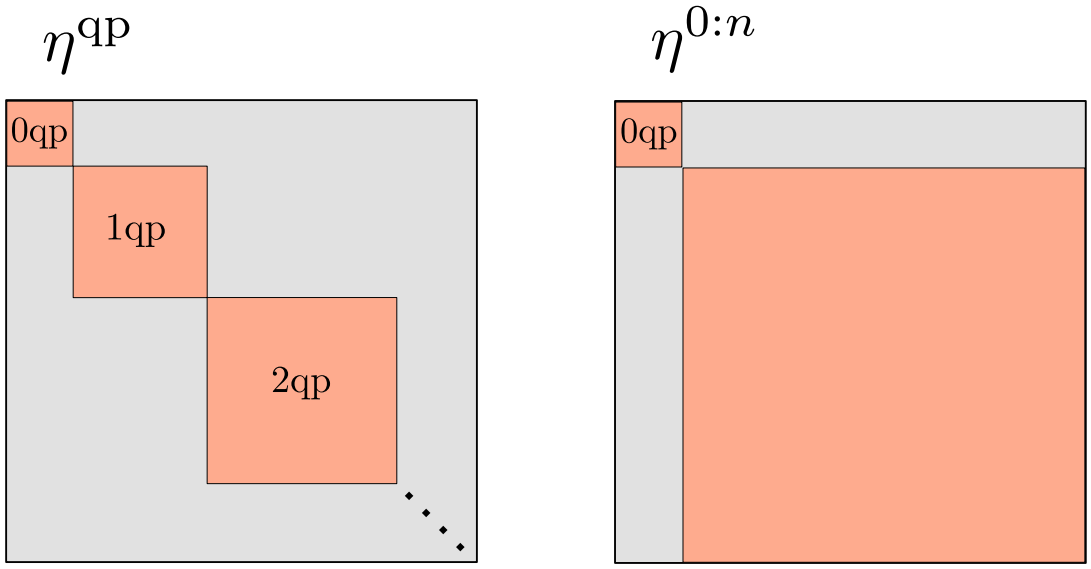

Figure 2.1: Illustration of the general structure for the effective Hamiltonian obtained by the η^{qp} generator scheme (left) and the $\eta^{0:n}$ generator scheme (right).

2.1.4 Truncation schemes

In general, the commutator $[\eta(H(\ell)), H(\ell)]$ in the flow equation (2.2) will introduce new terms that are not present in the initial Hamiltonian. Consequently, these new terms have to be taken into account in the Hamiltonian and the corresponding generator scheme. For typical condensed matter systems the successive evaluation of the commutator and the consistent expansion of the Hamiltonian (and generator) leads to an infinite set of operator terms that determine the structure of the Hamiltonian during the flow. In order to obtain a closed set of differential equations, it is necessary to truncate at some point. The CUT approach gives rise to manifold possibilities of truncation which are more sophisticated than plain restrictions of the considered Hilbert space. The choice of truncation is a decisive element as it specifies which physical processes, i.e., fluctuations and interactions, are incorporated in the effective model, and consequently determines the validity of the results. For this reason, the truncation scheme should justified physically.
In the following part a classification of the most important truncation schemes is presented in order to give the reader a brief overview. The technical details of the methods and corresponding truncation schemes used in this thesis are presented in the subsequent section 2.2.

Classification of truncation schemes

1. **Self similar truncation**
   In the self-similar approach the flowing Hamiltonian and generator are expanded in terms of a finite operator basis given by monomials of normal ordered operators. The restriction of the operator basis is accomplished by a selection rule which is applied to the operators emanating from the successive evaluation of the commutator. As a result, the flow equation assumes a self similar form, provided that no further operators are generated in compliance with the selection rule. This approach is referred to as self-similar CUT (sCUT). Typically, the selection criteria are constituted by a finite operator range in real space and a restriction in the quasi-particle number [47, 72].

2. **Strictly perturbative truncation**
   In strictly perturbative truncation schemes the Hamiltonian and the corresponding flow equations are rigorously expanded in terms of one (or more) perturbative parameters. The associated flow equations can be solved in a recursive fashion, whereby the computational effort grows with increasing order. The resulting effective model is a series expansion in terms of the perturbation parameter.
   The first perturbative approach introduced by Knetter and Uhrig [41] is specialized in problems which can be decomposed into an unperturbed part with equidistant spectrum and a perturbation which links states that are separated by a finite energy difference i.e., the perturbation is band-diagonal.[2] This method is referred to as perturbative CUT (pCUT). Based on the linked cluster theorem, one can compute relevant matrix elements in the thermodynamic limit, which are exact up to a given order in the perturbation parameter. In conjunction with linked cluster expansions, pCUT provides a versatile tool for the analysis of gapped quantum phases [35, 54, 55, 73].
   The enhanced pCUT (epCUT) is a generalization of the pCUT approach which does not require an equidistant spectrum as a starting point [44]. It is therefore applicable to a larger class of problems, thereby extending the scope of real space applications. Analogous to the sCUT approach the Hamiltonian is expanded in terms of a normal ordered operator basis in second quantization. In contrast to pCUT, the flow equations in epCUT are usually solved by numeric tools.

3. **Semi-perturbative truncation**
   In the directly evalued version of the epCUT (deepCUT) the truncated flow equations obtained from epCUT are integrated in a self consistent way for fixed values of the perturbation parameter [44, 74]. In this way *non-perturbative* results are obtained which comprise fluctuations up to infinite order in addition to the exact fluctuations of the corresponding perturbative treatment. Due to the self consistency, the structure of the flow equation depends on which quantities are targeted in the effective system. For example, the incorporation of all equations that consistently determine the dispersion up to order n will introduce additional terms to the truncated equation system of the ground state energy in that given order[3]. In this sense, there is a freedom of choice providing alternative ways of semi-perturbative truncation schemes (for further discussion of this issue see subsection 2.2.3). In the standard deepCUT approach the self consistent flow equations are restricted to those parts that exclusively contribute to a specific quantity of interest in the considered order. In real space applications it is observed that this scheme provides the most robust results, which is ascribed to the fact that it conforms perturbation theory in the most consistent way [71]. In other scenarios for which high orders are not accessible (e.g. in momentum space) it might be more appropriate to incorporate additional targeted quantities.

4. **Graph based truncation**
   The graph based CUT method (gCUT) is a non-perturbative approach for the derivation of effective low energy models on infinite lattices [34]. In gCUTs the flow equations are

[2] Note, that this approach already covers a large class of problems. Many system comprising local degrees of freedom which are coupled via short range interactions can be described in such a way. Though, due to its nature, it is restricted to real space applications

[3] In the perturbative evaluation the corresponding equations are not coupled. Hence, the results are not affected by the incorporation of further targeted quantities.

solved numerically on finite systems represented by graphs. Based on the linked cluster theorem, the results of the finite clusters are systematically recombined by means of an appropriate embedding scheme reproducing the effective model in the thermodynamic limit. The resulting effective Hamiltonian comprises all physical processes of the infinite lattice up to a finite range determined by the maximum size of the considered graphs. Therefore, quantum fluctuations are captured exactly up to a certain perturbative order, similar to the deepCUT approach. However, it should be noted that the higher order fluctuations included by the gCUT method are not identical to the contributions captured by the deepCUT approach in real space.
The gCUTs contribute greatly to the understanding of numerical linked cluster expansions and the connection between the physics of finite clusters and infinite systems [48, 53, 58].

2.2 CUTs in second quantization

In this section we discuss the methodical aspects of CUTs in second quantization as they are used in this thesis. The distinction between the presented methods is based on different truncation schemes which are explained in more detail.

2.2.1 Self-similar CUT

Instead of using a concrete matrix representation, the flow equations can be also deduced in second quantization. Accordingly, the Hamiltonian and the generator are expressed in terms of normal ordered sequences of annihilation and creation operators A_i. Any non trivial operator acting on the considered Hilbert space can be unambiguously decomposed into the sum of normal ordered operators. For fermionic and bosonic operators this procedure can be simplified considerably using Wick's theorem [75].
Therefore, the collection of all normal ordered operators $A = \{A_i\}$ (including the identity operator) provides a complete basis which enables the expansion of the form

$$\begin{aligned} H(\ell) &= \sum_{A_i \in A} h_i(\ell) A_i \\ \eta(\ell) &= \sum_{A_i \in A} \eta_i(\ell) A_i = \sum_{A_i \in A^+} h_i(\ell) A_i - \sum_{A_i \in A^-} h_i(\ell) A_i \quad . \end{aligned} \tag{2.9}$$

where A^+ and A^- denote the sets of normal ordered operators which increase (+) or decrease (-) the number of excitations. Following the nomenclature of reference [44] and [71], the operator sequences A_i are termed monomials, whereas the product of a monomial and the corresponding coefficient is referred to as an operator term. Note, that the dependence on the flow parameter ℓ resides solely in the coefficients while the operator basis $\{A_i\}$ is fixed.
The primary operator basis A^0 contains all monomials that form the operator terms in the initial Hamiltonian $H^{(0)} = H(\ell = 0)$ and the associated generator $\eta^{(0)} = \eta\left[H^{(0)}\right]$. In the evaluation of the commutator $\left[\eta^{(0)}, H^{(0)}\right]$ additional monomials $A'^{(0)}$ might be generated which are not part of A^0. Consequently, the Hamiltonian and the generator need to be updated $H^{(0)}, \eta^{(0)} \to H^{(1)}, \eta^{(1)}$ according to the extended operator basis $A^{(1)} = A^{(0)} \cup A'^{(0)}$ For systems

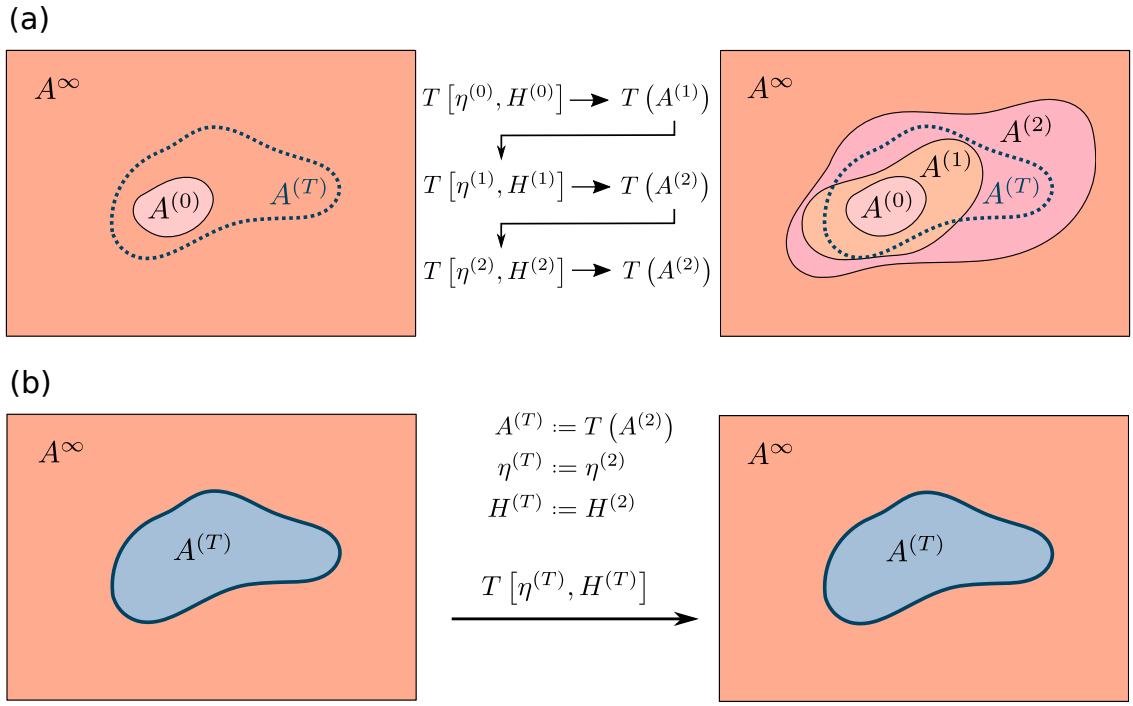

Figure 2.2: A schematic illustration of the self similar truncation scheme is depicted. (a) The operator basis $T\left(A^i\right)$ which spans the Hamiltonian $H^{(i)}$ and the generator $\eta^{(i)}$ is iteratively extended by the monomials emanating from the commutator in the flow equation. (b) Eventually, no further monomials are generated in compliance with the selection rule T and the truncated flow assumes a self similar form.

with an infinite-dimensional Hilbert space the successive iteration of this procedure in general does not close leading to an infinite set $A^\infty \subseteq A$.[4]. In the self similar approach the operator basis is restricted to a set of monomials $A^{(T)}$ that comply with a certain selection rule T

$$TA_i = \begin{cases} A_i & \text{if } A_i \text{ complies with the selection rule} \\ 0 & \text{otherwise} \end{cases} \quad .$$

The basis is expanded according to $A^{(n+1)} = T\left(A^{(n)} \cup A'^{(n)}\right)$ until no new monomials are created in the commutator in compliance with the selection scheme. The resulting operator basis $A^{(T)}$ spans the Hamiltonian and the generator giving rise to a self consistent flow equation

$$\partial_\ell H^{(T)}(\ell) = T\left[\eta^{(T)}(\ell), H^{(T)}(\ell)\right] \quad . \tag{2.10}$$

The derivation in the self similar truncation scheme is schematically depicted in Figure 2.2.

Based on the expansion in (2.9) the flow equation (2.10) translates into a set of coupled

[4] If the Hamiltonian exhibits certain symmetries, only a subset of A might suffice as an appropriate operator basis as the symmetries are retained during the unitary flow (e.g only monomials with an even number of creation and annihilation operators might occur during the flow). In general, this subset is still infinitely large.

differential equations for the scalar functions $h_i(\ell)$ by equating the coefficients on both sides:

$$\begin{aligned} \sum_i \partial_\ell A_i h_i(\ell) &= \sum_i A_i \sum_{j,k} D_i^{jk} h_j(\ell) h_k(\ell) \\ \rightarrow \partial_\ell h_i(\ell) &= \sum_{j,k} D_i^{jk} h_j(\ell) h_k(\ell) \quad . \end{aligned} \tag{2.11}$$

The tensor D_i^{jk} results from the commutator of the corresponding monomials A_k and A_j and denotes the prefactor of the contribution to the monomial A_i. The initial values of the functions $h_i(\ell = 0)$ are defined by the initial condition $H(\ell = 0) = \sum_{A_i \in A_0} h_i A_i$.
In the most simple truncation scheme the flow is restricted to the operator terms of the initial Hamiltonian, i.e., $A^{(T)} = A^{(0)}$, as done in first approaches [76, 77]. which incorporate information about higher terms by appropriate modifications of the initial coefficients.
In other self similar schemes the operator basis is restricted by the number of quasi-particles involved and the spatial range of operators [47, 72].
In this thesis the scaling dimension of operator terms is used as a truncation criterion. It is deduced from the scaling behavior of the system at small energies and provides a hierarchy for systems exhibiting gapless excitations. An elaborate discussion of the self similar truncation based on the scaling dimension is given in section 2.5.

2.2.2 Enhanced perturbative CUT

The rigorous perturbative expansion of the flow equation in second quantization is referred to as enhanced perturbative CUT (epCUT) [44]. This method can be seen as a hybrid CUT that combines the conceptual advantages of pCUT and sCUT. The epCUT approach is based on a perturbative problem of the form

$$H = H_0 + xV \tag{2.12}$$

where H_0 denotes the unperturbed system and the parameter x adiabatically introduces a perturbation V. Accordingly, the coefficients of the flowing Hamiltonian in (2.9) are assumed to be analytic functions of x which can be written as a power series in x

$$h_i(x) = \sum_{n=0}^{\infty} h_i^{(n)} x^n \quad . \tag{2.13}$$

The flow equations in (2.11) are sorted by powers of x giving rise to a hierarchical set of differential equations for the coefficients

$$\partial_\ell h_i^{(m)} = \sum_{j,k,p} D_i^{jk} h_j^{(m-p)}(\ell) h_k^{(p)}(\ell) \quad . \tag{2.14}$$

Note, that the flow in order m is solely determined by coefficients of the same or lower order, since there is no dependence on coefficients of higher order in (2.14). Moreover, the tensor D_i^{jk} does not depend on the considered order, as it results from the commutation of the corresponding monomials A_i and A_j. The general structure of the flow is specified by the tensor D_i^{jk}, since it determines the mutual influence between the coefficients during the flow.

The differential equations (2.14) can be obtained by successive evaluation of the commutator generating additional terms of higher order. In real space approaches, typically, high order expansions are accessed (n∼5-14) and, thus, a sophisticated way of evaluating nested commutators is highly desirable. Appropriate concepts for the derivation of perturbative flow equations in real space and the conditions required for a closed set of differential equations are thoroughly discussed in the Phd thesis of Nils Drescher [71] and in reference [44].
Given a Hamiltonian for which the unperturbed part describes a system of non-interacting quasi-particles, the number of independent coefficients $\partial_\ell h_i^{(m)}$ is limited for a finite perturbation V giving rise to a closed set of differential equations in any finite order n. Thus, the flow equations can be solved order by order in a recursive manner, whereby the maximum order $n(\max)$ is limited by the growing computational effort. The resulting effective Hamiltonian is a power series in x

$$H_{n(\max)} = \sum_{n=0}^{n(\max)} H^{(n)} x^n \quad , \tag{2.15}$$

which is valid for sufficiently small values of the perturbation parameter x. In order to obtain reliable results for higher values of x appropriate extrapolation schemes are required as for example Padé or Dlog Padé extrapolations [78, 79]. In the next subsection a robust extrapolation scheme for the epCUT is discussed.

2.2.3 directly evalued epCUT

The directly evalued epCUT (deepCUT) is a non perturbative approach which is derived straightaway from the epCUT method. The corresponding flow equations of a coefficient h_i are solely constituted by the contributions D_i^{kj} obtained from the perturbative expansion in (2.14) up to a given order. But, in contrast to the epCUT approach, one omits the Taylor expansion of the coefficients $h_i(x)$ and treats them as general functions in x. A targeted coefficient of the effective Hamiltonian is then determined by its own set of self consistent differential equations, which can be numerically evaluated for any fixed value of x. The hierarchical structure of the flow is thereby voided and, as a result, the coefficients are influencing each other in a non-perturbative way. In Figure 2.3 the relation between the epCUT and deepCUT is illustrated by means of a *flow diagram* for an quartic oscillator

$$H = h_0 + h_1\, a^\dagger a \;\; + h_2\, a^\dagger a \;\; a \;\; a \;\; + h_3\, a^\dagger a^\dagger a^\dagger a^\dagger + h_4\, a^\dagger a^\dagger a^\dagger a \;\; + h_5\, a \;\; a \;\; a \;\; a \tag{2.16}$$

using the particle conserving generator (see also Ref. [45]. The flow diagram illustrates the mutual dependence of the coefficients during the flow by means of arrows indicating which products of coefficients $h_k h_j$ account for the first derivative of a coefficient h_i.
The effective model reproduces the correct behavior in the perturbative regime as by definition its Taylor series is identical to the epCUT result up to the considered order, but in addition, it comprises contributions up to infinite order.[5] Those higher order contributions are a result of feedback effects emerging between the coefficients as they evolve during the flow, as illustrated in the flow diagram in Figure 2.3. Accordingly, this approach serves as an extrapolation

[5]Note, that the effective model $H(x)$ as a function of the parameter x is only defined by the corresponding set of differential equations which has to be integrated for each value of x. In general, it is not possible to determine the concrete analytic function $H(x)$.

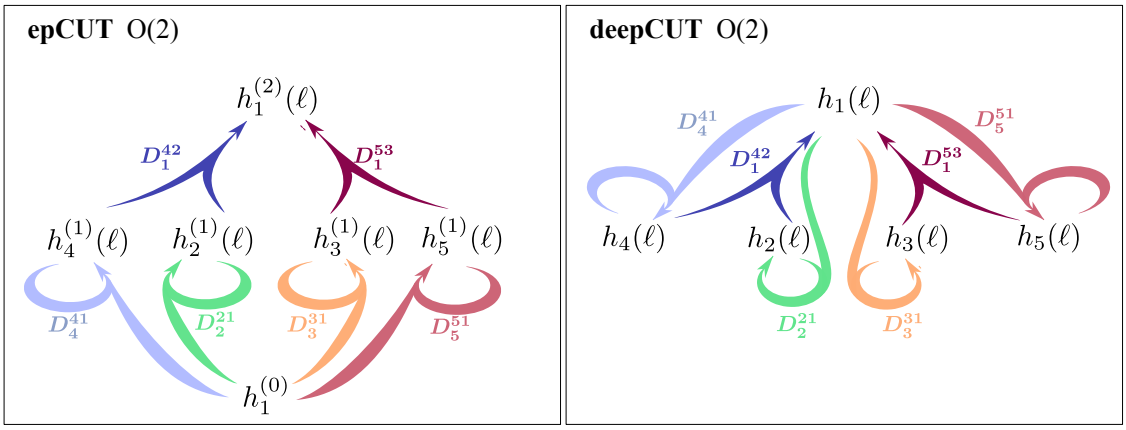

Figure 2.3: Illustration of the flow diagram for the exemplary Hamiltonian in (2.16) comparing the perturbative flow equations (epCUT) for the coefficient h_1 in order $n = 2$ and the corresponding directly evalued version (deepCUT). The perturbative flow equations exhibit a hierarchy from low to high orders. In the directly evalued flow equations this hierarchy is voided introducing feedback effects between h_1 and the remaining coefficients h_i. Thus, there is a wider interdependency between the flow of the coefficients. Different colors are used for the arrows to identify related interdependencies in the perturbative and non-perturbative flow.

scheme of the epCUT result providing a description whose validity goes beyond the perturbative regime.

In the standard deepCUT approach, as proposed in reference [44], the flow equations for each targeted quantity in the effective model, as for example the ground state energy or one quasi-particle energies, comprise only those contributions D_i^{jk} which arise in the corresponding perturbative expansion. However, the authors also mention the possibility to combine contributions of different targeted quantities, which in general extend the flow equations of certain coefficients depending on their hierarchy. In this sense, the equations of the considered target quantities are evaluated in parallel, thereby inducing further feedback effects. The flow diagram in Figure 2.4 shows how such an extension may influence the structure of the flow equations.

Previous studies based on high order series calculations in real space suggest that extensions of this kind provide less robust extrapolations [71]. The author argues that this behavior might occur due to the inclusion of spurious higher order contributions which overestimate certain physical effects. However, there are no general rules known yet concerning the validity of this approach known, yet. Especially, when high orders are not accessible, the extended truncation may improve the results and should be therefore considered as a valid alternative in individual cases.

So far, we have presented the general technical framework of the CUT methods mainly focusing on the sCUT and (de)epCUT approaches which are based on second quantization. In the following sections we want to discuss how these tools can be applied to systems exhibiting gapless excitations.

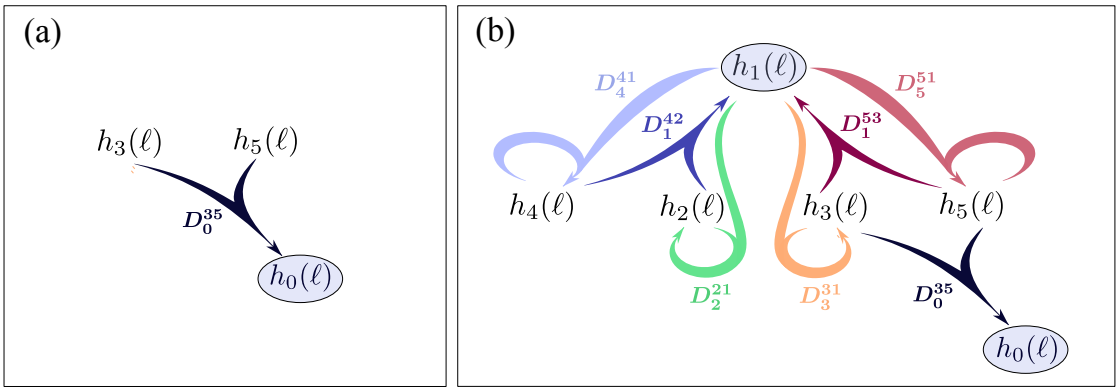

Figure 2.4: Two flow diagrams are illustrated exemplifying the effects which arise by the inclusion of an additional target quantity in the context of a deepCUT approach. Targeted quantities are highlighted by a surrounding ellipse. **(a)** The flow diagram for the coefficient h_0 (ground state energy) obtained by the deepCUT approach in order $n = 2$ is depicted. In **(b)** the coefficient h_1 is considered as an additional targeted quantity which is evalued in parallel to the flow of h_0. Consequently, the flow of h_0 is influenced by additional higher order contributions emanating from h_4 and h_2.

2.3 CUTs for gapless quantum phases

The quantitative description of gapless quantum systems presents a demanding challenge in many body theory. There is a multitude of scenarios, where gapless systems arise, for example, at critical points in continuous phase transitions [79] or when long range order spontaneously breaks a global continuous symmetry giving rise to massless Goldstone bosons [23, 24, 80]. An essential feature which all those systems have in common is the scale invariance at low energies which is associated with a diverging correlation length in the ground state [7, 81]. From a methodical point of view fundamental difficulties arise in CUT approach due to the lack of a characteristic energy and length scale complicating the derivation of effective low energy models for lattice systems with a gapless energy spectrum.
The CUT method provides a considerable contribution to the understanding of gapped quasi-particles. It allows the computation and in-depth interpretation of particle dynamics and interactions by describing intricate phenomena such as quasi-particle decay, the formation of bound states and the emergence of multi-particle resonances in a wide range of different systems. However, in standard CUT approaches quantum fluctuations are primarily truncated by their spatial range and as a consequence the application is limited to systems with a finite energy gap. The use of CUTs for the analysis of gapless quasi-particles is therefore highly desirable.
We motivate the application of CUTs in momentum space providing a methodical extension which enables the analysis of gapless excitations in quantum phases with long range order. In this context, we expose the difficulties and limitations of common approaches and discuss the primary challenges in the derivation of effective models for gapless quasi-particles.

2.3.1 Limitations of effective quasi-particle descriptions

In the standard CUT approach based on real space expansions the lattice Hamiltonian is separated into two parts $H = H_0 + V$, similar to a perturbative ansatz. The first part H_0 generally

describes local degrees of freedom which are completely decoupled from each other and, therefore, can be considered independently. Their local eigen space is used to define quasi-particles. The lowest eigenstate is interpreted as the vacuum, whereas the excited states are assigned to the corresponding quasi-particles. Consequently, the groundstate of H_0 is a product state of local vacua and the quasi-particles are identified with local excitations (see Figure 2.5(a)).
The remaining part V couples the local degrees of freedom turning the Hamiltonian into a complicated many body problem. Typically, this term describes dynamics and interactions, i.e., quasi-particles start to move and to influence each other. Moreover, it contains quantum fluctuations in the number of quasi-particles i.e., the number of quasi-particles is not conserved. The particle conserving CUT leads to a basis for which those quantum fluctuations in the Hamiltonian vanish, i.e., the number of quasi-particles is a conserved quantity. In the course of the CUT all quantum fluctuations which change the number of excitations are absorbed into particle conserving processes, thereby renormalizing the energetic and dynamic properties of the quasi-particles as well as their mutual interaction (see Figure 2.5(b)). Similar to a scaling approach, high energy degrees of freedom (i.e., large number of excitations) are integrated out [59] and lead to renormalized low energy degrees of freedom, which are assumed to be well described by the physics of a few quasi-particles.
The contributions that account for the renormalization can be ascribed to virtual quantum fluctuations in real space as illustrated in Figure 2.5.
The interpretation in terms of real space fluctuations has its origins in perturbative expansions; e.g. in pCUT [56], but it also applies to non-perturbative approaches [34]. The thermodynamic limit gives rise to an infinite number of real space fluctuations. However, one can exploit the linked cluster theorem, which states that only real space fluctuations on linked clusters have a finite contribution [82, 83].[6] Thus, all coefficients of the effective model can be decomposed into terms defined on finite clusters. This enables expansions about a local limit H_0, meaning that contributions with increasing spatial range are systematically incorporated into the effective model. Eventually, one has to truncate at some finite range due to increasing computational costs. This procedure is generally referred to as a linked cluster expansion [85, 86].
The resulting effective model contains quantum fluctuations up to a finite range R. For instance, the ground state can be seen as the local vacuum with additional zero point fluctuations up to a spatial range R. The effective excitations are spatially distributed composite states of local excitations also referred to as dressed quasi-particles. As a consequence of the real space truncation, the correlations between the local degrees of freedom in the effective system are vanishing $\langle\langle O(0)O(r)\rangle\rangle_{\text{eff}} = 0$ for any $r > R$. It may be inferred that the effective model is a good approximation as long as quantum fluctuations with a range $r > R$ are negligible. This is indeed the case for gapped systems for which the asymptotic behavior of the correlation function displays an exponential decay with $\langle\langle O(0)O(r)\rangle\rangle \propto \exp(-\zeta r)$ where ζ denotes the characteristic correlation length [81].
In typical applications (e.g. when analyzing a continuous quantum phase transition from a gapped phase) it is observed that, as the system $H(\lambda)$ approaches a critical point λ_c, the length scale of the quantum fluctuations increases and, thus, more and more contributions with larger and larger spatial range have to be taken into account.
From scaling theory it is known that, close to the critical point, the energy gaps scales as $\Delta \propto \zeta^{-z} \propto |\lambda - \lambda_c|^{\nu z}$ where ν is the corresponding critical exponent and z denotes the dynamic exponent. Thus, once the gap closes, the correlation length ζ diverges and the effective

[6] The linked cluster theorem is related to the linked diagram theorem known from Rayleigh-Schroedinger perturbation theory [84] For a discussion on linked cluster expansions in the context of CUTs see Ref. 53.

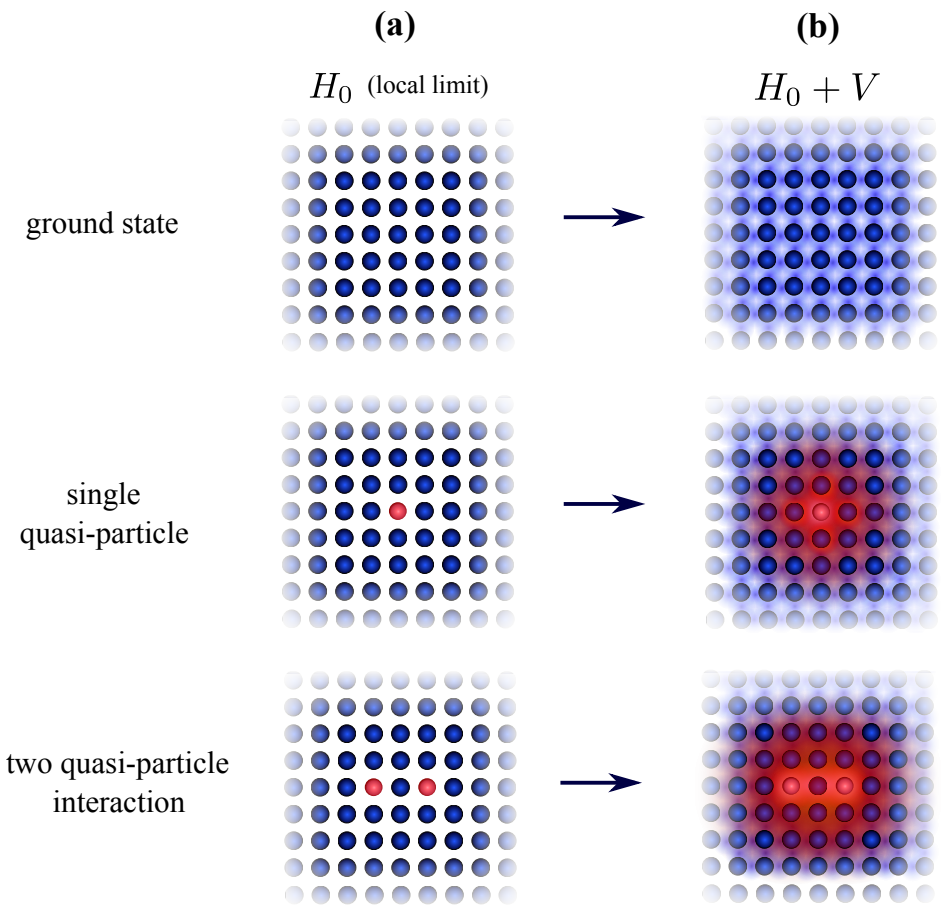

Figure 2.5: Illustration of the general idea behind the real space approach. In **(a)** the local limit is depicted. The eigen states are product states of local degrees of freedom illustrated by spheres. The ground state is given by a product state of local vacua (i.e., no local excitations) displayed as blue spheres. Local excitation are interpreted as quasi-particles represented by a red sphere. **(b)** The remaining part V couples the local degrees of freedom which are thereby delocalized due to quantum fluctuations.

description eventually breaks down. The elementary excitations can no longer be interpreted as local distortions but rather as objects with a spatial extension on arbitrary length scales. Consequently, it is very difficult to study gapless systems based on expansions about a gapped phase. Figure 2.6 illustrates the generic problems of the real space approach.
We encounter a similar situation when the system's ground state spontaneously breaks a global continuous symmetry evoking long range order. In this case the famous Goldstone theorem predicts the emergence of gapless bosons also known as Goldstone bosons [24]. These elementary excitations can be envisioned as collective modes inducing small deviations from the long range order with infinite spatial extension and arbitrary small energy. Two important examples of Goldstone bosons in condensed matter are acoustic phonons, which arise due to the broken translational symmetry in crystals [87], and spin waves in magnetic systems with broken rotational spin symmetry(SU(2) symmetry) [88].
Similar to a critical point the system is scale invariant at low energies, which also becomes manifest in the dispersion of the low energy excitations. The energy-momentum relation is

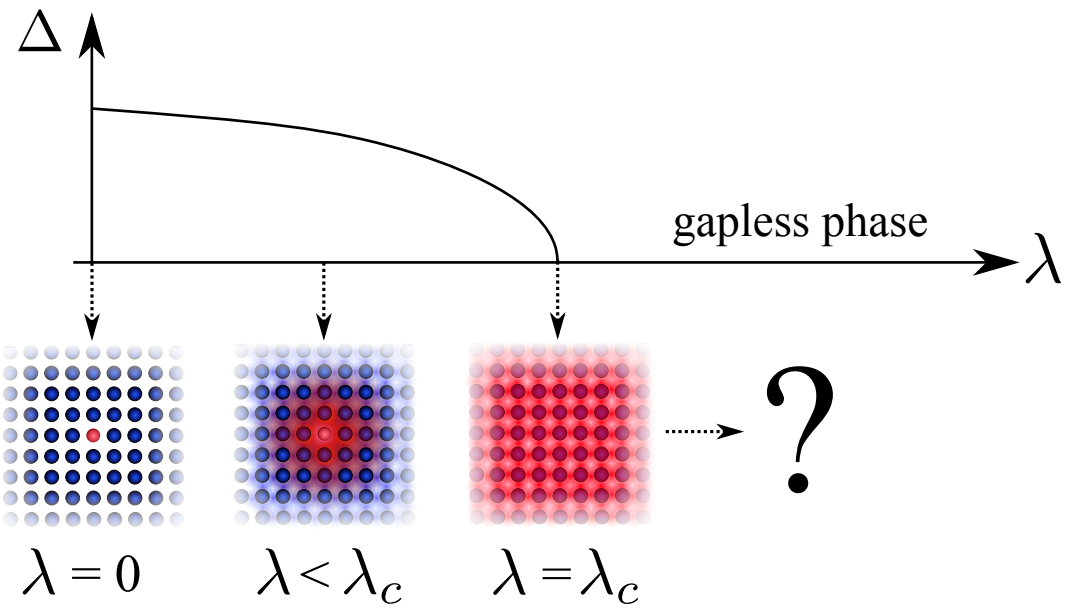

Figure 2.6: Illustrating the generic behavior of quantum fluctuations upon approaching a quantum critical point which, in this example, separates a gapped from a gapless phase. The initial particle description breaks down beyond the critical point.

invariant under scaling transformations, i.e., it does not change no matter how far one zooms in. This is not the case in the presence of a finite energy gap as seen in Figure 2.7. In general, it is difficult to capture this behavior by means of a linked cluster expansion. In order to reach the scaling limit, sophisticated extrapolation schemes are required, which are of moderate accuracy in the majority of cases. This fundamental limitations render it difficult to study gapless systems based on expansions about a gapped phase.

Common methods for the analysis of critical phenomena and gapless phases are based on renormalization group approaches and effective field theories [7, 36, 81, 89]. For instance, in the Landau Ginzburg Wilson approach a field is introduced representing the order parameter of the spontaneously broken symmetry in the continuum limit as depicted in Figure 2.8, where the dynamics and interactions of the excitations are expressed in powers and gradients of the field. These methods are powerful tools to study criticality and universal behavior as their particular strength lies in the direct exploitation of scale invariance. However, their validity is restricted to the limit of long wavelengths as they involve a certain momentum cutoff fading out the microscopic information (see also Figure. 2.8).

The field-theoretic approach can be viewed as an expansion about long wavelengths, whereas the real space expansions typically show a faster convergence at short wavelengths. In either way, it is difficult to obtain an effective quasi-particle description that is quantitatively valid for all length scales. This inevitably complicates the analysis of gapless phases, especially when physical processes on very different length scales are involved and detailed knowledge about particle dynamics and interactions in the whole Brillouin zone is required.

The presence of long range order and strong short range interactions is also the reason for the apparent incoherence between high energy magnons and spin wave theory discussed in section 4.1. Therefore, a methodical advancement is of crucial importance for a better understanding of the nature of gapless excitations.

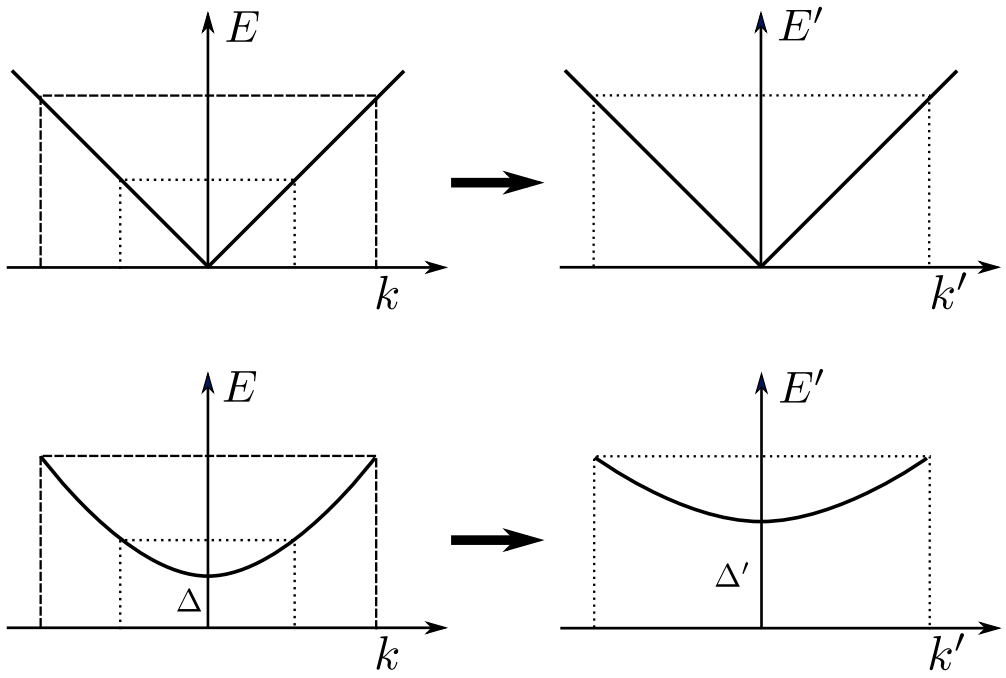

Figure 2.7: This sketch illustrates the scale invariance of the low energy excitations in a gapless phase (see **(a)**). The energy momentum relation can be described by a scale invariant curve $\omega(\lambda k) = \lambda^{\alpha}\omega(k)$ in the vicinity of the closing gap. In this example we have $\alpha = 1$. **(b)** By contrast, gapped excitations do not exhibit scale invariance at low energies.

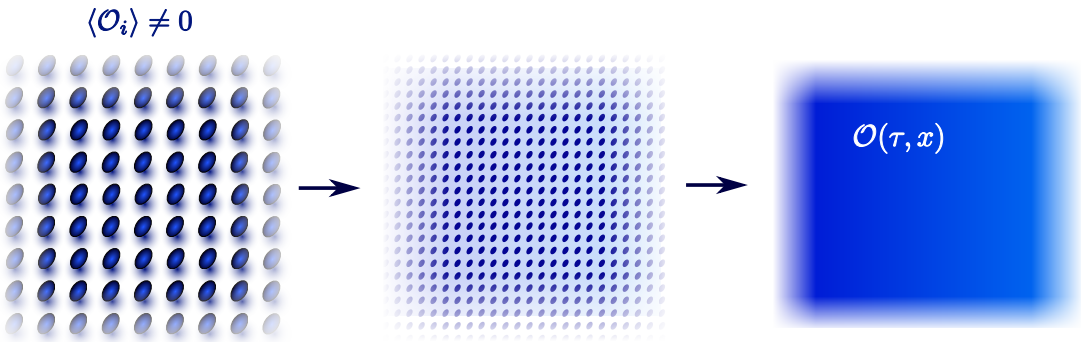

Figure 2.8: The idea behind the field theoretic analysis of systems with a broken continuous symmetry is sketched. The broken continuous symmetry is quantified by a local order parameter $\langle \mathcal{O}_i \rangle$. In the scaling limit the concrete microscopic information becomes irrelevant and the discrete order parameter can be replaced by a continuous field.

In the next section we turn our attention to the application of the CUT method in momentum space and its advantages for the description of gapless quasi-particles.

2.3.2 Momentum space representation

In quantum mechanics any representation is equally justified in the sense that the Hamiltonian describes the same physical laws independent of its representation. This is indeed true as long as the Hamiltonian is treated exactly. However, once a truncation scheme or approximation has to be employed the representation has a major impact on which part of the Hilbert space is discarded.
The representation of translational invariant lattice Hamiltonians in reciprocal or momentum space implies many advantages for the utilization of CUTs to gapless systems. In momentum space the basis states are described by Bloch wave functions $|\psi_k\rangle$ [90] which are eigenstates of translations by lattice vectors $\mathbf{r}$ with

$$T(\mathbf{r})\,|\psi_{\mathbf{k}}\rangle = \mathrm{e}^{\mathrm{i}\mathbf{k}\mathbf{r}}\,|\psi_{\mathbf{k}}\rangle \tag{2.17}$$

where $\mathbf{k}$ denotes the total momentum (or crystal momentum). The crystal momentum is a conserved quantum number of the system, which can take any value in the first Brillouin zone (1^{st}BZ), the primitive cell of the reciprocal lattice. Consequently, the basis states $|\psi_{\mathbf{k}}\rangle$ are completely determined by their behavior in a single BZ.
We use the formalism of second quantization as it provides a natural language in terms of quasi-particles. The particle creation operators in momentum space $a^\dagger_{\mathbf{k}}$ are related to local creation operators $a^\dagger_{\mathbf{r}}$ by a Fourier transform

$$a^\dagger_{\mathbf{k}} = \frac{1}{\sqrt{N}} \sum_{\mathbf{r}} a^\dagger_{\mathbf{r}} \mathrm{e}^{\mathrm{i}\mathbf{r}\mathbf{k}} \quad . \tag{2.18}$$

with N denoting the number of primitive cells. Thus, in momentum space the quasi-particle created by $a^\dagger_{\mathbf{k}}$ is not a local excitation but a collective mode distributed over the whole real space range. It is specified by its wave number $\mathbf{k}$ which is reciprocal to the coordinates in real space. This proves beneficial for the description of gapless lattice models, since, in principle, all length scales are represented in the first Brillouin zone (BZ): long wavelengths (small wave numbers $\mathbf{k} \sim 0$) in the center of the BZ are related to large length scales and small wavelengths (large wave numbers) at the border of the BZ are associated with short length scales.
In order to point out the major advantage of the momentum space representation we may consider, for instance, the standard linear spin wave theory for the antiferromagnetic Heisenberg model where the spin degrees of freedom are represented by bosons. On a bilinear level in boson operators the Hamiltonian can be diagonalized by a Bogoliubov transformation in momentum space giving rise to gapless spin waves with a linear dispersion in the vicinity of $\mathbf{k} = (0,0)$ and $\mathbf{k} = (\pi,\pi)$ [16, 21]. The description of those excitations in real space, however, is non-trivial even at the stage of the bilinear approximation, because the quantitative description of the closing gap at $\mathbf{k} = (0,0)$ or $\mathbf{k} = (\pi,\pi)$ based on real space expansions would require the incorporation of contributions up to infinite spatial range.
So in contrast to the real space approach, it is possible to decompose the Hamiltonian in momentum space according to $H_0 + V$ such that the initial excitations in H_0 are described in terms of gapless quasi-particles, whereas the residual part V introduces higher level interactions. This

marks an important advantage, because the initial basis already embodies excitations with arbitrary small energy and, hence, the effects of quasi-particles interactions contained in V can be studied directly within a gapless phase. Eventually, the effective model of the full Hamiltonian including the residual part V is obtained by means of a particle conserving CUT analogous to the real space approach.
The presented CUT methods in second quantization allow a direct evaluation in momentum space giving rise to a variety of possible truncation schemes which are inherently different from real space truncations.

2.3.3 Effective descriptions for gapless quasi-particles

Of course the applicability of the described approach requires the existence of a distinct quasi-particle describing the system's excitations. Analogous to gapped systems, quasi-particle decay can complicate the derivation of the effective model or even render the approach completely ineffecient. In fact, gapless quasi-particles is much more fragile, compared to particles with a finite gap, because there is no energy separation between subspaces of different quasi-particle number. In the following we explicate some of the consequences and restrictions for effective quasi-particle descriptions resulting from the absence of an energy gap. For this purpose, we briefly discuss how the spectral properties of a gapped system are interpreted in terms of quasi-particles and how this interpretation applies to gapless excitations in particular addressing the requirements for a well defined quasi-particle picture.

Effective spectral densities

The information about the dynamical properties of elementary excitations and their mutual interaction is encoded in the eigenstates and the corresponding energy spectrum. In experimental setups this spectral information can be probed indirectly by observables which couple to the eigenstates (e.g. in a certain subspace) providing a characteristic spectral imprint of the system. Theoretically, this spectral information is represented by spectral densities or dynamic structure factors.
As we already discussed, the quasi-particle conserving effective model leads to a considerable simplification in the evaluation and interpretation of spectral densities. We consider a momentum resolved observable $\mathcal{O}_{\text{eff}}(\mathbf{k})$ in the effective basis which in general does not conserve the number of quasi-particles. Thus, it contains operator terms of the form

$$\mathcal{O}^{\dagger}_{\text{eff}}(\mathbf{k}) = \sum_{n,m} \mathcal{O}^{(n,m)}_{\text{eff}}(\mathbf{k}) \tag{2.19}$$

where $\mathcal{O}^{(n,m)}_{\text{eff}}$ denotes the part of the observable containing m annihilation and n creation operators assuming normal ordering.
Due to the block diagonality of the effective Hamiltonian the relevant resolvent $\mathcal{R}^{\mathcal{O}}(\omega, \mathbf{k})$

obtained from the retarded zero temperature Greens function splits into contributions of separated quasi-particle sectors

$$\begin{aligned}\mathcal{R}^{\mathcal{O}}(\omega,\mathbf{k}) &= \langle 0|\,\mathcal{O}^{\dagger}_{\text{eff}}(\mathbf{k})\frac{1}{\omega-(H_{\text{eff}}-E_0)}\mathcal{O}_{\text{eff}}(k)\,|0\rangle \\ &= \sum_n \langle 0|\,\mathcal{O}^{(0,n)}_{\text{eff}}(\mathbf{k})\frac{1}{\omega-(H_{\text{eff}}-E_0)}\mathcal{O}^{(n,0)}_{\text{eff}}(\mathbf{k})\,|0\rangle \\ &= \sum_n \mathcal{R}^{(\mathcal{O},n)}(\omega,\mathbf{k}) \quad ,\end{aligned} \tag{2.20}$$

because any function $F(H_{\text{eff}})$ will maintain the conserved quantities of H_{eff}. Accordingly, the spectral density can be decomposed into parts with a distinct number of quasi-particles

$$\begin{aligned}I^{\mathcal{O}}(\omega,\mathbf{k}) &= -\frac{1}{\pi}\text{Im}\;\mathcal{R}^{\mathcal{O}}(\omega,\mathbf{k}) = \sum_n -\frac{1}{\pi}\text{Im}\;\mathcal{R}^{(\mathcal{O},n)}(\omega,\mathbf{k}) \\ &= \sum_n I^n(\omega,\mathbf{k}) \quad .\end{aligned} \tag{2.21}$$

In the one quasi-particle subspace the effective Hamiltonian is given by

$$H^{1\text{qp}}_{\text{eff}} = E_0 + \sum_{\mathbf{k}} \omega(\mathbf{k})\; n_{\mathbf{k}} \tag{2.22}$$

with the quasi-particle number operator $n_{\mathbf{k}} = a^{\dagger}_{\mathbf{k}} a_{\mathbf{k}}$, the effective quasi-particle dispersion $\omega(\mathbf{k})$ and the effective ground state energy E_0. The resulting spectral density in the single quasi-particle subspace reads

$$\begin{aligned}I^{1\text{qp}}(\omega,\mathbf{k}) &= -\frac{1}{\pi}\text{Im}\;\langle 0|\,\mathcal{O}^{(0,1)}_{\text{eff}}(\mathbf{k})\frac{1}{\omega-\sum_{\mathbf{k}}\omega(\mathbf{k})a^{\dagger}_{\mathbf{k}}a_{\mathbf{k}}}\mathcal{O}^{(1,0)}_{\text{eff}}(\mathbf{k})\,|0\rangle \\ &= -\frac{1}{\pi}\text{Im}\;\frac{\langle 0|\,\mathcal{O}^{(0,1)}_{\text{eff}}(\mathbf{k})\mathcal{O}^{(1,0)}_{\text{eff}}(\mathbf{k})\,|0\rangle}{\omega-\omega(\mathbf{k})} \\ &= \langle 0|\,\mathcal{O}^{(0,1)}_{\text{eff}}(\mathbf{k})\mathcal{O}^{(1,0)}_{\text{eff}}(\mathbf{k})\,|0\rangle\;\;\delta\left(\omega-\omega(\mathbf{k})\right) \quad .\end{aligned} \tag{2.23}$$

Note, that the states $\mathcal{O}^{(1,0)}_{\text{eff}}(\mathbf{k})\,|0\rangle$ describe single moving objects (particles or waves) and in translational invariant systems their energy is unambiguously determined by their total momentum. The resulting spectral density is a δ-peak located at the 1qp energies with a momentum dependent weight. This quasi-particle weight $W^{1\text{qp}}(\mathbf{k}) = \langle 0|\,\mathcal{O}^{(0,1)}_{\text{eff}}(\mathbf{k})\mathcal{O}^{(1,0)}_{\text{eff}}(\mathbf{k})\,|0\rangle$ specifies the response of the corresponding state to the observable.
States with more than one quasi-particle comprise additional degrees of freedom as the individual momenta of the quasi-particles are only confined by the conservation of the total momentum. In general, these independently moving particles will form a continuum of states.

The upper and lower edge of the corresponding energy spectrum is determined by the maximum and minimum energy of the free multi-particle states

$$E_l^{n\text{-qp}}(\mathbf{k}) = \min\left(\sum_{\mathbf{k}_1\ldots\mathbf{k}_n} \omega(\mathbf{k}_i)\middle|\sum_i \mathbf{k}_i = \mathbf{k}\right) \tag{2.24a}$$

$$E_u^{n\text{-qp}}(\mathbf{k}) = \max\left(\sum_{\mathbf{k}_1\ldots\mathbf{k}_n} \omega(\mathbf{k}_i)\middle|\sum_i \mathbf{k}_i = \mathbf{k}\right) \quad . \tag{2.24b}$$

The spectral density $I^{n\text{-qp}}(\omega, \mathbf{k})$ is a continuous distribution function rendering the weight of the observable in this energy band. The computation of these spectral densities is much more involved because one has to take multi-particle interactions into account. A procedure for the general evaluation of these resolvents is described in section 3.3.
Strong interactions can also lead to bound or anti-bound states at energies that are located outside the continuum. These multi-particle states arise, when the dynamics of the individual particles is confined by the interaction, for instance, when particles move as a single unit due to strong attractive mutual interaction. These states have the same spectral signature as single particle states, namely a δ-peak.
Figure 2.9 illustrates the decomposition of the spectral density in terms of quasi-particle sectors for a generic gapped system. This subdivision is well-defined, as long as the quasi-particle sectors connected by scattering processes in V are energetically well separated. The energetic separation is an important requirement for an adequate performance of the particle conserving approach. In the most extreme case, energetic overlaps between different quasi-particle states which share the same quantum numbers preclude a characterization in terms of quasi-particles and phenomena such as quasi-particle decay occur [51].

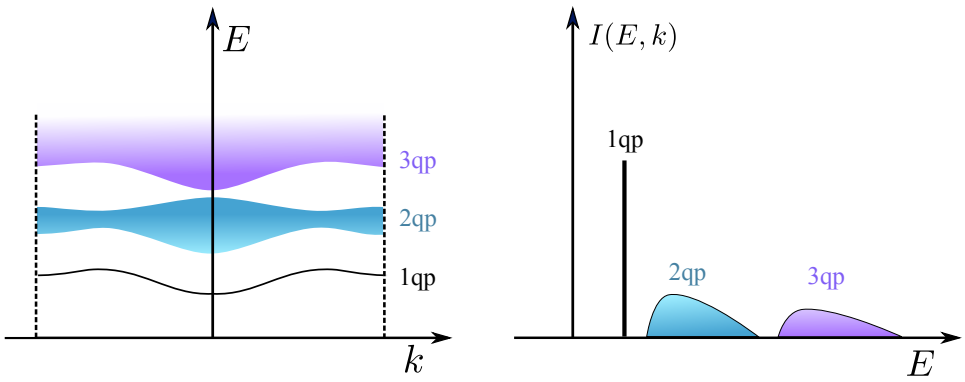

Figure 2.9: A generic energy spectrum of a gapped system is shown. In areas, where different quasi-particle states overlap, the quasi-particle description becomes deficient if the corresponding subspaces are connected by terms in the Hamiltonian.

In specific cases a substantial shift of 1qp spectral weight into the continuum due to interactions is observed when 1qp states are energetically close to the continuum as shown in Figure.2.10. The simultaneous reduction of the quasi-particle weight and the formation of resonances in the continuum is sometimes referred to as a precursor of fractionalization [13, 30].
The central idea behind the concept of *fractionalization* is, that the elementary excitations of the system move as if they were composed of smaller deconfined constituents with fractional

quantum numbers. This implies that the spectral weight in the continuous energy band is ascribed to a continuum of *fractional* excitations, in contrast to the conventional picture, where these states are interpreted as multi-particle states of dressed integer excitations.
An important example of fractionalized quasi-particles are gapless spinons in the uniform antiferromagnetic 1D chain [91–93]. For any finite dimerization, the elementary excitations are gapped and can be either described as integer quasi-particles, triplons (S = 1), or as a bound state of two spinons (S = 1/2) [13, 14, 94].
For zero dimerization the single triplon weight vanishes at all wavevectors leading to a singularity at the lower edge of the continuum as depicted in Figure 2.10. In this case, one would expect that the quasi-particle approach based on integer triplons is not suitable. But in fact, the situation is much more subtle. Schmidt and Uhrig have shown that both approaches provide quantitatively valid descriptions. i.e., the continuum can be either described in terms of two integer quasi-particles, triplons ($S = 1$), or two fractional spinons ($S = 1/2$) [14]. Consequently, both schemes may be viewed as different representations of the same phenomenon.

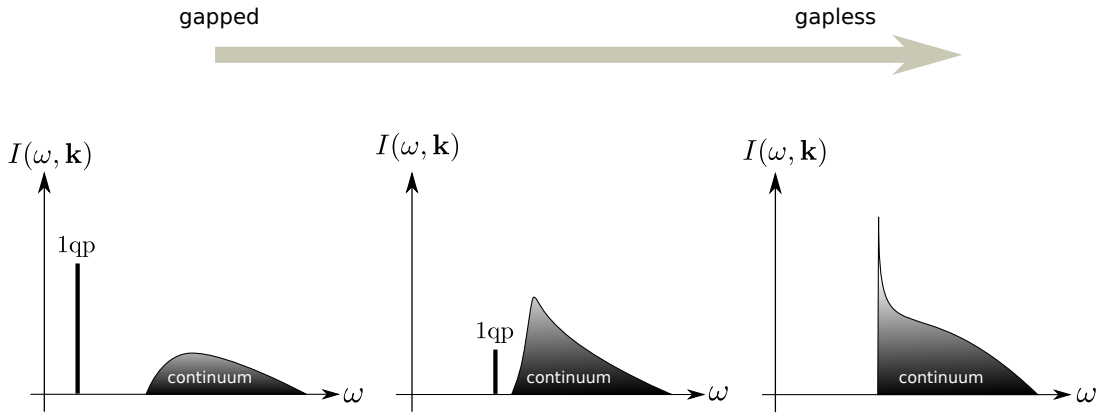

Figure 2.10: The phenomenon of a vanishing single particle weight is illustrated by means of the spectral density evolving from a gapped into a gapless system. This possible scenario is, for instance, observed in the dimerized spin-1/2 antiferromagnetic chain [14]. In the case of zero dimerization, the system becomes critical and the quasi-particle weight vanishes at all wave vectors $\mathbf{k}$.

This ambiguity has led to an extensive debate about the nature of the corresponding elementary excitations in quantum antiferromagnets [13, 14, 28, 95–97]. A further discussion on this issue in the context of the square lattice antiferromagnet is also given in section 4.1.
The requirement of energetic separation between different quasi-particle subspaces has important consequences for the effective description of gapless excitations. Here, the continuum is directly adjacent to the quasi-particle dispersion because a generic multi-particle state can be build by an arbitrary number of zero energy modes as illustrated in Figure 2.11. This leads to certain intricacies which we want to discuss in the following.
The initial quasi-particle description defined by H_0 is supposed to provide a distinct single particle state, which lies energetically below its multi-particle continuum. In general, there is no energetic separation between different multi-particle subspaces for gapless quasi-particles. In order to distinguish between these subspaces, additional conserved quantum numbers as for example the total spin are helpful.

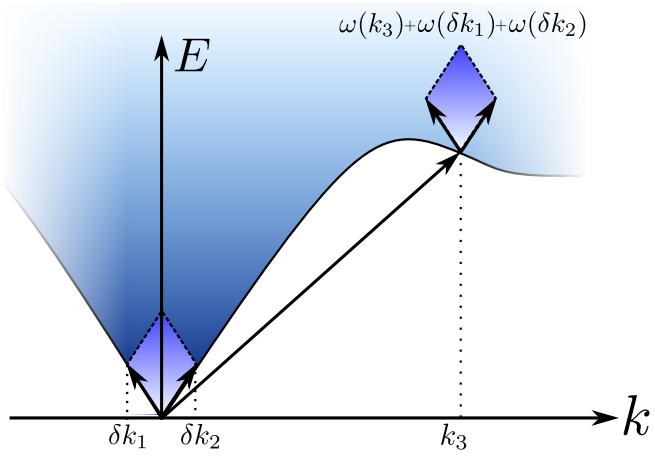

Figure 2.11: A sketch of the states at the lower edge of the multi-particle continuum is depicted. These states are mainly composed of low energy modes located at long wavelengths $\mathbf{k} = 0$. This principle also applies to subspaces of arbitrary quasi-particle number.

In a best case situation, the lower edge of the multi-particle continuum directly adjoins the dispersion in the whole Brillouin zone. The corresponding spectral density splits into a δ-function with finite weight located at the one particle dispersion and an incoherent part representing the multi-particle continuum as shown in Figure 2.12. As we already discussed, energetic over-

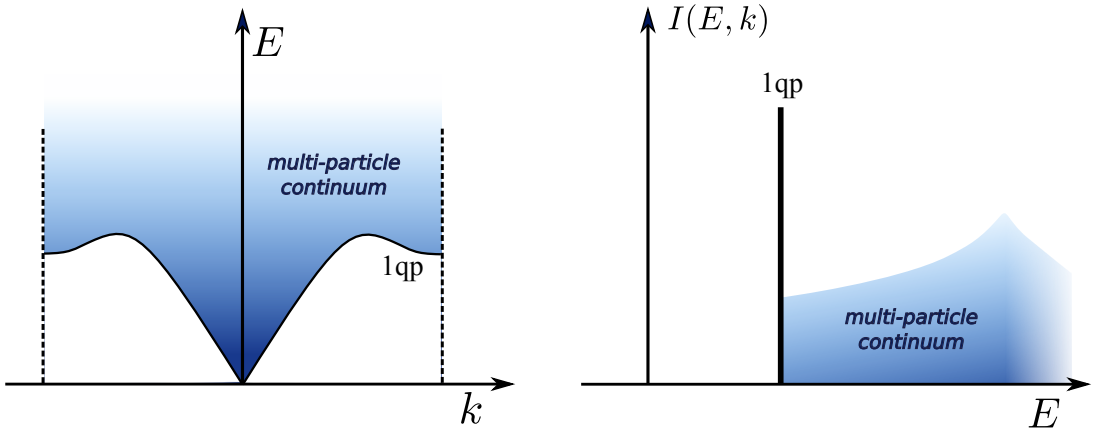

Figure 2.12: Illustration of the energy spectrum and spectral density of a gapless system with a distinct quasi-particle state. The quasi-particle dispersion is adjacent to the lowest edge of the multi-particle continuum (left panel) featuring a finite quasi-particle weight in the spectral density (right panel).

lap between the 1qp states and the multi-particle continuum leads to deficient quasi-particle states in the corresponding area. This imposes additional constraints on the particle dispersion in H_0 as the lower edge of the continuum is directly related to the contour of the dispersion. A necessary condition is that the particles exhibit a linear energy momentum $E \propto k^\nu$ with $\nu = 1$ relation at $\mathbf{k} = 0$.[7] By contrast, for quasi-particles with a non-linear dispersion relation $E \propto k^\nu$ and $\nu > 1$, the lower edge of the multi-particle continuum lies energetically below the

[7] A non-linear energy momentum relation $E \propto k^\nu$ with $0 < \nu < 1$ would also comply with the requirements, however, these particles would exhibit an infinite group velocity at $\mathbf{k} = 0$. Thus, we restrict our considerations to particles with a linear dispersion relation at long wavelengths.

one-particle dispersion at the whole BZ as illustrated in Figure 2.13.

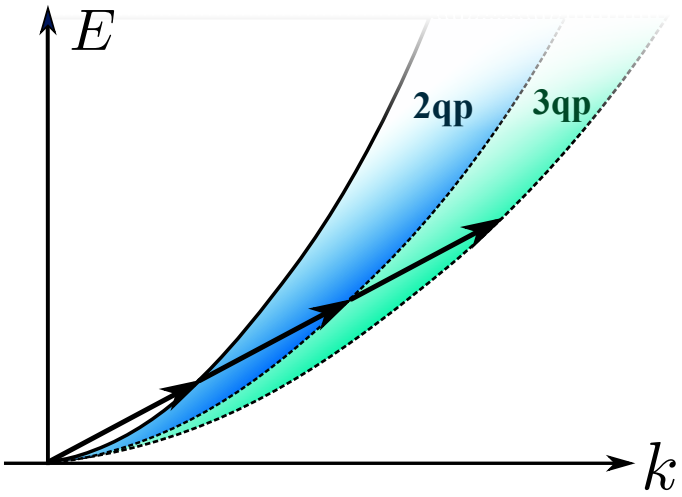

Figure 2.13: The lower edges of the multi-particle continua for a gapless quasi-particle with quadratic dispersion relation are sketched.

As a consequence, the description of excitations in terms of quasi-particles in H_0 is ill-posed, because the processes in the residual part V would inevitably lead to quasi-particle decay even at arbitrary small energies, i.e., the quasi-particle can no longer be described by a sharp δ-peak. The standard particle conserving CUT approach breaks down unless the qp-sectors are protected by additional conserved quantum numbers which would imply that all processes changing the number of quasi-particles are zero. Magnons in the Heisenberg ferromagnet, for instance, exhibit a quadratic dispersion relation [98, 99].
In summary, we infer that the quasi-particle approach is suitable for gapless systems with a linear dispersion at long wavelengths.

2.4 Application and interpretation of CUTs in momentum space

In this section, the concrete application of the CUT approach in momentum space is discussed. In this thesis, we restrict our considerations to bosonic excitations as we are interested in an effective description of gapless magnons.
In the first part the general setup is specified. Then we explicate the general derivation of flow equations in momentum space and introduce a concept which considerably simplifies this task by means of a pictorial representation of operator terms. Based on this concept, we examine the CUT approach in momentum space with regard to its diagrammatic representation. For this purpose, the generic structure of the perturbative solution is analyzed pointing out the link to diagrammatic perturbation theory and the interpretation in terms of virtual fluctuations. The extension of this interpretation to non-perturbative CUTs in momentum space allows us to translate the abstract flow equations into a more physical language. The diagrammatic approach visualizes the effects of non-perturbative truncation schemes and provides an intuitive picture of the resulting effective quasi-particle description.
The subsequent section deals with a non-perturbative truncation criterion, the scaling dimension of operator terms, which is particularly suited to the analysis of gapless quasi-particles.

2.4.1 General setup

We consider a translational invariant lattice Hamiltonian $\mathcal{H}_{\text{init}}$ in momentum space is decomposed into

$$\mathcal{H}_{\text{init}} = \mathcal{H}_0 + \mathcal{V} \quad . \tag{2.25}$$

The first part $\mathcal{H}_0$ describes a system of free gapless excitations

$$\mathcal{H}_0 = E_0 + \sum_{\mathbf{k}} \omega_{\mathbf{k}} \alpha_{\mathbf{k}}^\dagger \alpha_{\mathbf{k}} \tag{2.26}$$

where E_0 denotes the vacuum energy and $\omega_{\mathbf{k}}$ is the dispersion. The vacuum state is supposed to break a continuous symmetry giving rise to Goldstone bosons which are expressed in terms of creation and annihilation operators $\alpha_{\mathbf{k}}^\dagger$ and $\alpha_{\mathbf{k}}$. The excitations are considered to exhibit a linear dispersion $\omega_{\mathbf{k}} \propto |\mathbf{k}|$ at long wavelengths $|\mathbf{k}| \ll 1$.
The residual part can be decomposed into

$$\mathcal{V} = \mathcal{V}_0 + \mathcal{V}^+ + \mathcal{V}^- \quad . \tag{2.27}$$

The terms in $\mathcal{V}_0$ conserve the number of quasi-particles. They describe mutual interactions between multi-particle states

$$\mathcal{V}_0 = \sum_{n\geq 2} \sum_{\mathbf{k}_1 \ldots \mathbf{k}_{2n}} V_n^n(\mathbf{k}_1, \ldots \mathbf{k}_{2n})\, a_{\mathbf{1}}^\dagger \ldots a_{\mathbf{n}}^\dagger a_{\mathbf{n+1}} \ldots a_{\mathbf{2n}} \quad . \tag{2.28}$$

The parts $\mathcal{V}^+$ and $\mathcal{V}^-$ contain scattering processes which do not conserve the number of bosons

$$\begin{aligned}\mathcal{V}^+ &= \sum_{n>m} \sum_{\mathbf{k}_1 \ldots \mathbf{k}_{n+m}} V_m^n(\mathbf{k}_1, \ldots, \mathbf{k}_n, \mathbf{k}_{n+1}, \ldots, \mathbf{k}_{n+m})\, a_{\mathbf{1}}^\dagger \ldots a_{\mathbf{n}}^\dagger a_{\mathbf{n+1}} \ldots a_{\mathbf{n+m}} \\ \mathcal{V}^+ &= \sum_{n<m} \sum_{\mathbf{k}_1 \ldots \mathbf{k}_{n+m}} V_m^n(\mathbf{k}_1 \ldots, \mathbf{k}_n, \mathbf{k}_{n+1}, \ldots, \mathbf{k}_{n+m})\, a_{\mathbf{1}}^\dagger \ldots a_{\mathbf{n}}^\dagger a_{\mathbf{n+1}} \ldots a_{\mathbf{n+m}} \quad . \end{aligned} \tag{2.29}$$

We denote by $\mathcal{V}^+$ the terms which increase the number of bosons. Accordingly, $\mathcal{V}^-$ denotes the operators which reduce the number of bosons. Note, that we use a shorthand notation for the momenta $\mathbf{k}_i \to \mathbf{i}$ such that $a_{\mathbf{k}_i}^\dagger := a_{\mathbf{i}}^\dagger$ to lighten the notation.
Due to the conservation of total momentum the vertex functions $V_m^n(\mathbf{k}_1, \ldots, \mathbf{k}_n, \mathbf{k}_{n+1}, \ldots, \mathbf{k}_{n+m})$ are only non-zero for

$$\sum_{i \le n} \mathbf{k}_i - \sum_{i \le m} \mathbf{k}_{i+n} = \mathbf{G} \tag{2.30}$$

with $\mathbf{G}$ denoting a reciprocal lattice vector. Thus, they can be also written as

$$V_m^n(\mathbf{k}_1, \ldots, \mathbf{k}_n, \mathbf{k}_{n+1}, \ldots, \mathbf{k}_{n+m}) = \delta_{(n,m)}^{\mathbf{G}}\; v_m^n(\mathbf{k}_1, \ldots, \mathbf{k}_n, \mathbf{k}_{n+1}, \ldots \mathbf{k}_{n+m}) \tag{2.31}$$

with a generalized Kronecker-δ ensuring momentum conservation

$$\delta_{(n,m)}^{\mathbf{G}} = \begin{cases} 1 & \text{for } \sum_{i \le n} \mathbf{k}_i - \sum_{i \le m} \mathbf{k}_{i+n} = \mathbf{G} \\ 0 & \text{otherwise} \end{cases} \quad .$$

For the application of the CUT it is expedient to absorb this Kronecker-δ into the vertex functions because the CUT preserves this property. In the thermodynamic limit we have to consider the continuum limit for which the sums are converted into integrals and the Kronecker-δ is transformed into a δ-distribution. For the sake of clarity, however, we keep the notation for discrete momenta as the continuum limit does not provide any further information and the actual evaluation has to be performed for finite systems anyway.

Symmetrization of coefficients

The assignment of momentum indices among creation operators or annihilation operators of a given monomial is arbitrary because its constituents are commuting, i.e., $[\, a_{\mathbf{k}}^\dagger, a_{\mathbf{k}}^\dagger \,] = 0$ and $[\, a_{\mathbf{k}}, a_{\mathbf{k}} \,] = 0$. Therefore, it is convenient to symmetrize the associated coefficient by rearranging the sums

$$\sum_{\mathbf{k}_1 \ldots \mathbf{k}_{n+m}} V_m^n(\mathbf{k}_1, \ldots, \mathbf{k}_n, \mathbf{k}_{n+1}, \ldots, \mathbf{k}_{n+m})\, a_{\mathbf{1}}^\dagger \ldots a_{\mathbf{n}}^\dagger a_{\mathbf{n+1}} \ldots a_{\mathbf{n+m}} \tag{2.32a}$$

$$= \sum_{\mathbf{k}_1 \ldots \mathbf{k}_{n+m}} V_m^n(\mathbf{k}_1, \ldots, \mathbf{k}_n, \mathbf{k}_{n+1}, \ldots, \mathbf{k}_{n+m}) \frac{1}{n!m!} \sum_{i,j} \mathcal{P}_i(a_{\mathbf{1}}^\dagger \ldots a_{\mathbf{n}}^\dagger) \mathcal{P}_j(a_{\mathbf{n+1}} \ldots a_{\mathbf{n+m}}) \tag{2.32b}$$

$$= \sum_{\mathbf{k}_1 \ldots \mathbf{k}_{n+m}} \frac{1}{n!m!} \sum_{i,j} V_m^n(\mathcal{P}_i^{-1}(\mathbf{k}_1, \ldots, \mathbf{k}_n), \mathcal{P}_j^{-1}(\mathbf{k}_{n+1}, \ldots, \mathbf{k}_{n+m}))\, a_{\mathbf{1}}^\dagger \ldots a_{\mathbf{n}}^\dagger a_{\mathbf{n+1}} \ldots a_{\mathbf{n+m}} \tag{2.32c}$$

where $\mathcal{P}_i(a_{\mathbf{1}}^\dagger \dots a_{\mathbf{n}}^\dagger)$ and $\mathcal{P}_i(\mathbf{k}_1, \dots, \mathbf{k}_n)$ denote a distinct permutation of operators or momenta, respectively. The sums run over all permutations enumerated by the indices i and j. In the third line the permutations are transferred from the operators to the momentum arguments of the vertex functions by a redefinition of momentum indices.
Hence, in the following, the vertex functions are supposed to be symmetrized

$$V_m^n := \frac{1}{n!m!} \sum_{i,j} V_m^n(\mathcal{P}_i(\mathbf{k}_1, \dots \mathbf{k}_n), \mathcal{P}_j(\mathbf{k}_{n+1}, \dots \mathbf{k}_{n+m})) \tag{2.33}$$

This is an essential step to make the definitions of the V_m^n unambiguous. Next, we consider the actual derivation of the flow equations in momentum space.

Deriving flow equations in momentum space

We derive the flow equations (2.2) using the particle conserving generator $\eta(\ell) = \mathcal{V}^+(\ell) - \mathcal{V}^-(\ell)$. The coefficients are ℓ-dependent and become the effective coefficients for $\ell \to \infty$ yielding a quasi-particle conserving system $\mathcal{H}_{\text{eff}} = \mathcal{H}_{0,\text{eff}} + \mathcal{V}_{0,\text{eff}}$ with renormalized dynamics and interaction. The flow of a generic coefficient can be written as

$$\partial_\ell C_\alpha(\vec{i}) = \sum_{\beta,\gamma} \sum_{\vec{j}} D_\alpha^{\beta\gamma} C_\beta(\vec{i}_\beta, \vec{j}) C_\gamma(\vec{i}_\gamma, \vec{j}) \tag{2.34}$$

where $C_\alpha\left(\vec{\mathbf{i}}\right)$ can represent any coefficient in the flowing Hamiltonian. The greek indices denote different types of operator terms and are used to identify the associated coefficient function. The vectors $\vec{i} = (\mathbf{i}_1, \dots \mathbf{i}_l)$ and $\vec{j} = (\mathbf{j}_1, \dots \mathbf{j}_p)$ are used as a short-hand notation for containers of indices, which represent different momentum arguments $\mathbf{k}_i$ and $\mathbf{k}_j$. The momenta $\mathbf{k}_i \in \vec{i}$ are referred to as free momenta because they reflect the momentum dependence of the coefficient at hand. Every free momentum $\mathbf{k}_i \in \vec{i}$ appears as an argument of either C_β or C_γ such that $\vec{i}_\beta \cup \vec{i}_\gamma = \vec{i}$. The $\mathbf{k}_j \in \vec{j}$ are called contracted momenta as they introduce contractions of momentum arguments between pairs of coefficients (see also section 2.4.2 for a detailed explanation).
Evidently, the structure of the flow equations is fully determined by the prefactors $D_\alpha^{\beta\gamma}$ and the contractions between the corresponding coefficients. Then the truncation scheme defines which terms are eventually incorporated into the flow equation. In a rigorous perturbative truncation scheme the coefficients are expanded in powers of a perturbative parameter, which effectively increases the number of coefficients. The values of the prefactors $D_\alpha^{\beta\gamma}$ and the contractions, however, are not affected by the truncation scheme.
The derivation of the prefactors and contractions is based on the evaluation of commutators between the normal ordered monomials, which span the basis of the flowing Hamiltonian and the generator. Typically, the evaluation of these commutators can be cumbersome because one has to keep track of a large number of coefficients and indices. So, in general, it is advisable to perform the derivation by automated computer programs (see section 3.1).
At this point, however, we also want to advert the manual evaluation which can be simplified using a diagrammatic representation of operator terms. As we will discuss in the following, the diagrammatic representation of operator terms not only simplifies the derivation but also provides physical intuition and a better understanding of the flow equation approach in momentum space.

2.4.2 Diagrammatic representation

The diagrammatic approach, first introduced by Feynman [100], is a powerful tool to identify and compute contributions in perturbation theory in a pictorial way, providing visualization of complex phenomena in quantum field theory. The same advantages also apply to the CUT in momentum space for which the transformed coefficients can be interpreted in terms of virtual fluctuations visualized by diagrams.
First, we introduce the diagrammatic representation in the context of the evaluation of commutators. In the subsequent part this concept is extended to the representation of flow equations in momentum space.
In second quantization the commutator of two normal ordered operators can be computed using Wick's theorem [75]. For the purpose of the following derivation, we introduce a shorthand notation for normal ordered operators

$$\mathcal{N}^{\mathbf{i}_1\ldots\mathbf{i}_n}_{\mathbf{j}_1\ldots\mathbf{j}_m} := a^\dagger_{\mathbf{i}_1}\ldots a^\dagger_{\mathbf{i}_n}\, a_{\mathbf{j}_1}\ldots a_{\mathbf{j}_m} \quad . \tag{2.35}$$

with n and m referring to the number of creation or annihilation operators. In this notation Wick's theorem reads

$$\mathcal{N}_{\mathbf{j}_1\ldots\mathbf{j}_m}\mathcal{N}^{\mathbf{i}_1\ldots\mathbf{i}_n} = \mathcal{N}^{\mathbf{i}_1\ldots\mathbf{i}_n}_{\mathbf{j}_1\ldots\mathbf{j}_m} + \mathcal{C}\left(\mathcal{N}\right)^{\mathbf{i}_1,\ldots,\mathbf{i}_n}_{\mathbf{j}_1\ldots\mathbf{j}_m} \tag{2.36}$$

where $\mathcal{C}\left(\mathcal{N}\right)^{\mathbf{i}_1\ldots\mathbf{i}_n}_{\mathbf{j}_1\ldots\mathbf{j}_m}$ denotes all possible contractions between the upper and lower momentum indices

$$\mathcal{C}\left(\mathcal{N}\right)^{\mathbf{i}_1\ldots\mathbf{i}_n}_{\mathbf{j}_1\ldots\mathbf{j}_m} = \sum_k\sum_p \mathcal{N}^{\mathbf{i}_1\ldots\mathbf{i}_{k-1}\mathbf{i}_{k+1}\cdots\mathbf{i}_n}_{\mathbf{j}_1\ldots\mathbf{j}_{p-1}\mathbf{j}_{p+1}\ldots\mathbf{j}_m}\mathcal{C}(\mathcal{N})^{\mathbf{i}_k}_{\mathbf{j}_p} \tag{2.37a}$$

$$+\sum_{k<l}\sum_{p\neq q}\mathcal{N}^{\mathbf{i}_1\ldots(\mathbf{i}_{k-1})(\mathbf{i}_{k+1})\ldots(\mathbf{i}_{l-1})(\mathbf{i}_{l+1})\ldots i_n}_{\mathbf{j}_1\ldots(\mathbf{j}_{p-1})(\mathbf{j}_{p+1})\ldots(\mathbf{j}_{q-1})(\mathbf{j}_{q+1})\ldots\mathbf{j}_m}\mathcal{C}(\mathcal{N})^{\mathbf{i}_k}_{\mathbf{j}_p}\mathcal{C}(\mathcal{N})^{\mathbf{i}_l}_{\mathbf{j}_q} \tag{2.37b}$$

$$+\sum_{\text{triple}}\ldots \tag{2.37c}$$

$$\vdots \tag{2.37d}$$

The expression is subdivided into sums over terms with a distinct number of contracted pairs. Thus, the first sum contains all possible single contractions, the second sum comprises all double contractions and so forth. The maximum number of contractions is then given by $n^c_{\max} = \min(n,m)$. As we are considering boson operators the contractions introduce a Kronecker-δ

$$\mathcal{C}(\mathcal{N})^{\mathbf{i}_k}_{\mathbf{j}_p} = \delta^{\mathbf{i}_k}_{\mathbf{j}_p} \quad . \tag{2.38}$$

Based on this theorem the evaluation of commutators can be considerably simplified by using a basic pictorial representation for the normal ordered monomials and their contractions. We define a diagram representing a normal ordered monomial by means of a single vertex connecting in- and out-going lines. A particle creation operator in the monomial corresponds to an in-going line with an associated number denoting the index of its momentum. Similarly, a particle annihilation operator is represented by an out-going line. [8] The direction of those

[8] Note, that our convention differs from the standard conventions of Feynman diagrams where out-going lines refer to particle creation and vice versa.

lines is indicated by arrows which, by convention, are drawn from left to right. This pictorial representation is exemplified in Figure 2.14.

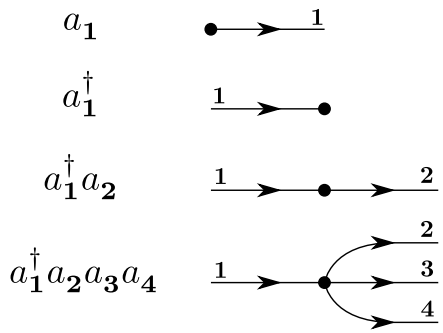

Figure 2.14: The pictorial representation of normal ordered monomials by means of diagrams is illustrated. By convention, we draw the arrows from left to right.

The contraction between two momenta is displayed as a connection between the associated in and out-going lines. We utilize this representation to visualize the commutator between two normal ordered monomials L and R. The commutator of these operators reads

$$\begin{aligned}
\Big[\, L,R \,\Big] &= \Big[\, \mathcal{N}^{\mathbf{i}_1^L\cdots\mathbf{i}_a^L}_{\mathbf{j}_1^L\cdots\mathbf{j}_b^L}\,,\, \mathcal{N}^{\mathbf{i}_1^R\cdots\mathbf{i}_c^R}_{\mathbf{j}_1^R\cdots\mathbf{j}_d^R} \,\Big] \\
&= \mathcal{N}^{\mathbf{i}_1^L\cdots\mathbf{i}_a^L}_{\mathbf{j}_1^L\cdots\mathbf{j}_b^L}\mathcal{N}^{\mathbf{i}_1^R\cdots\mathbf{i}_c^R}_{\mathbf{j}_1^R\cdots\mathbf{j}_d^R} \;-\; \mathcal{N}^{\mathbf{i}_1^R\cdots\mathbf{i}_c^R}_{\mathbf{j}_1^R\cdots\mathbf{j}_d^R}\mathcal{N}^{\mathbf{i}_1^L\cdots\mathbf{i}_a^L}_{\mathbf{j}_1^L\cdots\mathbf{j}_b^L} \\
&= \mathcal{N}^{\mathbf{i}_1^L\cdots\mathbf{i}_a^L}\Big(\mathcal{N}_{\mathbf{j}_1^L\cdots\mathbf{j}_b^L}\mathcal{N}^{\mathbf{i}_1^R\cdots\mathbf{i}_c^R}\Big)\mathcal{N}_{\mathbf{j}_1^R\cdots\mathbf{j}_d^R} \;-\; \mathcal{N}^{\mathbf{i}_1^R\cdots\mathbf{i}_c^R}\Big(\mathcal{N}_{\mathbf{j}_1^R\cdots\mathbf{j}_d^R}\mathcal{N}^{\mathbf{i}_1^L\cdots\mathbf{i}_a^L}\Big)\mathcal{N}_{\mathbf{j}_1^L\cdots\mathbf{j}_b^L} \\
&= \mathcal{N}^{\mathbf{i}_1^L\cdots\mathbf{i}_a^L}\,\mathcal{C}(\mathcal{N})^{\mathbf{i}_1^R\cdots\mathbf{i}_c^R}_{\mathbf{j}_1^L\cdots\mathbf{j}_b^L}\,\mathcal{N}_{\mathbf{j}_1^R\cdots\mathbf{j}_d^R} \;-\; \mathcal{N}^{\mathbf{i}_1^R\cdots\mathbf{i}_c^R}\,\mathcal{C}(\mathcal{N})^{\mathbf{i}_1^L\cdots\mathbf{i}_a^L}_{\mathbf{j}_1^R\cdots\mathbf{j}_d^R}\,\mathcal{N}_{\mathbf{j}_1^L\cdots\mathbf{j}_b^L}
\end{aligned} \tag{2.39}$$

The momenta $\vec{i}^L = (\mathbf{i}_1^L\cdots\mathbf{i}_a^L)$ and $\vec{j}^L = (\mathbf{j}_1^L\cdots\mathbf{j}_b^L)$ correspond to the in- and out-going lines in L and similarly $\vec{i}^R = (\mathbf{i}_1^R\cdots\mathbf{i}_c^R)$ and $\vec{j}^L = (\mathbf{j}_1^L\cdots\mathbf{j}_b^L)$ denote the in- and out-going lines in R. Consequently, the commutator is given by the sum over all contractions between the out-going lines in L and in-going lines in R, subtracted by all possible contractions between the in-going lines in L and out-going lines in R as shown in Figure 2.15.
The resulting two-vertex diagrams represent all normal ordered terms resulting from the commutator. The open lines represent the remaining annihilation and creation operators, whereas the connected lines between momentum pairs $\mathbf{k}_1$ and $\mathbf{k}_2$ indicate contractions which introduce a Kronecker-δ (see (2.38)). Note, that many terms are represented by the same diagram as the number of topologically distinct diagrams is much smaller than the total number of terms. In general, it is expedient to draw the diagrams without momentum assignments first. In a second step the actual terms are obtained by a permutation of assignments between contracted indices. Different contractions that are related by a symmetry transformation of the diagram are only counted once, as they describe identical terms. Finally, the number of different terms N_d corresponding to a given two-vertex diagram d equals the number of all distinct contractions. It is given by the formula

$$N_d = \frac{n_{\text{in}}!\,n_{\text{out}}!}{N_C!(n_{\text{in}}-N_C)!(n_{\text{out}}-N_C)!} \tag{2.40}$$

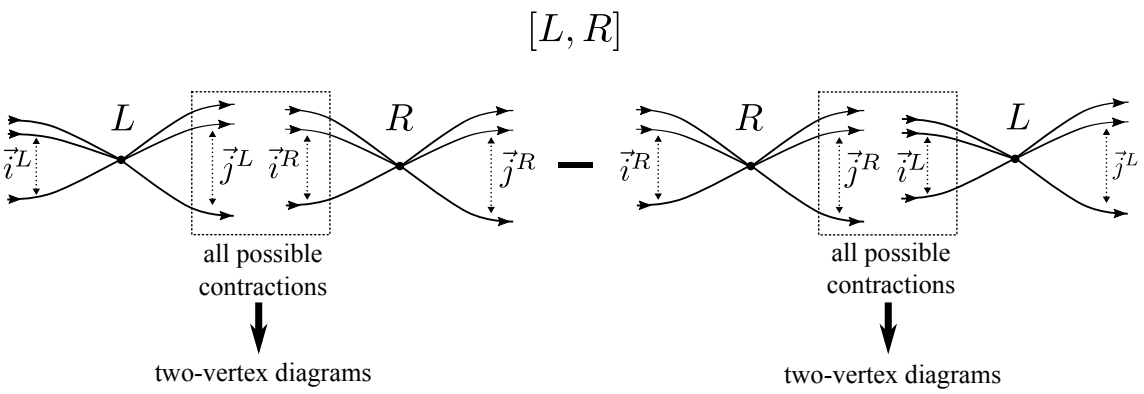

Figure 2.15: Illustration of the commutator equation (2.39)

.

where n_{in} and n_{out} denote the number of in-going and out-going lines which are available for contraction and N_C refers to the number of contractions. The diagrammatic evaluation is exemplified in Figure 2.16.
The pictorial representation also applies to the flow equations for which we replace the coefficients and their contractions by diagrams in a similar fashion. Due to the symmetrization in (2.33) the coefficients exhibit the same diagrammatic properties as their corresponding monomials. All contractions between the monomials obtained in the commutators of the flow equation can be directly transferred to the momentum arguments of the associated coefficients. Consequently, the coefficient and the monomial of a given operator term can be represented by the same diagram. This allows us to express the flow equations in (2.34) entirely in terms of a pictorial representation as illustrated in Figure 2.18.
Based on these rules, the derivation of the flow equations can be performed manually by a rigorous diagrammatic evaluation as summarized in the following steps.

1. First we draw all diagrams describing the terms in the inital Hamiltonian $H(\ell = 0)$ and generator $\eta(\ell = 0)$. Every term is represented by a single vertex diagram.

2. The additional diagrams in the truncated flowing Hamiltonian $H(\ell)$ and generator $\eta(\ell = 0)$ which are not part of the initial Hamiltonian can be determined by a successive evaluation of $\big[\, H(\ell), \eta(\ell) \,\big]$. For this purpose, we draw all possible contractions between the diagrams in $H(0)$ and $\eta(0)$ which leads to a set of two-vertex diagrams. The two-vertex diagrams are converted into single-vertex diagrams by combining the contracted pair of vertices into a single vertex as shown in Figure 2.17. The Hamiltonian and the generator are extended by new diagrams which comply with the truncation criterion. This is repeated until no further diagrams are produced in accordance with the truncation scheme.

3. The flow equation of a coefficient with n in-going and m out-going lines can be derived by determining all two-vertex diagrams in the commutator $\big[\, \mathcal{H}, \eta \,\big]$ featuring the same number of in- and out-going lines.

4. The pre-factors $D_\alpha^{\beta\gamma}$ can be determined by the multiplicities $N_d(\alpha)$ of the corresponding contractions between C_β and C_γ given by (2.40). If the pair of contracted coefficients

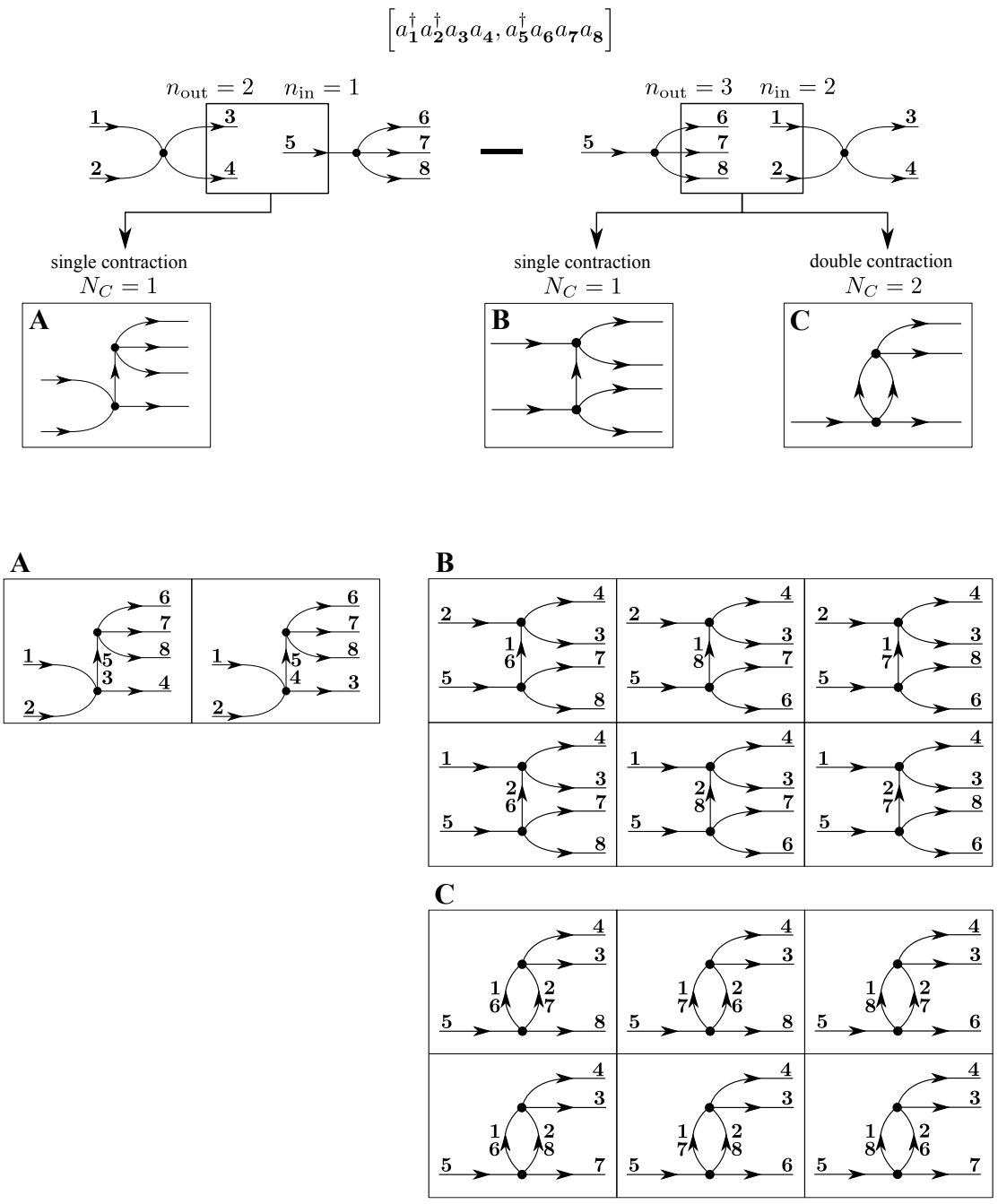

$$\left[a_1^\dagger a_2^\dagger a_3 a_4, a_5^\dagger a_6 a_7 a_8\right] \longrightarrow$$

A	$\delta_{35}\, a_1^\dagger a_2^\dagger a_4 a_6 a_7 a_8 + \delta_{45}\, a_1^\dagger a_2^\dagger a_3 a_6 a_7 a_8$
B	$-\delta_{26}\, a_1^\dagger a_5^\dagger a_3 a_4 a_7 a_8 - \delta_{27}\, a_1^\dagger a_5^\dagger a_3 a_4 a_6 a_8 - \delta_{28}\, a_1^\dagger a_5^\dagger a_3 a_4 a_6 a_7$ $-\delta_{16}\, a_2^\dagger a_5^\dagger a_3 a_4 a_7 a_8 - \delta_{17}\, a_2^\dagger a_5^\dagger a_3 a_4 a_6 a_8 - \delta_{18}\, a_2^\dagger a_5^\dagger a_3 a_4 a_6 a_7$
C	$-\delta_{16}\delta_{27}\, a_5^\dagger a_3 a_4 a_8 - \delta_{17}\delta_{26}\, a_5^\dagger a_3 a_4 a_8 - \delta_{18}\delta_{27}\, a_5^\dagger a_3 a_4 a_6$ $-\delta_{16}\delta_{28}\, a_5^\dagger a_3 a_4 a_7 - \delta_{17}\delta_{28}\, a_5^\dagger a_3 a_4 a_6 - \delta_{18}\delta_{26}\, a_5^\dagger a_3 a_4 a_7$

Figure 2.16: The diagrammatic evaluation of a commutator between normal ordered monomials is exemplified.

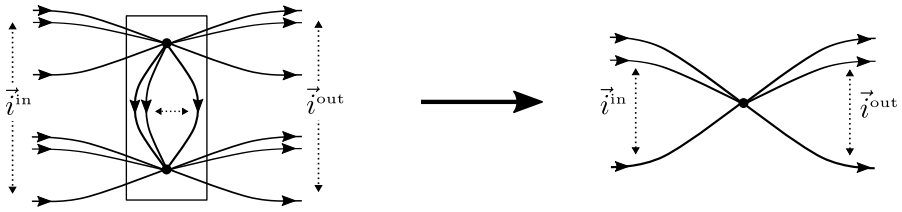

Figure 2.17: A two-vertex diagram is converted into a single-vertex diagram.

emanates from $\left[\mathcal{V}^+ - \mathcal{V}^-, \mathcal{H}_0 + \mathcal{V}_0\right]$, the corresponding pre-factor is given by $D_\alpha^{\beta\gamma} = \pm N_d(\alpha)$. The remaining terms from the commutator $2\left[V^+, V^-\right]$ acquire an additional factor of two $D_\alpha^{\beta\gamma} = \epsilon 2N_d(\alpha)$ with $\epsilon = \pm 1$. In general, the sign ϵ can be directly identified by the corresponding commutator in the flow equations. For the particle conserving generator the signs of the pre-factors can be obtained by $\epsilon = \mathrm{sign}(N_L - N_R)$ where N_L and N_R denote the number of created particles in the left and right vertex. Left and right vertex are distinguished by the arrows on the contracted lines in the two-vertex diagram which go from left to right according to our convention.

5. The flow equation of a given coefficient (which is represented by a single vertex diagram) is then determined by the set of matching two-vertex diagrams and the corresponding prefactors (see Figure 2.18).

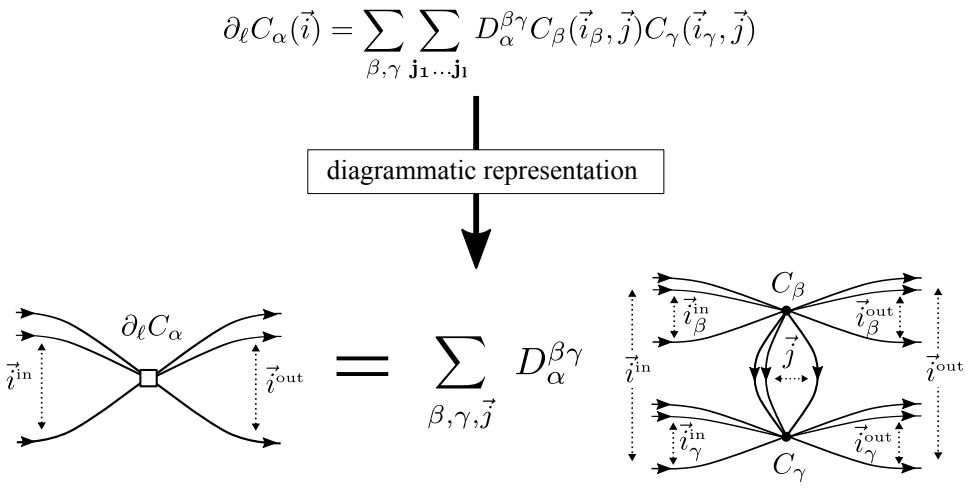

Figure 2.18: The diagrammatic representation of the flow equations in momentum space is depicted.

6. Finally, one has to symmetrize the two-vertex diagrams according to 2.33. The resulting terms can be further combined by exploiting conservation of momentum and vertex symmetries.

7. In the last step one has to sum (or integrate) over all contracted momenta.

Figure 2.19 exemplifies the diagrammatic derivation of the flow equation approach for a simple bilinear Hamiltonian.

Note, that the diagrammtic representation introduced in this section bears a resemblance

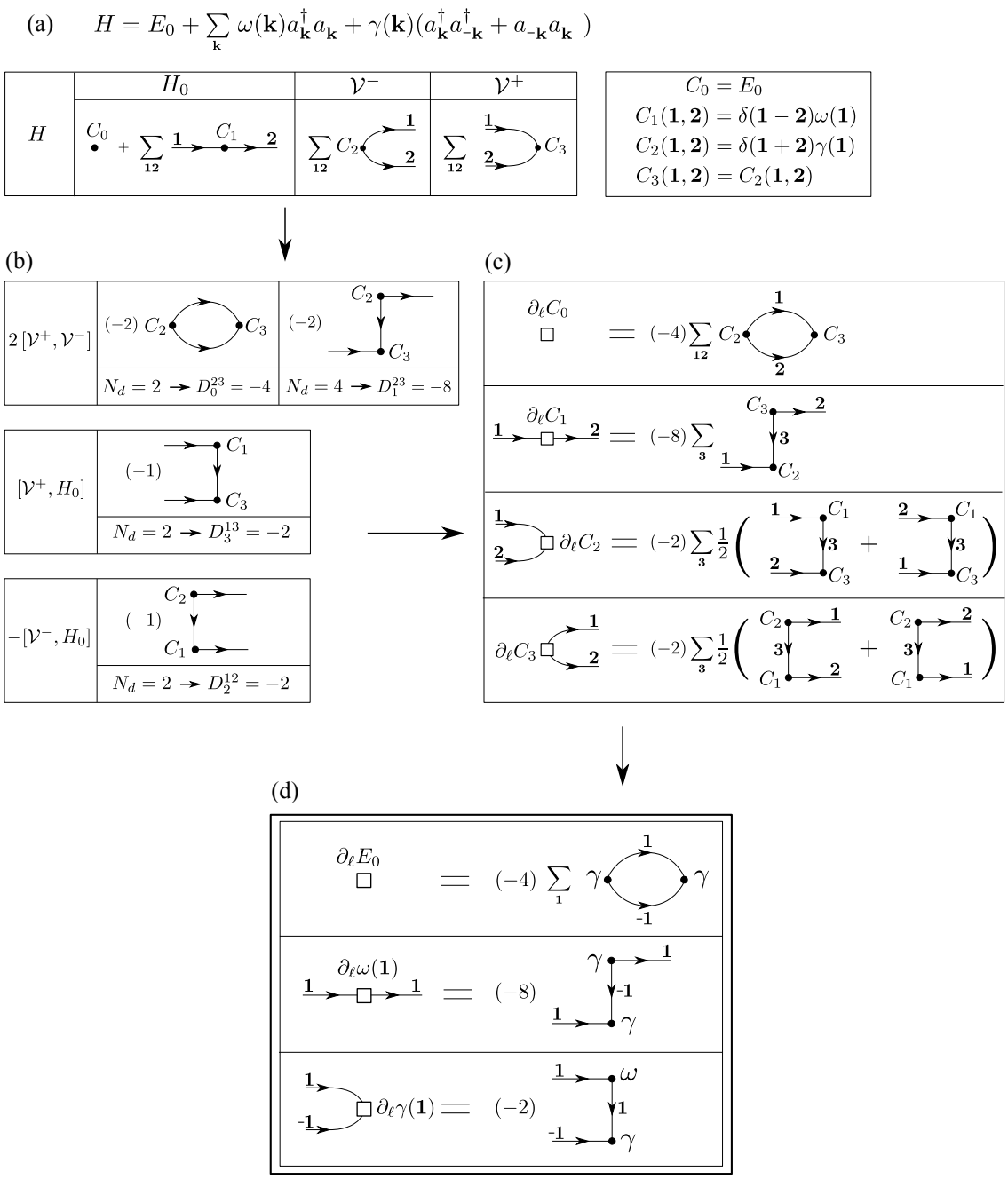

Figure 2.19: The diagrammatic derivation of the particle conserving flow equations for a bilinear Hamiltonian. **(a)** The flowing Hamiltonian is represented in terms of diagrams. The conservation of momentum is absorbed into the coefficients C_i. **(b)** The commutators in the flow equation are evaluated yielding the two-vertex diagrams and the corresponding prefactors $D_\alpha^{\beta\gamma}$. Note, that for the bilinear Hamiltonian no additional terms are created in the commutators. Thus, no truncation is required. **(c)** The flow equations with symmetrized coefficients are drawn. **(d)** The symmetries of the coefficients and the conservation of momentum are exploited in order to simplify the flow equations. The resulting differential equations are exact as no truncation scheme was employed.

to Feynman diagrams from standard perturbation theory. Indeed, an important similarity is that both schemes are used to visualize particle creation and annihilation processes. However, Feynman diagrams are typically used to simplify the evaluation of Greens functions, i.e., the lines represent propagators in time. By contrast, in our approach the diagrams are a pictorial representations of operator terms in momentum space.

2.4.3 Perturbative derivation

Next, we discuss the solution and diagrammatic representation of the perturbative flow equation approach. This allows us to draw a link to diagrammatic perturbation theory, which in turn motivates the interpretation in terms of virtual fluctuations. In the perturbative approach the equations 2.34 are decomposed and truncated in powers of a given perturbative parameter, as discussed in section 2.2.2. Therefore, the coefficients acquire an additional index denoting the order in the perturbative expansion

$$\partial_\ell C_\alpha^{(n)}(\vec{i}) = \sum_{p+q=n} \sum_{\beta,\gamma} \sum_{\vec{j}} D_\alpha^{\beta\gamma} C_\beta^{(p)}(\vec{i},\vec{j}) C_\gamma^{(q)}(\vec{i},\vec{j}) \tag{2.41}$$

In general, these equations can be solved analytically in a recursive fashion.
For the particle conserving generator, the flow equations of the decomposed Hamiltonian read

$$\partial_\ell \mathcal{H} = 2\Big[\, \mathcal{V}^+, \mathcal{V}^- \,\Big] + \Big[\, \mathcal{V}^+ - \mathcal{V}^-, H_0 + \mathcal{V}_0 \,\Big] \tag{2.42}$$

We discriminate between the non-block-diagonal part $\mathcal{V}^+ + \mathcal{V}^-$ which connects subspaces with a different quasi-particle number and the block-diagonal terms in $H_0 + \mathcal{V}_0$. Note, that the terms in $\Big[\, \mathcal{V}^+ - \mathcal{V}^-, H_0 + \mathcal{V}_0 \,\Big]$ do only contribute to the non-block-diagonal parts and that $2\Big[\, \mathcal{V}^+, \mathcal{V}^- \,\Big]$ is at least of second order in V.
The flow equations (2.41) can be decomposed further into

$$\partial_\ell C_\alpha^{(n)}(\vec{i}) = \Omega_\alpha^{(0)}(\vec{i}) C_\alpha^{(n)}(\vec{i}) + \sum_{p+q=n} \sum_{\beta,\gamma} \sum_{\vec{j}} D_\alpha^{\beta\gamma} C_\beta^{(p)}(\vec{i},\vec{j}) C_\gamma^{(q)}(\vec{i},\vec{j}) \qquad (p,q>0) \quad . \tag{2.43}$$

where we extracted the order n coefficient which is associated with the derivative on the left-hand side. The remaining sum comprises only coefficients of lower order $p,q<n$. The term $\Omega_\alpha^{(0)}(\vec{i})$ emerges from the contraction between a vertex function $C_\alpha(\vec{i})$ and the unperturbed one-particle operators in $\Big[\, V^+ - V^-, H_0 \,\Big]$as illustrated in Figure 2.20. It describes the energy difference between the free particle states that are connected by the associated operator term of C_α.

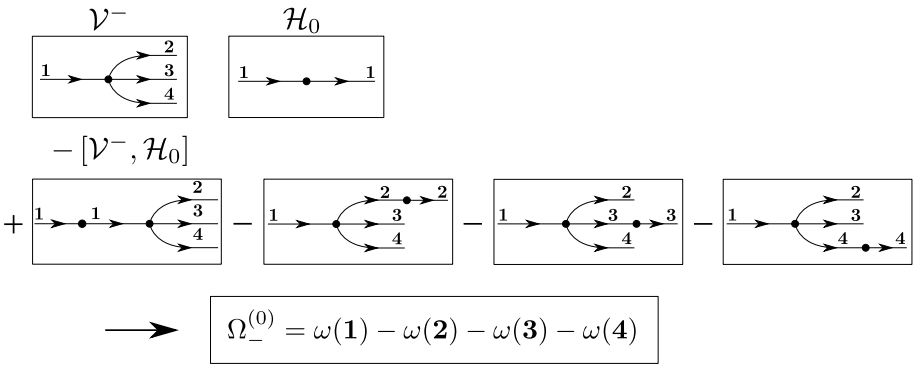

Figure 2.20: Illustration of the one-particle term $\Omega_-^{(0)}$ for an exemplary coefficient in $\mathcal{V}^-$. In the one-particle diagram we directly exploit conservation of momentum.

For a coefficient C_α which is associated with a vertex function $V_m^n(\mathbf{k}_1,\ldots,\mathbf{k}_n,\mathbf{k}_{n+1},\ldots,\mathbf{k}_{n+m}) = V_m^n(\vec{i})$ the corresponding energy term reads

$$C_\alpha(\vec{i}) \leftrightarrow V_m^n(\vec{i}): \quad \Omega_\alpha^{(0)}(\vec{i}) = -\mathrm{sign}(n-m)\left(\sum_{i=1}^{n}\omega(\mathbf{k}_i) - \sum_{i=n+1}^{m}\omega(\mathbf{k}_i)\right) \tag{2.44}$$

Note, that its sign is dominantly negative because one subtracts the energy of the state with more particles from the energy of the lower particle state. For the coefficients C_α in the block-diagonal part the energy term $\Omega_\alpha^{(0)}(\vec{i})$ is zero ($\mathrm{sign}(0) := 0$) because there is no commutator between the block-diagonal operators H_0 and V_0.
If the unperturbed part H_0 also contains non-diagonal interaction terms, the perturbative evaluation becomes more involved as different non-block-diagonal coefficients of the same order are coupled and the simple decomposition in (2.43) is not possible. In this case, one has to diagonalize H_0 first.
The negativity of the energy term $\Omega_\alpha < 0$ is an important requirement ensuring the convergence of the flow. The asymptotic behavior for $\ell \to \infty$ is dominated by the term $\Omega^{\alpha,(0)}(\vec{i})C_\alpha^{(n)}(\vec{i})$ as the residual sum in (2.43) stems from the commutator $2\left[\mathcal{V}^+,\mathcal{V}^-\right]$ which has to vanish presuming a convergent flow. In gapless systems the requirement $\Omega_\alpha \leq 0$ only holds for transitions in V_0^n, V_n^0 and V_1^n, V_n^1 which couple to the ground state or one-particle states. If the one particle dispersion is non-negative and coincides with the lower edge of its multi-particle continuum we find

$$\begin{aligned}
\Omega_\alpha^{(0)}(\vec{i}) &= -\sum_{i=1}^{n}\omega(\mathbf{k}_i) \leq 0 \qquad \text{for } V_0^n, V_n^0 \\
\Omega_\alpha^{(0)}(\vec{i}) &= \omega_{\mathbf{k}_1} - \sum_{i>1}^{n}\omega_{\mathbf{k}_i} \leq 0 \quad \text{for } V_1^n, V_n^1 \quad .
\end{aligned} \tag{2.45}$$

For the coefficients in the higher particle subspaces the energy term $\Omega_\alpha^{(0)}(\vec{i})$ can also take positive values which can lead to a divergent flow. As we already discussed, this is due to the nature of the multi-particle continuum in gapless systems. The corresponding states cannot be decoupled because there is no energetic hierarchy in the multi-particle subspaces, which means that one can only decouple the 0-qp and 1-qp states from the multi-particle continuum (e.g. by using the $\eta^{1:n}$ scheme [51, 71]). However, a decoupling of higher qp states is possible, if they are protected by additional conserved quantum numbers, e.g. the total spin. In fact, this is the case in the square lattice antiferromagnet. Here, the multi-particle continuum separates into subspaces with an odd and even number of quasi-particles which do not hybridize. Thus, we can use the full qp-generator scheme to decouple the subscpaces three quasi-particles as there are no processes which connect the two and three quasi-particle subspace.

Solution in second order

Next, we discuss the structure of the perturbative solution up to second order. After that, we sketch the generalization to higher orders and exemplify the diagrammatic interpretation. For the sake of clarity, we omit the indices of momentum $\vec{i},\vec{j}$ in the notation, keeping in mind that the coefficients have a momentum dependence and the sums include contractions between

different momenta. Moreover, we drop the superscript in the energy term $\Omega_\alpha^{(0)} \coloneqq \Omega_\alpha$
In first order the flow of the coefficients in the block-diagonal part is zero

$$\partial_\ell C_\alpha^{(1)} = 0 \quad \text{for} \quad C_\alpha \in \mathcal{H}_0 + \mathcal{V}_0 \tag{2.46}$$

as the coefficients are already determined by the particle conserving part of the perturbation $\mathcal{V}_0$. Only the terms in $\left[\mathcal{V}^+ - \mathcal{V}^-, \mathcal{H}_0 \right]$ provide a finite contribution given by

$$\partial_\ell C_\alpha^{(1)} = \Omega_\alpha C_\alpha^{(1)} + \sum_{\beta,\gamma \neq \alpha} D_\alpha^{\beta\gamma} \left(C_\beta^{(0)} C_\gamma^{(1)} + C_\beta^{(1)} C_\gamma^{(0)} \right) \quad \text{for} \quad C_\alpha \in \mathcal{V}^+, \mathcal{V}^- \tag{2.47}$$

As we presume that the unperturbed part $\mathcal{H}_0$ is given by a non-interacting Hamiltonian the equations reduce to

$$\partial_\ell C_\alpha^{(1)}(\ell) = \Omega_\alpha C_\alpha^{(1)}(\ell) \quad \text{for} \quad C_\alpha \in \mathcal{V}^+, \mathcal{V}^- \quad . \tag{2.48}$$

The resulting flow of the corresponding coefficients then reads

$$C_\alpha^{(1)}(\ell) = C_\alpha^{(1)}(0)\, e^{\Omega_\alpha \ell} \quad . \tag{2.49}$$

These non-diagonal coefficients vanish for $\ell \to \infty$ due to the exponential prefactor $e^{\Omega_\alpha \ell}$ for $\Omega_\alpha < 0$.
Based on this result we can determine the effective coefficients in second order defined by the flow equations

$$\begin{aligned} \partial_\ell C_\alpha^{(2)}(\ell) &= \Omega_\alpha^{(0)} C_\alpha^{(2)}(\ell) + \sum_{\beta,\gamma} D_\alpha^{\beta\gamma} C_\beta^{(1)}(\ell) C_\gamma^{(1)}(\ell) \\ &= \Omega_\alpha^{(0)} C_\alpha^{(2)}(\ell) + \sum_{\beta,\gamma} D_\alpha^{\beta\gamma} C_\beta^0 C_\gamma^0 e^{(\Omega_\beta + \Omega_\gamma)\ell} \end{aligned} \tag{2.50}$$

where $C_{\beta/\gamma}^0 \coloneqq C_{\beta/\gamma}^{(1)}(\ell = 0)$. This differential equation can be solved by the ansatz

$$C_\alpha^{(2)}(\ell) = G(\ell) e^{\Omega_\alpha \ell} \tag{2.51}$$

which yields

$$\partial_\ell G(\ell) = \sum_{\beta,\gamma} D_\alpha^{\beta\gamma} C_\beta^0 C_\gamma^0 e^{(\Omega_\beta + \Omega_\gamma - \Omega_\alpha)\ell} \tag{2.52}$$

The function $G(\ell)$ is obtained by an integration of the exponential function which introduces a denominator with the unperturbed single particle energies $\Omega_\beta + \Omega_\gamma - \Omega_\alpha$. The integration constant is determined by the initial condition $G(0) = 0$. Eventually, we obtain

$$C_\alpha^{(2)}(\ell) = e^{\Omega_\alpha \ell} \left(\sum_{\beta,\gamma} D_\alpha^{\beta\gamma} C_\beta^0 C_\gamma^0 \frac{e^{(\Omega_\beta + \Omega_\gamma - \Omega_\alpha)\ell} - 1}{\Omega_\beta + \Omega_\gamma - \Omega_\alpha} \right) \quad . \tag{2.53}$$

For the non-block-diagonal part the coefficient vanishes in the limit $\ell \to \infty$ as $\Omega_\alpha \leq 0$ and $\Omega_\beta + \Omega_\gamma \leq 0$.

For the coefficients of the particle conserving part the argument is zero $\Omega_\alpha = 0$ and, hence, the effective coefficient has a finite value. Eventually, we obtain the result

$$C^{(2)}_\alpha(\vec{i}) = -\sum_{\beta,\gamma}\sum_{\vec{j}} \frac{D^{\beta\gamma}_\alpha C^0_\beta(\vec{i}_\beta,\vec{j}) C^0_\gamma(\vec{i}_\gamma,\vec{j})}{\Omega_\beta(\vec{i}_\beta,\vec{j}) + \Omega_\gamma(\vec{i}_\gamma,\vec{j})} \quad . \tag{2.54}$$

where we reintroduced the momentum arguments $\vec{i}$ and the sum over contracted momenta $\vec{j}$. Note, that the formula (2.54) is equivalent to the result of standard second order perturbation theory.
The effective coefficients are now expressed in terms of the unperturbed coefficients and energies C^0_γ and Ω_β. In the effective model the dynamics and interactions are renormalized by perturbative contributions which describe fluctuations of the free excitations mediated by $\mathcal{V}$.

The diagrammatic representation provides an expedient tool to visualize these fluctuations in a simple fashion. Figure 2.21 illustrates the diagrammatic representation of (2.54) and exemplifies the interpretation in terms of virtual fluctuations.

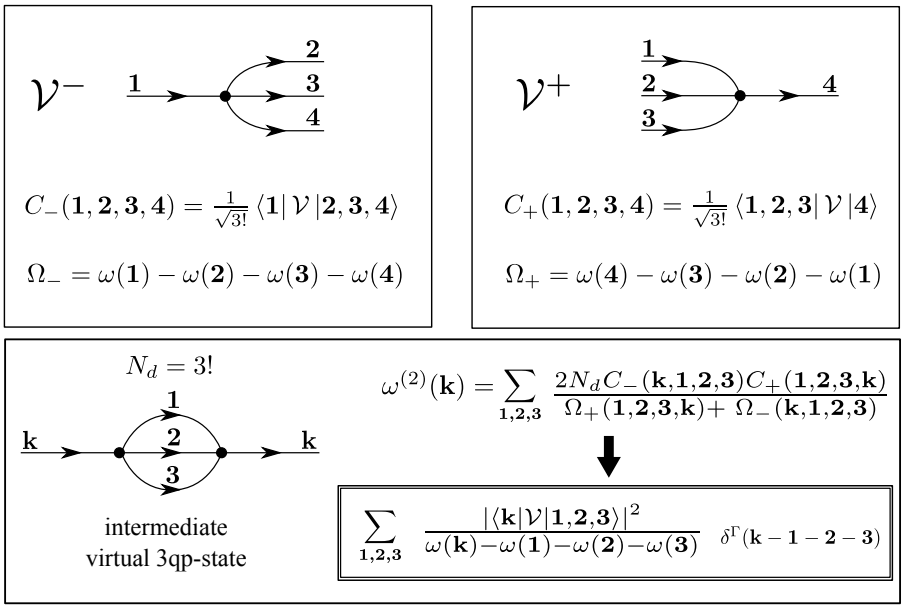

Figure 2.21: The diagrammatic representation of the second order contributions in (2.54) to the quasi-particle dispersion is illustrated with an exemplary perturbation $\mathcal{V}$. $\mathcal{V}$ describes scattering processes from a single particle state into a three-particle state and vice versa. The coefficients $\mathcal{V}$ induce transitions between these states and, hence, we can interpret the perturbative contributions as fluctuations into intermediate virtual states weighted by an energy denominator. In the end, the resulting contribution is a sum over all possible transitions mediated by $\mathcal{V}$. This principle also applies to effective interaction terms which are represented by diagrams with a higher number of in-going and out-going lines.

General perturbative solution

Next, we analyze the generic structure of the perturbative solution generalizing the diagrammatic approach to higher orders.
In order n the flow equations read

$$\begin{aligned}\partial_\ell C_\alpha^{(n)} &= \Omega_\alpha C_\alpha^{(n)} + \sum_{p+q=n}\sum_{\beta,\gamma} D_\alpha^{\beta\gamma} C_\beta^{(p)} C_\gamma^{(q)} \qquad (p,q>0) \\ &= \Omega_\alpha C_\alpha^{(n)} + g(\ell) \end{aligned} \tag{2.55}$$

where we extracted the term proportional to the unperturbed one-particle energies in Ω_α. Thus, the n-th order coefficient $C_\alpha^{(n)}$ does not occur in the residual sum $g(\ell)$. First, let us distinguish between coefficients of the block-diagonal part with $\Omega_\alpha = 0$ and the coefficients of the non-block-diagonal terms with $\Omega_\alpha \neq 0$. For $\Omega_\alpha = 0$ the formal solution is obtained by integration

$$\begin{aligned} C_\alpha^{(n)}(\ell) &= C_\alpha^{(n)}(0) + \int_0^\ell d\ell_1 g(\ell_1) \qquad C_\alpha^{(n)}(0) = 0 \quad \text{for } n>1 \\ &= \sum_{p+q=n}\sum_{\beta,\gamma} D_\alpha^{\beta\gamma} \int_0^\ell d\ell_1 C_\beta^{(p)}(\ell_1) C_\gamma^{(q)}(\ell_1) \quad . \end{aligned} \tag{2.56}$$

For the non-block-diagonal coefficients with $\Omega_\alpha \neq 0$ we insert the ansatz (2.51) into the flow equation (2.55) which leads to

$$\begin{aligned} \Omega_\alpha C_\alpha^{(n)} + e^{\Omega_\alpha \ell} &= \Omega_\alpha C_\alpha^{(n)} + g(\ell) \\ \rightarrow \partial_\ell G(\ell) &= e^{-\Omega_\alpha \ell} g(\ell) \quad . \end{aligned} \tag{2.57}$$

Hence, we can write the flow of the n-th order coefficient as follows

$$\begin{aligned} C_\alpha^{(n)}(\ell) &= \int_0^\ell d\ell_1 g(\ell_1) \\ &= \sum_{p+q=n}\sum_{\beta,\gamma} D_\alpha^{\beta\gamma} e^{\Omega_\alpha \ell} \int_0^\ell d\ell_1 e^{-\Omega_\alpha \ell_1} C_\beta^{(p)}(\ell_1) C_\gamma^{(q)}(\ell_1) \quad \text{for } n>1 \quad , \end{aligned} \tag{2.58}$$

which is equal to (2.56) for $\Omega_\alpha = 0$. Thus, we consider equation (2.58) as the general form of the flowing coefficients in order $n>1$. The contributions in order n of the effective coefficients are given by

$$C_\alpha^{\mathrm{eff},(n)} = \lim_{\ell\to\infty} C_\alpha^{(n)}(\ell) = \sum_{p+q=n}\sum_{\beta,\gamma} D_\alpha^{\beta\gamma} \int_0^\infty d\ell_1 C_\beta^{(p)}(\ell_1) C_\gamma^{(q)}(\ell_1) \quad . \tag{2.59}$$

Note, that $C_\alpha^{\mathrm{eff},(n)}$ is zero for each coefficient function in the non-block-diagonal part as the integral is damped by the exponential term $e^{\Omega_\alpha \ell}$, assuming that the integral has a finite value. Hence, we only have to consider particle conserving coefficient functions $C_\alpha^{\mathrm{eff},(n)}$. This is a direct consequence of the quasi-particle conserving generator scheme. The effective coefficient

$C_\alpha^{\mathrm{eff},(n)}$ is also referred to as the irreducible N^{qp}-particle matrix element.
To compute an effective coefficient one has to know the flow of the coupled coefficients in lower order which is determined by (2.58). This equation defines a recursive relation between the coeffients with decreasing perturbative order. Eventually, the recursion terminates at first order with

$$C_\alpha^{(1)}(\ell) = C_\alpha^{(1)}(0) e^{\Omega_\alpha \ell} \tag{2.60}$$

Consequently, every contribution at finite order can be obtained by a successive evaluation of the recursion scheme replacing the contracted coefficients on the right-hand side in (2.58) until the termination case (2.60) is reached. The recursion leads to expressions of nested integrals over different flow parameters ℓ_i. The arrangement of these nested integrals depends on the actual structure of the recursive decomposition. Note, that the recursive relation (2.58) gives rise to various kinds of decompositions as we sum over different combinations of orders p,q and coefficient types β, γ.
In the following, we want to examine the form of the resulting expressions in more detail. The symbol $\Theta(n)$ is used as an identifier for a concrete recursive decomposition in order n. The structure of a given recursive decomposition $\Theta(n)$ can be visualized by means of a binary tree as shown in Figure 2.22. Every recursive step, which replaces a coefficient $C_\alpha^{(l)}$ by a pair of coefficients $C_\beta^{(p)}(\ell_i)$, $C_\gamma^{(q)}(\ell_i)$ with $p+q=l$, is represented by a connection between a node and two child nodes. The nodes are enumerated by an index k. According to (2.58) the recursive step at node k for a coefficient C_α introduces a corresponding prefactor $D_\alpha^{\beta\gamma}$ and an integral

$$e^{\Omega_\alpha \ell_r} \int_0^{\ell_r} d\ell_k e^{-\Omega_\alpha \ell_k} \tag{2.61}$$

where k is a child node of the node with number r. The leafs of the binary tree display the terminating case. Each leaf (with number i) provides a coefficient $C_{\mu_i}^0$ from the initial perturbation $\mathcal{V}(\ell = 0)$ and an exponential factor $e^{\Omega_\gamma \ell_{r(i)}}$ where $r(i)$ is a parent node of leaf i. The number of leafs equals the order of the contribution as we have $p+q=l$ for every node. Based on these rules, every binary tree can be associated with a distinct contribution.
The coefficients $C_\alpha^{(1)}(0)$ from the terminating case and the prefactors $D_\alpha^{\beta\gamma}$ are not relevant for the evaluation of the nested integrals because they do not depend on any flow parameter. Thus, every contribution in order n splits into a product of n vertex functions $C_{\mu_i}^0$, a combinatorial prefactor accounting for the multiplicities $D_\alpha^{\beta\gamma}$ and a factor $E_{\Theta(n)}$, which contains the nested integrals of exponential functions. The nested integrals in $E_\alpha(\Theta(n))$ can be determined by means of the corresponding binary tree as shown in Figure 2.22(b). Figure 2.23 exemplifies the concrete evaluation of $E_\alpha(\Theta(n))$ for a third order contribution.
The arguments of the exponential functions are sums of energy terms Ω_α which contain energy differences of the unperturbed system. Thus, the resulting terms in E_Θ contain products of denominators which account for every vertex substitution.
Based on these considerations, a generic perturbative contribution (2.59) in order n can be written as

$$C_\alpha^{\mathrm{eff},(n)} = \sum_\Theta D_\alpha(\Theta) E_\alpha(\Theta) C_{\mu_1(\Theta)} \dots C_{\mu_n(\Theta)} \tag{2.62}$$

The sum runs over all possible decompositions of the coefficient function $C_\alpha^{\mathrm{eff},(n)}$. The indices $\mu_i(\Theta)$ are assigned to the resulting leafs and $D^\alpha(\Theta)$ denotes the product of all prefactors $D_\alpha^{\beta\gamma}$

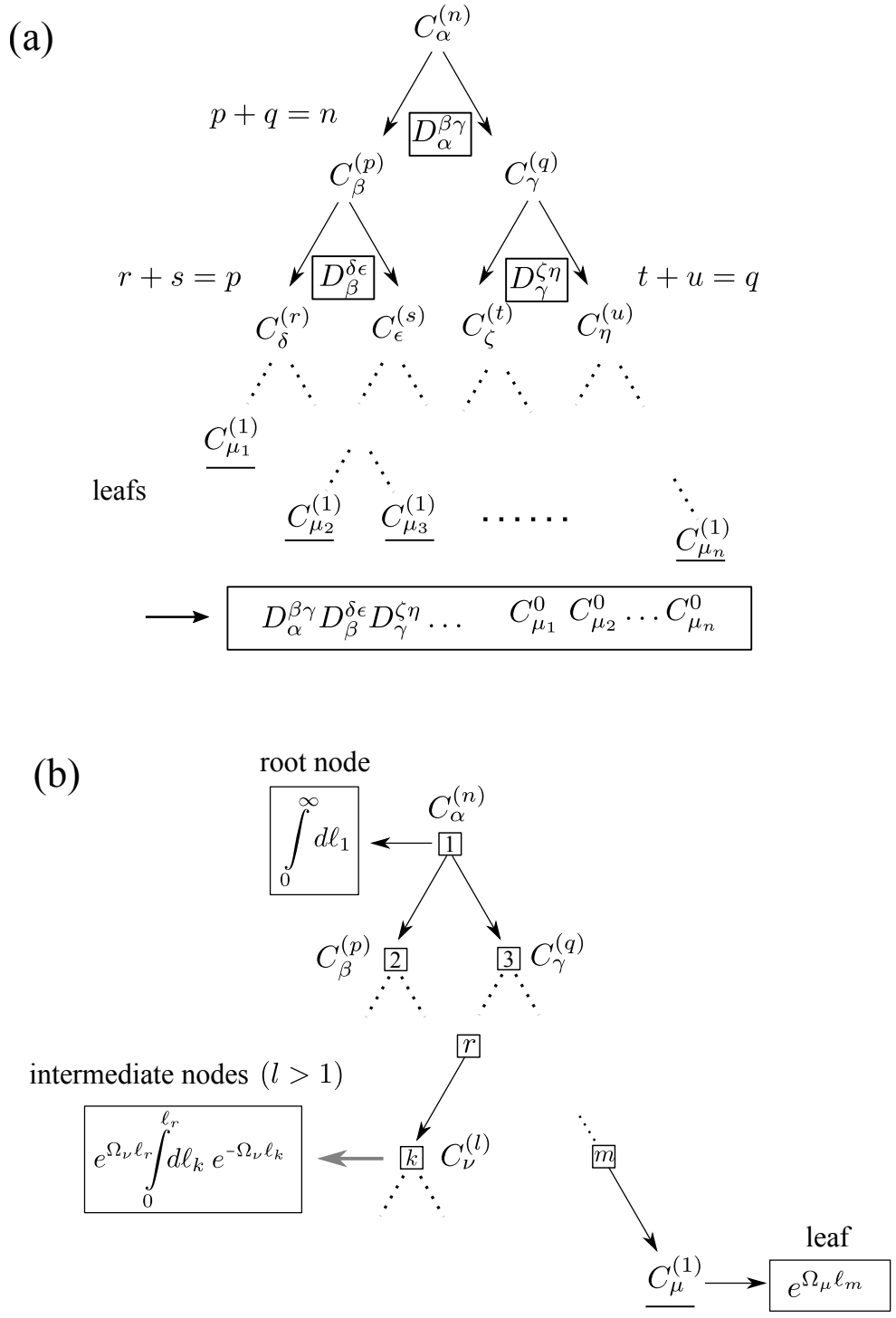

Figure 2.22: The generic structure of a recursive decomposition defined by (2.58),(2.60) and (2.59) is illustrated by means of a binary tree. In **(a)** the derivation of the multiplicities $D_\alpha(\Theta)$ and the product of coefficients in (2.62) is shown. In **(b)** the structure of the resulting nested integrals in $E(\Theta)$ is depicted.

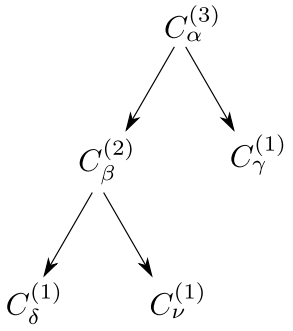

$$E(\Theta) = \int_0^\infty d\ell_1 e^{(\Omega_\gamma+\Omega_\beta)\ell_1} \int_0^{\ell_1} d\ell_2 e^{(-\Omega_\beta+\Omega_\delta+\Omega_\nu)\ell_2}$$

$$= \frac{-1}{(\Omega_\delta+\Omega_\nu+\Omega_\gamma)(\Omega_\delta+\Omega_\nu-\Omega_\beta)} + \frac{1}{(\Omega_\beta+\Omega_\gamma)(\Omega_\delta+\Omega_\nu-\Omega_\beta)}$$

$$\rightarrow \boxed{E(\Theta) = \frac{1}{(\Omega_\delta+\Omega_\nu+\Omega_\gamma)(\Omega_\gamma+\Omega_\beta)}}$$

Figure 2.23: The concrete evaluation of $E_\alpha(\Theta(n))$ is exemplified for a third order contribution.

of the corresponding decomposition Θ.
Recall, that the vertex functions $C_{\mu_i(\Theta)}$ and energy terms in $E_\alpha(\Theta)$ additionally feature a momentum dependence which we neglected in our notation. Thus, we also have to sum over all momenta associated with the contractions between the vertex functions and the energy denominators in $E_\alpha(\Theta)$. Writing down the explicit form of the resulting sum is very cumbersome. Though, its general structure can be understood in a simple fashion using the diagrammatic representation.
We consider the decomposition of a generic irreducible N^{qp}-particle matrix element, which is represented by a diagram with the N^{qp} in- and outgoing lines. In the diagrammatic language, every node of the binary tree splitting into two new nodes represents a vertex which is substituted by a pair of contracted vertices. The allowed substitutions for a given vertex are determined by the flow equations. Consequently, we can interpret the flow equations as substitution rules which can be directly visualized in the corresponding diagrammatic representation (see Figure 2.18). Note, that the number of in- and outgoing lines N^{qp} is not altered by a substitution. The successive recursive decomposition of the effective vertex function $C_\alpha^{\mathrm{eff},(n)}$ leads to different diagrams which contain n vertices provided by the initial perturbation $\mathcal{V}$. As we go through all possible substitutions, this procedure generates all corresponding n-vertex graphs with N^{qp} in-going and out-going lines. Additionally, the multiplicities $D_\alpha^{\beta\gamma}$ account for different possibilities of contractions between the vertices. Eventually, we can interpret equation (2.62) as the sum over all conceivable ways to connect two N^{QP} particle states using the vertices provided by $\mathcal{V}$.[9]
In the general qp-generator scheme all particle-number fluctuations in $\mathcal{V}$ are taken into account. By contrast, the set of valid fluctuations is restricted in modified qp-generator schemes. In the case of restricted generators $\eta^{n:m}$, we consider only those fluctuations in $\mathcal{V}$ which couple to the relevant particle subspaces (up to m particles).

[9] Note, that diagrammatic contributions which are solely composed of particle conserving fluctuations from $\mathcal{V}_0$ are zero as there are no contractions between particle conserving vertices in the flow equation.

These results are very similar to the rules known from perturbative linked diagram expansions [84]. Interestingly, the linked diagram theorem arises in a natural way as it is imposed by the generic structure of the flow equations. The CUT approach provides a convenient language which is particularly useful for the diagrammatic derivation of effective descriptions.

If we consider quantities that have a unique perturbative expansion (such as eigen-energies), both, perturbative qp-conserving CUT and conventional perturbation theory should yield identical results and the diagrammatic contributions obtained by the CUT approach can be directly identified with those from the conventional perturbative approach. Hence, if we collect all terms in (2.62) that correspond to the same diagram, we will obtain a perturbative contribution which is identical to the corresponding term from diagrammatic perturbation theory. We conclude, that the terms obtained by the CUT obey similar diagrammatic rules as the corresponding terms from conventional diagrammatic perturbation theory. We will not undertake a rigorous derivation of the diagrammatic rules for perturbative qp-conserving effective models because this is not of prime importance for this thesis. Instead, we focus on the physical interpretation of (2.62) in the context of non-perturbative CUT approaches.

2.4.4 Non-perturbative derivation

In the following we want to apply the diagrammatic interpretation of the flow equations to non-perturbative approaches. For this purpose, let us first summarize the relevant results obtained in the previous section.
According to Figure 2.21 we interpret the perturbative contributions of the irreducible N^{qp}-particle coefficient function in terms of virtual fluctuations of the free particle states, which are defined by the eigen basis of the unperturbed system H_0. The associated diagrams provides a simple visualization of these fluctuations. The open lines represent the initial and final state mediated by the effective N^{qp}-particle vertex function. The contracted vertex functions embedded in the diagram describe physical processes as particle scattering or spontaneous particle creation and annihilation giving rise to virtual intermediate states.
Provided that the Hamiltonian at hand is translational invariant, total momentum is a conserved quantity at every vertex However, the total energy (the sum of unperturbed one-particle energies) is not conserved by the virtual fluctuations. Every particle-number changing vertex is associated with an energy denominator containing the energy difference between the two corresponding virtual states. Thus, fluctuations with a higher energy difference have a smaller weight due to the denominators in $E_\alpha(\Theta)$. As the number of vertices is restricted by the considered order, only subspaces up to a finite particle number are accessed by virtual fluctuations at a finite order. Considering effective low energy descriptions, a truncation at finite order is reasonable, if the states with a large particle number are associated with high energies. Consequently, a rigorous perturbative evaluation of particle conserving CUTs should be appropriate as long as the energetic hierarchy is directly related to the particle number, which is typically the case for gapped systems.[10] For gapless systems, however, there is a lack of a characteristic energy scale and the hierarchical relation between particle number and energy is less clear, which may render a rigorous perturbative truncation ineffective. In such a case, non-perturbative truncation schemes may be more suitable. In order to visualize the effects

[10] Moreover, the interaction V should be small as it counteracts the energetic hierarchy induced by $E_\alpha(\Theta)$ which is of course a main requirement in any perturbative expansion.

of a non-perturbative CUT, we apply the diagrammatic interpretation to an effective model obtained by a non-perturbative evaluation of the flow equations (2.41). Regarding the resulting coefficient functions as a series expansion in terms of a perturbative parameter, we are allowed to sort the diagrammatic contributions according to powers of this parameter. Similar to the perturbative approach, we can interpret the flow equations as substitution rules which generate various types of diagrams by means of a recursive derivation. But, as the perturbative hierarchy is voided, the recursive scheme does not terminate after a finite number of steps and the effective coefficients will contain contributions up to infinite order. Hence, the non-perturbative evaluation corresponds to a summation of infinite classes of diagrams, which comply with the substitution rules defined by the flow equations. The general principle of this interpretation is illustrated in Figure 2.24.

As long as the exact solution can be written in terms of an infinite power series the diagrammatic decomposition is a valid representation. In this sense, the interpretation in terms of virtual fluctuations also applies to non-perturbative effective descriptions.

In contrast to the bare power series, the non-perturbative effective model includes an infinite set of higher order virtual fluctuations and, thus, we naively expect that it is more accurate, especially in non-perturbative regimes. However, the set of available vertex substitutions is restricted by the truncated flow equations and, hence, only a subset of higher order diagrams is included. It is often very difficult to quantify the approximation error constituted by the missing diagrams because the effects of non-perturbative truncation schemes are less intuitive. In the most extreme case, non-perturbative truncations may lead to diverging results. Therefore, it is essential to find a truncation scheme which incorporates the most relevant fluctuations in a systematic way. In the following section, we present a physical criterion which allows us to quantify the relevance of virtual fluctuations with regard to gapless systems.

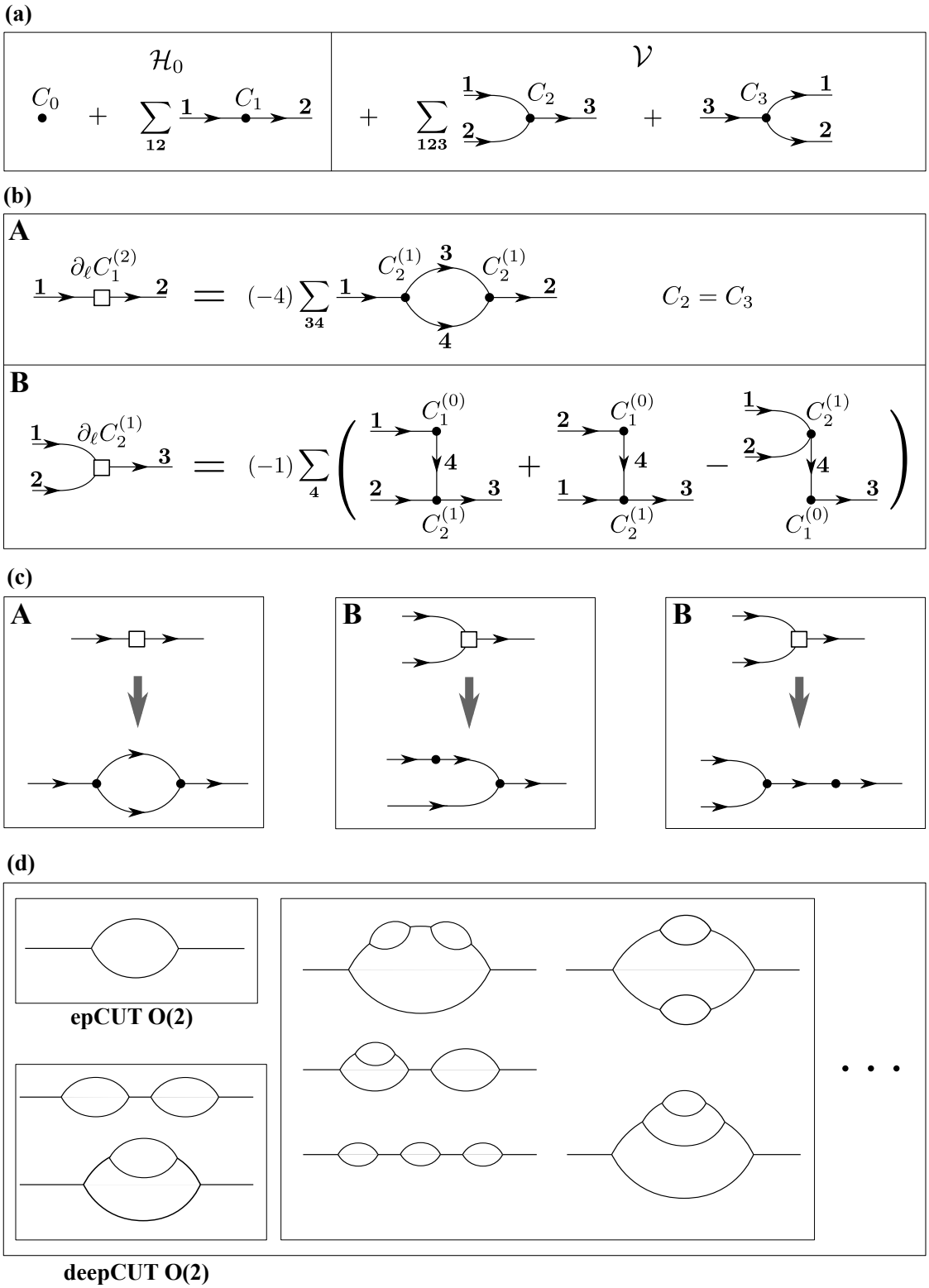

Figure 2.24: The diagrammatic interpretation of a perturbative (epCUT) and non-perturbative (deepCUT) flow equation approach is exemplified. In **(a)** the exemplary Hamiltonian is represented in terms of diagrams. **(b)** depicts the corresponding second order flow equations of the effective dispersion obtained for a particle conserving generator. In **(c)** the interpretation of the flow equations in terms of vertex substitutions is illustrated. **(d)** shows the resulting diagrammatic contributions contained by the perturbative and non-perturbative effective model.

2.5 Scaling dimension

In effective descriptions of gapless systems major difficulties arise due to arbitrary small energy differences between different quasi-particle states. In perturbative expansions this lack of a characteristic energy scale can lead to vanishing energy denominators in $E(\Theta)$. As a consequence, processes at arbitrary high orders may become relevant rendering the perturbative approach insufficient. In principle, the summation of infinite classes of diagrams has the potential to avoid these problems. This is achieved by non-perturbative truncation schemes, which specify these classes of diagrammatic contributions and, thus, determine the set of virtual processes comprised by the effective description.
The key question is: How can we classify the importance of different processes in order to define an appropriate truncation criterion for gapless systems?
A quantity, which is particularly suited to this problem, is the scaling dimension of operator terms. Originally, this concept was introduced to describe critical phenomena by means of renormalization group approaches and conformal field theories [7, 101]. In the context of CUTs, it is used in operator product expansions of vertex functions in one-dimensional systems [37, 102].
In the following, we give a brief introduction to the concept of scaling dimension in the context of momentum space CUTs.

2.5.1 Motivation and general idea

The scaling dimension of operator terms provides a suitable non-perturbative truncation criterion for systems with a diverging correlation length because it defines a natural hierarchy of operator terms which involve gapless excitations. Before introducing the concrete definition, we briefly motivate its application to momentum space CUTs outlining the main idea behind this concept.
As we discussed in section 2.3, the multi-particle continuum of gapless excitations is directly adjacent to the energy of a single excitation. This even holds for excited states with an arbitrary number of particles. However, we also know that these states are mainly composed of low energy particles at $\mathbf{k} = 0$ (see Figure 2.12). Thus, if interactions are taken into account, the multi-particle states will be predominantly renormalized by an interplay with long wavelength excitations. It is reasonable to assume, that the virtual fluctuations and interactions which are relevant for the effective low energy model are dominated by particles with long wavelengths close to $\mathbf{k} = 0$. Consequently, we have to find out which terms become more important, if we zoom into smaller energies or momenta, respectively. For this purpose, we classify the relevance of operator terms by their rescaling properties under momentum transformations $\mathbf{k}_i \to \lambda \mathbf{k}_i$ with $\lambda < 1$. In the thermodynamic limit, the bosonic creation and annihilation operators of a D-dimensional system exhibit the following scaling properties

$$a^\dagger_{\lambda \mathbf{k}} \to \lambda^{-\frac{D}{2}} \tilde{a}^\dagger_{\mathbf{k}} \tag{2.63}$$

This follows directly from the fundamental commutation relation provided that both types of operators fulfill

$$\left[a_{\mathbf{k}} , a^\dagger_{\mathbf{k}'} \right] = \left[\tilde{a}_{\mathbf{k}} , \tilde{a}^\dagger_{\mathbf{k}'} \right] = \delta(\mathbf{k} - \mathbf{k}') \quad . \tag{2.64}$$

From these properties of the single creation and annihilation operators we can derive the scaling behavior of an arbitrary operator term in a translational invariant Hamiltonian. We consider a generic term in momentum space

$$\mathcal{T}=\int_{\mathrm{BZ}} C_{\mathbf{k}_1\ldots\mathbf{k}_n}\mathcal{O}^n_{\mathbf{k}_1\ldots\mathbf{k}_n}\delta(\mathbf{k}_1+\ldots+\mathbf{k}_n)d^2\mathbf{k}_1\ldots d^2\mathbf{k}_n, \tag{2.65}$$

where $\mathcal{O}^n_{\mathbf{k}_1,\ldots\mathbf{k}_n}$ is a monomial of n bosonic operators of creation or annihilation type. Conservation of momentum is ensured by the delta function $\delta(\mathbf{k}_1+\ldots+\mathbf{k}_n)$. Note, that the momenta $\mathbf{k}_i$ are integrated over the whole Brillouin zone (BZ).
Now, we zoom into smaller energies and cut off the parts at the boundary of the Brillouin zone by a scaling down of the integration area BZ$\rightarrow\lambda$BZ with $\lambda<1$. The truncated part corresponds to the higher energy regime of the gapless quasi-particle. The inital integration boundaries are retrieved in terms of rescaled momenta $\tilde{\mathbf{k}}_i$ by the substitution $\mathbf{k}_i\rightarrow\lambda\tilde{\mathbf{k}}_i$ which yields the following expression

$$\mathcal{T}=\lambda^{D(\frac{n}{2}-1)}\int_{\mathrm{BZ}} C_{\lambda\tilde{\mathbf{k}}_1\ldots\lambda\tilde{\mathbf{k}}_n}\mathcal{O}^n_{\tilde{\mathbf{k}}_1\ldots\tilde{\mathbf{k}}_n}\delta(\tilde{\mathbf{k}}_1+\ldots+\tilde{\mathbf{k}}_n)d^2\tilde{\mathbf{k}}_1\ldots d^2\tilde{\mathbf{k}}_n \quad . \tag{2.66}$$

The factor $\lambda^{D(\frac{n}{2}-1)}$ is the generic dimensional contribution of the operator term. In order to restore the original form of $\mathcal{T}$ with rescaled momenta $\tilde{\mathbf{k}}_i$, we have to make assumptions about the scaling behavior of the coefficient $C_{\lambda\tilde{\mathbf{k}}_1\ldots\lambda\tilde{\mathbf{k}}_n}$. In general, the coefficients are no homogeneous functions and, hence, they exhibit no distinct scaling behavior. But, since the focus is on long wavelengths, we may consider the leading behavior of the coefficient in the vicinity of $\mathbf{k}_i=0$. Its scaling behavior is then determined by the first non-vanishing term in the series expansion of $C_{\lambda\tilde{\mathbf{k}}_1\ldots\lambda\tilde{\mathbf{k}}_n}$ in λ about $\mathbf{k}_i=0$.

$$C_{\lambda\tilde{\mathbf{k}}_1\ldots\lambda\tilde{\mathbf{k}}_n}=\sum_l c_l(\lambda\tilde{\mathbf{k}}_1\ldots\lambda\tilde{\mathbf{k}}_n)\lambda^l \quad . \tag{2.67}$$

If the leading term appears in order $l=c$, we make the replacement $C_{\lambda\mathbf{k}_1\ldots\lambda\mathbf{k}_n}\rightarrow\lambda^c C_{\mathbf{k}_1\ldots\mathbf{k}_n}$. Consequently, the operator term $\mathcal{T}$ acquires a prefactor $\lambda^{D(\frac{n}{2}-1)+c}$. The scaling dimension is then defined by the exponent $d(D,n,c):=D(\frac{n}{2}-1)+c$. Operator terms with a larger scaling dimension become less important upon scaling with $\lambda<1$. A very important result is, that the relevance of operator terms decreases with increasing number of involved creation and annihilation operators. Consequently, fluctuations and interactions between subspaces with high particle number are suppressed. This effect is even further amplified in higher dimensions. In infinite dimensions the truncation by scaling dimension reduces the Hamiltonian to the bilinear level, because $d(D,n=2,c)$ does not depend on D, whereas all other terms with $n>2$ vanish for $d\rightarrow\infty$ and arbitrary $\lambda<1$.
Thus, as we would expect, quantum fluctuations become less important in higher dimensions. A similar is encountered in mean field approximations, which typically become exact in infinite dimensions $D\rightarrow\infty$ [103].

2.5.2 Application in momentum space CUTs

In this thesis, the scaling dimension is applied to two dimensional gapless magnons in the Heisenberg antiferromagnet where quantum fluctuations play a major role. We utilize the scaling dimension in order to specify the relevance of different magnon interaction processes, which are incorporated in a self similar CUT approach. We obtain self consistent differential equations by retaining only operator terms up to a certain scaling dimension. Hence, the selection scheme T of the self similar approach (see section 2.2.1) is solely determined by the scaling dimension. This has the major advantage that we are only dealing with a single truncation parameter. By contrast, standard sCUT approaches in real space typically require a variety of truncation criteria, such as the maximum particle number and spatial range, which render the truncation very intricate [51].
In contrast to perturbative truncation parameters, the scaling dimension is not additive. More concretely, the scaling dimension of two contracted operator terms $C(\mathcal{T}_1\mathcal{T}_2)$ is not necessarily the sum of the respective scaling dimensions of $\mathcal{T}_1$ and $\mathcal{T}_2$. Thus, if we want to determine the dimensional contribution of operator terms, which are initially zero, we have to examine the contracted terms in the corresponding flow equations. Therefore, we consider the leading behavior of the coefficient for infinitesimal ℓ,

$$\begin{aligned} C_\alpha(\vec{i})(d\ell) &= \overbrace{C_\alpha(\vec{i})|_{\ell=0}}^{=0} + \partial_\ell C_\alpha(\vec{i})|_{\ell=0}\, d\ell + \mathcal{O}(d\ell^2) \\ &= \sum_{\beta,\gamma}\sum_{\vec{j}} C_\beta(\vec{i}_\beta,\vec{j})C_\gamma(\vec{i}_\gamma,\vec{j})d\ell + \mathcal{O}(d\ell^2) \end{aligned} \tag{2.68}$$

where $\vec{j}$ denote the contracted momenta between C_β and C_γ and $d\ell$ is an infinitesimal step in the flow parameter ℓ. The dimensional contribution c of the coefficient is then given by the rescaling properties of

$$\sum_{\beta,\gamma}\sum_{\vec{j}} C_\beta(\lambda\vec{i}_\beta,\vec{j})C_\gamma(\lambda\vec{i}_\gamma,\vec{j}) \to \lambda^c \sum_{\beta,\gamma}\sum_{\vec{j}} C_\beta(\vec{i}_\beta,\vec{j})C_\gamma(\vec{i}_\gamma,\vec{j}) \quad . \tag{2.69}$$

Let us stress, that we treat the contracted product as a function of the free momenta $\mathbf{k}_i \in \vec{i}$ and thus, we do not consider a rescaling of the contracted momenta $\vec{j}$.
If the contracted coefficients C_β and C_γ vanish for $\ell = 0$, this procedure is iterated to higher orders until a product of contracted coefficients from the initial Hamiltonian is obtained. Consequently, these contributions are of higher order in $d\ell$.[11] This way, the scaling dimension of an operator term is determined by the leading order contributions of the corresponding virtual fluctuations. Let us stress, that it is not trivial to decide, whether the scaling dimension can be altered by higher order contributions. In general, a rigorous definition of the scaling dimension of renormalized coefficients for finite ℓ is very elaborate. We do not address this issue in the scope of this particular work. But, concerning the model analyzed in this thesis, we observe that the scaling behavior of the vertex functions (as defined above) is retained during the flow

$$\begin{aligned} C_\alpha(\lambda\vec{i})(d\ell) &\to \lambda^c C_\alpha(\vec{i})(d\ell) + \mathcal{O}(d\ell^2) \\ C_\alpha(\lambda\vec{i})(\ell) &\to \lambda^{c'} C_\alpha(\vec{i})(\ell) \;\text{ with }\; c = c' \end{aligned} \tag{2.70}$$

[11] In our case, it is sufficient to access contractions in first order in $d\ell$.

which justifies our approach.
So far, we have discussed the theoretical background of the CUT approach in momentum space and its application to gapless systems. In the next section, we turn our attention to the utilization of the flow equation approach for non-hermitian problems.

2.6 Continous similarity transformations

The unitarity of the flow equation approach is ensured by an anti-hermitian generator scheme, which in turn requires the hermiticity of the Hamiltonian in the case of the standard generator schemes. In this thesis, however, we apply the continuous transformation to a system, which, for reasons of expediency, is expressed in a non-hermitian representation. As a consequence, the generator scheme induces a non-unitary similarity transformation.
Interestingly, in their original paper[33], Glazek and Wilson introduce the flow equation approach as a renormalization scheme based on continuous *similarity* transformations, despite the fact that they apply it exclusively in form of unitary transformations.
From a methodical point of view, it is of great interest to explore the capability of the flow equation approach in a non-unitary context expanding its potential range of application. In this section, we comment on some general aspects of non-unitary flow equations outlining the similarities and differences compared to the standard approach. Moreover, we discuss the consequences for the resulting effective model and observables, in particular with regard to their subsequent treatment.

2.6.1 General considerations

First, we give a brief discussion on some basic concepts of similarity transformations and the interpretation of non-hermitian operators in the context of quantum mechanics. For a more detailed and rigorous discussion the reader is referred to the standard literature on linear algebra and the mathematical foundations of quantum mechanics [104–106].
Conceptually, quantum mechanical systems are described by states $|\psi\rangle$ defined on a seperable Hilbert space and linear operators O which act on these states [107–109]. The linear operators are representations of physical observables. The eigenvalues of the linear operators o_n determine all possible outcomes of a measurement of the corresponding observable whereas the probabilities of the different outcomes are encoded in a state $|\psi\rangle$ in the sense that

$$\langle\psi|\, O\, |\psi\rangle = \sum_n o_n \underbrace{|\langle\psi|n\rangle|^2}_{=P(o_n)} \tag{2.71}$$

where $P(o_n)$ is the probability of the outcome o_n and $|n\rangle$ denotes the corresponding basis state. Since the values of a physical measurement are supposed to be real numbers, typically linear operators with a real spectrum are considered. This is particulary important for Hamilton operators which are supposed to describe the time evolution of the corresponding system.[12]
Seminal works on the mathematical foundation and understanding of quantum theory were made by John von Neumann [112]. Among other contributions, he generalized the spectral

[12] In the case of dissipative or decay phenomena, however, imaginary energy eigenvalues are explicitly utilized [110, 111]

theorem, which states that every self adjoint operator has a real spectrum and an associated orthonormal eigenbasis and pointed out the difference between hermitian and self adjoint operators [113]. A self-adjoint operator A is typically defined by the property

$$(v, Au) = (vA, u) \Rightarrow A^\dagger v = Av \tag{2.72}$$

where v and u denote arbitrary vectors and $(,)$ defines an inner product. We use parentheses instead of the bracket notation in order to discriminate between a general inner product and the standard scalar product used in quantum mechanics.
In physical textbooks, the terms 'hermitian' and 'self adjoint' are often used as synonyms. In a mathematical rigorous sense, however, there is a subtle difference between these two properties in infinite dimensional Hilbert spaces.[13] A readable and comprehensive review on those subtleties and the pitfalls of the simplified notation and convention in the quantum mechanical formalism (as used by physicists) is given in reference [114]. We neglect those details in the following as our discussion only addresses the basic ideas on a cursory and abstract level, but, the reader should be aware of these issues. For the sake of simplicity, we restrict our considerations to finite dimensional Hilbert spaces so that any operator can be represented by a finite matrix.
We consider an operator O as hermitian (or self adjoint) if there exists a diagonal operator O_D with real entries o_n and an unitary operator $U^\dagger$ such that

$$O = UO_D U^\dagger \tag{2.73}$$

which implies that O is diagonalizable. This also means that any state $|\psi\rangle$ can be expanded in the orthonormal eigen basis of O by $|\psi\rangle = \sum_n c_n |n\rangle$ where $c_n = \langle n|\psi\rangle$.
Unitary transformations map orthornormal basis states to new orthonormal basis states $|n\rangle \rightarrow U|n\rangle$ while preserving the inner product $(v, w) = \langle Uv|Uw\rangle$. The hermiticity of operators is retained in any orthonormal basis. Thus, we interpret the set of unitarily equivalent hermitian operators as different representations of the same physical observable.
Equation (2.72) indicates that the hermiticity of an operator depends on the definition of the inner product. Typically, in quantum mechanics the standard scalar product is utilized

$$(v, u)_{\mathbb{1}} := \langle u|v\rangle \quad . \tag{2.74}$$

However, the scalar product does not consitute a distinct or unique inner product. In fact, there are infinite ways to define an inner product, which are solely determined by the following properties

$$\text{Conjugate symmetry:} \qquad (v, u) = (u, v)^* \tag{2.75a}$$

$$\text{Linearity in the second argument:} \qquad (v, cu) = c\,(v, u) \quad c \in \mathbb{C} \tag{2.75b}$$

$$(v + w, u) = (v, u) + (w, u) \tag{2.75c}$$

$$\text{Positive definiteness:} \qquad (u, u) \geq 0 \tag{2.75d}$$

[13] In this case, one has to distinguish between the domains of the operator A and its hermitian conjugate $A^\dagger$. The operator A is called self adjoint if the domains of both, A and of its hermitian conjugate $A^\dagger$, are identical (in addition to (2.72)). Thus, a hermitian operator with $A^\dagger = A$ is not necessarily self adjoint in which case the spectral theorem does not apply. However, this poses no problems for operators acting on a finite dimensional Hilbert space for which both terms can be used interchangeably.

Thus, we might also consider a different inner product as for example

$$(v,u)_K = \langle u|\, K\, |v\rangle \tag{2.76}$$

(also known as the hermitian form [104]) where K is an arbitrary positive definite and hermitian operator ensuring the positive definiteness in (2.75d) In general an operator which is hermitian with respect to the standard scalar product will lose its hermiticity if we switch to a different inner product. In his seminal paper from 1998, Bender pointed out that the combination of parity and even time-reversal symmetry ($\mathcal{PT}$-symmetry with $\mathcal{T}^2 = +1$) gives rise to a whole class of non-hermitian Hamiltonians with real spectrum [115]. Moreover, a generalizion to Hamiltonians with odd time-revearsal symmetry ($\mathcal{T}^2 = -1$) is possible [116, 117]. This class of $\mathcal{PT}$-symmetric Hamiltonians is non-hermitian with respect to the standard scalar product, but it retrieves hermiticity if one considers the $\mathcal{PT}$-inner product $(u,v)_{\mathcal{PT}} = \langle \mathcal{PT}u|v\rangle$ [116][14]. The Dyson-Maleev representation for the spin degrees in quantum magnets also gives rise to a manifestly non-hermitian Hamilton operator. This is due to the fact that the resulting bosonic operators and the correponding Hamiltonian are self adjoint with respect to two different inner products [118].

In the following we want to discuss the use of non-hermitian representations of physical observables in the context of similarity transformations. As we will see, operator representations for different hermitian forms are related by a similarity map, which allows us to define an inner product such that (diagonalizable) non-hermitian operators with real spectrum retrieve hermiticity.

Although generic non-hermitian operators exhibit imaginary eigenvalues, they do not preclude a real spectrum in general. Similarity transformations preserve the spectrum and, thus, the set of operators which are similar to hermitian operators must exhibit the same eigenvalues and an associated bi-orthonormal eigenbasis. Consequently, they comprise the same information about the physical observable as their hermitian counterpart.

We consider the set of similar operators $\tilde{O} = SO_DS^{-1}$, which feature the same spectrum as $O = O^\dagger$. Unitarily equivalence is a special case of similarity where $S^{-1} = S^\dagger$. But, in contrast to a unitary transformation, the similarity transformation does not preserve the orthogonality of basis states. As a result, the description of physical states becomes more difficult as we encounter an asymmetry between bra and ket vectors. If we denote the eigenstates of O_D by $|n\rangle$, we can write the bra and ket eigenstates as

$$\overbrace{SO_DS^{-1}}^{\tilde{O}}\overbrace{S\,|n\rangle}^{|R_n\rangle} = o_n\,|R_n\rangle \tag{2.77a}$$

$$\overbrace{\langle n|\,S^{-1}}^{\langle L_n|}\overbrace{SO_DS^{-1}}^{\tilde{O}} = \langle L_n|\,o_n \tag{2.77b}$$

where we have used $SS^{-1} = \mathbb{1}$. Consequently, one has to distinguish between right and left eigenvectors. For a diagonalizable non-hermitian operator $\tilde{O}^\dagger \neq \tilde{O}$ with real spectrum we find

$$\tilde{O}\,|R_n\rangle = o_n\,|R_n\rangle \tag{2.78a}$$

$$\tilde{O}^\dagger\,|L_n\rangle = o_n\,|L_n\rangle \quad . \tag{2.78b}$$

[14] Note, that this inner product does not constitute a hermitian form because $\mathcal{T}$ is an anti-linear operator

The basis states are no longer orthonormal in the sense that

$$\langle R_n|R_m\rangle \neq \delta_{nm} \quad \langle L_m|L_n\rangle \neq \delta_{nm} \quad . \tag{2.79}$$

However, the set of left and right eigenstates constitutes a bi-orthonormal basis

$$\langle L_m|R_n\rangle = \delta_{nm} \quad . \tag{2.80}$$

They provide a generalized completeness relation

$$\sum_n |R_n\rangle \langle L_n| = \mathbb{1} \tag{2.81}$$

which can be shown in the following way. We presume that $|R_n\rangle$ and $\langle L_n|$ are eigenstates of an operator $\tilde{O}$ which is similar to an hermitian operator $\tilde{O} = SOS^{-1}$. Hence, we can write the left and right eigenvectors in terms of the orthonormal eigen basis of O

$$\sum_n |R_n\rangle \langle L_n| = \sum_{k,m,n} S_{nk} |k\rangle \langle m| S^{-1}_{mn} \tag{2.82a}$$

$$= \sum_{k,m} \underbrace{\left(\sum_n S^{-1}_{mn} S_{nk} \right)}_{\delta_{mk}} |k\rangle \langle m| \tag{2.82b}$$

$$= \sum_k |k\rangle \langle k| = \mathbb{1} \quad . \tag{2.82c}$$

where $\{|k\rangle\}$ is the complete orthonormal eigenbasis of O with $\delta_{km} = \langle k|m\rangle$. The terms $S_{nk} = \langle n| S |k\rangle$ and $S^{-1}_{mn} = \langle m| S^{-1} |n\rangle$ denote the matrix elements of the transformation matrix S in the corresponding basis.
Expectation values of observables are preserved under similarity transformation as

$$\langle v| O |v\rangle = \langle v| S^{-1}(SOS^{-1})S |v\rangle = \langle v_L| \tilde{O} |v_R\rangle \tag{2.83}$$

Similar to the hermitian case, the non-hermitian operator $\tilde{O}$ describe a series of measurements by

$$\langle v_L| \tilde{O} |v_R\rangle = \sum_n o_n \langle L_i|v_R\rangle \langle v_L|R_i\rangle \tag{2.84}$$

where $\langle L_i|v_R\rangle \langle v_L|R_i\rangle$ is the probability of a single measurement yielding the outcome o_n. Note, that $\langle L_i|v_R\rangle \langle v_L|R_i\rangle$ must be positive as we presumed that $\langle v| S^{-1} SOS^{-1} S |v\rangle = \langle v_L| \tilde{O} |v_R\rangle$ so that we have

$$\begin{aligned} \langle v_L| \tilde{O} |v_R\rangle = \langle v| S^{-1}(\tilde{O})S |v\rangle &= \sum_{m,n} \langle n| v_n^* S^{-1}(\tilde{O}) S v_m |m\rangle \\ &= \sum_{m,n} v_m v_n^* \langle L_n| (\tilde{O}) |R_m\rangle \\ &= \sum_n |v_n|^2 o_n \end{aligned} \tag{2.85}$$

Thus, from a conceptual point of view, non-hermitian operators with a real spectrum and bi-orthonormal eigenbasis are valid descriptions of physical states and observables, as well. The crucial difference however is that the information about the physical state, i.e., the probabilities of the different outcomes in a measurement, is encoded in a *pair* of states, $|v_R\rangle$ and $\langle v_L|$, which are not related by a simple hermitian conjugation. Instead, they are conjugate with respect to a non-trivial hermitian form (2.76)

$$|R_m\rangle = K\,|L_m\rangle \rightarrow |v_L\rangle = K\,|v_R\rangle \tag{2.86}$$

with

$$K = (S^{-1})^\dagger S^{-1} \tag{2.87}$$

The hermitian matrix K induces an inner product for which the vectors $|R_m\rangle$ constitute an orthonormal basis

$$(R_m, R_n)_K = \langle R_m|\,K\,|R_n\rangle = \langle S^{-1}R_m|S^{-1}R_n\rangle = \langle m|n\rangle = \delta_{nm} \tag{2.88}$$

Moreover, $\tilde{O}$ is hermitian with respect to this inner product

$$\begin{aligned}
(R_m, \tilde{O}R_n)_K &= \langle L_m|\,\tilde{O}\,|R_n\rangle = \langle m|\,O\,|n\rangle && \text{(2.89a)}\\
&= \langle m|\,OS^{-1}S\,|n\rangle = \langle (S^{-1})^\dagger Om|R_n\rangle && \text{(2.89b)}\\
&= \langle (S^{-1})^\dagger S^{-1}\tilde{O}R_m|R_n\rangle = \langle K\tilde{O}R_m|R_n\rangle && \text{(2.89c)}\\
&= (\tilde{O}R_m, R_n)_K && \text{(2.89d)}
\end{aligned}$$

and thus the spectral theorem applies in the same way. The matrix elements of $\tilde{O}$ and O are identical for the corresponding inner product

$$(R_m, \tilde{O}R_n)_K = (m, On)_{\mathbb{1}} \quad . \tag{2.90}$$

We conclude, that switching the inner product leads to a non-hermitian representation of the corresponding operator. From a conceptual point of view, non-hermitian representations rely on the same concepts as representations based on the standard scalar product. The main difference lies in the distinction between bra and ket states requiring the description in terms of bi-orthonormal basis states. But, ultimately, we can interpret similar operators as different representations of the same physical observable.
Indeed, one might argue that hermitian representations are much easier to handle, as they are accompanied with important properties. By contrast, the non-hermitian representation of operators based on similarity transformations is less intuitive and more difficult to manage in practical applications. A real-valued spectrum of a non-hermitian observable might be sensitive to truncation errors which could lead to eigenvalues with non-vanishing imaginary parts. Moreover, the time evolution becomes more complicated in non-hermitian representations. But, nevertheless, we want to stress that there is no fundamental reason to use hermitian operators exclusively. It is not clear, whether the restriction to hermitian Hamiltonians may even preclude the discovery of new concepts and phenomena, for which non-hermitian quantum mechanics provides a more convenient description. In general, it is advisable to explore the potential advantages of this approach, since in some cases the benefits of a non-hermitian

representation outweigh its drawbacks. For instance, this is the case for the Dyson-Maleev representation of the antiferromagnetic Heisenberg model, which also applies to hardcore bosons in general (see Appendix A).
The combination of non-hermitian representations with the flow equation approach has the potential to enable new and interesting applications. Thus, we advertize the utilization of the flow equation approach to non-hermitian problems such as the $\mathcal{PT}$-symmetric Hamiltonians. In particular, these problems may provide new and exotic phenomena as for instance phase transitions where imaginary eigenvalues evolve from entirely real spectra [115].
The flow equation approach in the context of similarity transformations and non-hermitian representations is addressed in the next part.

2.6.2 Non-unitary flow equations

Formally, the derivation of the flow equation as introduced by Glazek and Wilson is valid in a more general sense. Following their derivation, we consider a similarity transformation matrix S which can be expressed by $S = e^{-K}$, $S^{-1} = e^{K}$ where K is a generic linear operator. Note, that this form ensures that S is not singular, i.e., that the inverse of S exists. Accordingly, an infinitesimal similarity transformation of the Hamiltonian $H(\ell)$ with an auxillary parameter ℓ can be written as

$$\begin{aligned} H(\ell + d\ell) &= e^{K(\ell)d\ell} H(\ell) e^{-K(\ell)d\ell} \\ &= (1 + K(\ell)d\ell + \cdots) H(\ell) (1 - K(\ell)d\ell + \cdots) \\ &= H(\ell) + \Big[K(\ell), H(\ell) \Big] d\ell + \mathcal{O}(d\ell^2) \end{aligned}$$

which yields the flow equation

$$\partial_\ell H(\ell) = \Big[K(\ell), H(\ell) \Big] \quad . \tag{2.91}$$

In contrast to the unitary approach, the generator is not anti-hermitian $K(\ell) \neq -K(\ell)^\dagger$ and the flow equation describes a flow between similar Hamiltonians. However, the general structure of the flow equations is not altered by this definition and, thus, the derivation of the flow equations described in the previous sections can be performed in the same fashion. Both, unitary and similarity transformations are technically identical as we may write $K(\ell) = \eta(\ell)$ where $\eta(\ell) = -\eta^\dagger(\ell)$ represents the special case of a unitary transformation. Similar arguments hold for the flow of observables defined by equation 2.3, but we have to distinguish between the operator O and its hermitian conjugate $O^\dagger$ meaning that they must be treated as two different operators obeying their own flow equation.
An important property of the unitary flow is the fact, that it converges for $\ell \to \infty$ which was shown for all types of generators discussed in section 2.1.2. Unfortunately, the conditions which ensure convergence of the flow in the unitary case, do not hold in general for non-unitary similarity transformations. This makes it difficult to derive general statements about their convergence.
In the following, we discuss the convergence and the asymptotic behavior of the particle conserving generator scheme $\eta(\ell) = H^+(\ell) - H^-(\ell)$ in the context of a non-hermitian Hamiltonian with $H^+(\ell) \neq \big(H^-(\ell)\big)^\dagger$. For this purpose we reexamine the proof for the unitary flow equation

and point out the problems in the non-hermitian case. We follow the proof presented by Tim Fischer in Ref. [70] which is based on the arguments used for the Mielke generator [63].
First, we define the eigen states $|n\rangle$ of the particle number operator Q, such that $Q|n\rangle = q_n|n\rangle$, where $q_n \in \mathbb{N}$ is the quasi-particle number of the state $|n\rangle$. The matrix elements of the Hamiltonian $H(\ell)$ in this basis are given by $h_{n,m}(\ell) = \langle m|H(\ell)|n\rangle$. Accordingly, the matrix elements of the generator are given by $\eta_{n,m}(\ell) = \mathrm{sign}(q_n - q_m)h_{n,m}(\ell)$. For the sake of simplicity, we consider a finite dimensional Hilbert space with dimension D. The flow equation reads

$$\begin{aligned}\partial_\ell h_{n,m}(\ell) = &-\mathrm{sign}(q_n - q_m)(h_{n,n} - h_{m,m})h_{n,m}(\ell) \\ &+ \sum_{k\neq m,n}^{D} \{\mathrm{sign}(q_n - q_k) + \mathrm{sign}(q_m - q_k)\}\, h_{n,k}(\ell)h_{k,m}(\ell)\end{aligned} \tag{2.92}$$

The trace of H is a conserved quantity of the flow

$$\begin{aligned}\partial_\ell \sum_n^D h_{n,n}(\ell) &= 2\sum_{n=0}\sum_{k=0}^{D} \{\mathrm{sign}(q_n - q_k)\}\, h_{n,k}(\ell)h_{k,n}(\ell) \\ &= 0 \quad .\end{aligned} \tag{2.93}$$

The sum vanishes as the sign-function is anti-symmetric in k and n.
Next, we consider the derivative of the first r summands in the trace of H which is given by

$$\sum_{n=1}^{r} \partial_\ell h_{n,n}(\ell) = 2\sum_{n=0}^{r}\sum_{k=r+1}^{D} \mathrm{sign}(q_n - q_k)h_{n,k}(\ell)h_{k,n}(\ell) \tag{2.94}$$

If we assume that the basis states are ordered such that $q_n > q_m$ for $n > m$ the sign-function is solely negative $\mathrm{sign}(q_n - q_k) \leq 0$ as $k > n$. Thus, in the hermitian case, the sum over the first r diagonal elements is a monotonically decreasing function because $h_{n,m}(\ell)h_{m,n}(\ell) = \left|h_{n,m}(\ell)\right|^2 > 0$. Regarding systems with a spectrum that is bounded from below, this sum has to converge for arbitrary r. This also implies that every summand has to vanish for $\ell \to \infty$

$$\lim_{\ell\to\infty} \mathrm{sign}(q_n - q_m)h_{n,m}(\ell)h_{m,n}(\ell) = 0 \quad \forall n, m | q_n \neq q_m \tag{2.95}$$

This equation states, that all matrix elements $h_{n,m}(\ell)$ which couple states from different quasi-particle subspaces must vanish in the limit $\ell \to \infty$. Consequently, the effective Hamiltonian is block-diagonal in the quasi-particle number.
If we consider a non-Hermitian matrix with $\tilde{h}_{n,m}(\ell) \neq \tilde{h}_{m,n}(\ell)^*$ for $n \neq m$, the product of a hermitian conjugate pair of matrix elements $\tilde{h}_{n,m}(\ell)\tilde{h}_{m,n}(\ell)$ is not necessarily positive and, thus, the sum in (2.94) is not a monotonically decreasing function.
In order to examine the effects of a non-unitary flow, we decompose the Hamiltonian $\tilde{H}$ into a hermitian and an anti-hermitian part

$$\tilde{H}(\ell) = H_S(\ell) + H_A(\ell) \tag{2.96}$$

$$H_S^\dagger(\ell) = H_S(\ell) \tag{2.97}$$

$$H_A^\dagger(\ell) = -H_A(\ell) \quad . \tag{2.98}$$

As a result, we obtain two coupled flow equation for H_S and H_A

$$\partial_\ell H_S(\ell) = \Big[\, \eta(H_S)(\ell), H_S(\ell) \,\Big] + \Big[\, \eta(H_A)(\ell), H_A(\ell) \,\Big] \tag{2.99a}$$

$$\partial_\ell H_A(\ell) = \Big[\, \eta(H_S)(\ell), H_A(\ell) \,\Big] + \Big[\, \eta(H_A)(\ell), H_S(\ell) \,\Big] \quad . \tag{2.99b}$$

We define the matrix elements of the symmetric part $\langle m|\, H_S(\ell)\,|n\rangle = h_{n,m}(\ell)$ and and the skew-symmetric part $\langle m|\, H_A(\ell)\,|n\rangle = \Delta_{n,m}(\ell)$ which are assumed to be real in the following, for the sake of simplicity. In this case, the diagonal elements of H_A are zero such that $\mathrm{Tr}(H(\ell)) = \mathrm{Tr}\big(H^S(\ell)\big)$. The sum over the first r diagonal elements as defined in equation 2.94 yields

$$\sum_{n=0}^{r} \partial_\ell h_{n,n}(\ell) = 2 \sum_{n=0}^{r} \sum_{k=r+1}^{D} \mathrm{sign}(q_n - q_k)(h_{n,k}(\ell) h_{k,n}(\ell) + \Delta_{n,k}(\ell)\Delta_{k,n}(\ell)) \tag{2.100a}$$

$$= -2 \sum_{n=0}^{r} \sum_{k=r+1}^{D} \left(\big|h_{n,k}(\ell)\big|^2 - \big|\Delta_{n,k}(\ell)\big|^2\right) \quad . \tag{2.100b}$$

The coefficients $\Delta_{n,k}$ of the skew-symmetric part counteract the symmetric coefficients $h_{n,k}$ and as a result, the flow of the diagonal elements becomes more intricate compared to the unitary case. The reason for this intricacy lies in the fact, that the diagonal elements of a non-hermitian matrix are not bounded by their lowest and highest eigenvalues E_0 and E_{max} in contrast to hermitian matrices, i.e., the inequalities

$$E_0 \leq \langle \Psi|\, H\,|\Psi\rangle \leq E_{\mathrm{max}} \qquad \text{for } \langle \Psi|\Psi\rangle = 1 \tag{2.101}$$

do not hold for non-hermitian matrices H.[15]
In the following, we discuss some special cases for which convergence can be shown for the Mielke and the particle-conserving generator scheme.
First, let us consider a triangular matrix $\tilde{h}_{n,m} = h_{n,m} + \Delta_{n,m}$ which is defined by $\Delta_{n,m} = \mathrm{sign}(n-m)h_{n,m}$. In the case of a triangular Hamiltonian the flow equations assume a very simple form. For the Mielke generator the flow equations read

$$\begin{aligned} \partial_\ell h_{nm} &= \sum_k [\mathrm{sign}(n-k) + \mathrm{sign}(m-k)]\,(h_{nk}h_{km} + \mathrm{sign}(n-k)\mathrm{sign}(k-m))h_{nk}h_{km} \\ &= -\mathrm{sign}(n-m)(h_{nn} - h_{mm})h_{nm} \end{aligned} \tag{2.102}$$

where we used $\mathrm{sign}(n-m)\mathrm{sign}(n-m) = 1 \;\; \forall k \neq n$. Analogously, one finds

$$\partial_\ell \Delta_{nm} = -\mathrm{sign}(n-m)(h_{nn} - h_{mm})\Delta_{nm} \tag{2.103}$$

Due to the energetic hierarchy we have $\mathrm{sign}(n-m)(h_{n,n} - h_{m,m}) = \alpha_{n,m} \geq 0$ and, thus, all non-diagonal elements vanish in the limit $\ell \to \infty$ because they decrease exponentially as $h_{n,m}(\ell) \propto e^{-\alpha_{n,m}\ell}$. The reason for this simplicity lies in the fact, that the diagonal elements of a triangular matrix already correspond to the eigenvalues of the matrix.

[15] For infinite systems, the inequalities are reduced to the statement about the lowest eigenvalue E_0, i.e., the Hamilton operator must be bounded from below.

In the case of the particle-conserving generator the equations are genereliz ed to

$$\begin{aligned}\partial_\ell h_{\mathbf{i,j}} &= -\mathrm{sign}(q_i - q_j)(h_{\mathbf{i,i}} - h_{\mathbf{j,j}})h_{\mathbf{i,j}} \\ \partial_\ell \Delta_{\mathbf{i,j}} &= -\mathrm{sign}(q_i - q_j)(h_{\mathbf{i,i}} - h_{\mathbf{j,j}})\Delta_{\mathbf{i,j}} \quad ,\end{aligned} \tag{2.104}$$

where $\Delta_{\mathbf{i,j}}$ and $h_{\mathbf{i,j}}$ are matrices which link the subspaces with i and j quasi-particles. Thus, we are considering a block-triangular matrix. As we presume that the given Hamiltonian is diagonalizable, there exists a similarity transformation s_i and s_i^{-1} which diagonalizes the matrices $s_i h_{\mathbf{i,i}} s_i^{-1} = d_{\mathbf{i}}$. Then the flow of the matrix elements of $(\bar{h}_{\mathbf{i,j}})_{nm} = (s_i h_{\mathbf{i,j}} s_j^{-1})_{nm}$ is given by

$$\partial_\ell (\bar{h}_{\mathbf{ij}})_{nm} = -\mathrm{sign}(q_i - q_j)((d_{\mathbf{i}})_{nn} - (d_{\mathbf{jj}})_{mm})(\bar{h}_{\mathbf{ij}})_{nm} \tag{2.105}$$

which will decrease exponentially if the eigenvalues are ordered with respect to the particle number q_i. Similar relations are obtained, if we consider a Hamiltonian which is close to a diagonal or block diagonal form. Consequently, these forms constitute fixed points of the flow equation. We do not show the proof, as it follows the same arguments as for the triangular case. It should be stressed, however, that in contrast to the hermitian case it is not clear whether all starting points will converge to this fixed points. Figure 2.25 shows schematically a summary of the results.

It is a highly non-trivial task to show the convergence of the continuous similarity transformations for a more general setup. This is due to the lack of universal theorems which provide a priori information about the spectrum or eigenbasis of a generic non-hermitian matrix. From a theoretical point of view, we can not exclude the existence of other fixed points or non-converging flows, at least in the scope of this thesis. Regarding the practical application, though, this does not pose a particular problem as we have shown, that the principal function of the generalized approach is retained, i.e., the diagonal or block-diagonal matrices still constitute a fixed point of the corresponding generator scheme. Moreover, it should be stressed that even for the unitary approach a convergent flow can not be guaranteed in non-perturbative applications, as unitarity is violated due to truncation errors.

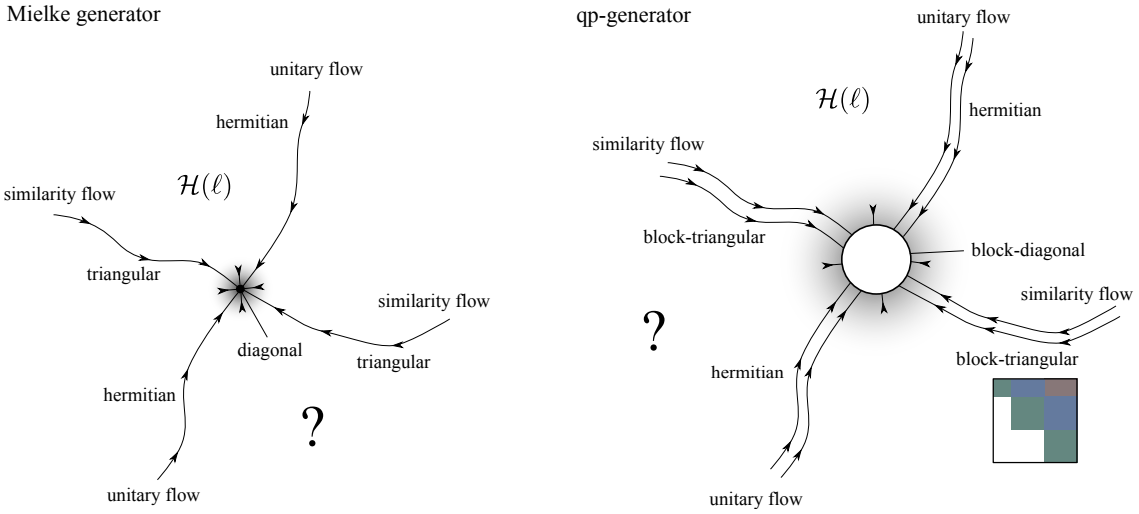

Figure 2.25: The convergence of a continuous similarity transformation for the Mielke and the η^{qp} generator is sketched.

2.7 Chapter summary

In this chapter the methodical foundation of this thesis is presented which is based on continuous unitary transformations (CUT). In the first part, a brief introduction to the CUT method is given explicating its general motivation and methodical framework.
The second part discusses the utilization of the CUT approach in momentum space focusing on its application to gapless systems. The primary goal is the derivation of a quasi-particle conserving model of gapless excitations. From a methodical point of view, the effective description of gapless excitations in real space poses major difficulties. In this context, the potential and the advantages of a momentum space CUT over the real space approach are pointed out.
Moreover, the momentum space CUT method is translated into a diagrammatic language, which simplifies the derivation and interpretation of the flow equations, providing an intuitive picture of the resulting effective model in terms of virtual fluctuations.
For concrete evaluation of the flow equations a physically justified truncation criterion is required. The concept of scaling dimension is particularly suited for gapless systems with infinite correlation length. In section 2.5 the use of scaling dimension of operator terms as a truncation criterion for the CUT method is introduced.
The last part discusses the generalization of the CUT approach to similarity transformations, which are referred to as continuous similarity transformations (CST).
The next chapter deals with methodical aspects, which are important for the concrete implementation and application of the CST approach in momentum space.

CHAPTER 3

Methodical Aspects

This chapter addresses important technical aspects concerning the application and implementation of the CST approach in momentum space. The first part gives a brief overview about the technical steps that were performed in order to derive and integrate the corresponding flow equations.
In the second part we discuss various methods for the subsequent evaluation of dynamic structure factors in the context of quasi-particle conserving Hamiltonians and effective observables in momentum space. An essential aspect is the treatment of non-hermitian problems. A generalized continued fraction expansion for resolvents of non-hermitian operators is presented which can be obtained by a non-symmetric Lanczos tridiagonalization.
The last section discusses various interpolation schemes required for the reduction of finite-size effects, which arise due to finite discretizations in momentum space.

3.1 Derivation and integration of flow equations in momentum space

In section 2.4 we have shown that the general form of flow equations in momentum space is given by

$$\partial_\ell C_\alpha(\vec{i}) = \sum_{\beta,\gamma} D_\alpha^{\beta\gamma} \sum_{\vec{j}} C_\beta(\vec{i}_\beta, \vec{j}) C_\gamma(\vec{i}_\gamma, \vec{j}) \quad .$$

These equations are fully determined by the prefactors $D_{\beta\gamma}^{\alpha}$ and the contracted momenta $\mathbf{k}_j \in \vec{j}$ between the coefficients of the Hamiltonian or the observable C_β and C_γ. In a perturbative analysis the operator terms are characterized by their leading order in a perturbative parameter also referred to as their minimal order [44].
In this thesis an automated program is developed which derives the flow equations for generic bosonic Hamiltonians and observables in momentum space for different types of quasi-particle generators and truncation schemes. In the following the general functionality of this program is explained. We want to give an brief overview about the general procedure, thus, the focus is on the description of the major steps in the automated derivation. However, we do not go into details of the concrete implementation.

General function

The main input is given by a generic Hamiltonian and observables in second quantization. Both, Hamiltonian and observables are sums of operator terms which are represented in form of a list. From this input, the program determines the form of the flowing generator $\eta(\ell)$, Hamiltonian $H(\ell)$ and the observables according to a specified generator and truncation scheme. We can choose between the standard η^{qp} or the $\eta^{n:0}$ generator. On this basis, the program provides an automated derivation of the flow equations determining the pre-factors $D_\alpha^{\beta\gamma}$ and the corresponding contractions between the coefficients.
The derivation can be conducted in a perturbative fashion, which requires the specification of the perturbative order for the coefficients in the initial Hamiltonian. The resulting flow equations can be further evaluated in the context of an epCUT or deepCUT approach [44]. Moreover, it is possible to determine self-similar flow equations based on individual truncation criteria, such as scaling dimension.
The program performs the computational derivation on a pure algebraic level. An important advantage in the momentum space representation is that the geometry and dimension of the Brillouin zone does not need to be specified in order to derive the flow equation on an algebraic level, because the prefactors and contractions do not depend on the concrete form of the momentum sums.
All operations in the derivation, such as the contractions of operator terms in the commutator, depend solely on the type of monomials. One does not need to consider concrete values of momenta and coefficient functions or the concrete structure of the Brillouin zone. This is also reflected in the diagrammatic representation discussed in section 2.4.2, which shows that there is no necessity to differentiate between two monomials of the same type, i.e., monomials represented by the same diagram. Thus, on an algebraic level, the resulting equations are valid for the same type of Hamiltonians featuring arbitrary Brilluoin zones.[1]
In contrast, in the real space approach one has to distinguish between monomials of similar type, if they are defined on different topologies (or graphs). Thus, one has to take into account additional geometric information about the lattice.
The geometric information of the model such as the coordination number and the lattice structure etc., is encoded in the momentum sums and the initial conditions for the coefficient functions. These become only relevant in the actual evaluation of the flow equations. Therefore, it is beneficial to perform the derivation and integration of the flow equations in two separate programs with a compatible interface.

Operator representation

The major part of the relevant information can be represented by a set of integer numbers referring to indices which distinguish between different coefficient functions, monomials, boson operators and momentum arguments.
Every term in the Hamiltonian or the observable is a product of a coefficient function $C_\alpha(\mathbf{k}_1, \ldots \mathbf{k}_n)$ and a normal ordered monomial $A_\alpha = a_{\mathbf{1}}^\dagger a_{\mathbf{2}}^\dagger \cdots a_{\mathbf{n}}$ of bosonic creation $a_{\mathbf{i}}^\dagger$ and annihilation operators $a_{\mathbf{i}}$ in momentum space. Each bosonic creation or annihilation operator in the monomial is associated with a distinct index $\mathbf{i}$ referring to its momentum $\mathbf{k}_i$. Moreover, it is possible to distinguish between different types of bosons (e.g. $a_{\mathbf{i}}^{(\dagger)}$ and $b_{\mathbf{i}}^{(\dagger)}$), which describe independent

[1] The type of the Hamiltonian is specified by the set of monomials and the corresponding boson types.

bosonic excitations $\left[a_1^\dagger, b_1^\dagger \right] = \left[a_1, b_1^\dagger \right] = 0$. The number of different boson types is not limited.
The operator terms and the corresponding coefficient function $C_\alpha(\mathbf{k}_1, \dots \mathbf{k}_n)$ are assigned by a pre-defined number α. In addition, the operator terms can be specified by their minimal order in a perturbative parameter.
Thus, a single boson operator can be identified by two integer numbers which denote the boson type and the momentum index, and a Boolean which distinguishes between boson creation or annihilation. A monomial is given by an ordered sequence of boson operators. The Hamiltonian and the observables can be represented as sets of monomial types which can be addressed by a distinct number α. This number serves as an identifier of the associate coefficient function. In addition, the operator term is characterized by its leading order in the perturbative parameter.
The indices of the momentum arguments in the coefficient function must be allocated unambiguously to the indices of the creation and annihilation operators in the monomial. Therefore, it is advisable to arrange the operator sequences in the monomials by a distinct order. Here, we arrange the opertors by monomials of a particular boson type which are further sorted by ascending index numbers

$$\begin{aligned} & C_\alpha(\vec{i}_\alpha)\; a_1^\dagger \dots a_{\mathbf{n(a)}} b_{\mathbf{n(a)+1}}^\dagger \dots b_{\mathbf{n(a)+n(b)}} \cdots \\ & \vec{i}_\alpha = \left(\mathbf{k}_1 \dots \mathbf{k}_{n(a)}, \mathbf{k}_{n(a)+1}, \dots \mathbf{k}_{n(a)+n(b)} \dots\right) \quad . \end{aligned} \tag{3.1}$$

This convention simplifies the subsequent treatement, which requires the comparison between types of monomials and the identification of similar operator terms. The general representation is illustrated in Figure 3.1.

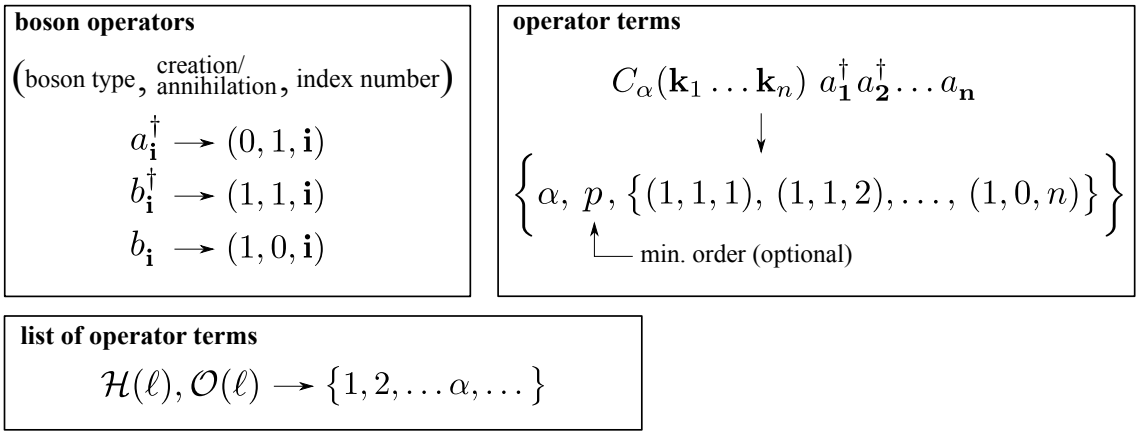

Figure 3.1: Computational representation of momentum space operators.

Evaluation of commutators

An important part in the derivation is the evaluation of commutators between normal ordered monomials. Therefore, a routine is required which conducts a normal ordering of any given operator sequence. The output of this routine is a set of normal ordered monomials of the form (3.1). Every monomial A_α is associated with a set of contractions $\delta^\alpha_{\beta\gamma}$ and a prefactor

$F^{\alpha}_{\beta\gamma}$

$$\left[A_\beta(\vec{i}_\beta), A_\gamma(\vec{i}_\gamma)\right] = \sum_\alpha F^{\alpha}_{\beta\gamma} A_\alpha(\vec{i}_\alpha)\, \delta^{\alpha}_{\beta\gamma}(\vec{j}_\beta, \vec{j}_\gamma) \quad . \tag{3.2}$$

The contractions are pairs of indices, each representing a Kronecker delta in the bosonic case

$$\delta_\alpha(\vec{j}_\beta, \vec{j}_\gamma) = \delta_{j_{\beta,1}, j_{\gamma,1}} \delta_{j_{\beta,2}, j_{\gamma,2}} \cdots \tag{3.3}$$

The sets of contracted indices $\vec{j}_\beta$ and $\vec{j}_\gamma$ are subsets of $\vec{i}_\beta$ and $\vec{i}_\gamma$. The remaining indices $\{\vec{i}_\alpha\} = \left(\{\vec{i}_\beta\} \cup \{\vec{i}_\gamma\}\right) \setminus \left(\{\vec{j}_\beta\} \cup \{\vec{j}_\gamma\}\right)$ refer to the open momentum arguments. The determination of the monomials and contractions is a combinatorial task, which, for example, can be solved by functions based on Wicks's theorem [75] (see also section 2.4.2).

Determining the flowing Hamiltonian and observables

In the first step, one has to determine all types of monomials that constitute the operator basis of the Hamiltonian and the observables in accordance to the truncation scheme. This can be done by an successive evaluation of the commutator $\left[\eta(\ell), H(\ell)\right]$. The monomials are converted into operator terms of the form (3.1) and then added to the Hamiltonian and the generator, if they comply with the truncation scheme. Once no additional operator terms conformable to the truncation criterion are created in the commutator, the desired form of $H(\ell)$ is reached. Based on the resulting generator the same procedure is applied to the observables. Note, that a concrete tracking of indices and contractions in the commutators is not necessary at this stage, because only the types of monomials are relevant for the expansion of $H(\ell)$ and $\eta(\ell)$.

Derivation of the flow equations

The main task in the derivation is the systematic book keeping of index assignments and contractions in the commutator. The relevant information consists of the resulting monomial type, the indices of its creation and annihilation operators (which are referred to as open indices) as well as the contracted indices. In order to simplify the resulting expressions one has to identify and combine similar terms. Therefore, also the prefactors of the resulting operator terms have to be tracked. Once all resulting operator terms are determined, one has to equate coefficients on the left- and right-hand side of flow equation. In this step the open indices on the right-hand side are allocated to the arguments of the first derivative of a coefficent function. A distinct index assignment is of major importance in the whole automated procedure. Figure 3.2 exemplifies the generic form of the resulting output.
The interpretation of the resulting data is straightforward. The open indices are represented by the numbers which occur on both sides of the flow equations. They correspond to the free momentum arguments in the coefficient at hand. The remaining numbers, which correspond to the coefficient functions at the right-hand side of the equations denote the contracted momenta. Thus, we have to attach additional sums over all contracted contracted indices.
As discussed in section 2.4 the conservation of momentum is encoded in the coefficient functions (see equation (2.31)). The conditions of the momentum arguments must be consistent on the left- and right-hand side of the corresponding flow equation. Hence, the conservation

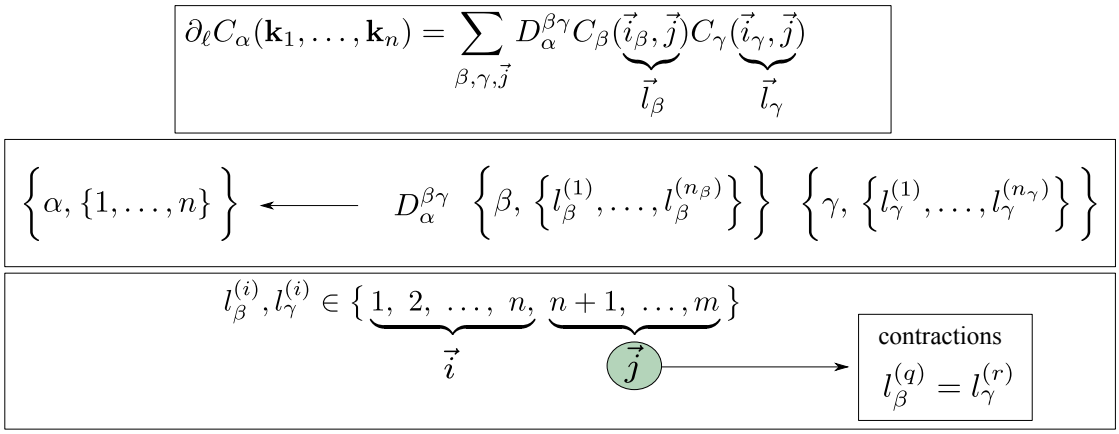

Figure 3.2: Generic output representing the resulting flow equations

of momentum in C_α must also follow from the constraints imposed by the respective conservation of momentum in the contracted coefficients C_β and C_γ for each term in the flow equation. This allows us to make a consistency check of the program verifying that the contractions are determined correctly. Moreover, the number of independent contracted momenta is reduced by one due to the additional constraint imposed by the total conservation of momentum.
In the last step, the program symmetrizes the flow equations according to (2.33).

3.2 Solving flow equations

Next, we discuss the numerical evaluation of the flow equations. Thus, we have to consider a concrete Hamiltonian specifying the momentum sums and the initial conditions of the coefficients. In the thermodynamic limit the resulting flow equations are non-linear integro-differential equations, which cannot be solved analytically. In order to obtain a numerical solution we use a finite discretization of the Brillouin zone. This allows us to represent the information about the flowing Hamiltonian in terms of a finite coefficient vector

$$\vec{y}(\ell) = \begin{pmatrix} \vec{C}_1(\vec{i}_1) \\ \vec{C}_2(\vec{i}_2) \\ \vdots \\ \vec{C}_\alpha(\vec{i}_\alpha) \\ \vdots \\ \vec{C}_{N_A(\vec{i}_{N_A})} \end{pmatrix} \tag{3.4}$$

with the coefficient functions

$$\vec{C}_\alpha(\vec{i}_\alpha) = \begin{pmatrix} C_\alpha(\mathbf{k}^{(1)},\cdots\mathbf{k}^{(1)}) \\ \vdots \\ C_\alpha(\mathbf{k}^{(N)},\cdots\mathbf{k}^{(N)})) \end{pmatrix} \tag{3.5}$$

The $\mathbf{k}^{(i)}$ are the momenta defined on the i-th grid point, whereas N is the number of grid points. The coefficient function of an operator term containing n_B bosonic creation or annihilation operators depends on $n(\alpha) = n_B - 1$ momentum arguments if conservation of total momentum is used. Hence, the number of different discretization points for this coefficient function is given by $N_\alpha = N^{n_B-1}$.
It is expedient to consider equidistant discretizations of the Brillouin zone as shown in Figure 3.3. The corresponding momentum grid points define a lattice $\kappa_{\mathrm{BZ}} = \left\{\mathbf{k}^{(i)} | i = 1 \dots N\right\}$ and, consequently, any sum of arbitrary momentum vectors coincides with another vector in the discretized Brillouin zone

$$\mathbf{k}^{(i)} + \mathbf{k}^{(j)} \in \kappa_{\mathrm{BZ}} \quad \forall\, \mathbf{k}^{(i)}, \mathbf{k}^{(j)} \in \kappa_{\mathrm{BZ}} \quad . \tag{3.6}$$

This is particularly important for maintaining the exact conservation of momentum which otherwise is violated by non-equidistant discretizations. Especially for gapless systems the violation of momentum conservation may lead spuriously to multi-particle states lying energetically below the single-particle state, which in turn gives rise to a divergent flow.
For a reduced Brillouin zone (e.g. a magnetic Brillouin zone) one might encounter sign changes in the coefficient functions due to umklapp processes $C_\alpha(\dots, \mathbf{k}_i + \mathbf{G}, \dots) = \Gamma^{\mathbf{G}} C_\alpha(\dots, \mathbf{k}_i, \dots)$ where $\mathbf{G}$ is a reciprocal lattice vector defined by the reduced Brillouin zone. The function $\Gamma^{\mathbf{G}}$ is either 1 or -1 depending on the MBZ in which the vector $\mathbf{G}$ is located (see also (4.18). The momentum sums in the Hamiltonian can be restricted to the reduced Brillouin zone. Hence, it is expedient to define the momentum arguments of the coefficient functions such that they are solely located in the reduced Brillouin zone. More concretely, we define the initial conditions

$$C_\alpha(\mathbf{k}_1 \dots \mathbf{k}_{n+m-1})(\ell = 0) := V_m^n(\mathbf{k}_1, \dots, \mathbf{k}_{n+m-1}, \mathbf{K}(\mathbf{k}_1, \dots, \mathbf{k}_{n+m-1})) \tag{3.7}$$

with

$$\mathbf{K}(\mathbf{k}_1, \dots, \mathbf{k}_{n+m-1}) = \sum_{i=m+1}^{n+m-1} \mathbf{k}_i - \sum_{i=1}^{n} \mathbf{k}_i + \mathbf{G}(\mathbf{k}_1, \dots, \mathbf{k}_{n+m-1}) \tag{3.8}$$

and a reciprocal lattice vector $\mathbf{G}(\mathbf{k}_1, \dots, \mathbf{k}_{n+m-1})$ such that $\mathbf{K} \in 1^{\mathrm{st}}\mathrm{BZ}$. Both definitions, (3.7) and (3.8), help to preclude any misasignments or confusion due to umklapp signs in the evaluation of the flow equations. This is important because it might happen that a reduced momentum argument $\mathbf{K}(\mathbf{k}_1, \dots, \mathbf{k}_{n+m-1})$ coincides with a free momentum argument $\mathbf{k}_i$. In this case, $\mathbf{k}_i$ appears indirectly as a part of a different contracted momentum argument $\mathbf{k}_j(\dots \mathbf{k}_i \dots)$ which is determined by conservation of momentum. If the indirectly evaluated momentum argument $\mathbf{k}_j(\dots \mathbf{k}_i \dots)$ is located outside the reduced Brillouin zone, we apply a function which maps the momentum argument onto the reduced Brillouin zone by determining the corresponding reciprocal lattice vector in (3.8).
Note, that the function imposes periodic boundary conditions in momentum space which requires a unique assignment of momenta at the zone boundary as shown in Figure 3.3.

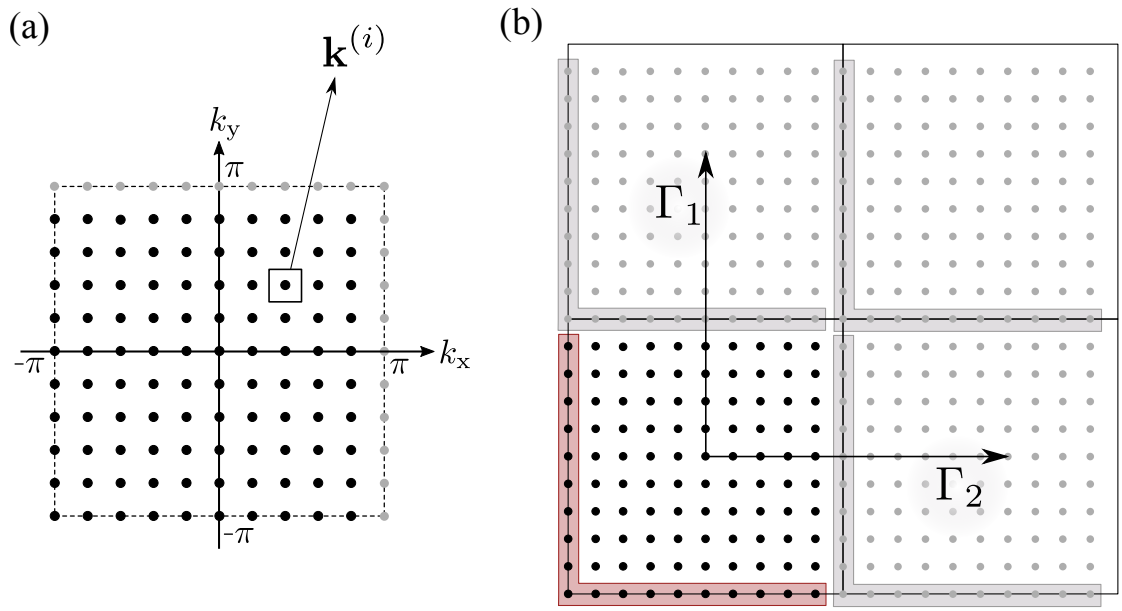

Figure 3.3: Equidistant discretization of a two dimensional Brillouin zone.

3.2.1 Integration of the flow equations

The flow equations constitute a system of first order ordinary differential equations of the form

$$\partial_\ell \vec{y}(\ell) = \vec{F}(\vec{y}(\ell)) \tag{3.9}$$

The computational costs for the evaluation of F depends on the size of the vector $\vec{y}$ which grows polynomially with the system size N. Thus, it is advisable to use methods which require a comparatively small number of evaluations of F. Typically, explicit Runge-Kutta methods are used in the CUT approach [71].
Formally, one has to integrate the flow equations up to $\ell \to \infty$. However, it is sufficient to stop the integration at finite ℓ, once the coefficients converged within a desired tolerance, as we expect an monotonic decrease of coefficients of the non-block-diagonal part for sufficiently large ℓ. In the CUT approach the residual off-diagonality (ROD) is tracked to determine how far the flow has converged. The ROD is defined as the square root of the sum of squared matrix elements in the generator $\eta(\ell)$ [51] and provides a measure for $|H_{\text{eff}} - H(\ell)|$. The integration is terminated when the ROD drops below a predefined accuracy.
The integration covers a large range in ℓ for which the the transformation determined by $\vec{F}(\vec{y}(\ell))$ exhibits different behavior. For small values of ℓ the ROD is relatively large and often increases in the beginning of the flow. As a consequence, the flow $\vec{F}(\vec{y}(\ell))$ assumes larger values and varies strongly for smaller increments $d\ell$. By contrast, the ROD exhibits an exponential decrease for large values of ℓ (provided that the flow is convergent) and the flow varies on larger scales of ℓ. Thus, it is advisable to use an adaptive step size to account for this changing behavior enhancing the efficiency and accuracy of the method.
In the scope of this thesis, a Runge-Kutta-Fehlberg 4(5) method is implemented which is particularly suited for the problem at hand. A brief description of this method is given in the next part.

Runge-Kutta-Fehlberg (4)5 method

The Runge-Kutta-Fehlberg method was originally introduced by Fehlberg in 1969 [119, 120]. It is based on the embedded Runge-Kutta procedures [121]. The idea is to compute two approximations for the solution which can be compared in order to obtain an estimated prediction of the error. In most applications, a combination of a fourth-order and a more accurate fifth order Runge-Kutta method is used. This algorithm is typically referred to as Runge-Kutta-Fehlberg 4(5) method or short RKF45. The fourth order approximation is given by

$$\vec{y}_{n+1}^{(4)} = \vec{y}_n + h\sum_{i=0}^{4}\gamma_i\vec{k}_i + \mathcal{O}(h^5) \quad . \tag{3.10}$$

The more accurate value is determined by the fifth order Runge-Kutta approximant

$$\vec{y}_{n+1}^{(5)} = \vec{y}_n + h\sum_{i=0}^{5}\delta_i\vec{k}_i + \mathcal{O}(h^6) \quad . \tag{3.11}$$

The vectors $\vec{k}_i$ are obtained in the following way

$$\vec{k}_0 = F\big(\ell,\ \vec{y}\big) \tag{3.12a}$$

$$\vec{k}_1 = F\big(\ell+\alpha_1,\ \vec{y}+h\beta_{1,0}\vec{k}_0\big) \tag{3.12b}$$

$$\vec{k}_2 = F\big(\ell+\alpha_2,\ \vec{y}+h\sum_{i=0}^{1}\beta_{2,i}\vec{k}_i\big) \tag{3.12c}$$

$$\vec{k}_3 = F\big(\ell+\alpha_3,\ \vec{y}+h\sum_{i=0}^{2}\beta_{3,i}\vec{k}_i\big) \tag{3.12d}$$

$$\vec{k}_4 = F\big(\ell+\alpha_4,\ \vec{y}+h\sum_{i=0}^{3}\beta_{4,i}\vec{k}_i\big) \tag{3.12e}$$

$$\vec{k}_5 = F\big(\ell+\alpha_5,\ \vec{y}+h\sum_{i=0}^{4}\beta_{5,i}\vec{k}_i\big) \tag{3.12f}$$

where α_i, γ_i, δ_i and $\beta_{i,j}$ are given by the Fehlberg coefficients shown in the Butcher tableau in Table 3.1. An estimate of the error is given by

$$\epsilon = \left|\vec{y}_{n+1}^{(5)} - \vec{y}_{n+1}^{(4)}\right| \tag{3.13}$$

From this the optimal step size can be estimated by

$$h_{\text{opt}} = \beta h\left|\frac{\epsilon_{\text{tol}}}{\epsilon}\right|^{0.2} \tag{3.14}$$

i	α_i	$\beta_{1,i}$	$\beta_{2,i}$	$\beta_{3,i}$	$\beta_{4,i}$	$\beta_{5,i}$	
1	$\frac{1}{4}$	$\frac{1}{4}$					
2	$\frac{3}{8}$	$\frac{3}{32}$	$\frac{9}{32}$				
3	$\frac{12}{13}$	$\frac{1932}{2197}$	$-\frac{7200}{2197}$	$\frac{7296}{2197}$			
4	1	$\frac{439}{216}$	-8	$\frac{3680}{513}$	$-\frac{845}{4104}$		
5	$\frac{1}{2}$	$-\frac{8}{27}$	2	$-\frac{3544}{2565}$	$\frac{1859}{4104}$	$-\frac{11}{40}$	
	j	0	1	2	3	4	5
	γ_j	$\frac{25}{216}$	0	$\frac{1408}{2565}$	$\frac{2197}{4104}$	$-\frac{1}{5}$	
	δ_j	$\frac{16}{135}$	0	$\frac{6656}{12825}$	$\frac{28561}{56430}$	$-\frac{9}{50}$	$\frac{2}{55}$

Table 3.1: Butcher tableau for the Fehlberg coefficients.

where h denotes the current step size and $\beta < 1$ is a safety factor. The step size is decreased if the estimated error is larger than the predefined control tolerance $\epsilon < \epsilon_{\text{tol}}$. Otherwise, the step size can be increased in the following step. The step size adaption is applied according to

$$h_{\text{opt}} = \begin{cases} \beta h \left|\frac{\epsilon_{\text{tol}}}{\epsilon}\right|^{0.2} & \text{for } \epsilon \geq \epsilon_{\text{tol}} \\ \beta h \left|\frac{\epsilon_{\text{tol}}}{\epsilon}\right|^{0.25} & \text{for } \epsilon \geq \epsilon_{\text{tol}} \end{cases} .$$

The formulas of the RKF4(5) method and the error estimates are taken from the numerical methods script provided by the Westfälische Wilhelms-Universität Münster [122].

3.3 Spectral densities of non-hermitian problems

This section addresses the evaluation of dynamic structure factors or spectral densities, in particular, with regard to non-hermitian representations. In general, spectral densities are obtained from resolvents of the form

$$R(\omega) = \langle v | \frac{1}{\omega - H} | v \rangle \tag{3.15}$$

In the standard approach for hermitian problems with $H = H^\dagger$ the concrete function $R(\omega)$ is determined by means of its continued fraction representation.

$$R(\omega) = \cfrac{\langle v|v\rangle}{a_0 - \omega - \cfrac{b_1^2}{a_1 - \omega - \cfrac{b_2^2}{\cdots}}} \tag{3.16}$$

where the a_i and b_i coefficients can be obtained by a Lanczos tridiagonalization of H using $|v\rangle$ as starting vector [123].

In the following we generalize this procedure for a non-symmetric problem

$$R(\omega) = \langle v_L | \frac{1}{\omega - H} | v_R \rangle \tag{3.17}$$

with $H \neq H^\dagger$ and $|v_L\rangle \neq |v_R\rangle$. For this purpose, we derive a generalized continued fraction representation of a non-symmetric resolvent (3.17) with $T := \omega - H$. First, we define a bi-orthonormal basis $|L_n\rangle$ and $\langle R_m|$ with $\langle L_n | R_m \rangle = \delta_{n,m}$, such that the matrix of T in this basis has a tridiagonal form. The initial vectors are set to $|R_0\rangle = \frac{1}{\langle v_R | v_L \rangle} |v_R\rangle$ and $|L_0\rangle = \frac{1}{\langle v_R | v_L \rangle} |v_L\rangle$. We attach an index to the matrix $T := T_{(0)}$ as we will iteratively reduce the problem to sub-matrices

$$T_{(m)} := Q_m T Q_m \tag{3.18a}$$

$$Q_{(0)} = \mathbb{1} \tag{3.18b}$$

$$Q_{(m)} = \mathbb{1} - \sum_{n=1}^{m} |R_{n-1}\rangle \langle L_{n-1}| \quad \text{for } m > 0$$

which are related by the recursive formula

$$\langle L_n | \frac{1}{T_{(n)}} | R_n \rangle = \frac{1}{a_n - \gamma_{n+1}\beta_{n+1} \langle L_{n+1} | \frac{1}{T_{(n+1)}} | R_{n+1} \rangle} \quad . \tag{3.19}$$

determining the continued fraction of (3.17). The operators $Q_{(m)}$ are projectors on the sub-space of the reduced bi-orthonormal basis $\{|L_n\rangle, \langle R_n| \,|\, n \geq m\}$. The structure of the matrix $T_{(m)}$ is illustrated in Figure 3.4.

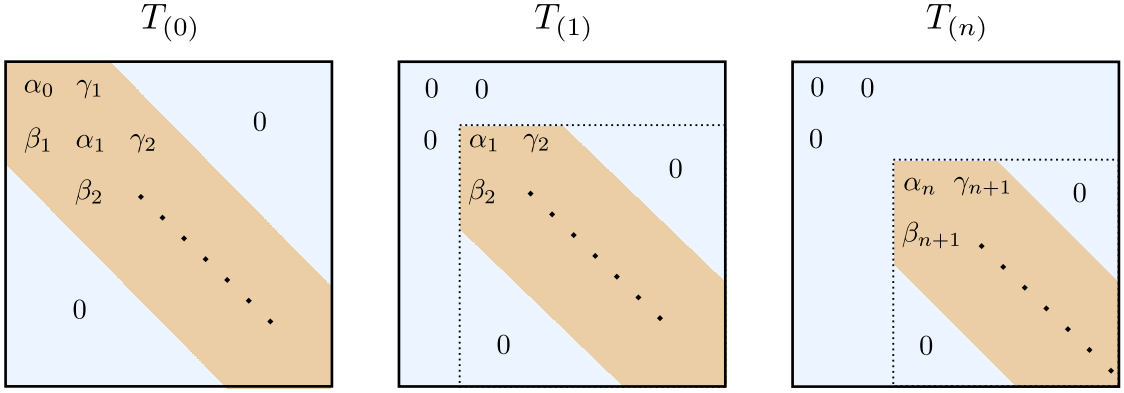

Figure 3.4: Illustration of the matrix $T_{(n)}$ as defined in (3.18a)

In the following, we derive the recursive formula (3.19). By definition, the action of $T_{(0)}$ on the basis vectors is given by

$$T_{(0)}\,|R_0\rangle = a_0\,|R_0\rangle + \gamma_1\,|R_1\rangle \tag{3.20a}$$

$$T_{(0)}\,|R_n\rangle = a_n\,|R_n\rangle + \beta_n\,|R_{n-1}\rangle + \gamma_{n+1}\,|R_{n+1}\rangle \quad \text{for } n \geq 1 \tag{3.20b}$$

$$\langle L_0|\,T_{(0)} = a_0\,\langle L_0| + \beta_1\,\langle L_1| \tag{3.20c}$$

$$\langle L_n|\,T_{(0)} = a_n\,\langle L_n| + \gamma_n\,\langle L_{n-1}| + \beta_{n+1}\,\langle L_{n+1}| \quad \text{for } n \geq 1 \tag{3.20d}$$

We decompose the operator into $T_{(0)} = B_0 + T_{(1)}$. The matrix B_0 comprises the first entries a_0, β_1 and γ_1, and is zero otherwise. The remaining block is given by the sub-matrix $T_{(1)}$. The action of B_0 and $T_{(1)}$ on the basis vectors is defined by

$$B_0\,|R_0\rangle = a_0\,|R_0\rangle + \gamma_1\,|R_1\rangle \tag{3.21a}$$

$$B_0\,|R_1\rangle = \beta_1\,|R_0\rangle \tag{3.21b}$$

$$\langle L_0|\,B_0 = a_0\,\langle L_0| + \beta_1\,\langle L_1| \tag{3.21c}$$

$$\langle L_1|\,B_0 = \gamma_1\,\langle L_0| \tag{3.21d}$$

$$B_0\,|R_n\rangle = \langle L_n|\,B_0 = 0 \quad \text{for } n \geq 2 \tag{3.21e}$$

and

$$T_{(1)}\,|R_0\rangle = \langle L_0|\,T_{(1)} = 0 \tag{3.22a}$$

$$T_{(1)}\,|R_1\rangle = a_1\,|R_1\rangle + \gamma_2\,|R_2\rangle \tag{3.22b}$$

$$T_{(1)}\,|R_n\rangle = a_n\,|R_n\rangle + \beta_n\,|R_{n-1}\rangle + \gamma_{n+1}\,|R_{n+1}\rangle \quad \text{for } n \geq 2 \tag{3.22c}$$

$$T_{(1)}\,\langle L_1| = a_1\,\langle L_1| + \beta_2\,\langle L_2| \tag{3.22d}$$

$$\langle L_n|\,T_{(1)} = a_n\,\langle L_n| + \gamma_n\,\langle L_{n-1}| + \beta_{n+1}\,\langle L_{n+1}| \quad \text{for } n \geq 2 \tag{3.22e}$$

Additionally, it is expedient to define an inverse operator $\frac{1}{T_{(1)}}$ for the remaining block, such that

$$\langle L_0|\,\frac{1}{T_{(1)}} = \frac{1}{T_{(1)}}\,|R_0\rangle = 0 \tag{3.23a}$$

$$\frac{1}{T_{(1)}}\,T_{(1)} = Q_{(1)} \quad , \tag{3.23b}$$

where $Q_{(1)}$ is the projector on the remaining subspace $\{\langle L_n|\,, |R_n\rangle\,|n \geq 1\}$. This additional definition is required because $T_{(1)}$ is singular in the full Hilbert space. Taking the scalar product

of equation (3.20a) with $\langle L_0| \frac{1}{T_{(0)}}$ and the scalar product of (3.20c) with $\frac{1}{T_{(0)}} |R_1\rangle$ yields

$$a_0 \langle L_0| \frac{1}{T_{(0)}} |R_0\rangle + \gamma_1 \langle L_0| \frac{1}{T_{(0)}} |R_1\rangle = 1 \tag{3.24a}$$

$$a_0 \langle L_0| \frac{1}{T_{(0)}} |R_1\rangle + \beta_1 \langle L_1| \frac{1}{T_{(0)}} |R_1\rangle = 0 \tag{3.24b}$$

$$\Rightarrow a_0 \langle L_0| \frac{1}{T_{(0)}} |R_0\rangle - \frac{\beta_1\gamma_1}{a_0} \langle L_1| \frac{1}{T_{(0)}} |R_1\rangle = 1 \tag{3.24c}$$

Next, we derive a relation between the matrix elements $\langle L_0| \frac{1}{T_{(0)}} |R_0\rangle$ and $\langle L_1| \frac{1}{T_{(1)}} |R_1\rangle$. To this end, we express $\langle L_1| \frac{1}{T_{(0)}} |R_1\rangle$ in terms of the operator $\frac{1}{T_{(1)}}$ by considering the following relation

$$\begin{aligned} \frac{1}{T_{(1)}} &= \frac{1}{T_{(1)}}(T_{(0)} + B_0)\frac{1}{T_{(0)}}Q_{(1)} \\ &= Q_{(1)}\frac{1}{T_{(0)}}Q_{(1)} + \frac{1}{T_{(1)}}B_0\frac{1}{T_{(0)}}Q_{(1)} \end{aligned} \tag{3.25}$$

which yields

$$\begin{aligned} \langle L_1| \frac{1}{T_{(1)}} |R_1\rangle &= \langle L_1| \frac{1}{T_{(0)}} |R_1\rangle + \langle L_1| \frac{1}{T_{(1)}} B_0 \frac{1}{T_{(0)}} |R_1\rangle \\ &= \langle L_1| \frac{1}{T_{(0)}} |R_1\rangle + \sum_n \langle L_1| \frac{1}{T_{(1)}} |n_R\rangle \langle n_L| B_0 \frac{1}{T_{(0)}} |R_1\rangle \\ &= \langle L_1| \frac{1}{T_{(0)}} |R_1\rangle + \langle L_1| \frac{1}{T_{(1)}} |R_1\rangle \gamma_1 \langle L_0| \frac{1}{T_{(0)}} |R_1\rangle \end{aligned} \tag{3.26}$$

In the third line we used equations (3.21d-3.22a). From this we obtain the relation

$$\begin{aligned} \langle L_1| \frac{1}{T_{(0)}} |R_1\rangle &= \langle L_1| \frac{1}{T_{(1)}} |R_1\rangle \left(1 - \gamma_1 \langle L_0| \frac{1}{T_{(0)}} |R_1\rangle\right) \\ &= a_0 \langle L_1| \frac{1}{T_{(1)}} |R_1\rangle \langle L_0| \frac{1}{T_{(0)}} |R_0\rangle \end{aligned} \tag{3.27}$$

where we also used (3.24a).
Eventually, we combine equation (3.27) with (3.24c) and find the following important result

$$\langle L_0| \frac{1}{T_{(0)}} |R_0\rangle = \frac{1}{a_0 - \gamma_1\beta_1 \langle L_1| \frac{1}{T_{(1)}} |R_1\rangle} \quad . \tag{3.28}$$

The term $\langle L_1| \frac{1}{T_{(1)}} |R_1\rangle$ is the resolvent of the tridiagonal sub-matrix $T_{(1)}$ with initial vectors $\langle L_1|$ and $|R_1\rangle$. It has the same structure as the initial resolvent $\langle L_0| \frac{1}{T_{(0)}} |R_0\rangle$. Since we can apply the same derivation for an arbitrary sub-matrix $T_{(m)}$, we can interpret equation (3.28) as a recursive relation between all sub-matrices given by (3.19).
In order to obtain the continued fraction representation of (3.17), we reintroduce the definition $T_{(0)} = \omega - H$, which corresponds to a shift and a sign change of the diagonal elements $a_n =$

$\omega - \alpha_n$ with α_n denoting the diagonal elements of H. Eventually, the successive iteration of (3.19) leads to the corresponding continued fraction representation

$$\langle \nu_L | \frac{1}{T_{(n)}} | \nu_R \rangle = \cfrac{\langle \nu_L | \nu_R \rangle}{\omega - \alpha_0 - \cfrac{\beta_1 \gamma_1}{\omega - \alpha_1 - \cfrac{\beta_2 \gamma_2}{\cdots}}} \quad . \tag{3.29}$$

The coefficients α_i, β_i and γ_i can be obtained by a non-symmetrical Lanczos tri-diagonalization [124] for H with starting vectors $\langle \nu_L |$ and $| \nu_R \rangle$. The implemented Lanczos method is described in the next part.

3.3.1 Non-symmetric Lanczos tridiagonalization

The idea of the non-symmetric Lanczos tridiagonalization method is to determine a bi-orthonormal basis $Q_N = (q_1, q_2, \cdots q_N)$ and $\bar{Q}_N = (\bar{q}_1, \bar{q}_2, \cdots \bar{q}_N)$ such that the non-hermitian matrix $H \neq H^\dagger$ assumes a tridiagonal form

$$\bar{Q}_N^T H Q_N = H_{\text{tri}} = \begin{bmatrix} \alpha_0 & \gamma_1 & 0 & \cdots & 0 \\ \beta_1 & \alpha_1 & \gamma_2 & \ddots & \vdots \\ 0 & \beta_2 & \alpha_2 & \ddots & 0 \\ \vdots & \ddots & \ddots & \ddots & \gamma_N \\ 0 & \cdots & 0 & \beta_N & \alpha_N \end{bmatrix} \tag{3.30}$$

The concrete tridiagonalization algorithm for the matrix H with starting vectors $|\bar{\nu}_0\rangle$ and $|\nu_0\rangle$ is defined by

$$|q_0\rangle = 0 \quad |\bar{q}_0\rangle = 0 \tag{3.31a}$$

for $i = 1 \ldots N$

$$\gamma_{i-1} = \sqrt{|\langle \bar{\nu}_{i-1} | \nu_{i-1} \rangle|} \tag{3.31b}$$

$$\beta_{i-1} = \frac{\langle \bar{\nu}_{i-1} | \nu_{i-1} \rangle}{\gamma_{i-1}} \tag{3.31c}$$

$$|q_i\rangle = \frac{1}{\gamma_{i-1}} |\nu_{i-1}\rangle \tag{3.31d}$$

$$|\bar{q}_i\rangle = \frac{1}{\beta^*_{i-1}} |\nu_{i-1}\rangle \tag{3.31e}$$

$$|\nu_i\rangle = H |q_i\rangle \quad |\bar{\nu}_i\rangle = H^\dagger |\bar{q}_i\rangle \tag{3.31f}$$

$$\alpha_i = \langle \bar{q}_i | \nu_i \rangle \ \vee \ \alpha_i = \langle \bar{\nu}_i | q_i \rangle \tag{3.31g}$$

$$|\nu_i\rangle = |\nu_i\rangle - \alpha_i |q_i\rangle - \beta_{i-1} |q_{i-1}\rangle \tag{3.31h}$$

$$|\bar{\nu}_i\rangle = |\bar{\nu}_i\rangle - \alpha_i |\bar{q}_i\rangle - \beta^*_{i-1} |\bar{q}_{i-1}\rangle \quad . \tag{3.31i}$$

This procedure determines the coefficients of the tridiagonal matrix in 3.30 where N refers to the number of Lanczos steps.
In concrete applications one typically encounters a violation of bi-orthonormality with increasing number of Lanczos steps due to numerical errors. In order to increase the numerical stability, we apply a re-orthonormalization for each new pair $|q_i\rangle$ and $|\bar{q}_i\rangle$ in (3.31d) and (3.31e)

$$|q_i\rangle = |q_i\rangle - \sum_{j<i} |q_j\rangle \langle \bar{q}_j | q_i\rangle \tag{3.32a}$$

$$|\bar{q}_i\rangle = |q_i\rangle - \sum_{j<i} |\bar{q}_j\rangle \langle q_j | \bar{q}_i\rangle \tag{3.32b}$$

and conduct a subsequent normalization

$$n_i = \sqrt{\langle \bar{q}_i | q_i\rangle} \tag{3.33a}$$

$$|q_i\rangle = \frac{1}{n_i} |q_i\rangle \tag{3.33b}$$

$$|q_i\rangle = \frac{1}{n_i} |q_i\rangle \quad . \tag{3.33c}$$

3.3.2 Evaluation of spectral densities

For a finite number of Lanczos steps N the corresponding spectral density is a finite sum of weighted δ-peaks located at the eigenvalues ω_i of H

$$I(\omega) = -\frac{1}{\pi} \mathrm{Im} R(\omega) \tag{3.34a}$$

$$= \sum_{i=0}^{N} W_i \delta(\omega - \omega_i) \quad . \tag{3.34b}$$

which becomes a continuous function in the limit $N \to \infty$. The weights W_i are given by the overlap between the starting vectors and the corresponding left and right eigenvector of H, i.e., $W_i = \langle L_i | v_R\rangle \langle v_L | R_i\rangle$ with $\langle L_i | H = \langle L_i | \omega_i$ and $H |R_i\rangle = \omega_i |R_i\rangle$.
In order to obtain a continuous function for a finite system, we have to approximate the coefficients α_i, β_i and γ_i for $i > N$ based on additional information about their asymptotic behavior for $i \to \infty$. For systems with a bounded spectrum the asymptotic behavior of the coefficients is related to the upper bound E_u and lower bound E_l of the spectrum

$$E_u = a_\infty + 2\sqrt{(\beta_\infty \gamma_\infty)} \tag{3.35a}$$

$$E_l = a_\infty - 2\sqrt{(\beta_\infty \gamma_\infty)} \tag{3.35b}$$

[125]. Hence, it is possible to approximate the coefficients α_i and $\gamma_i \cdot \beta_i$ by α_∞ and $\gamma_\infty \cdot \beta_\infty$ for sufficiently large $i > n_{\max}$. However, for systems with a finite Hilbert space the behavior of coefficients will deviate from this asymptotic rule at larger i depending on the actual size of the Hilbert space.

In this case we have to enlarge the Hilbert space by appropriate interpolation schemes increasing the number of grid points in the BZ. This, in turn, increases the maximum number $n_{\max}$ of Lanczos steps before the coefficients start to deviate from the asymptotic behavior. Eventually, the sequence is approximated for $n > n_{\max}$ by constant coefficients α_∞ and $\gamma_\infty \cdot \beta_\infty$. In typical approaches, this infinite sequence in the continued fraction representation is replaced by a square root terminator [123]. Alternatively, it is possible to introduce an artificial broadening by replacing the δ-peaks in (3.34b) with Lorentzian or Gaussian distribution functions of the same weight W_i.
In the following section, we discuss the interpolation methods used to enlarge the system size of the effective model.

3.4 Multivariate interpolation schemes

The arguments of coefficient functions in the effective Hamiltonian and observables are defined on a discrete and regular grid in momentum space. In order to obtain information about values on intermediate points appropriate interpolation schemes are required. This is particularly important for the evaluation of spectral densities for which we have to increase the system size to reduce finite size effects.
The computational costs for the interpolation of a function F grows considerably with the dimension of its domain. The domain of a coefficient functions depends on the number of independent momentum arguments and the dimensionality D of the system. If n is the number of momentum arguments in the coefficient function C_α the dimension of its domain is given by $\mathcal{D}_\alpha = D \cdot n$.
In the scope of this thesis we consider a two-dimensional system. Consequently, the one-particle dispersion, which depends on a single momentum, is described by a two dimensional coefficient function, whereas the coefficient of a two-particle interaction term depends on three momentum arguments and, thus, has a six-dimensional domain. Therefore, it is expedient to use diverse interpolation schemes which are appropriate for different types of coefficient functions.
In the interpolation schemes we can directly exploit the periodicity of the functions in momentum space. Moreover, it is possible to enhance the efficiency of the interpolation by using the information about the initial coefficient functions before the transformation which in most cases are known analytically.
In the following we present various interpolation schemes which are suited for different types of coefficients.

3.4.1 Nearest neighbor interpolation

The nearest neighbor interpolation is the most simple interpolation scheme. It is based on the idea to approximate the function at some intermediate point by its value at a nearest grid point. The resulting interpolant is a piecewise constant as illustrated in Figure 3.5. Due to its simplicity its computational cost is virtually independent of the domain. Hence, it can be applied to functions with a high-dimensional domain. A major drawback is, that the interpolation errors can become very large. Thus, it should only be used if the subsequent treatment is less sensitive to deviations of the interpolated input.

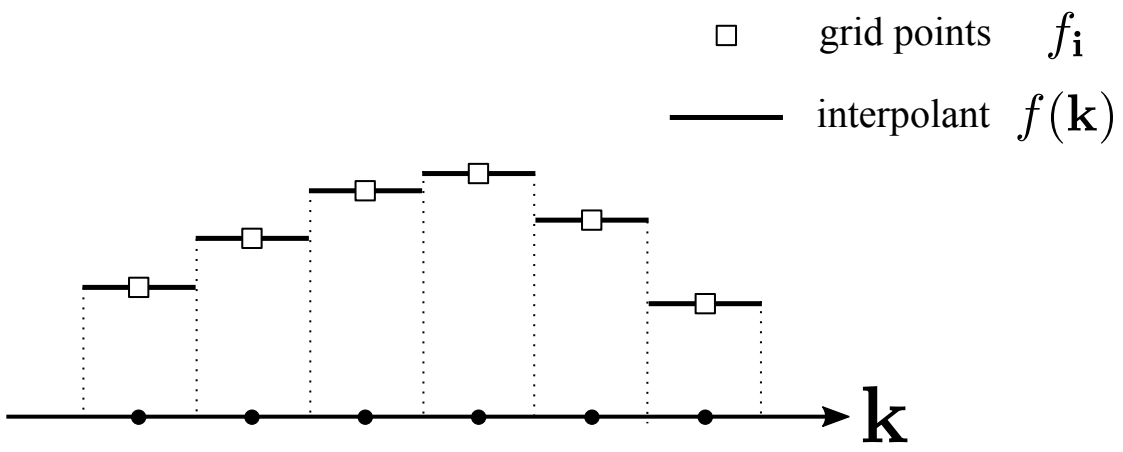

Figure 3.5: Illustration of the nearest neighbour interpolation scheme.

3.4.2 Multi-linear interpolation

The multi-linear interpolation scheme constitutes a compromise between simplicity and accuracy. Typically, this scheme is applied in the form of a bilinear ($\mathcal{D}=2$) or trilinear interpolation ($\mathcal{D}=3$), but a generalization to higher dimensions is straightforward to implement. The multi-linear interpolation takes into account information about all neighbouring grid points contributing with a certain weight. It approximates the function at some intermediate point $\vec{y}$ which lies inside the hyper cube with the associated corners located at the $2^{\mathcal{D}}$ neighbouring grid points $\vec{x}^{(i_1\ldots i_{\mathcal{D}})}=(x_1^{(i_1)},\ldots x_1^{(i_{\mathcal{D}})})$ with $i_n=0,1$ and $x_n^{(0)}\leq y_n<x_n^{(1)}$. The known values of the function at the corners are given by $f(\vec{x}^{(i_1\ldots i_{\mathcal{D}})})=f_{i_1,\ldots,i_{\mathcal{D}}}$. The interpolant $f(y_1,\ldots,y_{\mathcal{D}})$ inside the hyper cube can be written in a compact form if we consider normalized spacings $x_n^{(0)}-x_n^{(1)}=1$

$$f(y_1,\ldots,y_{\mathcal{D}})=\sum_{i_1\ldots i_{\mathcal{D}}} f_{i_1,\ldots,i_{\mathcal{D}}}\prod_{n=1}^{\mathcal{D}}\left|y_n-x_n^{(0)}-k(i_n)\right| \tag{3.36}$$

where the sum runs over all $i_n=0,1$ and the function $k(i_n)$ is defined by $k(1)=0$ and $k(0)=1$. The geometric interpretation of the multi-linear scheme is shown in Figure 3.6.

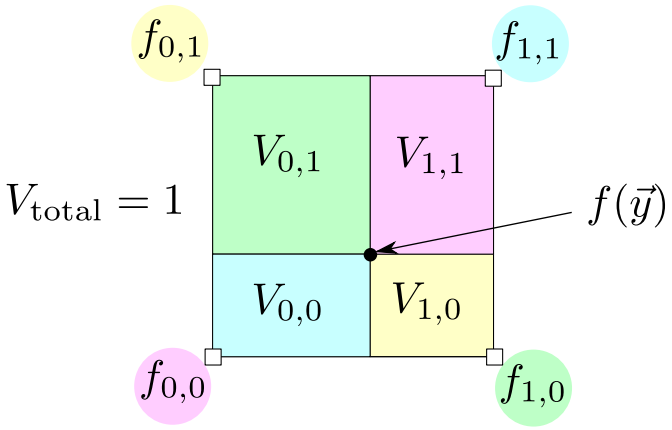

$$f(\vec{y}) = V_{0,0} \cdot f_{1,1} + V_{0,1} \cdot f_{1,0} + V_{1,0} \cdot f_{0,1} + V_{1,1} \cdot f_{0,0}$$

Figure 3.6: Geometric interpretation of the multi-linear interpolation scheme in two dimensions. The interpolant at some intermediate point $\vec{y}$ is given by a weighted sum of the known values f_{i_1,i_2} at the neighbouring grid points. The weights are given by the area of the corresponding opposite partition $V_{\bar{i}_1,\bar{i}_2}$

3.4.3 Lanczos interpolation

The Lanczos interpolation scheme or Lanczos resampling is a more sophisticated interpolation method which is typically used for resampling problems in digital signal processing and digital imaging [126, 127]. It was first introduced by Cornelius Lanczos in 1938 [128].
The method is based on a reconstruction kernel $L(x)$ also referred to as the Lanczos kernel

$$L^a(x) = \begin{cases} 1 \text{ for } x = 0 \\ \frac{a}{\pi^2 x^2} \sin(\pi x) \sin(\frac{\pi x}{a}) \text{ for } -a \leq x < a \; x \neq 0 \\ 0 \text{ otherwise} \end{cases} \tag{3.37}$$

where a is a positive integer parameter which sets the size of the Kernel. The Lanczos Kernel for $a = 3$ is shown in Fig. 3.7. Considering a discrete one-dimensional input function with samples f_i, the interpolant at an arbitrary real value x is given by a discrete convolution of the input function and the Lanczos Kernel

$$S_a(x) = \sum_{i=\lfloor x \rfloor - a + 1}^{\lfloor x \rfloor + a} f_i L^a(x - i) \quad , \tag{3.38}$$

where we presume normalized spacings. In higher dimensional spaces we interpolate the input function in one direction, first. Then we use the additional points for an interpolation in orthogonal directions as shown in Fig. 3.8.

An important advantage of this method is its efficiency as it provides a smooth interpolant by comparatively simple means. The derivative of the resulting interpolant is a continuous function. Moreover, the interpolation can be controlled by the parameter a. For larger values of a information about more distant grid points is taken into account and the resulting interpolant becomes smoother.

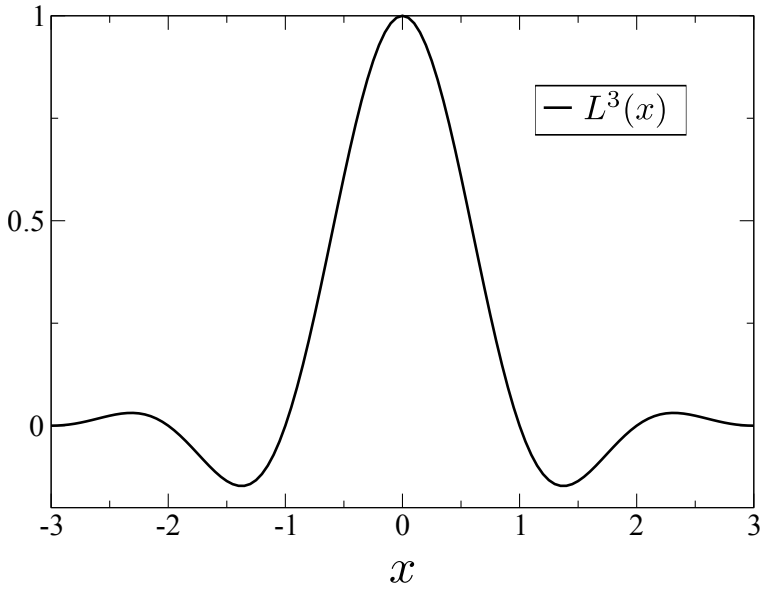

Figure 3.7: The Lanczos kernel (3.37) for $a = 3$.

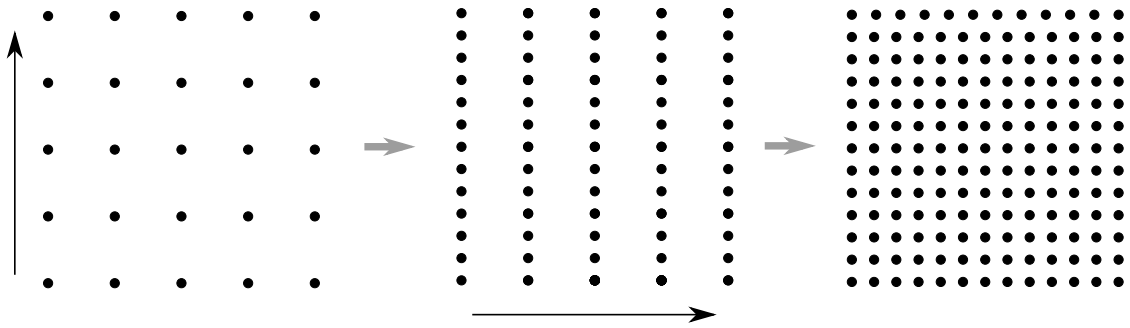

Figure 3.8: The multivariate interpolation procedure is exemplified in two dimensions.

3.4.4 Interpolation of effective models

Typically, the initial coefficient functions in the Hamiltonian before the transformation are known analytically. By contrast, the transformation is only tracked on discrete points in momentum space. The resulting effective coefficients can be viewed as samples of a renormalized initial coefficient function. In many cases, it is reasonable to assume a similar analytical behavior of the initial and the effective functions. Thus, it is possible to enhance the efficiency of the interpolation by using the information about the initial coefficients. This is particularly

important in cases where the coefficient functions exhibit poles which complicate the interpolation drastically.
In order to overcome this problem, we use a heuristic approach interpolating the function $\frac{\bar{s}(\mathbf{k})+c}{s(\mathbf{k})+c}$ where $\bar{s}(\mathbf{k})$ is the function transformed by the CST and $s(\mathbf{k})$ denotes the corresponding function before the transformation. The constant shift c is introduced to avoid zeroes in the denominator. If we assume that the renormalization of the CST does not shift or alter the pole in $\bar{s}(\mathbf{k})$ the resulting function $f(\mathbf{k})$ is finite and smooth.
Furthermore, this indirect interpolation scheme can improve the accuracy of the interpolant compared to a direct interpolation scheme, even if the coefficients do not exhibit poles. However, both functions $\bar{s}(\mathbf{k})$ and $s(\mathbf{k})$ are supposed to exhibit a similar analytic behavior, otherwise, the accuracy of the interpolation might be spoiled. Figure 3.9 illustrates the enhancement of the interpolation using the indirect interpolation scheme in the context of a nearest neighbor interpolation for two exemplary functions.

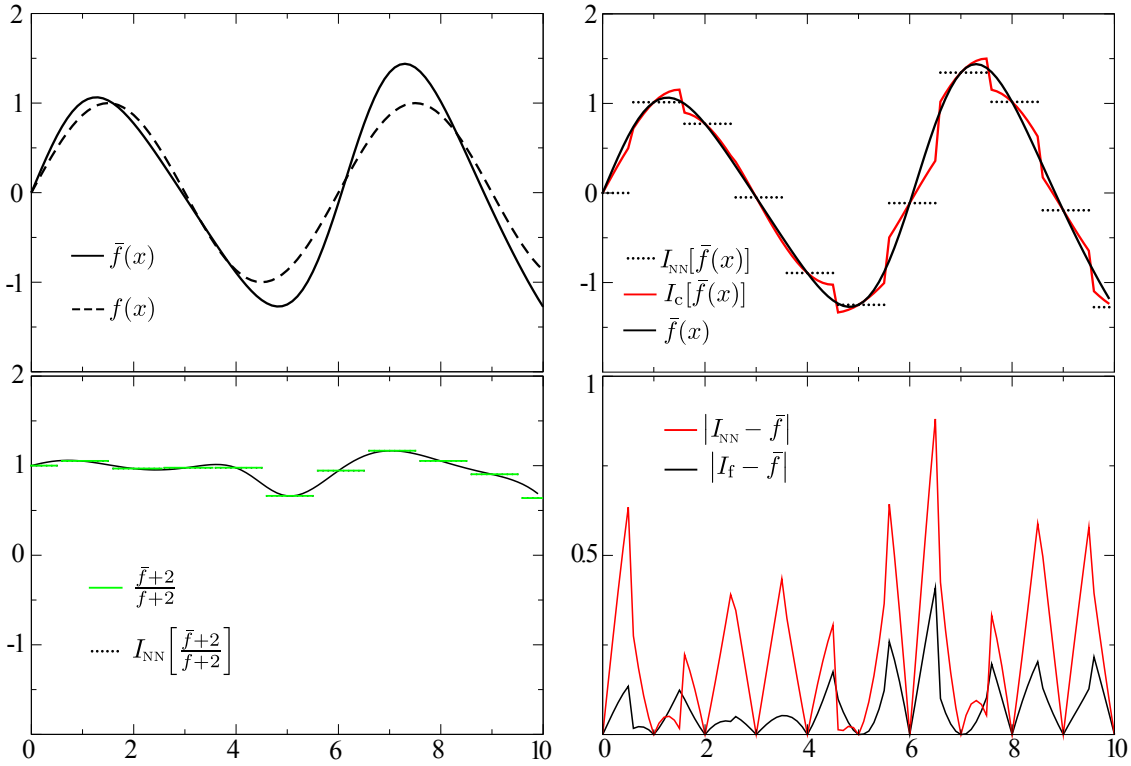

Figure 3.9: Comparison between a direct and indirect nearest neighbor interpolation scheme for an exemplary function $f(x)=\sin\left(\frac{2\pi}{6}x\right)$ and a representative transformed function $\bar{f}(x)=\sin\left(\frac{2\pi}{6}x+0.3\sin(x)\right)e^{0.05x}$. We chose an artificial transformation $f\rightarrow\bar{f}$ as it can not be viewed as a trivial rescaling and shift, however, both functions have a similar analytic behavior. We assume, that $\bar{f}$ is only known on discrete points. In the indirect scheme the function $(\bar{f}+2)/(f+2)$ is interpolated by a nearest neighbour scheme yielding the interpolant $I_c[\bar{f}(x)]$. This function is compared to a nearest neighbour interpolant $I_{\mathrm{NN}}[\bar{f}(x)]$ obtained in a direct scheme.

CHAPTER 4

Two dimensional Heisenberg Antiferromagnet

The following chapter constitutes the major part of this thesis. It discusses the dynamics and interactions of the elementary excitations in the Heisenberg antiferromagnet on the square lattice, one of the simplest and paradigmatic strong-coupling models in condensed matter physics. Over the last decades this model was extensively studied by a multitude of different techniques which, despite the lack of an exact solution, have lead to a profound understanding of the corresponding low energy properties. In particular, the fundamental concept of spin waves provides a very intuitive and well substantiated description of the elementary excitations at long wavelengths.
Nevertheless, the Heisenberg antiferromagnet is still subject of intense research and ongoing debates, in particular, due to its decisive relevance for the understanding of undoped parent compounds of cuprate high-temperature superconductors. The focus is on high energy magnons at short wave lengths as they are believed to be of importance for the comprehension of the magnetic 'glue' in high T_c-superconductors. Recent experimental findings and numerical simulations revealed an apparent failure of the conventional spin wave description. Significant effort was made to dissolve this discrepancy, either by extending the spin wave theory or resorting to alternative descriptions, but the nature of the elementary excitations at short wavelengths is still unclear.
The aim of the following chapter is the derivation of an comprehensive spin wave description which is quantitatively valid for all wave lengths. To this end we derive an effective magnon description based on spin wave theory using the techniques presented in the previous chapters. First, a brief overview about the relevant literature on the Heisenberg antiferromagnet is given, discussing the theoretical model and its principle realization in real materials. Moreover, important results of numerical and analytical techniques are summarized, in particular, with regard to recent experimental findings.
The second part deals with the spin wave formalism and its physical interpretation. We describe the Dyson-Maleev representation for the Hamiltonian and the relevant observables which constitute the initial point of the CST analysis. The epCUT approach is used to reproduce the results of the conventional spin wave expansions up to third order in $1/S$, which are then compared to known results from literature.
In addition, the spin wave expansions are extended by means of the deepCST method. The corresponding results further suggest that the standard expansion in $1/S$ is problematic at

short length-scales.
In the third section the main results of this thesis are presented and discussed. We derive an effective magnon description using a selfsimilar CST approach based on a truncation of magnon operators by their scaling dimension. Based on the effective model we provide a careful analysis of the dynamics and interactions of the renormalized spin waves and point out the relevance of strong magnon attraction. The interpretation is visualized by means of the diagrammatic representation introduced in the previous chapter. The results are compared with current numerical and experimental data.

4.1 Introduction

The Heisenberg model is one of the oldest and paradigmatic models of quantum magnetism. Its origin can be traced back to discussions by Heisenberg and Dirac on the emergence of ferromagnetism pointing out that the quantum mechanical exchange of indistinguishable electrons can lead to an effective spin interaction [129, 130]. In fact, there are a lot of different mechanisms besides the direct exchange which give rise to an effective Heisenberg Hamiltonian. For instance, the antiferromagnetic Heisenberg Hamiltonian is obtained in second order perturbation theory in the large U limit of the Hubbard model [15]. Another important example is the theory of super exchange, which was mainly developed by Anderson [131, 132].
From a general point of view, the Heisenberg model can be seen as an effective model, describing the mutual interaction between localized spin degrees of freedom in many body systems. In the isotropic case the Hamiltonian is given by

$$H = \sum_{\langle i,j \rangle} J_{ij}\, \vec{S}_i \cdot \vec{S}_j \tag{4.1}$$

where J_{ij} denotes the exchange coupling between the spins i and j which favor either a parallel alignment for $J_{ij} < 0$ or anti parallel alignment for $J_{ij} > 0$. The spin variable $\vec{S}_i$ is a three dimensional vector with spin components $S_{\alpha,i}$ and $\alpha = x, y, z$ which obey the spin commutation relations

$$\left[S_{\alpha,i}, S_{\beta,j} \right] = \mathrm{i}\delta_{i,j}\hbar\epsilon_{\alpha\beta\gamma}S_{\gamma,i} \tag{4.2}$$

Despite its simplicity the Heisenberg model has wide spread applications and explains a myriad of different phenomena such as ferromagnetism, ferrimagnetism or antiferromagnetism [16, 99]. In combination with geometric frustration, this model also gives rise to exotic states such as spin glasses [133] or various kinds of fractional spin liquids [134–137].
In the scope of this thesis we consider the isotropic spin-1/2 Heisenberg antiferromagnet on the square lattice (spin-1/2 HAFSQ). A very concise review on analytical, numerical and experimental studies of the spin-1/2 HAFSQ and a further discussion about relevant materials is given in Ref. [17, 20].
The spin-1/2 HAFSQ is regarded as a rather conventional model, as it was extensively studied in the last 70 years. Nevertheless, there are still interesting and open questions.
The discovery of high-T_c superconductivity by Bednorz and Müller in 1987 [138] has revived the interest in this model because it is realized in a large class of copper oxides which are known as the undoped parent compounds of cuprate high-T_c superconductors [17, 139–142]. Although cuprate superconductors have been subject of intense research the mechanism of

high-T_c superconductivity and the relevance of magnetic fluctuations are not fully understood yet [143–148]. A comprehensive review on this topic is given in Ref. [149].
The quantitative description of hole dynamics and interactions in an antiferromagnetic background is a very intricate problem which is described theoretically by means of the $t-J$ model [150, 151]. Recent studies show that short range processes play a decisive role in the understanding of the hole pairing mechanism [152–155]. But even the description of the plain magnetic problem which is the undoped quantum antiferromagnet turns out to be complicated at short length scales. As we will discuss in the scope of this section magnons, i.e, spin waves, provide a quantitative and consistent description of the low energy excitations in the spin-1/2 HAFSQ but their nature at high energies, i.e short wavelengths, is still not clarified to this day. Due to their relevance for undpoped cuprates, there is a great interest in a full theoretical comprehension of the excitations in the spin-1/2 HAFSQ.
Before we further elaborate on the issue of short wavelength spin waves we give a brief summary of the theoretical and experimental findings about the spin-1/2 HAFSQ.
Although there is no exact solution in two dimensions, the low energy physics of the spin-1/2 HAFSQ is well understood. There is strong evidence that the ground state exhibits long range Néel order for zero temperature [17]. This ordering is associated with a finite staggered magnetization which breaks the continuous SU(2) symmetry of the Hamiltonian [156]. As a result, the ground state gives rise to gapless bosonic excitations according to Goldstone's theorem [24]. The corresponding bosons can be identified as quantized spin waves, i.e., magnons which exhibit a linear dispersion at long wavelengths [21, 22].
Interestingly, quantum fluctuations play a major role as they lead to a considerable reduction of the staggered magnetization to 62% of its classical value and a renormalized spin wave velocity [17, 21].
The emergence of gapless excitations is also consistent with exact statements such as the Lieb-Schultz-Mattis. This important theorem implies that the ground state of the Heisenberg antiferromagnet on a bipartite lattice (with isomorphic sublattices) is non-degenerate and the excitation gap is arbitrary small [157, 158].[1].
Spin wave theory is well established and supported by numerical simulations and analytical approaches which are also in agreement with experimental results [17, 140, 160, 161]. Exact diagonalization studies on finite systems show a non-zero staggered magnetization and a diverging correlations length [162]. The results are consistent with a whole series of quantum Monte Carlo simulations [163–168] and series expansions from the Ising limit [169]. Moreover, this picture is confirmed by renormalization group approaches for the non-linear σ-model in (2+1) dimensions which is an effective field theory describing the low energy regime of the HAF [170].
It is also worth to mention that long range order can even occur in the presence of geometric frustration such as in the triangular Heisenberg antiferromagnet [171]. This is surprising since the long range order has to compete with the geometric frustration in addition to strong quantum fluctuations.
The idea of spin waves also plays an important role for studies at finite temperatures T even though the long range order is destroyed by thermal fluctuations for any arbitrary small T, according to the Mermin Wagner theorem [172]. This is due to the fact that the correlation length is exponentially large for small T and spin waves with wavelengths shorter than the correlation length are still defined [17]. In the case of finite temperature, a modified spin

[1]The original theorem does only holds for one dimensional spin systems but there is also a generalization to higher dimensions by Hastings [159]

wave theory has to be applied describing a softening and damping of magnons due to thermal fluctuations [173].
To sum up, spin wave theory provides a fundamental concept for the understanding of long range ordered magnets. Even in the quantum case for $S = 1/2$ the low energy excitations are well described within spin wave theory, despite the fact that it is based on a semi classical approach. However, seminal developments in the last two decades point out the relevance of short range quantum correlations giving rise to discrepancies of spin wave theory at short wavelengths.
In 1995 Singh and Gelfand used high order series expansion about the Ising limit to calculate the spin wave spectrum [174]. Their results show a considerable deviation from linear spin wave theory at higher energies encouraging experimentalists to search beyond long wavelength spin waves. Unfortunately, the experimental verification of high-energy spin waves is demanding due to reduced signal rates in inelastic neutron scattering experiments and, thus, first measurements of the spin wave dispersion in materials such as La_2CuO_4 were limited to long wavelength excitations [175]. In 1991 Hayden et al. have been the first to show experimental evidence for high energy magnons at the zone boundary [176]. However, their experimental resolution was not high enough to point out any insufficiency of linear spin wave theory.
Nevertheless, seminal technical developments in the last two decades have led to an increased resolution and momentum coverage and the focus was directed more to high-energy magnons [139, 140, 161, 176–178].
In particular, recent measurements of the cuprate $Cu(DCOO)_2{\cdot}4D_2O$, also referred to as copper deuteroformate tetradeuterate (CFTD), provided new insights into the physics of high energy magnons [27–29, 179, 180]. Similar to La_2CuO_4, CFTD is considered as a very good realization of the square lattice Heisenberg antiferromagnet [139, 140]. Interestingly, the results obtained from inelastic neutron scattering of CFTD by Ronnow et al. confirmed the results of high order series expansions exposing considerable discrepancies between the experiment and linear spin wave theory at short wavelengths [179]. They observed an anomalous dispersion between the wavevectors $\mathbf{k} = (\pi, 0)$ and $\mathbf{k} = (\pi/2, \pi/2)$ leading to an energy dip of $7 \pm 1\%$ at $\mathbf{k} = (\pi, 0)$ as shown in Figure 4.1. Subsequent experiments of higher resolution confirm the anomalous dispersion in CFTD [27–29] which is also in agreement with quantum monte carlo simulations [25] and extended high order series expansions about the Ising limit [26] (see also Figure 4.2 indicating a seizable energy dip of $7-9\%$. Moreover, the anomalous dispersion is accompanied by an increased weight in the higher magnon continuum at $\mathbf{k} = (\pi, 0)$ [28, 29]. The results clearly show that the energy dip is an inherent feature of the spin-1/2 HAFSQ which is caused by short range quantum entanglement [29].
Since conventional spin wave theory can be seen as an expansion about a semi-classical limit in orders of $\frac{1}{S}$, it seems reasonable that the incorporation of higher order terms may capture the relevant processes. But even corrections of the spin wave dispersion up to third order in $1/S$ do not explain this phenomenon quantitatively [31]. Although the expansion in $1/S$ does account for an additional dispersion at the zone boundary the results show a very slow convergence at $\mathbf{k} = (\pi, 0)$ yielding an energy dip of only 3.1%. The corresponding data are shown in Figure 4.2. This seeming failure of spin wave theory has sparked a debate about the nature of the magnetic excitations in the spin-1/2 HAFSQ and provided further motivation to search beyond the conventional spin wave approach. In particular, there were attempts to draw a connection to the resonating valence bond state (RVB) [181] which was proposed by Anderson in 1987 as a possible ground state of the cuprate La_2CuO_4 [134]. This new state

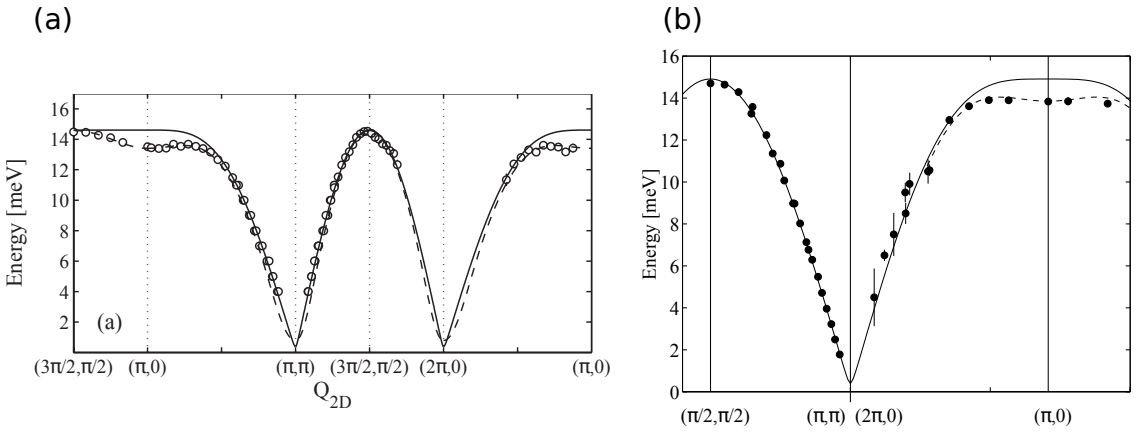

Figure 4.1: Spin wave dispersion in CFTD taken from Ref. [179][2]in (a) and Ref. [27][3]in (b). The dots represent the results obtained by inelastic neutron scattering experiments. The solid lines correspond to predictions by linear spin wave theory with an additional small gap to account for a small anisotropy [177, 179]. The dashed line displays the data of series expansion about the Ising limit from Ref. [174].

is characterized by a spin liquid phase with no magnetic order but long range entanglement giving rise to fractional excitations, also referred to as spinons. It is known that spinons are the elementary excitations of the 1D spin-1/2 HAF where true long range order is suppressed by the combination of low dimensionality and quantum fluctuations[91, 182] but in two dimensions the situation is much more subtle. A lot of work has been devoted to the question whether spinons could also occur in two dimensional spin systems [28, 137, 183–187].
Even for the spin-1/2 HAFSQ the emergence of a RVB state was debated [188, 189]. The seeming discrepancies of spin wave theory incited physicists to speculate about a fractionalization of magnons into spinons [29, 190]. Recent data obtained by polarized neutron spectroscopy for CFTD eventually led to the idea that a spinon description accounts for the anomaly at the zone boundary. Due to a sophisticated experimental setting the authors were able to distinguish between the response of transverse and longitudinal excitations. Their data show a considerable reduction of the magnon weight at $\mathbf{k} = (\pi, 0)$ compared to $\mathbf{k} = (\pi/2, \pi/2)$. Moreover, it is observed that this weight is shifted to an energetically higher continuum in the transverse channel which is consistent with previous experiments with non polarized neutrons [29, 190]. Based on an effective spinon description the authors argue in favor of a fractionalization of magnons in the vicinity of $\mathbf{k} = (\pi, 0)$ implying that spin waves emerge as confined spinons at the remaining part of the Brillouin zone [28]. Although their approach does account for the energy dip at $\mathbf{k} = (\pi, 0)$, a close analysis of their results in comparison to the experimental data and to various theoretically established results shows a lack of consistency. Most importantly, their approach leads to a considerable residual gap due to the absence of long range order. In addition, the theoretical explanation for the increased weight of the continuum in the transverse channel is only based on heuristic arguments. There is no distinct evidence that the less pronounced peak at $\mathbf{k} = (\pi, 0)$ (see Figure 2b in Ref. [28]) corresponds to a continuum of spinons.
Taking all these factors into account, the emergence of spinons in the the spin-1/2 HAFSQ is

[2] © 2001 The American Physical Society
[3] © 2004 Published by Elsevier B.V.

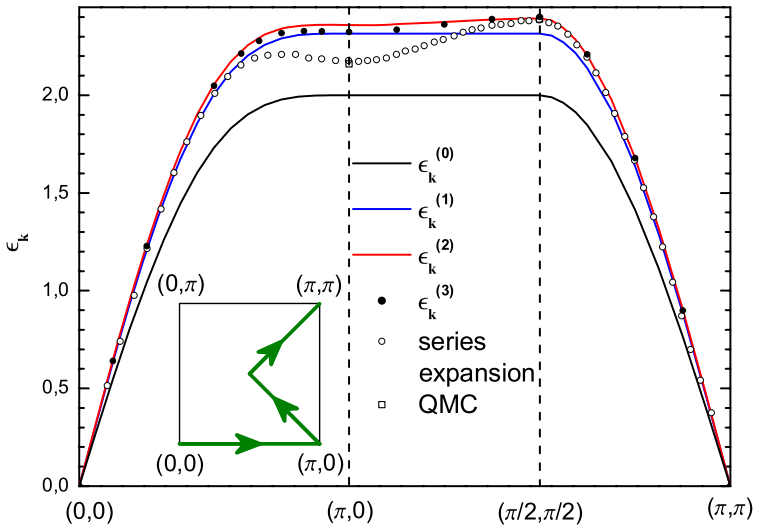

Figure 4.2: The results of higher order spin wave theory are compared to quantum monte carlo simulations and series expansions about the Ising limit for the magnon dispersion along symmetry paths of the Brilluoin zone. The data in $\epsilon_{\mathbf{k}}^{(n)}$ indicate n-th order spin wave results calculated in Ref. [31]. The QMC results are taken from Ref. [25] and the series results are from Ref. [26]. The figure is taken from Ref. [31][1]

disputable and the nature of high energy spin waves remains unclear. However, the data definitely indicate the relevance and intricacy of quantum correlations in this part of the Brillouin zone. Recent calculations based on a singlon approach also show a strong attractive interaction between pairs of magnons at short length scales [191].

Since the renormalization effects at the zone boundary are relatively small compared to the spin wave energy of $2J$ we assume that the deviations are rather a result of a methodical insufficiency and not the indicator of fundamentally new physics. This view is also supported by calculations of Uhrig and Majumdar who achieved improvements by means of a varied perturbation theory [30].

The lack of a comprehensive picture of the elementary excitations in the spin-1/2 HAFSQ is one of the main motivations for this thesis. The aim is a quantitative description which resolves the discrepancies between spin wave theory and the theoretical and experimental results. The working hypothesis is that the anomalous dispersion in the magnon spectrum is caused by strong attraction between pairs of spin waves. In order to obtain a quantitative description within spin wave theory it is therefore crucial to take into account the relevant interactions by means of appropriate methodical tools.

For this purpose, we use the CUT method in momentum space as introduced in the previous chapters to derive an effective magnon description based on spin wave theory. Moreover, we derive the corresponding effective observables and calculate the dynamic structure factors for a direct comparison with experimental INS data.

[4]

4.2 Spin wave theory

Linear spin wave theory is a standard tool which is taught in most condensed matter courses. The basic formalism can be found in various standard textbooks [16, 99] or in the original papers [21, 22, 98, 192]. Nevertheless, we want to give a brief introduction to the spin wave formalism and its physical interpretation before we present our main results because it represents the theoretical foundation of our approach.
In the second part of this section we reproduce the perturbative results of high order spin wave expansions for the dispersion and the ground state energy [31, 193, 194] by means of the epCUT approach. This allows us to verify that the CUT method and the computer programs work correctly. Moreover, the perturbative results are extrapolated by means of the deepCUT method. We identify generic problems of the conventional spin wave expansion and point out the relevance of short range spin wave interactions.

4.2.1 Spin waves

The Hamiltonian of the isotropic Heisenberg model is given by

$$H = J \sum_{\langle i,j \rangle} S_i^x S_j^x + S_i^y S_j^y + S_i^z S_j^z \quad , \tag{4.3}$$

where $J > 0$ denotes the antiferromagnetic nearest neighbour exchange coupling and S_i^α denotes the α component of the spin operator acting on site i. It is expedient to work with local spin eigen states $|S, m\rangle$ with respect to the spin axis in z direction, where S denotes the total spin and m is the quantum number of the S_z component which can take the values $m = -S, S-+1 \ldots S$. Using the spin ladder operators $S_j^\pm = S_j^x \pm \mathrm{i} S_j^y$ the Hamiltonian can be written in the following form

$$H = J \sum_{\langle i,j \rangle} S_i^z S_j^z + \frac{1}{2} \left(S_i^+ S_j^- + S_i^- S_j^+ \right) \quad . \tag{4.4}$$

The classical Néel state $|AF\rangle$ (see Figure 4.3) is chosen as a reference state of the antiferromagnetic system as it minimizes the Ising term in z direction. The order parameter is defined by the staggered magnetization which corresponds to an anti-parallel alignment between spins on sublattice A and B $\hat{M}_{\text{stagg}} = \sum_{i \in A} S_i^z - \sum_{j \in B} S_j^z$. For practical reasons it is useful to perform a sublattice rotation such that spin deviations are measured with respect to an alternating direction depending on the considered sublattice as illustrated in Figure 4.3. The resulting Hamiltonoperator is then given by

$$H = -J \sum_{\langle i,j \rangle} S_i^z S_j^z + \frac{1}{2} \left(S_i^+ S_j^+ + S_i^- S_j^- \right) \quad . \tag{4.5}$$

In these coordinates the reference state is represented by a classical ferromagnetic state with all spins pointing in $-z$ direction such that $M_{\text{stagg}} \to \hat{M}_{\text{F}} = \sum_{i \in A} S_i^z + \sum_{j \in B} S_j^z$. From a physical point of view, however, the spins point in alternating directions giving rise to a classical staggered magnetization per site of $M_{\text{classical}} = \langle \text{AF} | \hat{M}_{\text{stagg}} | \text{AF} \rangle = S$.

In contrast to the ferromagnetic case ($J < 0$), the classically ordered Néel state is not the

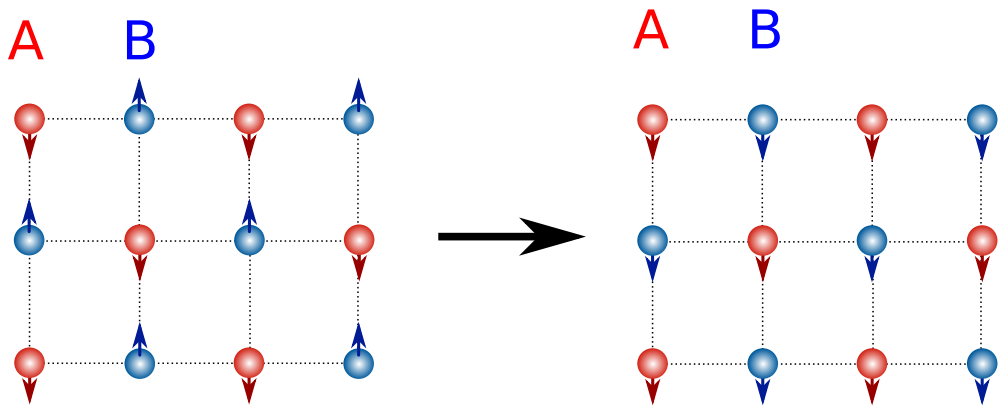

Figure 4.3: The sublattice rotation of the Néel ordered reference state in the left panel to the ferromagnetically ordered reference state on the right panel is illustrated. In the Néel ordered state (left pabel) the spins on sublattice A and B exhibit an anti-parallel alignment.

exact ground state of the the antiferromagnetic Heisenberg system due to spin fluctuations induced by the spin ladder terms. Consequently, the true ground state will exhibit a reduced staggered magnetization $M_{\text{QM}} < M_{\text{classical}}$ because quantum fluctuations are competing energetically with the classical order.

The main idea of spin wave theory is to represent the spin deviations from the classical Néel order by bosonic excitations. In the main literature two different approaches are used, the Holstein-Primakoff formalism [22, 98] and the Dyson-Maleev representation [195, 196]. In standard spin wave expansions both approaches lead to the same results but they involve different advantages and drawbacks which we will examine later.

For pedagogical reasons we discuss the Holstein-Primakoff representation first. It is defined by the following relations

$$S_i^z = -S + a_i^\dagger a_i \qquad S_i^+ = a_i^\dagger \sqrt{2S - a_i^\dagger a_i} \qquad S_i^- = \sqrt{2S - a_i^\dagger a_i}\, a_i \tag{4.6}$$

where $a_i^\dagger$ and a_i denote Boson creation and annihilation operators on site i. Based on the bosonic commutation relation $\left[a_i^\dagger, a_i \right] = \delta_{ij}$ one can show that the operators in (4.6) fulfill the standard spin commutation relations (4.2). In this representation the boson number n corresponds to the difference in the magnetic S^z quantum number relative to the Néel state $n = m - (-S)$. Hence, the spin ladder operators effectively create or annihilate bosons. However, the local Hilbert space of a spin is restricted by the total spin S in contrast to the local bosonic Hilbert space which is infinitely large. In the Holstein-Primakoff approach this restriction is incorporated by the square root expressions which ensure that the states do not leave the physical Hilbert space

$$a^\dagger \sqrt{2S - a^\dagger a}\ |S, m = S\rangle = 0 \tag{4.7}$$

Unfortunately, the square root terms cannot be treated exactly. They comprise non trivial boson interactions which become manifest if we expand the operator as follows

$$\sqrt{2S}\sqrt{1-\frac{a_i^\dagger a_i}{2S}} = \sqrt{2S}\left(1-\frac{a_i^\dagger a_i}{2S}-\frac{(a_i^\dagger a_i)^2}{32S^2}-\dots\right) \quad . \tag{4.8}$$

Note, that the truncation at any finite order will lead to a violation of (4.7) giving rise to non physical states with $m > S$. Thus, this approximation is only justified as long as the local density of bosons is small compared to S, i.e., $\langle a_i^\dagger a_i \rangle \ll S$. First discuss the classical limit $S \to \infty$. In this case the local spin Hilbert space is infinitely large and the spin ladder operators can be replaced by simple boson creation and annihilation operators. This truncation corresponds to the zeroth order, i.e., $\sqrt{1-\frac{a_i^\dagger a_i}{2S}} \approx 1$, and is also referred to as the linear spin wave approximation. The truncated Hamiltonian can be diagonalized in momentum space by a Bogoliubov transformation introducing new bosons $\alpha_{\mathbf{k}}^\dagger = l_{\mathbf{k}} a_{\mathbf{k}}^\dagger + m_{\mathbf{k}} a_{-\mathbf{k}}$ such that the Hamiltonian becomes diagonal

$$H = E_0 + \sum_{\mathbf{k}} \omega_0(\mathbf{k}) \alpha_{\mathbf{k}}^\dagger \alpha_{\mathbf{k}} \tag{4.9}$$

with the disperson relation $\omega_0(\mathbf{k}) = SJ\sqrt{2-\frac{1}{2}\left(\cos(k_x)+\cos(k_y)\right)^2}$ [16]. In this approximation the x and y components of the spins are effectively treated as conjugate pairs $\left[S_i^x, S_j^y\right] \propto \delta_{ij}$ which behave analogous to the momentum and position operators in the problem of coupled harmonic oscillators. Note, that the Hamiltonian actually is equivalent to a system of coupled harmonic oscillators. Thus, in this semi classical picture the excitations can be envisioned as oscillations between the x and y components of the spins around the ordered Néel state propagating as quantized spin waves, i.e., magnons[5]. Due to zero point fluctuations the staggered magnetization is reduced to $m = S - \delta m \approx 0.303$ for $S = 1/2$ [17].
Typically, one also takes into account the next leading order in the spin wave expansion. In this approximation the dispersion is only renormalized by a constant overall factor

$$\omega = \omega_0(\mathbf{k}) \cdot (1 + A/S) \tag{4.10}$$

which is $Z_c \approx 1.158$ in the case of $S = 1/2$ and the ground state energy per site is further reduced from $e_0^{(0)} \approx -0.659$ to $e_0^{(1)} \approx -0.6705$ [17].
Despite its simplicity, linear spin wave theory already provides a good description of the low energy excitations in long range ordered quantum antiferromagnets [176]. Higher order terms in $1/S$ correspond to interactions or scattering processes between spin waves. They comprise dynamical interactions which simply arise due to the fact that the Hamiltonian is not-diagonal such as interactions originating from the $S_i^z S_j^z$ term. Furthermore, there are also non-trivial interactions resulting from the finite local Hilbert space, also referred to as kinematical interactions [195]. The effects of the restricted Hilbert space are actually very strong for $S = 1/2$ systems, where magnons are basically hardcore bosons [197]. Nevertheless, one can show that at long wavelengths spin waves propagate almost freely because the spin deviation is widely distributed and the scattering due to the magnonic hardcore property is very small [192, 195]. Thus, spin wave theory is essentially based on the assumption that $\langle a_i^\dagger a_i \rangle \ll S$.

[5] Magnons in the antiferromagnet are a direct analog of phonons which are quantized oscillations of nuclei in a crystal structure. Accordingly, phonons are the Goldstone Bosons of the broken continuous translation symmetry of space.

In the case of short wavelength spin waves, however, these assumptions, are not necessarily true. The combination of magnon attraction and the hardcore property can lead to non-trivial quantum correlations on short length scales. We suppose, that the observed anomalous dispersion of spin waves at the zone boundary can indeed be attributed to such quantum effects. In general, the Hamiltonian also contains scattering processes from single spin waves to multi-magnon states at higher energies which possibly do not meet the requirement that $\langle a_i^\dagger a_i \rangle \ll S$. In this case, the conventional expansion in $1/S$ would be inefficient. The existence of such states would also account for the slow convergence in the $1/S$ expansions at $\mathbf{k} = (\pi, 0)$ [31].
In the following, we want to overcome these problems by a suitable methodical treatement based on a quasi-particle conserving CUT. To this end, we derive an effective model where the number of magnons is conserved, i.e., scattering processes into multi-magnon states are transformed into magnon-conserving terms. The resulting Hamiltonian describes dressed magnons with renormalized dynamical properties and interactions.
Unfortunately, the Holstein-Primakoff representation generally requires an expansion of the square root operators in $1/S$. Hence, processes which might be relevant in order to capture short range correlations are discarded a priori for any finite truncation. In the next section, we discuss an alternative representation which is better suited to our approach because it allows us to define magnon interaction terms exactly on a quartic level in boson operators.

4.2.2 Dyson-Maleev representation

Dyson was the first to address the problems of kinematical spin wave interactions in ferromagnets [195]. In order to overcome some generic obstacles imposed by the Holstein-Primakoff formalism he introduced an alternative boson representation which was further developed by Maleev [198, 199]. Nowadays this approach is known as the Dyson-Maleev representation.
In 1960 Oguchi extended this representation to the Heisenberg antiferromagnet [192]. Moreover, he showed that the Dyson-Maleev and Holstein-Primakoff formalism yield identical results for a rigorous expansion up to first order in $1/S$. This is also confirmed for higher order calculations in $1/S$ suggesting that both approaches describe essentially the same physics [193].
A major advantage of the Dyson-Maleev representation is that it does not introduce intricate square root expressions and, as a result, the kinematical spin wave interactions are expressed exactly on a quartic level in creation and annihilation operators. It is typically used in high order spin wave calculations [30, 31, 193, 194].
However, due to an asymmetry between bra and ket basis states the resulting Hamiltonian is superficially non-hermitian in the extended bosonic Hilbert space. This property can be attributed to the fact that the spin operators and Dyson-Maleev bosons are self adjoint with respect to two different inner products [118]. Thus, the Holstein-Primakoff and Dyson-Maleev representations are related by a non-orthogonal similarity transformation, i.e., both representations should yield the same results as long as they are treated exactly (or rigorously in some expansion parameter).
Nevertheless, the Dyson-Maleev approach is accompanied with important technical assets because it does not impose an expansion in the parameter $1/S$. Most importantly, it allows us to apply truncation schemes which go beyond the conventional expansion in $1/S$.
The idea is to use a self similar CUT approach based on the scaling dimension of spin wave operators in the Dyson-Maleev representation. This way, we take into account the full renormalization of magnon interactions which turns out to be essential in the case of the spin-1/2

HAFSQ. As we encounter a non-hermitian Hamiltonian the CUT method generalizes to a similarity transformation which in the following is referred to as a continuous similarity transformation (CST).
Before we discuss this more elaborate approach, let us introduce the Dyson-Maleev formalism for the HAFSQ. The resulting Hamiltonian constitutes the initial point of the CST approach. In order to verify the general functionality of the method we reproduce the main results of high order spin wave expansions which were calculated in Ref. [193, 194] and Ref. [31]. Moreover, we examine a non-perturbative extrapolation of the $1/S$-expansion by means of a deepCST method.

General formalism

For the Heisenberg antiferromagnet on the square lattice given by (4.4) it is expedient to define the following relations

$$S_i^+ = \sqrt{2S}\left(a_i - \frac{a_i^\dagger a_i a_i}{2S}\right) \qquad S_i^- = \sqrt{2S}\, a_i^\dagger \qquad S_i^z = S - a_i^\dagger a_i \tag{4.11a}$$

$$S_j^+ = \sqrt{2S}\left(b_j^\dagger - \frac{b_j^\dagger b_j^\dagger b_j}{2S}\right) \qquad S_j^- = \sqrt{2S}\, b_j \qquad S_j^z = -S + b_j^\dagger b_j \quad . \tag{4.11b}$$

This representation incorporates a sublattice rotation and discriminates between two different bosons which are defined by the respective sublattice A or B. The resulting Dyson-Maleev Hamiltonian in real space reads

$$H_{\mathrm{DM}} = -JS^2ZN + JS\left(Z\sum_{i\in A} a_i^\dagger a_i + Z\sum_{j\in A} b_j^\dagger b_j + \sum_{\langle i,j\rangle} a_i^\dagger b_j^\dagger + a_i\, b_j\right) \tag{4.12a}$$

$$-J\sum_{\langle i,j\rangle}\left(a_i^\dagger a_i\, b_j^\dagger b_j + \frac{1}{2}a_i^\dagger b_j^\dagger b_j^\dagger b_j + \frac{1}{2}a_i^\dagger a_i\, a_i\, b_j\right) \tag{4.12b}$$

where $Z = 2$ denotes the coordination number and N is the number of sites on sublattice A (or B). The representation in momentum space can be obtained by introducing Fourier transformed operators

$$a_{\mathbf{k}}^\dagger = \frac{1}{\sqrt{N}}\sum_{\mathbf{r}_i\in A} a_i^\dagger\, \mathrm{e}^{-\mathrm{i}(\mathbf{k}\cdot\mathbf{r}_i)} \qquad a_i^\dagger = \frac{1}{\sqrt{N}}\sum_{\mathbf{k}\in\mathrm{MBZ}} a_{\mathbf{k}}^\dagger\, \mathrm{e}^{\mathrm{i}(\mathbf{k}\cdot\mathbf{r}_i)} \tag{4.13a}$$

$$[0.5cm] b_{\mathbf{k}}^\dagger = \frac{1}{\sqrt{N}}\sum_{\mathbf{r}_j\in B} b_j^\dagger\, \mathrm{e}^{-\mathrm{i}(\mathbf{k}\cdot\mathbf{r}_j)} \qquad b_j^\dagger = \frac{1}{\sqrt{N}}\sum_{\mathbf{k}\in\mathrm{MBZ}} b_{\mathbf{k}}^\dagger\, \mathrm{e}^{\mathrm{i}(\mathbf{k}\cdot\mathbf{r}_j)} \tag{4.13b}$$

where the sum over the momenta $\mathbf{k}$ is restricted to the reduced magnetic Brillouin zone (MBZ) because we consider two flavors of bosons on a magnetic two-site unit cell. We obtain the

following Hamiltonian

$$\begin{aligned}\mathcal{H}_{\mathrm{DM}} = &-JS^2ZN + JSZ\sum_{\mathbf{k}}\left\{a_{\mathbf{k}}^\dagger a_{\mathbf{k}} + b_{\mathbf{k}}^\dagger b_{\mathbf{k}} + \gamma(k)\left(a_{\mathbf{k}}^\dagger b_{\text{-}\mathbf{k}}^\dagger + a_{\mathbf{k}} b_{\text{-}\mathbf{k}}\right)\right\} \\ &-\frac{JZ}{N}\sum_{\mathbf{1,2,3,4}}\Big\{\ \delta_G(\mathbf{1-2+3-4})\,\gamma(\mathbf{3-4})\ a_{\mathbf{1}}^\dagger a_{\mathbf{2}} b_{\mathbf{3}}^\dagger b_{\mathbf{4}} \\ &\qquad + \delta_G(\mathbf{1+2+3-4})\,\frac{1}{2}\gamma(\mathbf{2+3-4})\ a_{\mathbf{1}}^\dagger b_{\mathbf{2}}^\dagger b_{\mathbf{3}}^\dagger b_{\mathbf{4}} \\ &\qquad +\delta_G(\mathbf{1-2-3-4})\,\frac{1}{2}\gamma(\mathbf{4})\ a_{\mathbf{1}}^\dagger a_{\mathbf{2}} a_{\mathbf{3}} b_{\mathbf{4}}\ \Big\}\quad . \end{aligned} \tag{4.14}$$

where

$$\gamma(\mathbf{k}) = \frac{1}{Z}\sum_{\mathbf{d}} \mathrm{e}^{-\mathrm{i}(\mathbf{k}\cdot\mathbf{d})} = \frac{1}{2}\left(\cos\left(k_x\right) + \cos\left(k_y\right)\right)\quad . \tag{4.15}$$

The subscripts $i = 1,2,3,4$ stand for the momenta $\mathbf{k}_i$ and $-i$ stands for $-\mathbf{k}_i$. The conservation of momentum is ensured by the Kronecker symbol $\delta_G(\mathbf{1+2-3-4})$ implying $\mathbf{k}_1+\mathbf{k}_2 = \mathbf{k}_3+\mathbf{k}_4$ modulo reciprocal lattice vectors $\mathbf{G}$ from the reciprocal lattice Γ_A^* of the A-sites. Thus, $\mathbf{G}\in\Gamma_A^*$ means $\mathbf{G} = (n\pi, m\pi)$ with the integers n, m if the lattice constant of the original square-lattice is set to unity.
Due to our definitions one has to distinguish between the commutator of the a and b bosons leading to a subtlety in the definition of the Kronecker-δ (or δ-function in the thermodynamic limit). We distinguish two different bosonic commutators

$$[\,a_{\mathbf{k}'}, a_{\mathbf{k}}^\dagger\,] = \frac{1}{N}\sum_{j\in A}\mathrm{e}^{-\mathrm{i}(\mathbf{k}-\mathbf{k}')\cdot\mathbf{r}_j} = \delta_G\left(\mathbf{k}-\mathbf{k}'\right) \tag{4.16a}$$

$$[\,b_{\mathbf{k}'}, b_{\mathbf{k}}^\dagger\,] = \frac{1}{N}\sum_{j\in B}\mathrm{e}^{-\mathrm{i}\left(\mathbf{k}-\mathbf{k}'\right)\cdot\mathbf{r}_j} = \frac{1}{NZ}\sum_{j\in A,\mathbf{d}}\mathrm{e}^{-\mathrm{i}\left(\mathbf{k}-\mathbf{k}'\right)\cdot\left(\mathbf{r}_j+\mathbf{d}\right)} \tag{4.16b}$$

$$= \gamma\left(\mathbf{k}-\mathbf{k}'\right)\delta_G\left(\mathbf{k}-\mathbf{k}'\right) \tag{4.16c}$$

$$:= \overline{\delta}_G\left(\mathbf{k}-\mathbf{k}'\right)\quad . \tag{4.16d}$$

and define

$$\overline{\delta}_G(\mathbf{K}) = \Gamma_{\mathbf{K}}\ \delta_G(\mathbf{K}) \tag{4.17}$$

with

$$\Gamma_{\mathbf{K}} = \begin{cases} 1 & \text{for } \mathbf{K}\in Z^{(+)} \\ -1 & \text{for } \mathbf{K}\in Z^{(-)} \end{cases}\quad . \tag{4.18}$$

Since the lattice vectors correspond to the A lattice, the commutator of the B-bosons acquires a factor $\Gamma_{\mathbf{K}}$ which tracks the reciprocal lattice vector $\mathbf{K} = \mathbf{k}-\mathbf{k}'$. Depending on the MBZ in which this vector $\mathbf{K}\in\Gamma_A^*$ is located the function takes the values $\Gamma_{\mathbf{K}} = 1$ or $\Gamma_{\mathbf{K}} = -1$. It is positive in the 1st MBZ and negative in the adjacent edge-sharing MBZs, i.e., it switches sign each time

one enters another MBZ across an edge as shown in Figure 4.4. These sign changes actually pose no problems in the Hamiltonian because the sums are restricted to momenta of the 1. MBZ. where $\Gamma_{\mathbf{K}} = 1$.

However, we also want to compute dynamic structure factors which describe inelastic neutron

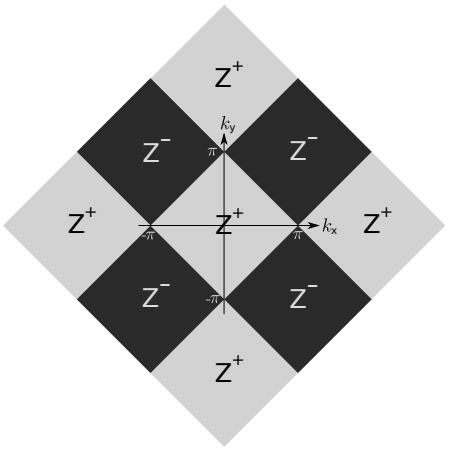

Figure 4.4: Illustration of the sign structure of the factor $\Gamma_{\mathbf{K}}$. The factor takes the value $\Gamma_{\mathbf{K}} = +1$ for $K \in Z^+$ or $\Gamma_{\mathbf{K}} = +1$ for $K \in Z^-$.

scattering. The corresponding observables depend on momenta which may lie outside the 1st MBZ, i.e., they induce Umklapp processes in the system. In this case, the sign changes become relevant. The Dyson-Maleev representation of the observables is discussed in section 4.2.2.

The Hamiltonian in (4.14) is diagonalized by a Bogoliubov transformation

$$a_{\mathbf{k}}^{\dagger} = l_{\mathbf{k}} \alpha_{\mathbf{k}}^{\dagger} + m_{\mathbf{k}} \beta_{\text{-}\mathbf{k}} \tag{4.19a}$$

$$b_{\mathbf{k}}^{\dagger} = m_{\mathbf{k}} \alpha_{\text{-}\mathbf{k}} + l_{\mathbf{k}} \beta_{\mathbf{k}}^{\dagger} \tag{4.19b}$$

with

$$l_{\mathbf{k}}^2 - m_{\mathbf{k}}^2 = 1 \quad . \tag{4.20}$$

Following Ref. [30] we use the parametrization

$$l_{\mathbf{k}} = \sqrt{\frac{1+\epsilon_{\mathbf{k}}}{2\epsilon_{\mathbf{k}}}} \qquad m_{\mathbf{k}} = -\text{sign}\,(\gamma_{\mathbf{k}}) \sqrt{\frac{1-\epsilon_{\mathbf{k}}}{2\epsilon_{\mathbf{k}}}} = -x_{\mathbf{k}} l_{\mathbf{k}} \tag{4.21a}$$

$$x_{\mathbf{k}} := \text{sign}\,(\gamma_{\mathbf{k}}) \sqrt{\frac{1-\epsilon_{\mathbf{k}}}{1+\epsilon_{\mathbf{k}}}} \tag{4.21b}$$

$$\epsilon_{\mathbf{k}} = \sqrt{1-\gamma_{\mathbf{k}}^2} \quad . \tag{4.21c}$$

and bring the operator terms into a normal ordered form with respect to the new bosons $\alpha_{\mathbf{k}}^{\dagger}$ and $\beta_{\mathbf{k}}^{\dagger}$. The resulting Hamiltonian then reads

$$\mathcal{H}_{\text{DM}} = E_0 + \sum_{\mathbf{k}} \omega_{\mathbf{k}} (\alpha_{\mathbf{k}}^{\dagger} \alpha_{\mathbf{k}} + \beta_{\mathbf{k}}^{\dagger} \beta_{\mathbf{k}}) + \mathcal{V} \tag{4.22}$$

where the coefficients $e_0^{(1)} := E_0/N = -2J(S^2 + AS + A^2/4)$, $\omega_{\mathbf{k}} = 2J(2S+A)\sqrt{1-\gamma(\mathbf{k})^2}$ with $A := \frac{2}{N}\sum_{\mathbf{k}}(1-\sqrt{1-\gamma(\mathbf{k})^2}) \approx 0.158$ correspond to the ground-state energy per site and the one-magnon dispersion in next-to-leading order spin wave theory [30, 193].
The remaining part $\mathcal{V}$ contains spin wave scattering and interaction terms which are quartic in boson annihilation and creation operators

$$\begin{aligned}\mathcal{V} = -\frac{J}{N}\sum_{1234}\delta_G(1+2-3-4)\; l_1 l_2 l_3 l_4 \Big[& V^{(1)}_{1234}\alpha_1^\dagger\alpha_2^\dagger\alpha_3\alpha_4 \\ & + 2V^{(2)}_{1234}\alpha_1^\dagger\beta_{-2}\alpha_3\alpha_4 + 2V^{(3)}_{1234}\alpha_1^\dagger\alpha_2^\dagger\beta_{-3}^\dagger\alpha_4 \\ & + 4V^{(4)}_{1234}\alpha_1^\dagger\alpha_3\beta_{-4}^\dagger\beta_{-2} + 2V^{(5)}_{1234}\beta_{-4}^\dagger\alpha_3\beta_{-2}\beta_{-1} \\ & + 2V^{(6)}_{1234}\beta_{-4}^\dagger\beta_{-3}^\dagger\alpha_2^\dagger\beta_{-1} + V^{(7)}_{1234}\alpha_1^\dagger\alpha_2^\dagger\beta_{-3}^\dagger\beta_{-4}^\dagger \\ & + V^{(8)}_{1234}\beta_{-1}\beta_{-2}\alpha_3\alpha_4 + V^{(9)}_{1234}\beta_{-4}^\dagger\beta_{-3}^\dagger\beta_{-2}\beta_{-1}\Big].\end{aligned} \tag{4.23}$$

The explicit expressions for the vertex functions $V^{(i)}_{1234}$ are given by

$$\begin{aligned} V^{(1)}_{1234} &= x_1x_3\gamma(1-3) + x_1x_4\gamma(1-4) + x_2x_3\gamma(2-3) + x_2x_4\gamma(2-4) \\ &\quad - x_1\gamma(1) - x_2\gamma(2) - x_1x_3x_4\gamma(1-3-4) - x_2x_3x_4\gamma(2-3-4) \end{aligned} \tag{4.24a}$$

$$\begin{aligned} V^{(2)}_{1234} &= -x_3\gamma(2-3) - x_4\gamma(2-4) - x_1x_2x_3\gamma(1-3) - x_1x_2x_4\gamma(1-4) \\ &\quad + x_1x_2\gamma(1) + \gamma(2) + x_1x_2x_3x_4\gamma(1-3-4) + x_3x_4\gamma(2-3-4) \end{aligned} \tag{4.24b}$$

$$\begin{aligned} V^{(3)}_{1234} &= -x_1\gamma(1-3) - x_2\gamma(2-3) - x_1x_3x_4\gamma(1-4) - x_2x_3x_4\gamma(2-4) \\ &\quad + x_1x_3\gamma(1) + x_2x_3\gamma(2) + x_1x_4\gamma(1-3-4) + x_2x_4\gamma(2-3-4) \end{aligned} \tag{4.24c}$$

$$\begin{aligned} V^{(4)}_{1234} &= x_1x_2x_3x_4\gamma(1-3) + x_1x_2\gamma(1-4) + x_3x_4\gamma(2-3) + \gamma(2-4) \\ &\quad - x_4\gamma(1) - x_1x_2x_4\gamma(1) - x_3\gamma(1-3-4) - x_1x_2x_3\gamma(1-3-4) \end{aligned} \tag{4.24d}$$

$$\begin{aligned} V^{(5)}_{1234} &= -x_2x_3x_4\gamma(1-3) - x_1x_3x_4\gamma(2-3) - x_1\gamma(2-4) - x_2\gamma(1-4) \\ &\quad + x_1x_3\gamma(2) + x_2x_4\gamma(1) + x_1x_3\gamma(2-3-4) + x_2x_3\gamma(1-3-4) \end{aligned} \tag{4.24e}$$

$$\begin{aligned} V^{(6)}_{1234} &= -x_4\gamma(1-3) - x_3\gamma(1-4) - x_1x_2x_3\gamma(2-4) - x_1x_2x_4\gamma(2-3) \\ &\quad + \gamma(1-3-4) + x_1x_2\gamma(2-3-4) + x_3x_4\gamma(1) + x_1x_2x_3x_4\gamma(1) \end{aligned} \tag{4.24f}$$

$$\begin{aligned} V^{(7)}_{1234} &= x_1x_4\gamma(1-3) + x_1x_3\gamma(1-4) + x_2x_3\gamma(2-4) + x_2x_4\gamma(2-3) \\ &\quad - x_1x_3x_4\gamma(1) - x_2x_3x_4\gamma(2) - x_1\gamma(1-3-4) - x_2\gamma(2-3-4) \end{aligned} \tag{4.24g}$$

$$\begin{aligned} V^{(8)}_{1234} &= x_1x_4\gamma(2-4) + x_2x_4\gamma(1-4) + x_1x_3\gamma(2-3) + x_2x_3\gamma(1-3) \\ &\quad - x_1\gamma(2) - x_2\gamma(1) - x_1x_3x_4\gamma(2-3-4) - x_2x_3x_4\gamma(1-3-4) \end{aligned} \tag{4.24h}$$

$$\begin{aligned} V^{(9)}_{1234} &= +x_1x_3\gamma(2-4) + x_2x_3\gamma(1-4) + x_1x_4\gamma(2-3) + x_2x_4\gamma(1-3) \\ &\quad - x_1\gamma(2-3-4) - x_2\gamma(1-3-4) - x_1x_3x_4\gamma(2) - x_2x_3x_4\gamma(1) \end{aligned} \tag{4.24i}$$

where we symmetrized each function according to (2.33) (see also Ref. [30, 193]).
Note, that the Hamiltonian is not manifestly hermitian but it is invariant under the exchange

of α and β bosons and an additional hermitian conjugation. We could have chosen the inverse sublattice rotation and rename the a bosons into b bosons (and vice versa) which should yield an identical Hamiltonian. This property translates into the following relations between the coefficient functions

$$V^{(1)}_{1234} = V^{(9)}_{1234} \cdot \Gamma_{\mathbf{K}} \tag{4.25a}$$
$$V^{(2)}_{1234} = V^{(6)}_{1234} \cdot \Gamma_{\mathbf{K}} \tag{4.25b}$$
$$V^{(3)}_{1234} = V^{(5)}_{1234} \cdot \Gamma_{\mathbf{K}} \tag{4.25c}$$
$$V^{(7)}_{1234} = V^{(8)}_{1234} \cdot \Gamma_{\mathbf{K}} \tag{4.25d}$$
$$\Gamma_{\mathbf{K}} = \gamma(\mathbf{1}+\mathbf{2}-\mathbf{3}-\mathbf{4}) \tag{4.25e}$$

which can be derived from (4.24b)-(4.24i) if the conservation of total momentum is taken into account.
For small momenta $\mathbf{k}_i \ll 1$ the vertex functions of the quartic terms can be written as

$$V^{(i)}_{1234} = -\frac{1}{2}\frac{|\mathbf{k}_3|\,|\mathbf{k}_4| - \mathbf{k}_3\cdot\mathbf{k}_4}{\sqrt{|\mathbf{k}_1|\,|\mathbf{k}_2|\,|\mathbf{k}_3|\,|\mathbf{k}_4|}} \quad \text{for } i = 1,7,8,9 \tag{4.26a}$$
$$V^{(i)}_{1234} = \frac{1}{2}\frac{|\mathbf{k}_3|\,|\mathbf{k}_4| - \mathbf{k}_3\cdot\mathbf{k}_4}{\sqrt{|\mathbf{k}_1|\,|\mathbf{k}_2|\,|\mathbf{k}_3|\,|\mathbf{k}_4|}} \quad \text{for } i = 2,6 \tag{4.26b}$$
$$V^{(i)}_{1234} = -\frac{1}{2}\frac{|\mathbf{k}_3|\,|\mathbf{k}_4| + \mathbf{k}_3\cdot\mathbf{k}_4}{\sqrt{|\mathbf{k}_1|\,|\mathbf{k}_2|\,|\mathbf{k}_3|\,|\mathbf{k}_4|}} \quad \text{for } i = 3,5 \tag{4.26c}$$
$$V^{(4)}_{1234} = \frac{1}{2}\frac{|\mathbf{k}_3|\,|\mathbf{k}_4| + \mathbf{k}_3\cdot\mathbf{k}_4}{\sqrt{|\mathbf{k}_1|\,|\mathbf{k}_2|\,|\mathbf{k}_3|\,|\mathbf{k}_4|}} \quad . \tag{4.26d}$$

All interaction functions exhibit a very similar behavior for small momenta which is a manifestation of the scale invariance at long wavelengths. Note, that the vertex functions diverge in the limit $\mathbf{k}_i \to 0$ if we consider a single momentum argument $\mathbf{k}_i$. However, if we take the limit $\mathbf{k}_i \to 0$ simultaneously for all momenta $\mathbf{k}_i$ the vertex functions assume a finite value.
In the evaluation of the CST we set the interaction terms to zero for $\mathbf{k}_i = 0$ in order to avoid poles. This is reasonable since we expect that the interactions and scattering processes between spin waves should cancel out in the limit of long wavelengths [192, 195]. Indeed, this assumption is confirmed by the consistency of the perturbative and non-perturbative results presented in the subsequent sections.

Observables

In this part we give a brief overview about the observables which are required for the theoretical description of inelastic scattering of polarized neutrons. A comprehensive introduction to the theory of inelastic neutron scattering (INS) is given in Ref. [200].
The spectral density provides a theoretical description of the momentum and energy resolved intensity $I^{\text{exp}}(\omega, Q)$ measured in INS experiments. For sufficiently low temperatures it is proportional to the dynamic structure factor at zero Temperature

$$I^{\text{exp}}(\omega,Q) \propto S^{\alpha\alpha}(\omega,Q) = -\frac{1}{\pi}\text{Im}\left(\langle 0|\, S^{\alpha}(-Q)\frac{1}{\omega-(H-\bar{E}_0)}S^{\alpha}(Q)\,|0\rangle\right) \tag{4.27}$$

where $|0\rangle$ is the ground state of the Hamiltonian H with the ground state energy E_0 and $S^{\alpha}(-Q)$ are the Fourier transformed components of the spin operator with $\alpha = x, y, z$.
Inelastic scattering experiments with polarized neutrons allows one to distinguish between the longitudinal part $\alpha = z$ and the transverse parts $\alpha = x, y$ which correspond to the longitudinal or transverse excitations of the system.
Since we consider an isotropic Hamiltonian the dynamic structure factor is invariant under the exchange of the x and y direction. In this case, it is expedient to define the transverse dynamic structure factor as follows

$$S^{xx}(\omega,Q) + S^{yy}(\omega,Q) = -\frac{1}{\pi}\text{Im}\left(\langle 0|\, S^{-}(-Q)\frac{1}{\omega-(H_{\text{eff}}-\bar{E}_0)}S^{+}(Q)\,|0\rangle\right) \quad . \tag{4.28}$$

combining the x and y contribution (see also [201]).
Parallel to the derivation of the effective Hamiltonian, we also have to transform the effective observables for $S^{-}(-Q)$, $S^{+}(-Q)$ and $S^{z}_{\mathbf{Q}}$ by means of the flow equation (2.3). The corresponding initial conditions are defined by the Dyson-Maleev representation of the respective operators presented in the following.
The observable of the longitudinal dynamic structure factor is given by

$$S^{z}_{\mathbf{Q}} = \sum_{\mathbf{r}_i \in A} S^{z}_{i} e^{-i(\mathbf{Q}\cdot\mathbf{r}_i)} \quad + \quad \sum_{\mathbf{r}_j \in B} S^{z}_{j} e^{-i(\mathbf{Q}\cdot\mathbf{r}_j)} \tag{4.29}$$

After the Dyson Maleev transformation (4.11) and a subsequent Bogoliubov transformation (4.19a). we eventually obtain the following expression

$$\begin{aligned} S^{z}(Q) = S^{z}_{A}(Q) + S^{z}_{B}(Q) &= \left(m_Q^2 - SN\right)\left(\Gamma_Q - 1\right)\delta_G(Q) \\ &+ \sum_{1,2}\delta_G(Q-1+2)\Big\{ \quad [\Gamma_K l_1 l_2 - m_1 m_2]\,\beta_{\mathbf{1}}^{\dagger}\beta_{\mathbf{2}} \\ &\qquad + [\Gamma_{\mathbf{K}} m_1 m_2 - l_1 l_2]\,\alpha_{\mathbf{1}}^{\dagger}\alpha_{\mathbf{2}} \\ &\qquad + [\Gamma_{\mathbf{K}} m_1 l_2 - l_1 m_2]\,\alpha_{\mathbf{1}}^{\dagger}\beta_{\mathbf{-2}}^{\dagger} \\ &\qquad + [\Gamma_{\mathbf{K}} m_2 l_1 - l_2 m_1]\,\alpha_{\mathbf{2}} b_{\mathbf{-1}} \quad \Big\} \end{aligned} \tag{4.30}$$

with the factor $\Gamma_{\mathbf{K}} = \gamma(\mathbf{Q}-\mathbf{1}+\mathbf{2})$ which tracks the reciprocal lattice vector $\mathbf{G} = \mathbf{Q}-\mathbf{1}+\mathbf{2}$. Similarily, we transform the operators of the transverse part

$$\begin{aligned}
S^{+}(Q) = \sqrt{2SN}\left(1-\frac{1}{SN}\sum_{1} m_1^2\right)\left(\left(l_Q+\Gamma_Q\, m_Q\right)\alpha_{\text{-}\mathbf{Q}} + \left(m_Q+\Gamma_Q\, l_Q\right)\beta^{\dagger}_{\mathbf{Q}}\right) \\
-\frac{1}{\sqrt{2SN}}\sum_{1,2,3}\delta_G\left(Q-1+2+3\right)\Big\{\times \\
+\quad [l_1 l_2 l_3 + \Gamma_K\, m_1 m_2 m_3]\,\alpha^{\dagger}_{\mathbf{1}}\alpha_{\mathbf{2}}\alpha_{\mathbf{3}} \\
+\quad [m_1 l_2 l_3 + \Gamma_K\, m_2 m_3 l_1]\,\alpha_{\mathbf{2}}\alpha_{\mathbf{3}}\beta_{\text{-}\mathbf{1}} \\
+\;2\,[l_1 l_2 m_3 + \Gamma_K\, m_2 l_3 m_1]\,\alpha^{\dagger}_{\mathbf{1}}\alpha_{\mathbf{2}}\beta^{\dagger}_{\text{-}\mathbf{3}} \\
+\;2\,[m_1 l_2 m_3 + \Gamma_K\, l_1 m_2 l_3]\,\alpha_{\mathbf{2}}\beta^{\dagger}_{\text{-}\mathbf{3}}\beta_{\text{-}\mathbf{1}} \\
+\quad [l_1 m_2 m_3 + \Gamma_K\, m_1 l_2 l_3]\,\alpha^{\dagger}_{\mathbf{1}}\beta^{\dagger}_{\text{-}\mathbf{2}}\beta^{\dagger}_{\text{-}\mathbf{3}} \\
+\quad [m_1 m_2 m_3 + \Gamma_K l_1 l_2 l_3]\,\beta^{\dagger}_{\text{-}\mathbf{2}}\beta^{\dagger}_{\text{-}\mathbf{3}}\beta_{\text{-}\mathbf{1}} \quad \Big\}
\end{aligned} \tag{4.31}$$

and

$$S^{-}(Q) = \sqrt{2SN}\left(\left[l_{\mathbf{Q}}+\Gamma_Q m_Q\right]\alpha^{\dagger}_{\mathbf{Q}} + \left[m_Q+\Gamma_Q l_Q\right]\beta_{\text{-}\mathbf{Q}}\right) \tag{4.32}$$

Note, that the external momentum $\mathbf{Q}$ can also take values outside the 1$^{\text{st}}$ MBZ and that $S_Q \neq S_{Q+g}$. Due to the non-hermiticity of the the Dyson-Maleev representation we have $S^{-}_{\text{-}\mathbf{Q}} \neq \left(S^{+}_{Q}\right)^{\dagger}$ and, thus, both operators have to be treated independently. Similar to the vertex functions we set the observables to zero for $\mathbf{k}_i = 0$ in order to avoid poles.

4.2.3 Expansion in $1/S$

In this section the perturbative spin wave expansion for the ground state energy and the dispersion up third order in $1/S$ is calculated by means of the epCST method. The results are compared to Ref. [193, 194] and Ref. [31]. Thereby, we verify the general functionality of the CST method.
The perturbative flow equations are derived in momentum space and solved either analytically or numerically by means of the the RKF 4(5) method. A direct comparison between the analytical and numerical results allows us to estimate the errors made in the numerical evaluation due the finite step size. With this information we can adjust the control tolerance for the subsequent non-perturbative evaluations based on the deepCUT and sCUT method.

Perturbative analysis (epCST)

For the perturbative treatement the Hamiltonian in (4.22) is divided by S which yields

$$\mathcal{H}_{\mathrm{DM}}/S = E_0 + \sum_{\mathbf{k}} \left(\omega_1^{(0)} + \frac{1}{S}\omega_1^{(1)} \right) (\alpha_{\mathbf{k}}^\dagger \alpha_{\mathbf{k}} + \beta_{\mathbf{k}}^\dagger \beta_{\mathbf{k}}) + \frac{1}{S}\mathcal{V} \quad . \tag{4.33}$$

The unperturbed Hamiltonian H_0 describes the renormalized spin waves whereas the second part $\mathcal{V}$ is considered as the perturbation. Note, that the unperturbed part is exact up to first order in $1/S$ as the corrections due to the perturbation are at least of second order in $1/S$.
The commutators in the flow equation are evaluated and sorted by powers of $(1/S)^n$. We keep all operator terms which contribute to the second and third order corrections of the ground state energy and the magnon dispersion

$$E_0(\ell) = \bar{E}_0^{(0)} + \frac{1}{S}E_0^{(1)} + \frac{1}{S^2}E_0^{(2)}(\ell) + \frac{1}{S^3}E_0^{(3)}(\ell) \tag{4.34a}$$

$$\omega_{\mathbf{k}}(\ell) = \omega_{\mathbf{k}}^{(0)} + \frac{1}{S}\omega_{\mathbf{k}}^{(1)} + \frac{1}{S^2}\omega_{\mathbf{k}}^{(2)}(\ell) + \frac{1}{S^3}\omega_{\mathbf{k}}^{(3)}(\ell) \quad . \tag{4.34b}$$

The coefficients of the resulting effective Hamiltonian for $\ell \to \infty$ are defined by

$$E_{0,\mathrm{eff}} = \bar{E}_0 + \frac{1}{S}E_0^{(1)} + \frac{1}{S^2}E_{0,\mathrm{eff}}^{(2)} + \frac{1}{S^3}E_{0,\mathrm{eff}}^{(3)} \tag{4.35a}$$

$$\omega_{\mathrm{eff}}(\mathbf{k}) = \omega_{\mathbf{k}}^{(0)} + \frac{1}{S}\omega_{\mathbf{k}}^{(1),\mathrm{eff}} + \frac{1}{S^2}\omega_{\mathrm{eff}}^{(2)}(\mathbf{k}) + \frac{1}{S^3}\omega_{\mathrm{eff}}^{(3)}(\mathbf{k}) \quad . \tag{4.35b}$$

For technical reasons it is expedient to write the flowing Hamiltonian in the following form

$$\begin{aligned}
H(\ell) = E_0 &+ \sum_{1} \omega(\mathbf{1})\left(\alpha_1^\dagger\alpha_1 + \beta_1^\dagger\beta_1\right) + \Gamma(\mathbf{1})\left(\alpha_1^\dagger\beta_{\bar{1}}^\dagger + \alpha_1\beta_{\bar{1}}\right) \\
&+ \sum_{1,2,3,4} \Big\{ C_1(\mathbf{1},\mathbf{2},\mathbf{3},\mathbf{4})\,\alpha_1^\dagger\alpha_2^\dagger\alpha_3\alpha_4 + C_2(\mathbf{1},\mathbf{2},\mathbf{3},\mathbf{4})\,\alpha_1^\dagger\alpha_2\beta_3^\dagger\beta_4 \\
&+ C_3(\mathbf{1},\mathbf{2},\mathbf{3},\mathbf{4})\,\beta_1^\dagger\beta_2^\dagger\beta_3\beta_4 + C_4(\mathbf{1},\mathbf{2},\mathbf{3},\mathbf{4})\,\alpha_1^\dagger\alpha_2^\dagger\alpha_3\beta_4^\dagger + \\
&+ C_5(\mathbf{1},\mathbf{2},\mathbf{3},\mathbf{4})\,\alpha_1^\dagger\beta_2^\dagger\beta_3^\dagger\beta_4 + C_6(\mathbf{1},\mathbf{2},\mathbf{3},\mathbf{4})\,\alpha_1^\dagger\alpha_2\alpha_3\beta_4 \\
&+ C_7(\mathbf{1},\mathbf{2},\mathbf{3},\mathbf{4})\,\alpha_1\beta_2^\dagger\beta_3\beta_4 + C_8(\mathbf{1},\mathbf{2},\mathbf{3},\mathbf{4})\,\alpha_1^\dagger\alpha_2^\dagger\beta_3^\dagger\beta_4^\dagger \\
&+ C_9(\mathbf{1},\mathbf{2},\mathbf{3},\mathbf{4})\,\alpha_1\alpha_2\beta_3\beta_4 + C_{10}(\mathbf{1},\mathbf{2},\mathbf{3},\mathbf{4},\mathbf{5},\mathbf{6})\,\alpha_1^\dagger\alpha_2^\dagger\alpha_3^\dagger\alpha_4\beta_5^\dagger\beta_6^\dagger + \\
&+ C_{11}(\mathbf{1},\mathbf{2},\mathbf{3},\mathbf{4},\mathbf{5},\mathbf{6})\,\alpha_1^\dagger\alpha_2\alpha_3\alpha_4\beta_5\beta_6 \Big\} \quad . \qquad (4.36)
\end{aligned}$$

where we rearranged the momentum indices according to (3.1). The flowing generator is then given by

$$\begin{aligned}
\eta(\ell) = &\sum_{1} \Gamma(\mathbf{1})\left(\alpha_1^\dagger\beta_{\bar{1}}^\dagger - \alpha_1\beta_{\bar{1}}\right) \\
&+ \sum_{1,2,3,4} \Big\{ C_4(\mathbf{1},\mathbf{2},\mathbf{3},\mathbf{4})\,\alpha_1^\dagger\alpha_2^\dagger\alpha_3\beta_4^\dagger + C_5(\mathbf{1},\mathbf{2},\mathbf{3},\mathbf{4})\,\alpha_1^\dagger\beta_2^\dagger\beta_3^\dagger\beta_4 \\
&- C_6(\mathbf{1},\mathbf{2},\mathbf{3},\mathbf{4})\,\alpha_1^\dagger\alpha_2\alpha_3\beta_4 - C_7(\mathbf{1},\mathbf{2},\mathbf{3},\mathbf{4})\,\alpha_1\beta_2^\dagger\beta_3\beta_4 \\
&+ C_8(\mathbf{1},\mathbf{2},\mathbf{3},\mathbf{4})\,\alpha_1^\dagger\alpha_2^\dagger\beta_3^\dagger\beta_4^\dagger - C_9(\mathbf{1},\mathbf{2},\mathbf{3},\mathbf{4})\,\alpha_1\alpha_2\beta_3\beta_4 \\
&+ C_{10}(\mathbf{1},\mathbf{2},\mathbf{3},\mathbf{4},\mathbf{5},\mathbf{6})\,\alpha_1^\dagger\alpha_2^\dagger\alpha_3^\dagger\alpha_4\beta_5^\dagger\beta_6^\dagger - C_{11}(\mathbf{1},\mathbf{2},\mathbf{3},\mathbf{4},\mathbf{5},\mathbf{6})\,\alpha_1^\dagger\alpha_2\alpha_3\alpha_4\beta_5\beta_6 \Big\} \quad . \qquad (4.37)
\end{aligned}$$

The coefficients E_0, $\omega(\mathbf{1})$, $\Gamma(\mathbf{1})$, $C_i(\mathbf{1},\mathbf{2},\mathbf{3},\mathbf{4})$ and $C_i(\mathbf{1},\mathbf{2},\mathbf{3},\mathbf{4},\mathbf{5},\mathbf{6})$ depend on the flow parameter ℓ and satisfy the initial conditions

$$E_0\big|_{\ell=0} = -2J(S+A+A^2/(4S)) \tag{4.38a}$$

$$\omega(\mathbf{1})\big|_{\ell=0} = 2J(2+A/S)\sqrt{1-\gamma(\mathbf{1})^2} \tag{4.38b}$$

$$\Gamma(\mathbf{1})\big|_{\ell=0} = 0 \tag{4.38c}$$

$$C_1(\mathbf{1},\mathbf{2},\mathbf{3},\mathbf{4})\big|_{\ell=0} = -l_1l_2l_3l_4\frac{J}{SN}V^{(1)}_{1234}\delta_G(1+2-3-4) \tag{4.38d}$$

$$C_2(\mathbf{1},\mathbf{2},\mathbf{3},\mathbf{4})\big|_{\ell=0} = -4l_1l_2l_3l_4\frac{J}{SN}V^{(4)}_{1\text{-}42\text{-}3}\delta_G(1-2+3-4) \tag{4.38e}$$

$$C_3(\mathbf{1},\mathbf{2},\mathbf{3},\mathbf{4})\big|_{\ell=0} = -l_1l_2l_3l_4\frac{J}{SN}V^{(9)}_{\text{-}4\text{-}3\text{-}2\text{-}1}\delta_G(1+2-3-4) \tag{4.38f}$$

$$C_4(\mathbf{1},\mathbf{2},\mathbf{3},\mathbf{4})\big|_{\ell=0} = -2l_1l_2l_3l_4\frac{J}{SN}V^{(3)}_{12\text{-}43}\delta_G(1+2-3+4) \tag{4.38g}$$

$$C_5(\mathbf{1},\mathbf{2},\mathbf{3},\mathbf{4})\big|_{\ell=0} = -2l_1l_2l_3l_4\frac{J}{SN}V^{(6)}_{\text{-}4\text{-}1\text{-}2\text{-}3}\delta_G(1+2+3-4) \tag{4.38h}$$

$$C_6(\mathbf{1},\mathbf{2},\mathbf{3},\mathbf{4})\big|_{\ell=0} = -2l_1l_2l_3l_4\frac{J}{SN}V^{(2)}_{1\text{-}423}\delta_G(1-2-3-4) \tag{4.38i}$$

$$C_7(\mathbf{1},\mathbf{2},\mathbf{3},\mathbf{4})\big|_{\ell=0} = -2l_1l_2l_3l_4\frac{J}{SN}V^{(5)}_{\text{-}4\text{-}31\text{-}2}\delta_G(-1+2-3-4) \tag{4.38j}$$

$$C_8(\mathbf{1},\mathbf{2},\mathbf{3},\mathbf{4})\big|_{\ell=0} = -l_1l_2l_3l_4\frac{J}{SN}V^{(7)}_{12\text{-}3\text{-}4}\delta_G(1+2+3+4) \tag{4.38k}$$

$$C_9(\mathbf{1},\mathbf{2},\mathbf{3},\mathbf{4})\big|_{\ell=0} = -l_1l_2l_3l_4\frac{J}{SN}V^{(8)}_{\text{-}3\text{-}412}\delta_G(-1-2-3-4) \tag{4.38l}$$

$$C_{10}(\mathbf{1},\mathbf{2},\mathbf{3},\mathbf{4},\mathbf{5},\mathbf{6})\big|_{\ell=0} = 0 \tag{4.38m}$$

$$C_{11}(\mathbf{1},\mathbf{2},\mathbf{3},\mathbf{4},\mathbf{5},\mathbf{6})\big|_{\ell=0} = 0 \quad . \tag{4.38n}$$

Figure 4.5 shows the diagrammatic representation of all relevant operator terms in the flowing Hamiltonian. The resulting flow equations are given in Appendix B.1.

The numerically most expensive terms arise from the vertex functions of the hexatic operators $C_{10}(\mathbf{1},\mathbf{2},\mathbf{3},\mathbf{4},\mathbf{5},\mathbf{6})$ and $C_{11}(\mathbf{1},\mathbf{2},\mathbf{3},\mathbf{4},\mathbf{5},\mathbf{6})$ which are required for the calculation of the third order correction of the dispersion. However, one does not need the full information about the momentum dependence of the hexatic terms in order to determine the flow of $\omega^{(}3)(\ell)$. Note, that there is an additional constraint on the corresponding momentum arguments, besides the standard conservation of momentum. Therefore, it is sufficient to consider reduced coefficient functions

$$\tilde{C}_{10}(\mathbf{1},\mathbf{2},\mathbf{3},\mathbf{4},\mathbf{5}) := \frac{1}{3}\Big\{C_{10}(\mathbf{1},\mathbf{2},\mathbf{3},\mathbf{1},\mathbf{4},\mathbf{5}) + C_{10}(\mathbf{2},\mathbf{1},\mathbf{3},\mathbf{1},\mathbf{4},\mathbf{5}) + C_{10}(\mathbf{3},\mathbf{1},\mathbf{2},\mathbf{1},\mathbf{4},\mathbf{5})\Big\} \tag{4.39a}$$

$$\tilde{C}_{11}(\mathbf{1},\mathbf{2},\mathbf{3},\mathbf{4},\mathbf{5}) := \frac{1}{3}\Big\{C_{11}(\mathbf{1},\mathbf{2},\mathbf{3},\mathbf{1},\mathbf{4},\mathbf{5}) + C_{11}(\mathbf{1},\mathbf{1},\mathbf{2},\mathbf{3},\mathbf{4},\mathbf{5}) + C_{11}(\mathbf{1},\mathbf{3},\mathbf{1},\mathbf{2},\mathbf{4},\mathbf{5})\Big\} \tag{4.39b}$$

which depend on four independent momentum arguments.

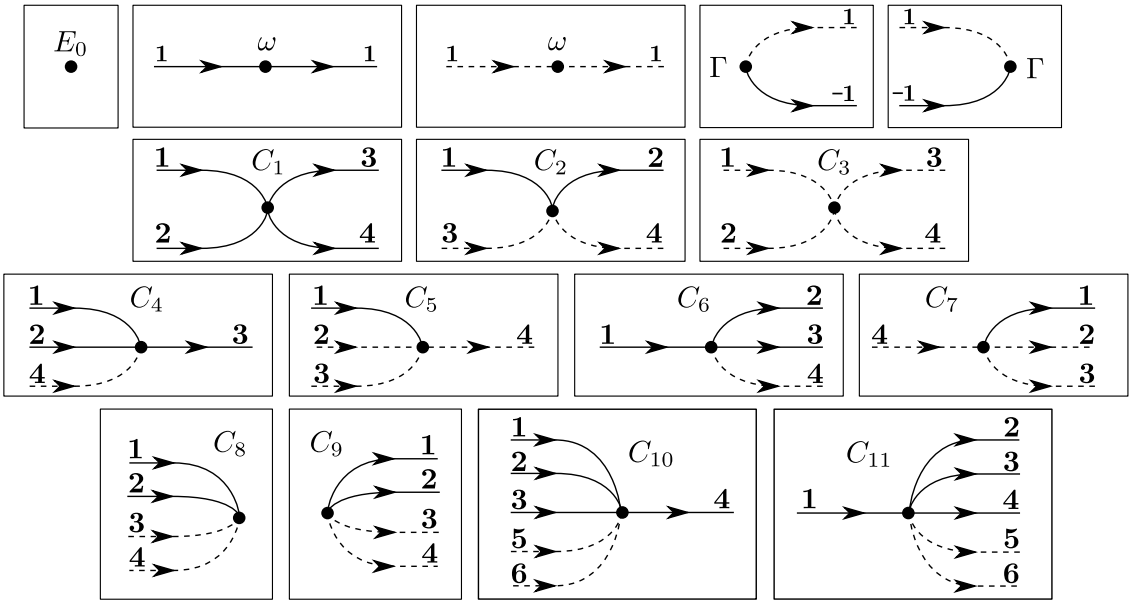

Figure 4.5: Diagrammtic representation of the operator terms in the Hamiltonian which are required to determine the perturbative flow for the ground state energy and the dispersion up to third order $\frac{1}{S}^3$

Ground state energy

The results for the ground state energy are compared to the perturbative corrections given in Ref. [193] and Ref. [194]. Note, that the authors use a different convention defining the leading terms in the Hamiltonian proportional to S^2 as the zeroth order, i.e., the third order contributions are referred to as fourth order spin wave theory.
For a direct comparison we consider the following relations

$$\delta e_b^{(3)} = \frac{1}{2N} E_{0,\text{eff}}^{(2)} \tag{4.40a}$$

$$\delta e_g^{(3)} = \frac{1}{2N} E_g^{(3)} \coloneqq S^2 \frac{\Delta E_g^{(-2)}}{N_{\text{sys}}} \tag{4.40b}$$

$$\delta e_f^{(3)} = \frac{1}{2N} E_f^{(3)} \coloneqq S^2 \frac{\Delta E_f^{(-2)}}{N_{\text{sys}}} \tag{4.40c}$$

$$\delta e_b^{(3)} = \frac{1}{2NS} E_b^{(3)} \coloneqq (2S)^2 \frac{\Delta E_b^{(-2)}}{N_{\text{sys}}} \tag{4.40d}$$

where $N_{\text{sys}} = 2N$ is the total number of A and B spins. The quantities $\Delta E_g^{(-2)}, \Delta E_f^{(-2)}, \Delta E_b^{(-2)}$ denote different diagrammatic contributions of the third order corrections to the ground state energy as defined in Ref. [194].
The analytical epCST results are given by

$$\begin{aligned}\frac{1}{S^3} E_f^{(3)} = \sum_{\mathbf{123456}} & \frac{8C_8(\mathbf{1,2,3,4})}{\omega_{\mathbf{1}}^{(0)} + \omega_{\mathbf{2}}^{(0)} + \omega_{\mathbf{3}}^{(0)} + \omega_{\mathbf{4}}^{(0)}} \delta_G(\mathbf{1+2+3+4}) \Big\{ \\ & \frac{C_1(\mathbf{5,6,1,2}) C_9(\mathbf{5,6,3,4})}{2\omega_{\mathbf{3}}^{(0)} + 2\omega_{\mathbf{4}}^{(0)} + \omega_{\mathbf{1}}^{(0)} + \omega_{\mathbf{2}}^{(0)} + \omega_{\mathbf{5}}^{(0)} + \omega_{\mathbf{6}}^{(0)}} \delta_G(\mathbf{5+6+3+4}) \\ & \frac{C_3(\mathbf{5,6,3,4}) C_9(\mathbf{1,2,5,6})}{2\omega_{\mathbf{1}}^{(0)} + 2\omega_{\mathbf{2}}^{(0)} + \omega_{\mathbf{3}}^{(0)} + \omega_{\mathbf{4}}^{(0)} + \omega_{\mathbf{5}}^{(0)} + \omega_{\mathbf{6}}^{(0)}} \delta_G(\mathbf{5+6+1+2}) \Big\}\end{aligned} \tag{4.41}$$

$$\begin{aligned}\frac{1}{S^3} E_g^{(3)} = \sum_{\mathbf{123456}} & \frac{16C_8(\mathbf{1,2,3,4})}{\omega_{\mathbf{1}}^{(0)} + \omega_{\mathbf{2}}^{(0)} + \omega_{\mathbf{3}}^{(0)} + \omega_{\mathbf{4}}^{(0)}} \delta_G(\mathbf{1+2+3+4}) \Big\{ \\ & \frac{C_2(\mathbf{5,2,6,4}) C_9(\mathbf{1,5,3,6})}{2\omega_{\mathbf{1}}^{(0)} + 2\omega_{\mathbf{3}}^{(0)} + \omega_{\mathbf{2}}^{(0)} + \omega_{\mathbf{4}}^{(0)} + \omega_{\mathbf{5}}^{(0)} + \omega_{\mathbf{6}}^{(0)}} \delta_G(\mathbf{5+6+1+3}) \Big\}\end{aligned} \tag{4.42}$$

The sums are evaluated for finite systems. To this end, we consider an equidistant discretization of the MBZ with $L \times L = N$ grid points and extrapolate the results by means of a polynomial fit $A_\infty + A_1(1/L) + A_2(1/L)^2 + \ldots A_n(1/L)^n$ with $n = 3$ or $n = 4$. The coefficients in the thermodynamic limit are then defined by the intersection point at $1/L = 0$ given by A_∞. Our results for (4.40b-4.40d) are displayed in Table 4.1.
The comparison between the epCST data and the results from Ref. [194] shows a very good agreement for all contributions, except for $\delta e_g^{(3)}$. The data suggest a factor of two between both results. In order to verify this assumption, we implement and evaluate the formulas given in

	energy correction$[10^{-5}J]$			
L	$\delta e_0^{(2)}$	$\delta e_b^{(3)}$	$\delta e_f^{(3)}$	$\delta e_g^{(3)}$
16	2.4840	−7.84668	9.3663	7.83334
20		−7.48871	9.7667	7.65402
24	2.3049	−7.28114	9.9936	7.53979
28		−7.15110	10.1338	7.46459
32	2.2364	−7.06459	10.2263	7.41307
40	2.2034	−6.96057	10.3366	7.34957
48	2.1852			
∞	2.143(3)	−6.77(8)	10.54(6)	7.23(5)
Ref.[194]	2.142(2)	−6.768(6)	10.54(4)	3.61(4)

Table 4.1: Comparison between the second and third order contributions to the ground state energy per spin obtained by epCST and diagrammatic perturbation theory from Ref.[194]. The results in the thermodnamic limit are highlighted in blue.

Ref. [194] for finite discretizations and, indeed, we find an exact factor of two. Moreover, we determine the analytical expressions by means of standard perturbation theory based on our notation. The results agree with the formulas obtained by the epCST approach. Thus, we assume that the factor of two is missing in the contribution $\Delta E_g^{(-2)}$ in Ref. [194].

Dispersion

Next, we compare the epCST data for the magnon dispersion with the results in Ref.[31]. For the second order corrections of the magnon dispersion we obtain

$$\frac{1}{S^2}\omega_{\mathbf{1}}^{(2)} = \sum_{\mathbf{234}} \frac{2\,C_4(\mathbf{2},\mathbf{3},\mathbf{1},\mathbf{4})\,C_6(\mathbf{1},\mathbf{2},\mathbf{3},\mathbf{4})}{\omega_{\mathbf{1}}^{(0)}-\omega_{\mathbf{2}}^{(0)}-\omega_{\mathbf{3}}^{(0)}-\omega_{\mathbf{4}}^{(0)}}\delta_G(\mathbf{1}-\mathbf{2}-\mathbf{3}-\mathbf{4}) + \frac{8\,C_9(\mathbf{1},\mathbf{2},\mathbf{3},\mathbf{4})\,C_8(\mathbf{1},\mathbf{2},\mathbf{3},\mathbf{4})}{\omega_{\mathbf{1}}^{(0)}+\omega_{\mathbf{2}}^{(0)}+\omega_{\mathbf{3}}^{(0)}+\omega_{\mathbf{4}}^{(0)}}\delta_G(\mathbf{1}+\mathbf{2}+\mathbf{3}+\mathbf{4}) \quad . \tag{4.43}$$

The third order corrections are given by $\frac{1}{S^3}\omega_1^{(3)} = \omega_1^a + \omega_1^b + \omega_1^c$ with

$$
\begin{aligned}
\omega_1^a = \sum_{345} & \frac{2\,C_4^0(\mathbf{3},\mathbf{4},\mathbf{1},\mathbf{5})}{\omega_4^{(0)} - \omega_1^{(0)} + \omega_3^{(0)} + \omega_5^{(0)}} \delta_G(\mathbf{1}\text{-}\mathbf{3}\text{-}\mathbf{4}\text{-}\mathbf{5}) \cdot \Bigg\{ \\
& \frac{A}{2} \frac{2\,C_6^0(\mathbf{3},\mathbf{4},\mathbf{1},\mathbf{5})}{\omega_3^{(0)} - \omega_1^{(0)} + \omega_4^{(0)} + \omega_5^{(0)}} \\
+ \sum_{67} & \frac{2\,C_1^0(\mathbf{6},\mathbf{7},\mathbf{3},\mathbf{4})\,C_6^0(\mathbf{1},\mathbf{6},\mathbf{7},\mathbf{5})}{2(\omega_5^{(0)} - \omega_1^{(0)}) + \omega_3^{(0)} + \omega_4^{(0)} + \omega_6^{(0)} + \omega_7^{(0)}} \delta_G(\mathbf{1}\text{-}\mathbf{5}\text{-}\mathbf{6}\text{-}\mathbf{7}) \\
& + \frac{2\,C_2^0(\mathbf{6},\mathbf{3},\mathbf{7},\mathbf{5})\,C_6^0(\mathbf{1},\mathbf{4},\mathbf{6},\mathbf{7})}{2(\omega_4^{(0)} - \omega_1^{(0)}) + \omega_3^{(0)} + \omega_5^{(0)} + \omega_6^{(0)} + \omega_7^{(0)}} \delta_G(\mathbf{1}\text{-}\mathbf{4}\text{-}\mathbf{6}\text{-}\mathbf{7}) \\
& + \frac{8\,C_4^0(\mathbf{1},\mathbf{6},\mathbf{3},\mathbf{7})\,C_9^0(\mathbf{4},\mathbf{6},\mathbf{5},\mathbf{7})}{\omega_4^{(0)} + \omega_5^{(0)} + \omega_6^{(0)} + \omega_7^{(0)}} \delta_G(\text{-}\mathbf{4}\text{-}\mathbf{5}\text{-}\mathbf{6}\text{-}\mathbf{7}) \\
& + \frac{2\,C_5^0(\mathbf{1},\mathbf{6},\mathbf{7},\mathbf{5})\,C_9^0(\mathbf{3},\mathbf{4},\mathbf{6},\mathbf{7})}{\omega_4^{(0)} + \omega_5^{(0)} + \omega_6^{(0)} + \omega_7^{(0)}} \delta_G(\text{-}\mathbf{3}\text{-}\mathbf{4}\text{-}\mathbf{6}\text{-}\mathbf{7}) \quad \Bigg\} \\
+ \sum_{345} & \delta_G(\mathbf{1}\text{-}\mathbf{3}\text{-}\mathbf{4}\text{-}\mathbf{5}) \frac{2\,C_6^0(\mathbf{3},\mathbf{4},\mathbf{1},\mathbf{5})}{\omega_3^{(0)} - \omega_1^{(0)} + \omega_4^{(0)} + \omega_5^{(0)}} \cdot \Bigg\{ \\
& \frac{A}{2} \frac{2\,C_4^0(\mathbf{3},\mathbf{4},\mathbf{1},\mathbf{5})}{\omega_4^{(0)} - \omega_1^{(0)} + \omega_3^{(0)} + \omega_5^{(0)}} \\
+ \sum_{67} & \frac{2\,C_1^0(\mathbf{3},\mathbf{4},\mathbf{6},\mathbf{7})\,C_4^0(\mathbf{6},\mathbf{7},\mathbf{1},\mathbf{5})}{2(\omega_5^{(0)} - \omega_1^{(0)}) + \omega_3^{(0)} + \omega_4^{(0)} + \omega_6^{(0)} + \omega_7^{(0)}} \delta_G(\mathbf{1}\text{-}\mathbf{5}\text{-}\mathbf{6}\text{-}\mathbf{7}) \\
& + \frac{2\,C_2^0(\mathbf{3},\mathbf{6},\mathbf{5},\mathbf{7})\,C_4^0(\mathbf{4},\mathbf{6},\mathbf{1},\mathbf{7})}{2(\omega_4^{(0)} - \omega_1^{(0)}) + \omega_3^{(0)} + \omega_5^{(0)} + \omega_6^{(0)} + \omega_7^{(0)}} \delta_G(\mathbf{1}\text{-}\mathbf{4}\text{-}\mathbf{6}\text{-}\mathbf{7}) \\
& + \frac{8\,C_6^0(\mathbf{1},\mathbf{6},\mathbf{3},\mathbf{7})\,C_8^0(\mathbf{4},\mathbf{6},\mathbf{5},\mathbf{7})}{\omega_4^{(0)} + \omega_5^{(0)} + \omega_6^{(0)} + \omega_7^{(0)}} \delta_G(\text{-}\mathbf{4}\text{-}\mathbf{5}\text{-}\mathbf{6}\text{-}\mathbf{7}) \\
& + \frac{2\,C_7^0(\mathbf{1},\mathbf{5},\mathbf{6},\mathbf{7})\,C_8^0(\mathbf{3},\mathbf{4},\mathbf{6},\mathbf{7})}{\omega_4^{(0)} + \omega_5^{(0)} + \omega_6^{(0)} + \omega_7^{(0)}} \delta_G(\text{-}\mathbf{3}\text{-}\mathbf{4}\text{-}\mathbf{6}\text{-}\mathbf{7}) \quad \Bigg\}
\end{aligned}
\tag{4.44}
$$

$$
\begin{aligned}
\omega_1^b = & \sum_{345} \frac{8\, C_8^0(1,3,4,5)}{\omega_1^{(0)}+\omega_3^{(0)}+\omega_4^{(0)}+\omega_5^{(0)}} \delta_G(\text{-}1\text{-}3\text{-}4\text{-}5) \cdot \Bigg\{ \\
& \frac{A}{2} \frac{8\, C_9^0(1,3,4,5)}{\omega_1^{(0)}+\omega_3^{(0)}+\omega_4^{(0)}+\omega_5^{(0)}} \\
& \sum_{67} \frac{2\, C_1^0(6,7,1,3)\, C_9^0(6,7,4,5)}{2(\omega_4^{(0)}+\omega_5^{(0)})+\omega_1^{(0)}+\omega_3+\omega_6^{(0)}+\omega_7^{(0)}} \delta_G(\text{-}4\text{-}5\text{-}6\text{-}7) \\
& \quad + \frac{2\, C_2^0(6,3,7,5)\, C_9^0(1,6,4,7)}{2\omega_1^{(0)}+2\omega_4^{(0)}+\omega_3^{(0)}+\omega_5^{(0)}+\omega_6^{(0)}+\omega_7^{(0)}} \delta_G(\text{-}1\text{-}4\text{-}6\text{-}7) \\
& \quad + \frac{2\, C_2^0(6,1,7,5)\, C_9^0(3,6,4,7)}{2\omega_3^{(0)}+2\omega_4^{(0)}+\omega_1^{(0)}+\omega_5^{(0)}+\omega_6^{(0)}+\omega_7^{(0)}} \delta_G(\text{-}3\text{-}4\text{-}6\text{-}7) \\
& \quad + \frac{2\, C_3^0(6,7,4,5)\, C_9^0(1,3,6,7)}{2\omega_1^{(0)}+2\omega_3^{(0)}+\omega_4^{(0)}+\omega_5^{(0)}+\omega_6^{(0)}+\omega_7^{(0)}} \delta_G(\text{-}3\text{-}4\text{-}6\text{-}7) \quad \Bigg\} \\
& \sum_{345} \frac{8\, C_9^0(1,3,4,5)}{\omega_1^{(0)}+\omega_3^{(0)}+\omega_4^{(0)}+\omega_5^{(0)}} \delta_G(\text{-}1\text{-}3\text{-}4\text{-}5) \cdot \Bigg\{ \\
& \frac{A}{2} \frac{8\, C_8^0(1,3,4,5)}{\omega_1^{(0)}+\omega_3^{(0)}+\omega_4^{(0)}+\omega_5^{(0)}} \\
& \sum_{67} \frac{2\, C_1^0(1,3,6,7)\, C_8^0(6,7,4,5)}{2\omega_4^{(0)}+2\omega_5^{(0)}+\omega_1^{(0)}+\omega_3^{(0)}+\omega_6^{(0)}+\omega_7^{(0)}} \delta_G(\text{-}4\text{-}5\text{-}6\text{-}7) \\
& \quad + \frac{2\, C_2^0(3,6,5,7)\, C_8^0(1,6,4,7)}{2\omega_1^{(0)}+\omega_4^{(0)}+\omega_3^{(0)}+\omega_5^{(0)}+\omega_6^{(0)}+\omega_7^{(0)}} \delta_G(\text{-}1\text{-}4\text{-}6\text{-}7) \\
& \quad + \frac{8\, C_2^0(1,6,5,7)\, C_8^0(3,6,4,7)}{+2\omega_3^{(0)}+2\omega_4^{(0)}+\omega_1^{(0)}+\omega_5^{(0)}+\omega_6^{(0)}+\omega_7^{(0)}} \delta_G(\text{-}3\text{-}4\text{-}6\text{-}7) \\
& \quad + \frac{2\, C_3^0(4,5,6,7)\, C_8^0(1,3,6,7)}{2\omega_1^{(0)}+2\omega_3^{(0)}+\omega_4^{(0)}+\omega_5^{(0)}+\omega_6^{(0)}+\omega_7^{(0)}} \delta_G(\text{-}3\text{-}4\text{-}6\text{-}7) \quad \Bigg\}
\end{aligned}
\tag{4.45}
$$

$$
\begin{aligned}
\omega_1^c = \sum_{34567} & \frac{4\,C_9^0(3,4,5,6)}{\omega_3^{(0)}+\omega_4^{(0)}+\omega_5^{(0)}+\omega_6^{(0)}}\delta_G(\text{-3-4-5-6})\cdot\Bigg\{ \\
& \frac{4\,C_1^0(3,4,1,7)\,C_8^0(1,7,5,6)}{2\omega_5^{(0)}+2\omega_6^{(0)}+\omega_1^{(0)}+\omega_3^{(0)}+\omega_4^{(0)}+\omega_7^{(0)}}\delta_G(\text{-1-5-6-7}) \\
& + \frac{8\,C_1^0(1,4,1,7)\,C_8^0(3,7,5,6)}{2\omega_3^{(0)}+2\omega_5^{(0)}+2\omega_6^{(0)}+\omega_4^{(0)}+\omega_7^{(0)}}\delta_G(\text{-3-4-6-7}) \\
& + \frac{4\,C_2^0(4,1,5,7)\,C_8^0(1,3,6,7)}{2\omega_3^{(0)}+2\omega_6^{(0)}+\omega_1^{(0)}+\omega_4^{(0)}+\omega_5^{(0)}+\omega_7^{(0)}}\delta_G(\text{-1-3-6-7}) \\
& + \frac{2\,C_2^0(1,1,5,7)\,C_8^0(3,4,6,7)}{2\omega_3^{(0)}+2\omega_4^{(0)}+2\omega_6^{(0)}+\omega_5^{(0)}+\omega_7^{(0)}}\delta_G(\text{-3-4-6-7})\Bigg\} \\
\sum_{34567} & \frac{4\,C_8^0(3,4,5,6)}{\omega_3^{(0)}+\omega_4^{(0)}+\omega_5^{(0)}+\omega_6^{(0)}}\delta_G(\text{-3-4-5-6})\cdot\Bigg\{ \\
& \frac{4\,C_1^0(1,7,3,4)\,C_9^0(1,7,5,6)}{2\omega_5^{(0)}+2\omega_6^{(0)}+\omega_1^{(0)}+\omega_3^{(0)}+\omega_4^{(0)}+\omega_7^{(0)}}\delta_G(\text{-1-5-6-7}) \\
& + \frac{8\,C_1^0(1,7,1,4)\,C_9^0(3,7,5,6)}{2\omega_3^{(0)}+2\omega_5^{(0)}+2\omega_6^{(0)}+\omega_4^{(0)}+\omega_7^{(0)}}\delta_G(\text{-3-4-6-7}) \\
& + \frac{4\,C_2^0(1,4,7,5)\,C_9^0(1,3,6,7)}{2\omega_3^{(0)}+2\omega_6^{(0)}+\omega_1^{(0)}+\omega_4^{(0)}+\omega_5^{(0)}+\omega_7^{(0)}}\delta_G(\text{-1-3-6-7}) \\
& + \frac{2\,C_2^0(1,1,7,5)\,C_9^0(3,4,6,7)}{2\omega_3^{(0)}+2\omega_4^{(0)}+2\omega_6^{(0)}+\omega_5^{(0)}+\omega_7^{(0)}}\delta_G(\text{-3-4-6-7})\Bigg\}
\end{aligned}
\tag{4.46}
$$

Similar to the evaluation of the ground state energy we calculate the sums for finite systems with an equidistant discretization of the MBZ and extrapolate the data in $1/L$ using a polynomial fit $A_\infty + A_1(1/L) + A_2(1/L)^2 + \ldots A_n(1/L)^n$ with $n = 4$.
The resulting second and third order contributions for selected momenta are shown in Table 4.2 and Table 4.3. Note, that the displayed margin of error does not correspond to the error of the least squares fit which is much smaller ($\sim$0.1%). Instead, we take into account that the results vary depending on which data points are included in the fitting procedure. The deviations are used to estimate the error of the finite size scaling.
As we can see the epCST data are in very good agreement with the results from Ref. [31]. We conclude, that the epCST approach indeed reproduces the correct results. In the next part, we examine the extrapolation in $(1/S)$ based on the deepCST method.

	k						
L	$(\frac{\pi}{4},0)$	$(\frac{\pi}{2},0)$	$(\frac{3\pi}{4},0)$	$(\pi,0)$	$(\frac{3\pi}{4},\frac{\pi}{4})$	$(\frac{\pi}{2},\frac{\pi}{2})$	$(\frac{3\pi}{4},\frac{3\pi}{4})$
8	0.01300	0.01744	0.01451	0.01078	0.01856	0.02638	0.01755
16	0.02092	0.02518	0.02193	0.01798	0.02617	0.03440	0.02542
24	0.02287	0.02705	0.02372	0.01972	0.02799	0.03630	0.02733
32	0.02363	0.02776	0.02440	0.02039	0.02869	0.03702	0.02807
40	0.02401	0.02812	0.02474	0.02072	0.02903	0.03737	0.02844
48	0.02422	0.02831	0.02492	0.02090	0.02922	0.03757	0.02864
56	0.02436	0.02843	0.02504	0.02102	0.02934	0.03769	0.02877
64	0.02444	0.02852	0.02512	0.02109	0.02942	0.03778	0.02885
∞	0.02477	0.02880	0.02538	0.02135	0.02968	0.03805	0.02915
Ref. [31]	0.02476	0.02879	0.02538	0.02134	0.02967	0.03805	0.02914

Table 4.2: Comparison between the second order contributions to the one-magnon dispersion obtained by epCST and diagrammatic perturbation theory from Ref.[31]. The results in the thermodnamic limit are highlighted in blue.

	k						
L	$(\frac{\pi}{4},0)$	$(\frac{\pi}{2},0)$	$(\frac{3\pi}{4},0)$	$(\pi,0)$	$(\frac{3\pi}{4},\frac{\pi}{4})$	$(\frac{\pi}{2},\frac{\pi}{2})$	$(\frac{3\pi}{4},\frac{3\pi}{4})$
8	−0.00996	−0.01027	−0.01632	−0.02094	−0.01187	−0.00264	−0.00747
16	−0.00589	−0.00655	−0.01364	−0.01889	−0.00861	0.00184	−0.00319
24	−0.00456	−0.00540	−0.01272	−0.01810	−0.00759	0.00310	−0.00188
32	−0.00401	−0.00493	−0.01234	−0.01776	−0.00717	0.00361	−0.00134
40	−0.00372	−0.00469	−0.01215	−0.01759	−0.00696	0.00386	−0.00106
∞	−0.0031(4)	−0.0042(2)	−0.0118(2)	−0.0172(2)	−0.0065(2)	0.0044(3)	−0.0005(1)
Ref. [31]	−0.0033(3)	−0.0042(1)	−0.0118(1)	−0.0172(1)	−0.0065(1)	0.0043(1)	−0.0005(1)

Table 4.3: Comparison between the third order contributions to the one-magnon dispersion obtained by epCST and diagrammatic perturbation theory from Ref.[31]. The results in the thermodnamic limit are highlighted in blue.

Non-perturbative analysis (deepCST)

In the following we extrapolate the $1/S$ expansion using the deepCST method. For this purpose, we directly integrate the flow equations in a self consistent way by means of a Runge-Kutta-Fehlberg 4(5) method. For methodical details the reader is referred to section 3.2.1 and section 2.2.3.
In contrast to the perturbative flow equations, there is no exact solution for the deepCST. Therefore, we have to track the ℓ dependent coefficients for each discretization point. The most expensive terms are the reduced vertex functions of the hexatic operators. They depend on four momentum arguments. Consequently, the maximum number of discretization points for these coefficients grows as $\mathcal{O}(N^4)$.
The maximum system size is limited by memory usage. If we take into account the contributions of the hexatic operators the maximum system size is restricted to $L = 10$. We also perform calculations up to a system size of $L = 12$ for which we neglect the hexatic terms.
Moreover, we improve the computational efficiency by exploiting the symmetries the vertex functions given in (4.25a–4.25d).
We are mainly interested in the magnon dip at the boundary of the MBZ. Thus, we only consider the maximum magnon energy at the momentum $\mathbf{k}_{\text{max}} = (\pi/2, \pi/2)$ and the local minimum of the dispersion located at $\mathbf{k}_{\text{min}} = (\pi, 0)$. The dip is then quantified by

$$\delta_{\text{dip}} = 1 - \frac{\omega(\mathbf{k}_{\text{min}})}{\omega(\mathbf{k}_{\text{max}})} \quad . \tag{4.47}$$

The results of the deepCST for the dispersion at both momenta are displayed in Figure 4.6.
For the thermodynamic limit we find a dip of $\delta_{\text{dip}} \approx 5.2\%$ which is a considerable improvement compared to the perturbative result $\delta_{\text{dip}} \approx 3.1\%$.
Nevertheless, there is still an significant deviation at $\mathbf{k}_{\text{min}} = (\pi, 0)$ from the results of quantum Monte Carlo simulations [25] and series expansions about the Ising limit [26]. The deviation even increases for larger system size.
These results indicate that the truncation in the parameter $1/S$ is indeed not appropriate to capture all relevant processes required for a quantitative description of the dip.
On the one hand the truncated flow equations for the dispersion do not comprise a renormalization of the two-magnon interaction (described by the coefficients C_1,C_2 and C_3). This renormalization first contributes at fourth order $\mathcal{O}(1/S^4)$ but it may be important for short wavelength magnons at higher energies.[6] On the other hand the truncation at higher orders in $1/S$ gives rise to additional contributions from hexatic operators which are computationally expensive. Moreover, the deepCST data clearly show that the effects of the hexatic terms are negligible.
We assume that the truncation by means of scaling dimension of operator terms is better suited for the derivation of an effective magnon description. A detailed analysis of an effective magnon description for scaling dimension $d = 2$ is presented in the following.

[6] For a more detailed discussion about this issue see section 4.4.2

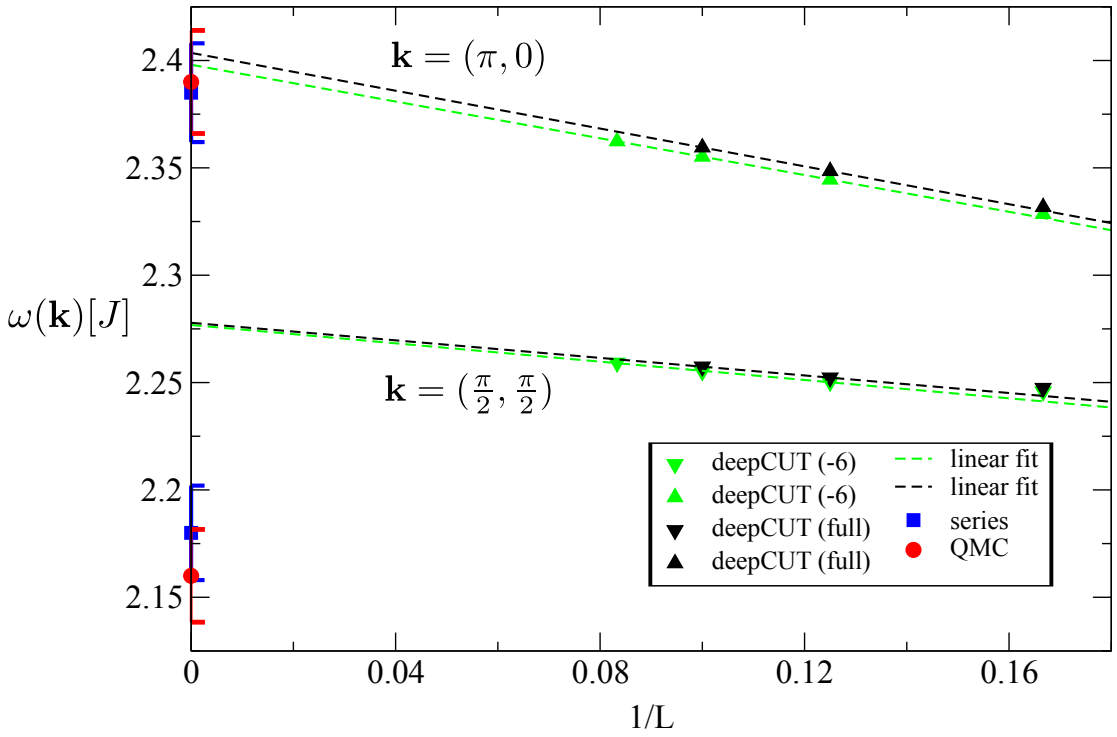

Figure 4.6: Extrapolation of the dispersion obtained by the deepCST in $(1/S)^3$ at momenta $(\pi, 0)$ and $(\pi/2, \pi/2)$. The green triangles show to the deepCST data where we neglected the hexatic term, whereas the black triangles depict the results of the full deepCST. The results are compared to quantum Monte Carlo simulations (QMC) [25] and series expansions about the Ising limit [26].

4.3 Effective spin wave theory

In this section an effective spin wave model is derived by means of a magnon conserving CST. In contrast to the conventional spin wave approach, the flow equations are not truncated by powers of the parameter $1/S$. Instead, we use the scaling dimension of operator terms to define a hierarchy of magnon processes. As we will discuss in the following, this approach incorporates the renormalization of the magnon interaction which turns out to be essential for the quantitative description of magnon dynamics at short wavelengths. The CST method and its diagrammatic representation enable us to identify and visualize all relevant processes.
Moreover, we derive the effective observables of the static and dynamic structure factors which are required for a direct comparison with the experimental data of inelastic neutron scattering.
The first section describes the truncation of the Hamiltonian and the observables based on the scaling dimension of operator terms.
The resulting flow equations are presented and examined in the second section. In addition, we discuss some technical aspects regarding the numerical evaluation.
The third section deals with the evaluation of the dynamic structure factors.
In the final section we present and discuss our main results.

4.3.1 Truncation

Hamiltonian: scaling dimension

As we discussed in section 2.5 the scaling dimension of the operators terms is determined by the dimensional contribution of the bosonic operators and the scaling behavior of the coefficient function in the limit of small momenta. The coefficient functions of terms which are contained by the initial Hamiltonian are known analytically and, thus, their scaling dimension can be directly identified. For instance, the dispersion is $\omega = v_c |\mathbf{k}|$ for $\mathbf{k} \ll 1$ so that the single magnon terms have scaling dimension $d = 1$.
The quartic operator terms have scaling dimension $d = 2$ because the vertex functions are essentially bounded, i.e., $c = 0$ (see 4.26). Thus, keeping only operator terms with scaling dimension $d = 1$ corresponds to the next-leading order spin wave theory.
The main idea is to include all operator terms with scaling dimension $d = 2$ based on a self similar CST approach. To this end, we also have to determine the scaling dimension of operator terms which arise in the commutator of the flow equation and which are not part of the initial Hamiltonian. In this case, the corresponding coefficient functions are not known analytically. Their scaling dimension is determined by their leading order behavior in the flow as defined in (2.69).
For the Hamiltonian at hand one has to examine the coefficients of the Bogoliubov terms $\Gamma(\mathbf{k})$ and the hexatic terms, i.e. terms with six bosonic creation or annihilation operators which arise in commutators between quartic operator terms.
The leading order contribution to the Bogoliubov coefficient in the flow is given by

$$\begin{aligned}\Delta\Gamma(\mathbf{1}) = \sum_{234} &(-8) C_6(\mathbf{1},\mathbf{2},\mathbf{3},\mathbf{4})\, C_8(\mathbf{2},\mathbf{3},\text{-}\mathbf{1},\mathbf{4})\, \delta_G(\mathbf{1}-\mathbf{2}-\mathbf{3}-\mathbf{4}) + \\ &(-8) C_7(\mathbf{2},\text{-}\mathbf{1},\mathbf{3},\mathbf{4})\, C_8(\mathbf{1},\mathbf{2},\mathbf{3},\mathbf{4})\, \delta_G(\mathbf{1}+\mathbf{2}+\mathbf{3}+\mathbf{4}) \quad . \end{aligned} \tag{4.48}$$

This integral (or sum) can be evaluated numerically. Its momentum dependence for small momenta $\mathbf{k}_1$ is shown in Figure 4.7 for two distinct directions. We conclude that the coefficient is linear for small momenta $\Gamma(\mathbf{1}) \propto |k_1|$. Therefore, it has scaling dimension $d = 1$.
For the hexatic terms this graphical analysis is intricate because they depend on five independent momentum arguments, i.e. the vertex functions have a ten dimensional domain. However, we can determine their scaling dimension by means of general arguments.
The leading order of the hexatic vertex function in the flow is essentially given by products of two quartic vertex functions with no additional integration over momenta. Thus, we expect the hexatic terms to be bounded at small momenta, i.e. $c = 0$, exhibiting scaling dimension $d = 4$. As we keep operator terms with a scaling dimension up to $d = 2$ we may discard the hexatic terms. This is also consistent with the observations in section 4.2.3 which show that the contributions of the hexatic terms are small compared to the effects of the quartic terms.
The resulting flowing Hamiltonian reads

$$\begin{aligned} H(\ell) = E_0 + \sum_{1} \quad & \omega(\mathbf{1})\left(\alpha_1^\dagger \alpha_1 + \beta_1^\dagger \beta_1\right) + \Gamma(\mathbf{1})\left(\alpha_1^\dagger \beta_{-1}^\dagger + \alpha_1 \beta_{-1}\right) \\ + \sum_{1,2,3,4} \Big\{ & C_1(\mathbf{1},\mathbf{2},\mathbf{3},\mathbf{4})\, \alpha_1^\dagger \alpha_2^\dagger \alpha_3 \alpha_4 + C_2(\mathbf{1},\mathbf{2},\mathbf{3},\mathbf{4})\, \alpha_1^\dagger \alpha_2 \beta_3^\dagger \beta_4 \\ & + C_3(\mathbf{1},\mathbf{2},\mathbf{3},\mathbf{4})\, \beta_1^\dagger \beta_2^\dagger \beta_3 \beta_4 + C_4(\mathbf{1},\mathbf{2},\mathbf{3},\mathbf{4})\, \alpha_1^\dagger \alpha_2^\dagger \alpha_3 \beta_4^\dagger \\ & + C_5(\mathbf{1},\mathbf{2},\mathbf{3},\mathbf{4})\, \alpha_1^\dagger \beta_2^\dagger \beta_3^\dagger \beta_4 + C_6(\mathbf{1},\mathbf{2},\mathbf{3},\mathbf{4})\, \alpha_1^\dagger \alpha_2 \alpha_3 \beta_4 \\ & + C_7(\mathbf{1},\mathbf{2},\mathbf{3},\mathbf{4})\, \alpha_1 \beta_2^\dagger \beta_3 \beta_4 + C_8(\mathbf{1},\mathbf{2},\mathbf{3},\mathbf{4})\, \alpha_1^\dagger \alpha_2^\dagger \beta_3^\dagger \beta_4^\dagger \\ & + C_9(\mathbf{1},\mathbf{2},\mathbf{3},\mathbf{4})\, \alpha_1 \alpha_2 \beta_3 \beta_4 \Big\} \quad . \end{aligned} \tag{4.49}$$

The flowing generator is then given by

$$\begin{aligned} \eta(\ell) = \sum_{1} \quad & \Gamma(\mathbf{1})\left(\alpha_1^\dagger \beta_{-1}^\dagger - \alpha_1 \beta_{-1}\right) \\ + \sum_{1,2,3,4} \Big\{ & C_4(\mathbf{1},\mathbf{2},\mathbf{3},\mathbf{4})\, \alpha_1^\dagger \alpha_2^\dagger \alpha_3 \beta_4^\dagger + C_5(\mathbf{1},\mathbf{2},\mathbf{3},\mathbf{4})\, \alpha_1^\dagger \beta_2^\dagger \beta_3^\dagger \beta_4 \\ & - C_6(\mathbf{1},\mathbf{2},\mathbf{3},\mathbf{4})\, \alpha_1^\dagger \alpha_2 \alpha_3 \beta_4 - C_7(\mathbf{1},\mathbf{2},\mathbf{3},\mathbf{4})\, \alpha_1 \beta_2^\dagger \beta_3 \beta_4 \\ & + C_8(\mathbf{1},\mathbf{2},\mathbf{3},\mathbf{4})\, \alpha_1^\dagger \alpha_2^\dagger \beta_3^\dagger \beta_4^\dagger - C_9(\mathbf{1},\mathbf{2},\mathbf{3},\mathbf{4})\, \alpha_1 \alpha_2 \beta_3 \beta_4 \Big\} \quad . \end{aligned} \tag{4.50}$$

The coefficients E_0, $\omega(\mathbf{1})$, $\Gamma(\mathbf{1})$, and $C_i(\mathbf{1},\mathbf{2},\mathbf{3},\mathbf{4})$ depend on the flow parameter ℓ and satisfy the initial conditions

$$E_0\big|_{\ell=0} = -2J(S^2 + SA + A^2/(4)) \tag{4.51a}$$

$$\omega(\mathbf{1})\big|_{\ell=0} = 2J(2S+A)\sqrt{1-\gamma(\mathbf{1})^2} \tag{4.51b}$$

$$\Gamma(\mathbf{1})\big|_{\ell=0} = 0 \tag{4.51c}$$

$$C_1(\mathbf{1},\mathbf{2},\mathbf{3},\mathbf{4})\big|_{\ell=0} = -l_1 l_2 l_3 l_4 \frac{J}{N} V^{(1)}_{1234}\delta_G(1+2-3-4) \tag{4.51d}$$

$$C_2(\mathbf{1},\mathbf{2},\mathbf{3},\mathbf{4})\big|_{\ell=0} = -4l_1 l_2 l_3 l_4 \frac{J}{N} V^{(4)}_{1\text{-}42\text{-}3}\delta_G(1-2+3-4) \tag{4.51e}$$

$$C_3(\mathbf{1},\mathbf{2},\mathbf{3},\mathbf{4})\big|_{\ell=0} = -l_1 l_2 l_3 l_4 \frac{J}{N} V^{(9)}_{\text{-}4\text{-}3\text{-}2\text{-}1}\delta_G(1+2-3-4) \tag{4.51f}$$

$$C_4(\mathbf{1},\mathbf{2},\mathbf{3},\mathbf{4})\big|_{\ell=0} = -2l_1 l_2 l_3 l_4 \frac{J}{N} V^{(3)}_{12\text{-}43}\delta_G(1+2-3+4) \tag{4.51g}$$

$$C_5(\mathbf{1},\mathbf{2},\mathbf{3},\mathbf{4})\big|_{\ell=0} = -2l_1 l_2 l_3 l_4 \frac{J}{N} V^{(6)}_{\text{-}4\text{-}1\text{-}2\text{-}3}\delta_G(1+2+3-4) \tag{4.51h}$$

$$C_6(\mathbf{1},\mathbf{2},\mathbf{3},\mathbf{4})\big|_{\ell=0} = -2l_1 l_2 l_3 l_4 \frac{J}{N} V^{(2)}_{1\text{-}423}\delta_G(1-2-3-4) \tag{4.51i}$$

$$C_7(\mathbf{1},\mathbf{2},\mathbf{3},\mathbf{4})\big|_{\ell=0} = -2l_1 l_2 l_3 l_4 \frac{J}{N} V^{(5)}_{\text{-}4\text{-}31\text{-}2}\delta_G(-1+2-3-4) \tag{4.51j}$$

$$C_8(\mathbf{1},\mathbf{2},\mathbf{3},\mathbf{4})\big|_{\ell=0} = -l_1 l_2 l_3 l_4 \frac{J}{N} V^{(7)}_{12\text{-}3\text{-}4}\delta_G(1+2+3+4) \tag{4.51k}$$

$$C_9(\mathbf{1},\mathbf{2},\mathbf{3},\mathbf{4})\big|_{\ell=0} = -l_1 l_2 l_3 l_4 \frac{J}{N} V^{(8)}_{\text{-}3\text{-}412}\delta_G(-1-2-3-4) \tag{4.51l}$$

The diagrammatic representations of all relevant operator terms in the flowing Hamiltonian are depicted in Figure 4.8. The resulting flow equations are illustrated and discussed in section 4.3.2. They are also given in standard notation in Appendix B.2.
In the next section, we disuss the truncation of the observables.

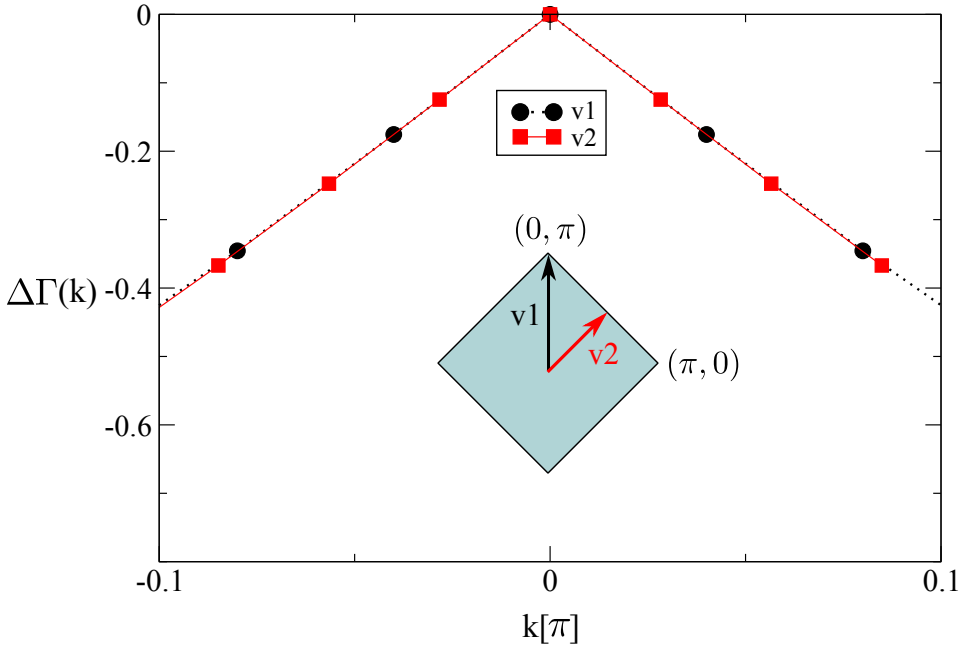

Figure 4.7: The momentum dependence of the Bogoliubov coefficient in the leading order of $d\ell$ along two distinct directions in the MBZ is displayed. Both directions are parametrized by k where $|k|$ is the length of the corresponding momentum vector.

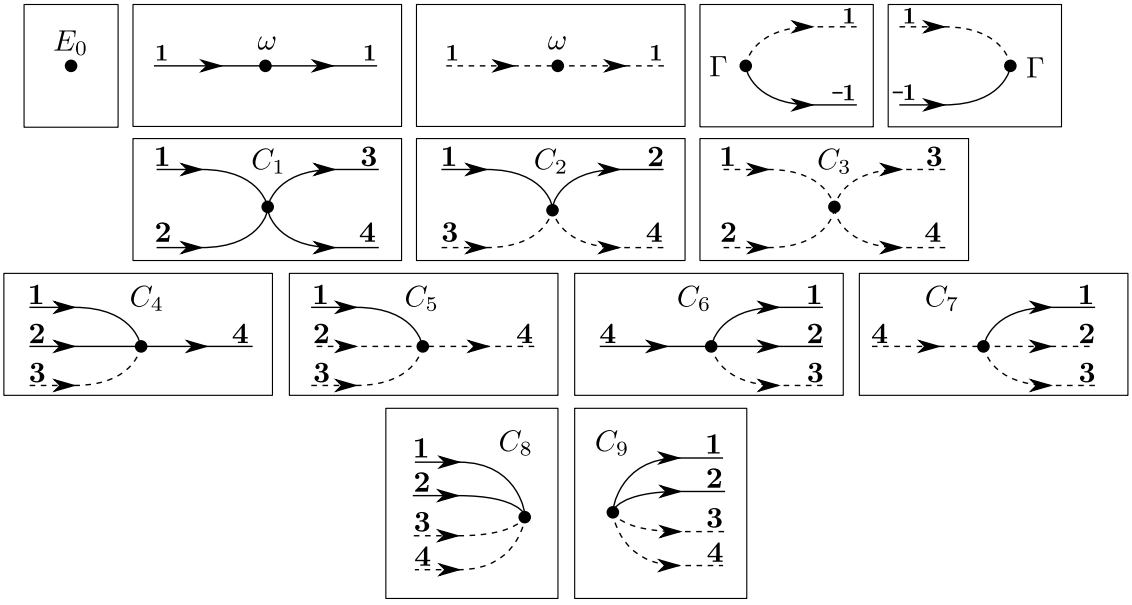

Figure 4.8: Diagrammtic representation of the operator terms in the Hamiltonian with a scaling dimension up to $d = 2$.

Observables

Similar to the Hamiltonian, the observables have to be truncated as well. However, the corresponding spin operators are not evaluated directly but as a part of a resolvent. Hence, we do not truncate the spin operators in terms of scaling dimension. Instead, we keep those terms which couple the ground state to the relevant magnon channels. As we are interested in the subspaces up to three magnons, we include operator terms up to a cubic level in annihilation and creation operators. The flowing observables are then given by

$$\begin{aligned} S^z_{\mathbf{Q}} = \sum_{\mathbf{1,2}} \Big\{ \quad & s^z_1(\mathbf{Q},\mathbf{1},\mathbf{2})\, \alpha^\dagger_{\mathbf{1}} \alpha_{\mathbf{2}} + s^z_2(\mathbf{Q},\mathbf{1},\mathbf{2})\, \beta^\dagger_{\mathbf{1}} \beta_{\mathbf{2}} \\ & + s^z_3(\mathbf{Q},\mathbf{1},\mathbf{2})\, \alpha_{\mathbf{1}} \beta_{\mathbf{2}} + s^z_4(\mathbf{Q},\mathbf{1},\mathbf{2})\, \alpha^\dagger_{\mathbf{1}} \beta^\dagger_{\mathbf{2}} \quad \Big\} + C(\mathbf{Q}) \end{aligned} \tag{4.52}$$

with initial conditions

$$s^z_1(\mathbf{Q},\mathbf{1},\mathbf{2})|_{\ell=0} = \quad \delta_G(\mathbf{Q}+\mathbf{1}-\mathbf{2}) \left[\Gamma_{\mathbf{Q}+\mathbf{1}-\mathbf{2}} l_{\mathbf{1}} l_{\mathbf{2}} - m_{\mathbf{1}} m_{\mathbf{2}} \right] \tag{4.53a}$$

$$s^z_2(\mathbf{Q},\mathbf{1},\mathbf{2})|_{\ell=0} = \quad \delta_G(\mathbf{Q}+\mathbf{1}-\mathbf{2}) \left[\Gamma_{\mathbf{Q}+\mathbf{1}-\mathbf{2}} m_{\mathbf{1}} m_{\mathbf{2}} - l_{\mathbf{1}} l_{\mathbf{2}} \right] \tag{4.53b}$$

$$s^z_3(\mathbf{Q},\mathbf{1},\mathbf{2})|_{\ell=0} = \quad \delta_G(\mathbf{Q}-\mathbf{1}-\mathbf{2}) \left[\Gamma_{\mathbf{Q}-\mathbf{1}-\mathbf{2}} m_{\mathbf{1}} l_{\mathbf{2}} - l_{\mathbf{1}} m_{\mathbf{2}} \right] \tag{4.53c}$$

$$s^z_4(\mathbf{Q},\mathbf{1},\mathbf{2})|_{\ell=0} = \quad \delta_G(\mathbf{Q}+\mathbf{1}+\mathbf{2}) \left[\Gamma_{\mathbf{Q}+\mathbf{1}+\mathbf{2}} m_{\mathbf{1}} l_{\mathbf{2}} - m_{\mathbf{1}} l_{\mathbf{2}} \right] \tag{4.53d}$$

$$C(\mathbf{Q})|_{\ell=0} = \left(m_Q^2 - SN \right) \left(\Gamma_{\mathbf{Q}} - 1 \right) \delta_G(\mathbf{Q}) \tag{4.53e}$$

,

$$\begin{aligned} S^+_{\mathbf{Q}} = {} & s^+_1(\mathbf{Q})\, \alpha_{\text{-}\mathbf{Q}} + s^+_2(\mathbf{Q})\, \beta^\dagger_{\mathbf{Q}} \\ & + \sum_{\mathbf{1,2,3}} \Big\{ \quad s^+_3(\mathbf{Q},\mathbf{1},\mathbf{2},\mathbf{3})\, \beta^\dagger_{\mathbf{1}} \beta^\dagger_{\mathbf{2}} \beta_{\mathbf{3}} + s^+_4(\mathbf{Q},\mathbf{1},\mathbf{2},\mathbf{3})\, \alpha^\dagger_{\mathbf{1}} \alpha_{\mathbf{2}} \alpha_{\mathbf{3}} \\ & \quad + s^+_5(\mathbf{Q},\mathbf{1},\mathbf{2},\mathbf{3})\, \alpha^\dagger_{\mathbf{1}} \beta^\dagger_{\mathbf{2}} \beta^\dagger_{\mathbf{3}} + s^+_6(\mathbf{Q},\mathbf{1},\mathbf{2},\mathbf{3})\, \alpha_{\mathbf{1}} \beta^\dagger_{\mathbf{2}} \beta_{\mathbf{3}} \\ & \quad + s^+_7(\mathbf{Q},\mathbf{1},\mathbf{2},\mathbf{3})\, \alpha^\dagger_{\mathbf{1}} \alpha_{\mathbf{2}} \beta^\dagger_{\mathbf{3}} + s^+_8(\mathbf{Q},\mathbf{1},\mathbf{2},\mathbf{3})\, \alpha_{\mathbf{1}} \alpha_{\mathbf{2}} \beta_{\mathbf{3}} \quad \Big\} \end{aligned} \tag{4.54}$$

with initial conditions

$$s_1^+(\mathbf{Q})|_{\ell=0} = \sqrt{2SN}\left(1-\frac{1}{SN}\sum_{\mathbf{k}} m_{\mathbf{k}}^2\right)\left(l_{\mathbf{Q}} + \Gamma_{\mathbf{Q}}\, m_{\mathbf{Q}}\right) \tag{4.55a}$$

$$s_2^+(\mathbf{Q})|_{\ell=0} = \sqrt{2SN}\left(1-\frac{1}{SN}\sum_{\mathbf{k}} m_{\mathbf{Q}}^2\right)\left(m_{\mathbf{Q}} + \Gamma_{\mathbf{Q}}\, l_{\mathbf{Q}}\right) \tag{4.55b}$$

$$s_3^+(\mathbf{Q},\mathbf{1},\mathbf{2},\mathbf{3})|_{\ell=0} = \delta_G(\mathbf{Q}+\mathbf{1}+\mathbf{2}-\mathbf{3})\left[m_1 m_2 m_3 + \Gamma_{\mathbf{Q}+\mathbf{1}+\mathbf{2}-\mathbf{3}}\, l_1 l_2 l_3\right] \tag{4.55c}$$

$$s_4^+(\mathbf{Q},\mathbf{1},\mathbf{2},\mathbf{3})|_{\ell=0} = \delta_G(\mathbf{Q}+\mathbf{1}-\mathbf{2}-\mathbf{3})\left[l_1 l_2 l_3 + \Gamma_{\mathbf{Q}+\mathbf{1}-\mathbf{2}-\mathbf{3}}\, m_1 m_2 m_3\right] \tag{4.55d}$$

$$s_5^+(\mathbf{Q},\mathbf{1},\mathbf{2},\mathbf{3})|_{\ell=0} = \delta_G(\mathbf{Q}+\mathbf{1}+\mathbf{2}+\mathbf{3})\left[l_1 m_2 m_3 + \Gamma_{\mathbf{Q}+\mathbf{1}+\mathbf{2}+\mathbf{3}}\, m_1 m_2 l_3\right] \tag{4.55e}$$

$$s_6^+(\mathbf{Q},\mathbf{1},\mathbf{2},\mathbf{3})|_{\ell=0} = 2\,\delta_G(\mathbf{Q}-\mathbf{1}+\mathbf{2}-\mathbf{3})\left[l_1 l_2 l_3 + \Gamma_{\mathbf{Q}-\mathbf{1}+\mathbf{2}-\mathbf{3}}\, m_1 m_2 m_3\right] \tag{4.55f}$$

$$s_7^+(\mathbf{Q},\mathbf{1},\mathbf{2},\mathbf{3})|_{\ell=0} = 2\,\delta_G(\mathbf{Q}+\mathbf{1}-\mathbf{2}+\mathbf{3})\left[l_1 l_2 l_3 + \Gamma_{\mathbf{Q}+\mathbf{1}-\mathbf{2}+\mathbf{3}}\, m_1 m_2 m_3\right] \tag{4.55g}$$

$$s_8^+(\mathbf{Q},\mathbf{1},\mathbf{2},\mathbf{3})|_{\ell=0} = \delta_G(\mathbf{Q}-\mathbf{1}-\mathbf{2}-\mathbf{3})\left[l_1 l_2 l_3 + \Gamma_{\mathbf{Q}-\mathbf{1}-\mathbf{2}-\mathbf{3}}\, m_1 m_2 m_3\right] \tag{4.55h}$$

and

$$\begin{aligned} S_{\mathbf{Q}}^- = {} & s_1^-(\mathbf{Q})\,\alpha_{\mathbf{Q}}^\dagger + s_2^-(\mathbf{Q})\,\beta_{\text{-}\mathbf{Q}} \\ & + \sum_{\mathbf{1},\mathbf{2},\mathbf{3}}\Big\{\; s_3^-(\mathbf{Q},\mathbf{1},\mathbf{2},\mathbf{3})\,\alpha_1^\dagger\alpha_2^\dagger\beta_3^\dagger + s_4^-(\mathbf{Q},\mathbf{1},\mathbf{2},\mathbf{3})\,\alpha_1^\dagger\alpha_2^\dagger\alpha_3 \\ & \qquad + s_5^-(\mathbf{Q},\mathbf{1},\mathbf{2},\mathbf{3})\,\alpha_1^\dagger\beta_2^\dagger\beta_3 + s_6^-(\mathbf{Q},\mathbf{1},\mathbf{2},\mathbf{3})\,\alpha_1^\dagger\alpha_2\beta_3 \\ & \qquad + s_7^-(\mathbf{Q},\mathbf{1},\mathbf{2},\mathbf{3})\,\beta_1^\dagger\beta_2\beta_3 + s_8^-(\mathbf{Q},\mathbf{1},\mathbf{2},\mathbf{3})\,\alpha_1\beta_2\beta_3 \;\Big\} \end{aligned} \tag{4.56}$$

with initial conditions

$$s_1^-(\mathbf{Q})|_{\ell=0} = \sqrt{2SN}\left(l_{\mathbf{Q}} + \Gamma_{\mathbf{Q}}\, m_{\mathbf{Q}}\right) \tag{4.57a}$$

$$s_2^-(\mathbf{Q})|_{\ell=0} = \sqrt{2SN}\left(m_{\mathbf{Q}} + \Gamma_{\mathbf{Q}}\, l_{\mathbf{Q}}\right) \tag{4.57b}$$

$$s_3^-(\mathbf{Q},\mathbf{1},\mathbf{2},\mathbf{3})|_{\ell=0} = 0 \tag{4.57c}$$

$$s_4^-(\mathbf{Q},\mathbf{1},\mathbf{2},\mathbf{3})|_{\ell=0} = 0 \tag{4.57d}$$

$$s_5^-(\mathbf{Q},\mathbf{1},\mathbf{2},\mathbf{3})|_{\ell=0} = 0 \tag{4.57e}$$

$$s_6^-(\mathbf{Q},\mathbf{1},\mathbf{2},\mathbf{3})|_{\ell=0} = 0 \tag{4.57f}$$

$$s_7^-(\mathbf{Q},\mathbf{1},\mathbf{2},\mathbf{3})|_{\ell=0} = 0 \tag{4.57g}$$

$$s_8^-(\mathbf{Q},\mathbf{1},\mathbf{2},\mathbf{3})|_{\ell=0} = 0 \quad . \tag{4.57h}$$

The flow of $C(Q)$ does not influence the remaining coefficients of the observables and it is not required in the evaluation of the relevant resolvents. Thus, it is not considered in the

flow equations. The diagrammatic representation of the operator terms in the flowing observables is displayed in Figure 4.9. Note, that the observables transfer momentum $\mathbf{Q}$ into the system. Consequently, the total momentum is not conserved at the vertices of the corresponding diagrams. Instead, the sum over momenta of in and out-going lines is given by $\mathbf{Q}$ modulo reciprocal lattice vectors. The observables $S^+_{\mathbf{Q}}, S^-_{\mathbf{Q}}$ and $S^z_{\mathbf{Q}}$ are transformed for all momenta in the first Brillouin zone $Q \in 1^{\text{st}}$ BZ because their values in the first and second MBZ differ due to Umklapp processes.
Similar to the coefficients of the Hamiltonian, the observable coefficients exhibit certain symmetries given by the following relations

$$s^z_2(\mathbf{Q},\mathbf{1},\mathbf{2}) = s^z_1(\text{-}\mathbf{Q},\mathbf{2},\mathbf{1})\,\Gamma_{\mathbf{Q}+\mathbf{1}-\mathbf{2}} \tag{4.58a}$$
$$s^z_3(\mathbf{Q},\mathbf{1},\mathbf{2}) = s^z_4(\text{-}\mathbf{Q},\mathbf{2},\mathbf{1})\,\Gamma_{\mathbf{Q}+\mathbf{1}-\mathbf{2}} \tag{4.58b}$$
$$s^+_2(\mathbf{Q}) = s^+_1(\text{-}\mathbf{Q})\,\Gamma_{\mathbf{Q}-\bar{\mathbf{Q}}} \tag{4.58c}$$
$$s^+_4(\mathbf{Q},\mathbf{1},\mathbf{2},\mathbf{3}) = s^+_3(\text{-}\mathbf{Q},\mathbf{3},\mathbf{2},\mathbf{1})\,\Gamma_{\mathbf{Q}+\mathbf{1}-\mathbf{2}-\mathbf{3}} \tag{4.58d}$$
$$s^+_8(\mathbf{Q},\mathbf{1},\mathbf{2},\mathbf{3}) = s^+_5(\text{-}\mathbf{Q},\mathbf{3},\mathbf{2},\mathbf{1})\,\Gamma_{\mathbf{Q}-\mathbf{1}-\mathbf{2}-\mathbf{3}} \tag{4.58e}$$
$$s^+_7(\mathbf{Q},\mathbf{1},\mathbf{2},\mathbf{3}) = s^+_6(\text{-}\mathbf{Q},\mathbf{3},\mathbf{2},\mathbf{1})\,\Gamma_{\mathbf{Q}+\mathbf{1}-\mathbf{2}+\mathbf{3}} \tag{4.58f}$$
$$s^-_2(\mathbf{Q}) = s^-_1(\text{-}\mathbf{Q})\,\Gamma_{\mathbf{Q}-\bar{\mathbf{Q}}} \tag{4.58g}$$
$$s^-_8(\mathbf{Q},\mathbf{1},\mathbf{2},\mathbf{3}) = s^-_3(\text{-}\mathbf{Q},\mathbf{3},\mathbf{2},\mathbf{1})\,\Gamma_{\mathbf{Q}-\mathbf{1}-\mathbf{2}-\mathbf{3}} \tag{4.58h}$$
$$s^-_7(\mathbf{Q},\mathbf{1},\mathbf{2},\mathbf{3}) = s^-_4(\text{-}\mathbf{Q},\mathbf{3},\mathbf{2},\mathbf{1})\,\Gamma_{\mathbf{Q}+\mathbf{1}-\mathbf{2}-\mathbf{3}} \tag{4.58i}$$
$$s^-_6(\mathbf{Q},\mathbf{1},\mathbf{2},\mathbf{3}) = s^-_5(\text{-}\mathbf{Q},\mathbf{3},\mathbf{2},\mathbf{1})\,\Gamma_{\mathbf{Q}+\mathbf{1}-\mathbf{2}-\mathbf{3}} \quad , \tag{4.58j}$$

where $\bar{\mathbf{Q}} = \mathbf{Q} + \mathbf{G}$ such that $\bar{\mathbf{Q}} \in 1^{\text{st}}$ MBZ. These relations are retained during the flow. We exploit these symmetries to reduce memory usage.

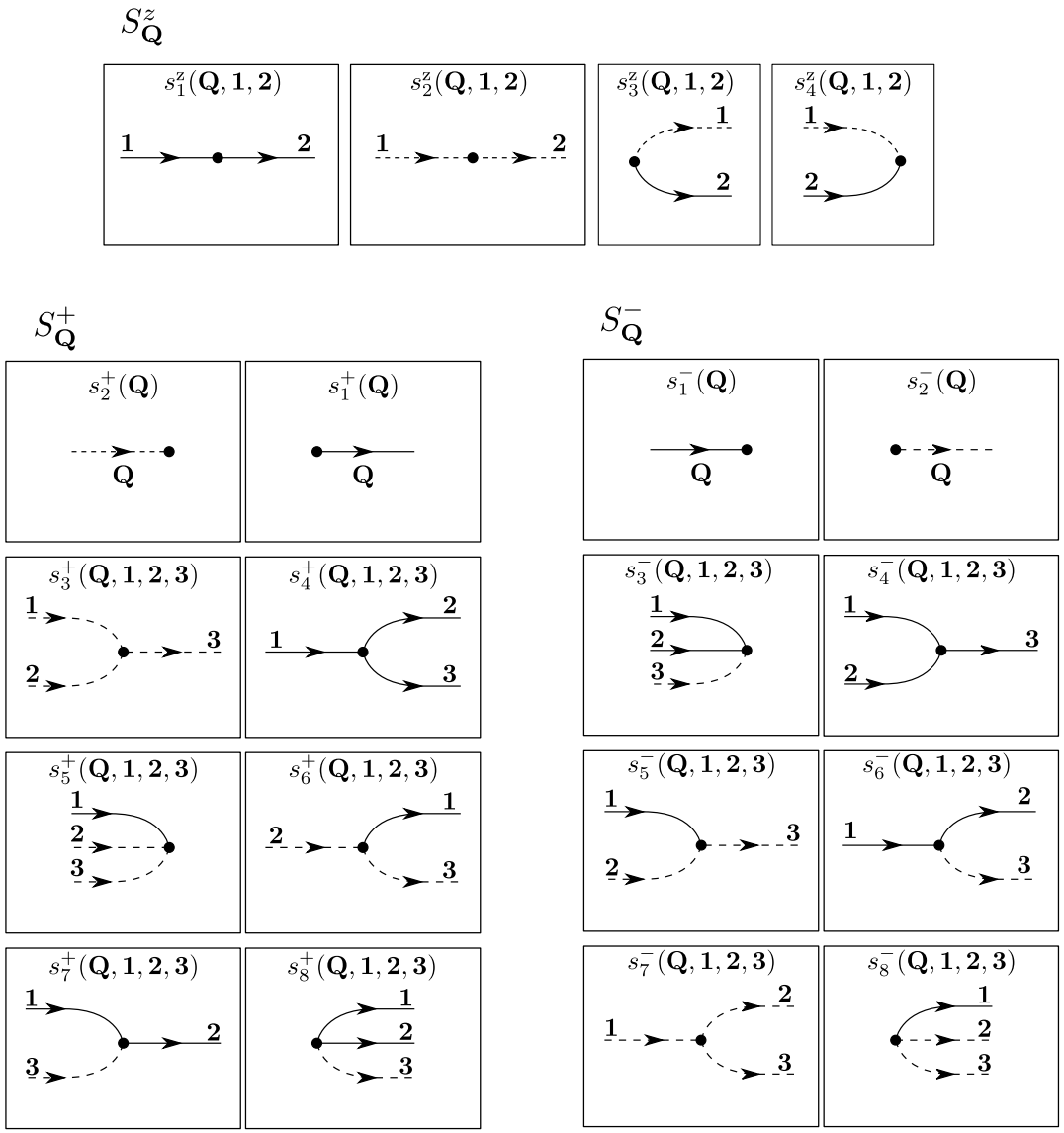

Figure 4.9: Diagrammatic representation of the operator terms in the flowing observables which are transformed in order to obtain the longitudinal and transverse structure factor.

4.3.2 Flow equations

In this section the diagrammatic representation of the flow equations for the Hamiltonian and the observables is shown. Basically, we use the conventions introduced in section 2.4.2 (see also Figure2.19).
For better visibility we discard the symbols for the momentum sums. Instead, we employ the Einstein summation convention, i.e. we sum over all momentum indices which appear only on the right hand side of the flow equations.
Symmetrized contributions which arise from the same diagram are framed by a dotted rectangular.
Note, that we directly exploit the conservation of total momentum for the diagrams of the bilinear terms in the Hamiltonian, but not for the quartic terms. In general, the sum over momenta of all in and out-going lines is zero modulo reciprocal lattice vectors.
By contrast, for the vertices of the observables the sum over momenta of in and out-going lines is given by $\mathbf{Q}$ modulo reciprocal lattice vectors. In order to avoid any confusion, this relation is directly evaluated in the diagrams of the corresponding flow equations.
Alternatively, all flow equations are presented in standard notation in Appendix B.2.

Flowing Hamiltonian

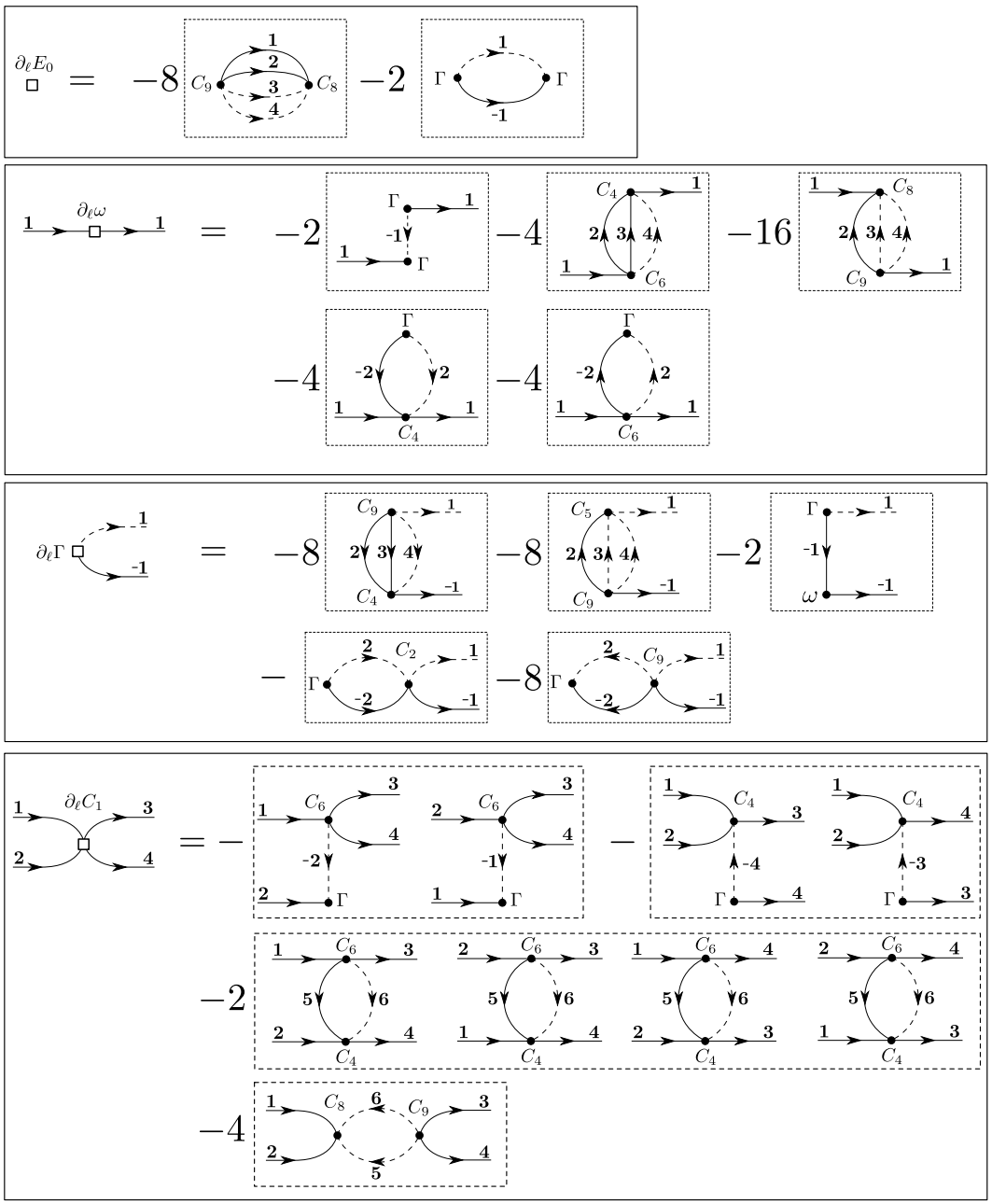

Figure 4.10: Diagrammatic representation of the flow equation for the effective coefficients in the flowing Hamiltonian up to scaling dimension $d = 2$.

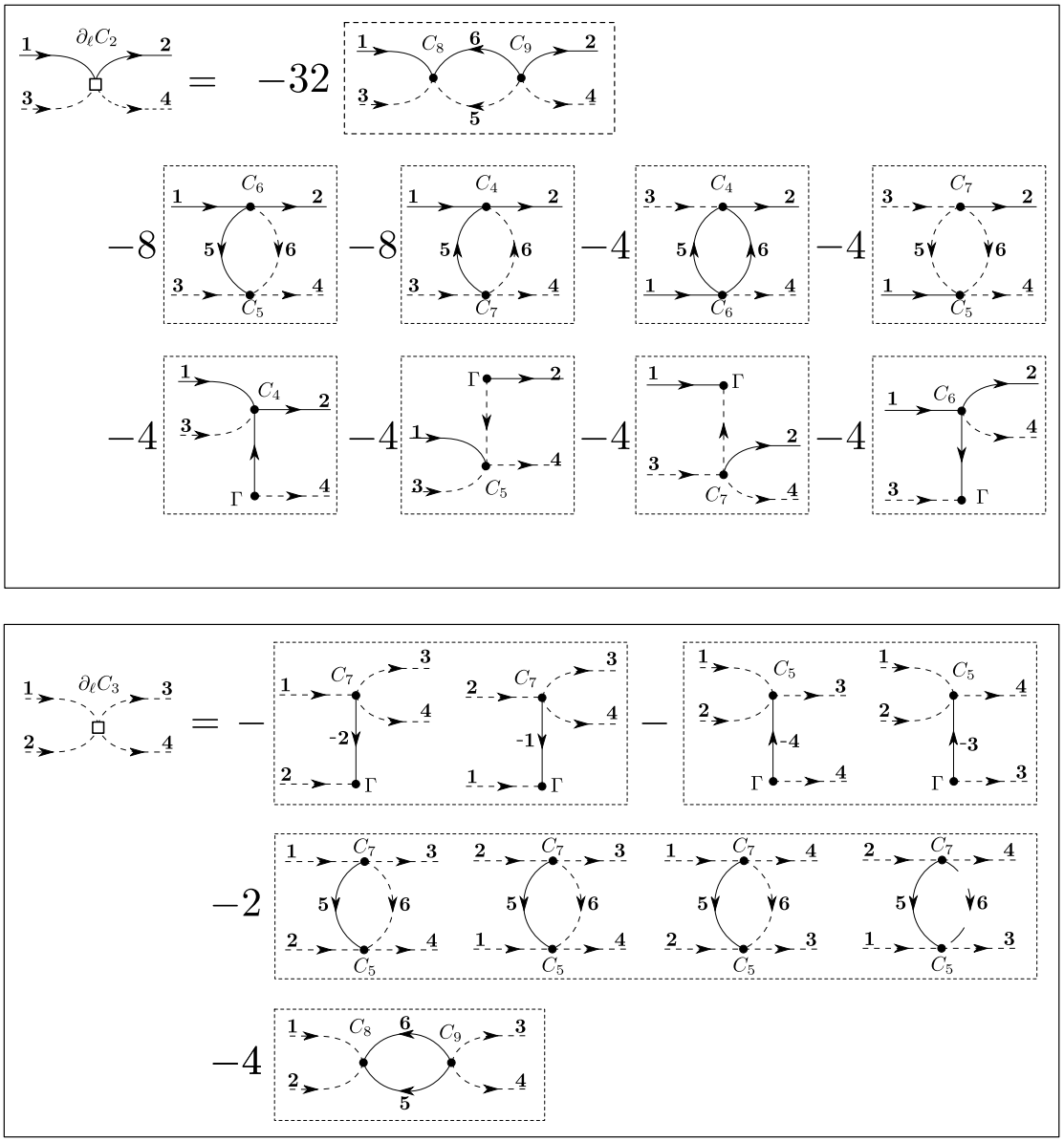

Figure 4.11: Diagrammatic representation of the flow equation for the effective coefficients in the flowing Hamiltonian up to scaling dimension $d = 2$.

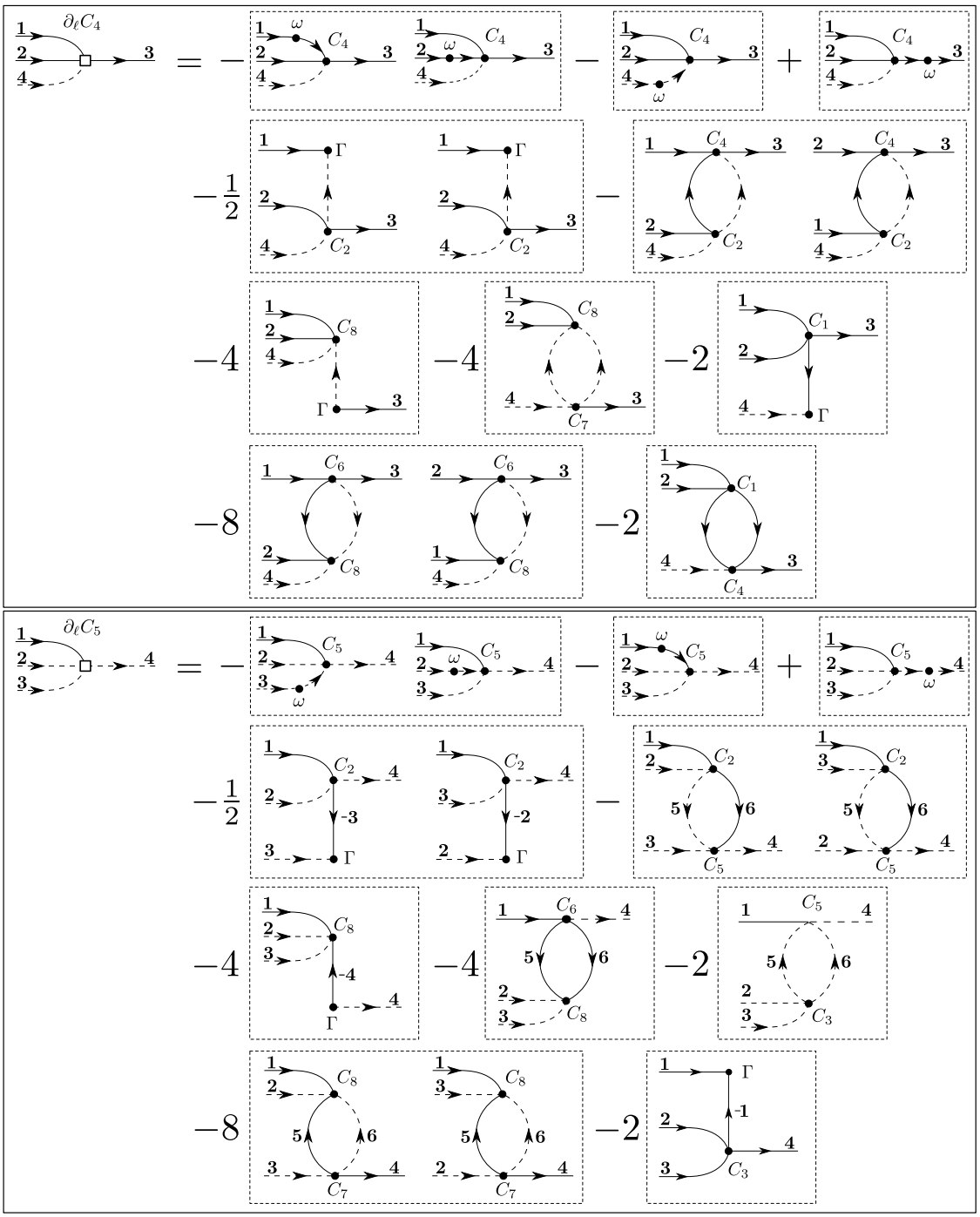

Figure 4.12: Diagrammatic representation of the flow equation for the effective coefficients in the flowing Hamiltonian up to scaling dimension $d = 2$.

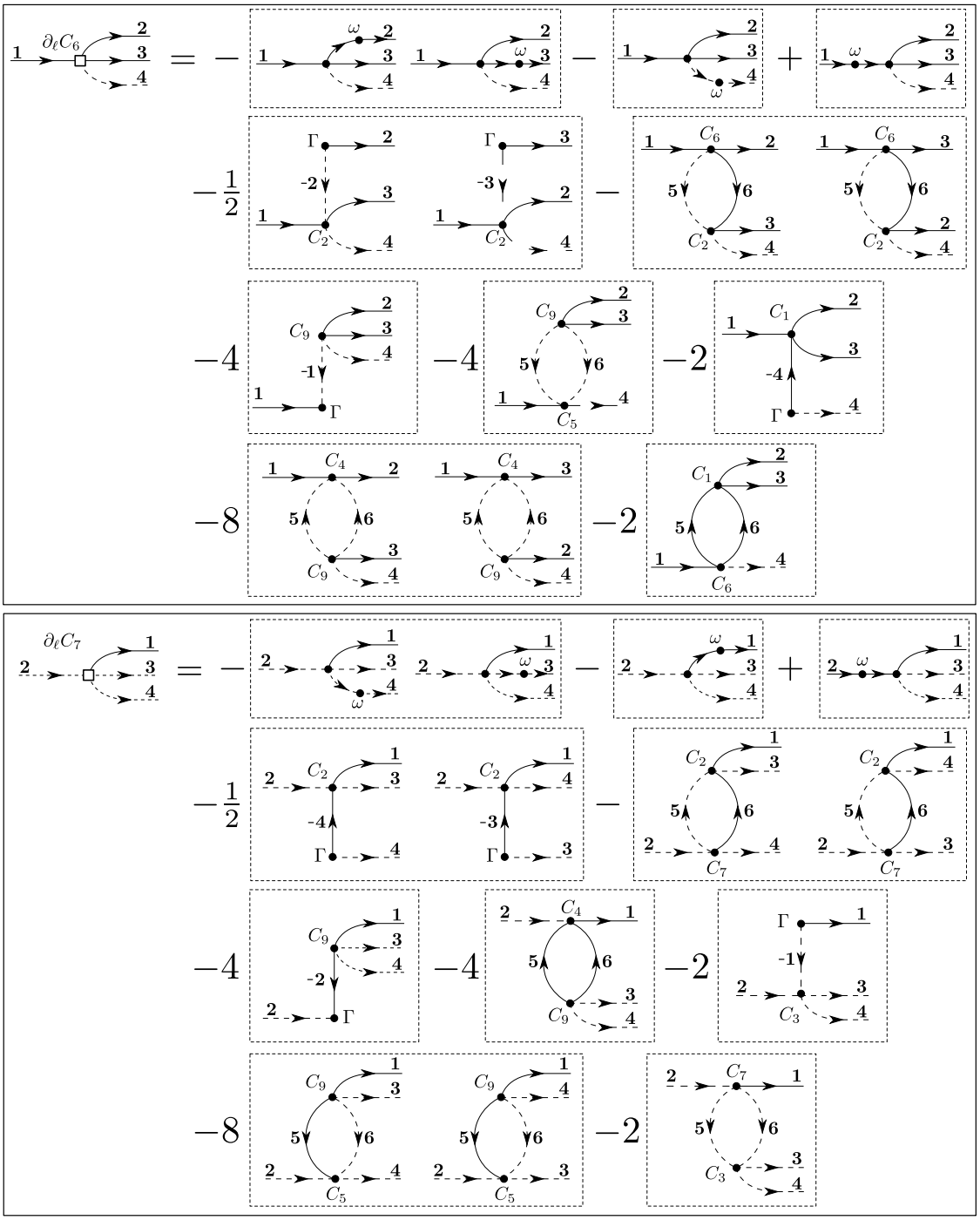

Figure 4.13: Diagrammatic representation of the flow equation for the effective coefficients in the flowing Hamiltonian up to scaling dimension $d = 2$.

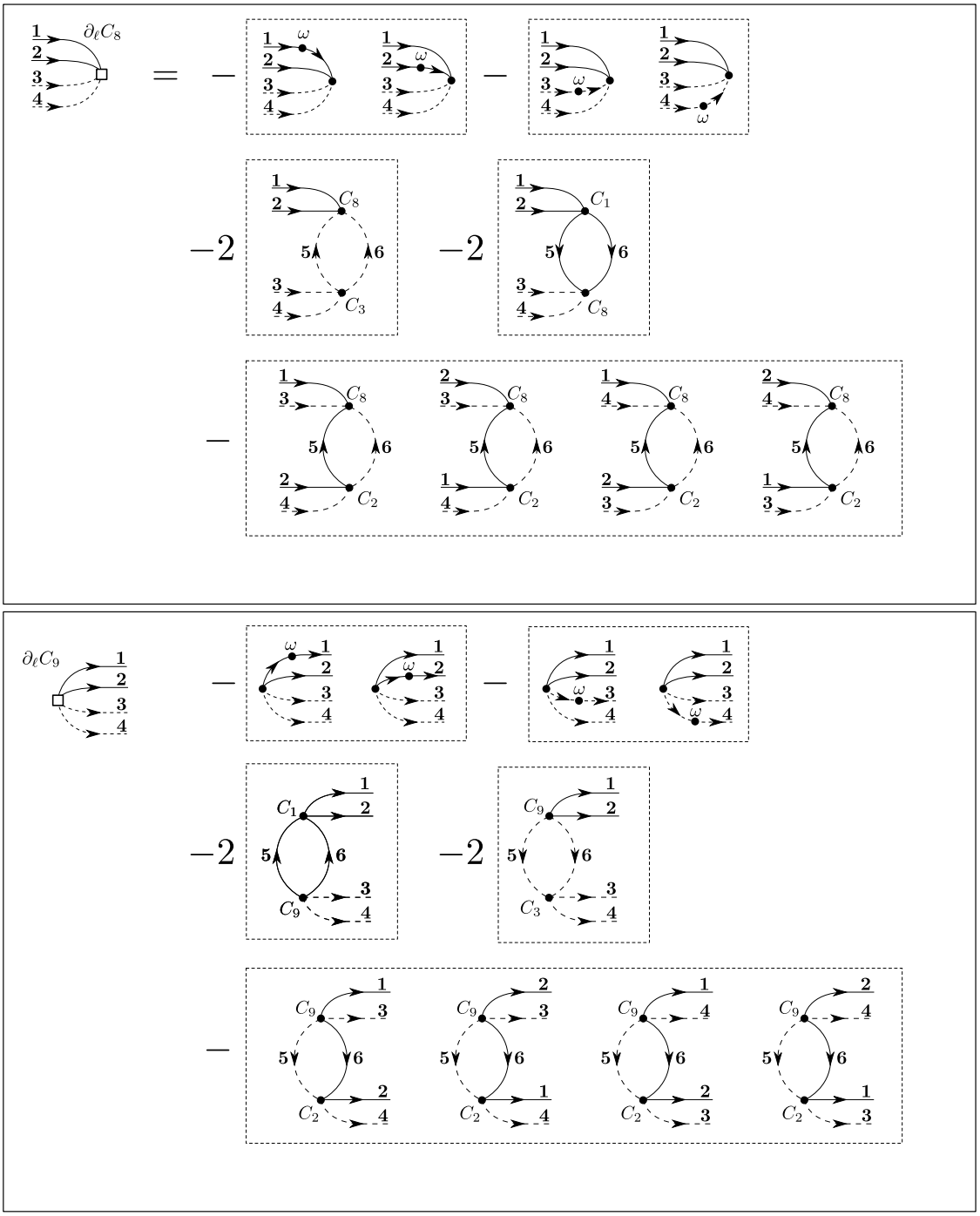

Figure 4.14: Diagrammatic representation of the flow equation for the effective coefficients in the flowing Hamiltonian up to scaling dimension $d = 2$.

Flowing observables

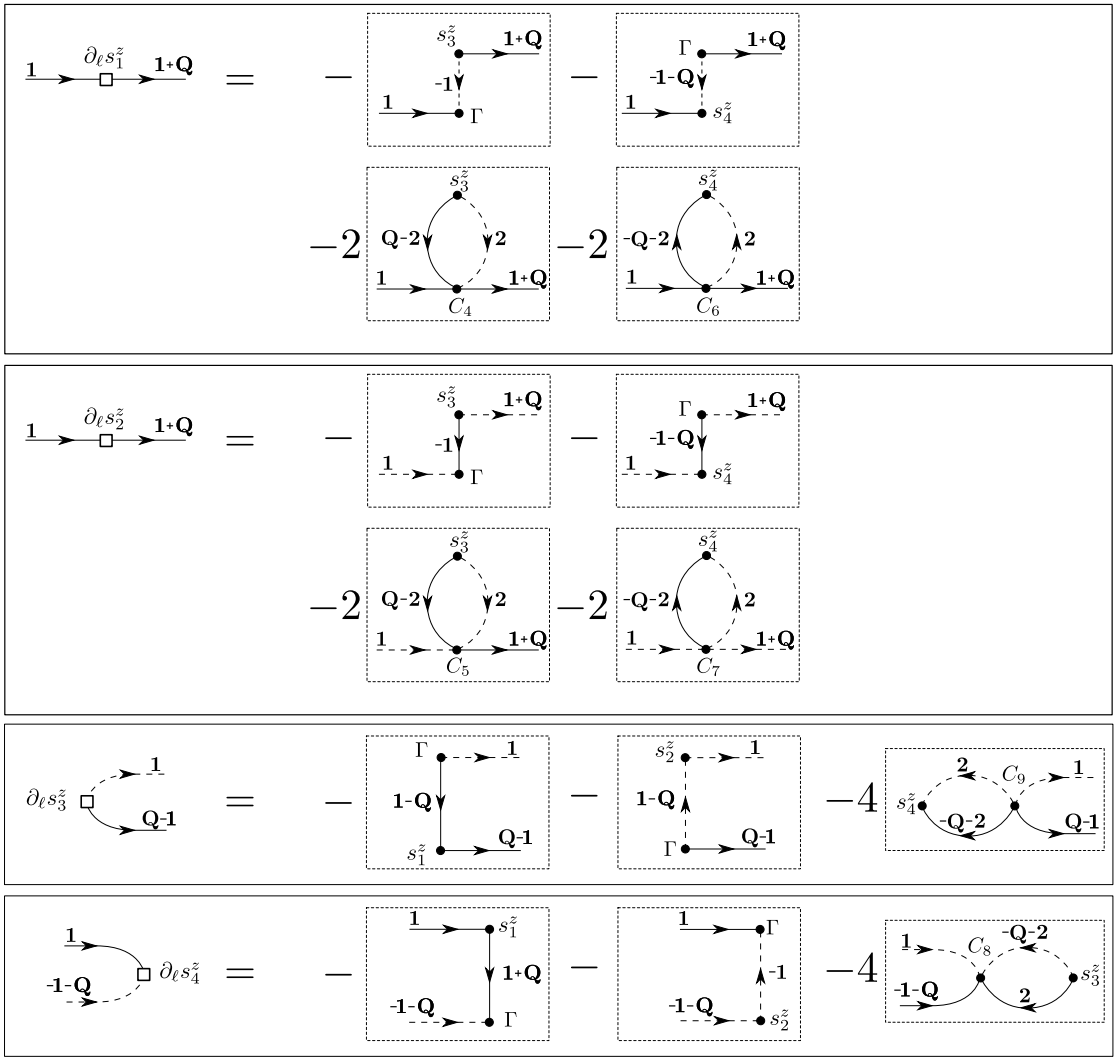

Figure 4.15: Diagrammatic representation of the flow equation for the effective coefficients in $S^z_{\mathbf{Q}}(\ell)$.

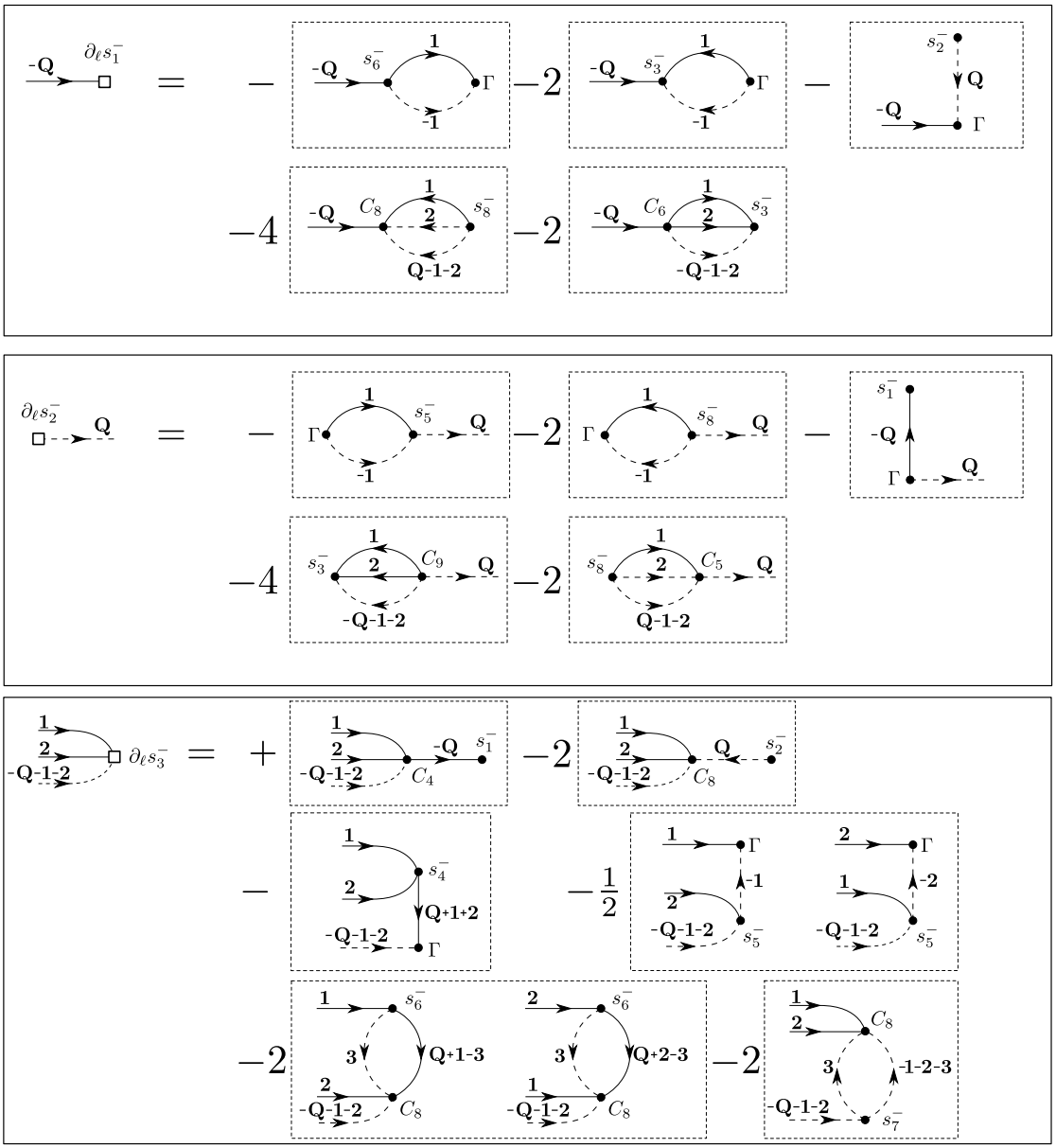

Figure 4.16: Diagrammatic representation of the flow equation for the effective coefficients in $S^-_{\mathbf{Q}}(\ell)$

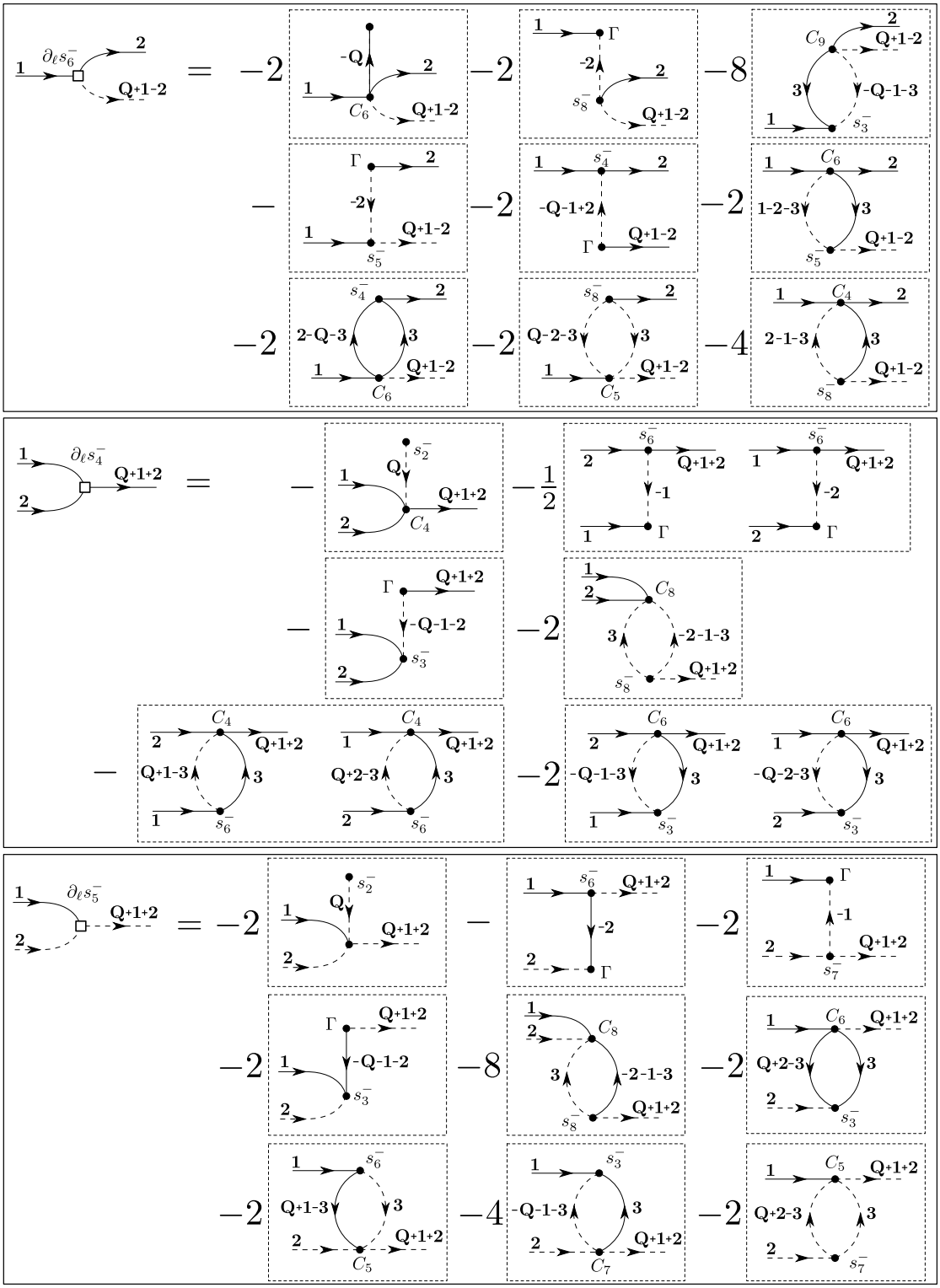

Figure 4.17: Diagrammatic representation of the flow equation for the effective coefficients in $S^{-}_{\mathbf{Q}}(\ell)$

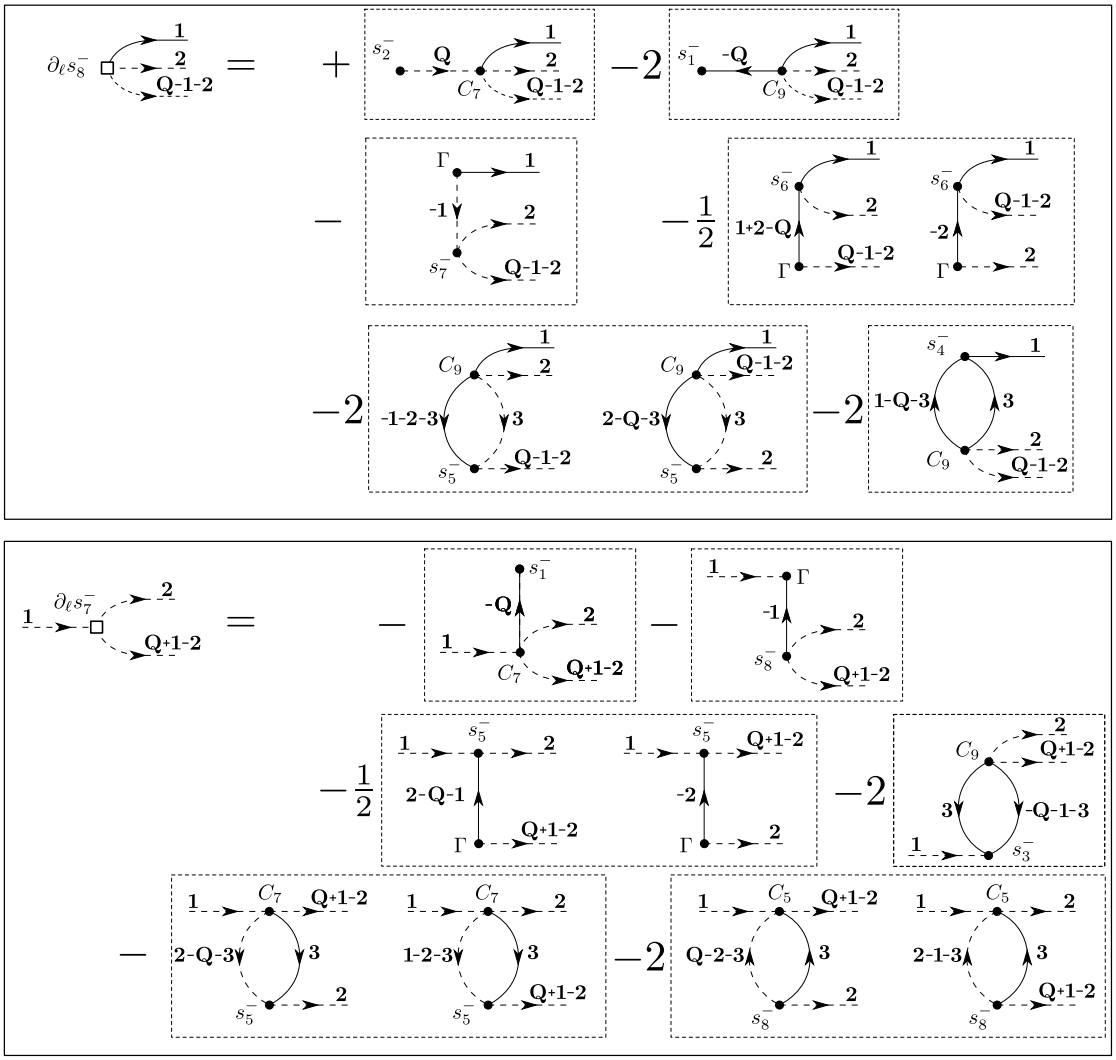

Figure 4.18: Diagrammatic representation of the flow equation for the effective coefficients in $S^-_{\mathbf{Q}}(\ell)$

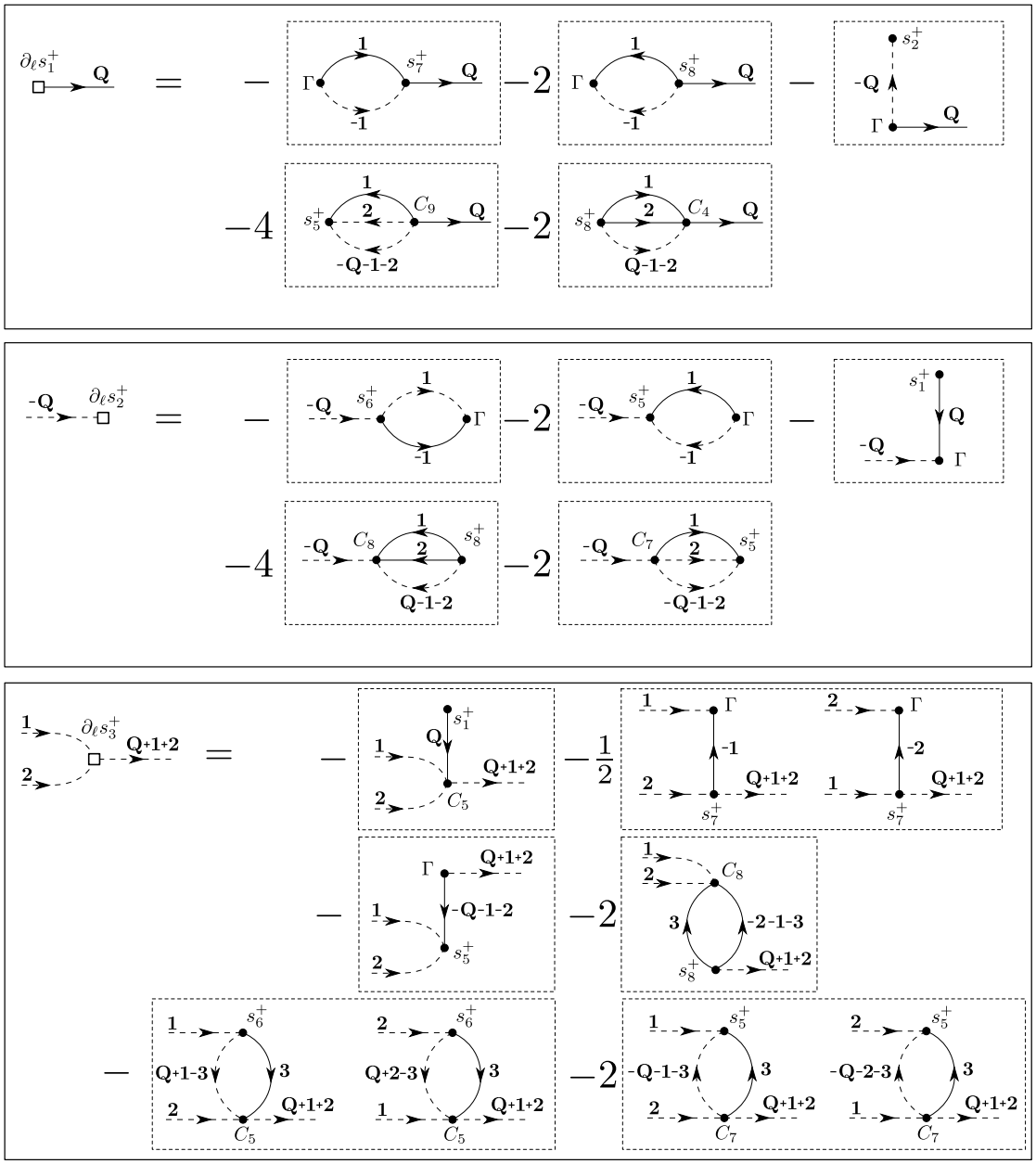

Figure 4.19: Diagrammatic representation of the flow equation for the effective coefficients in $S^+_{\mathbf{Q}}(\ell)$

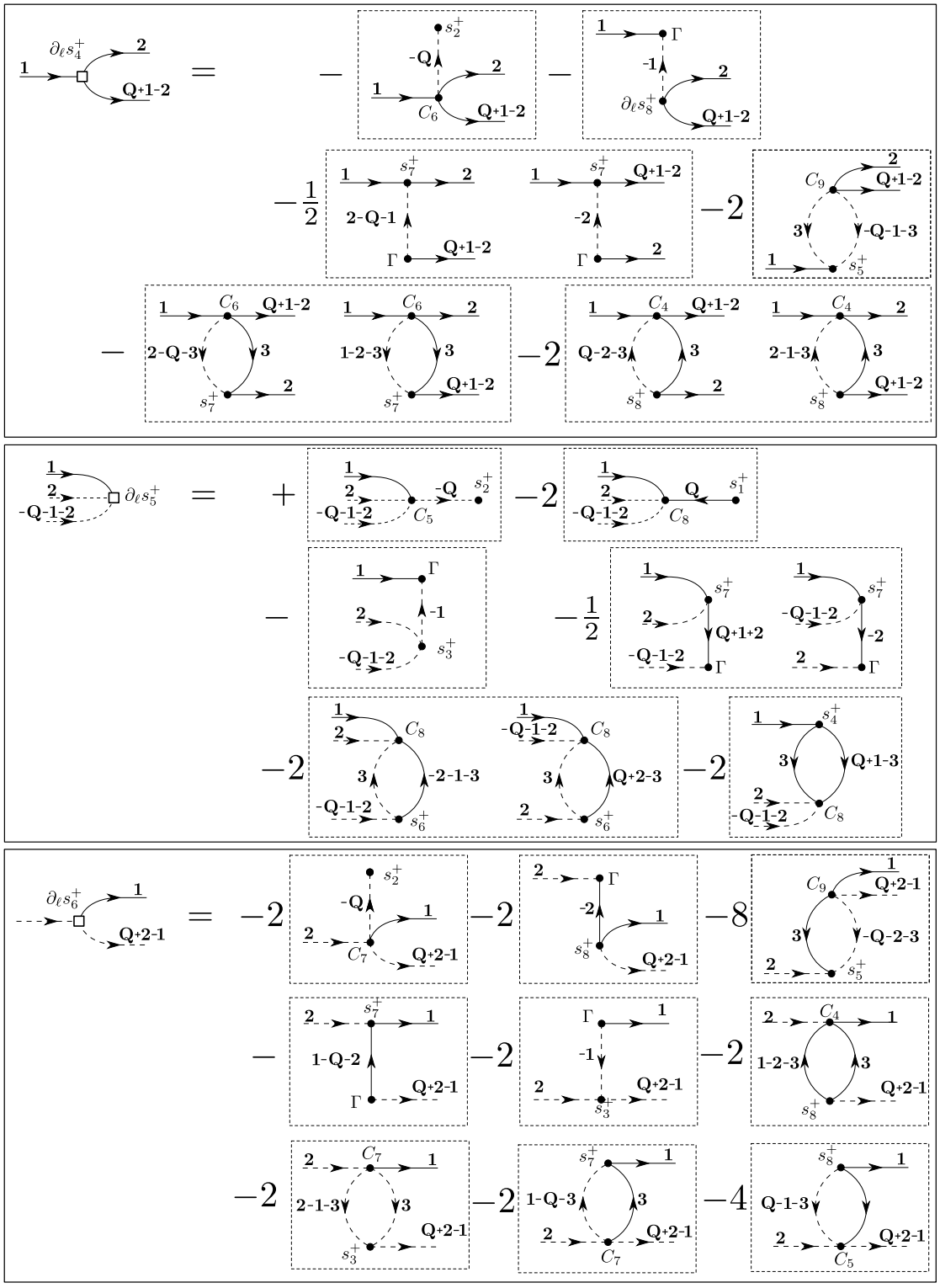

Figure 4.20: Diagrammatic representation of the flow equation for the effective coefficients in $S^+_{\mathbf{Q}}(\ell)$

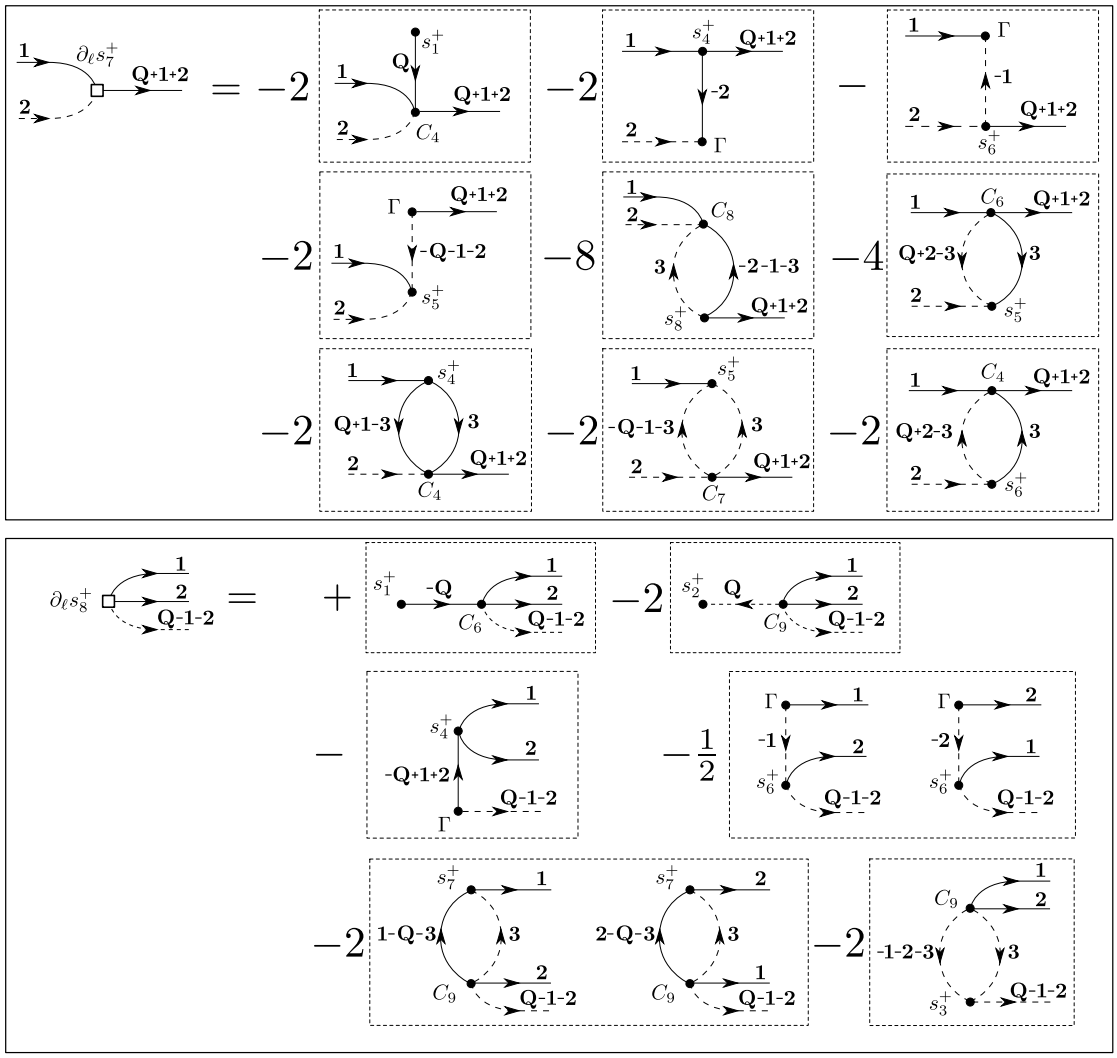

Figure 4.21: Diagrammatic representation of the flow equation for the effective coefficients in $S^+_{\mathbf{Q}}(\ell)$

Technical details

Similar to the deepCST evaluation in section 4.2.3 we consider equidistant discretizations of the MBZ with $N = L \times L$ grid points leading to a finite number of coefficients. Due to the quartic operator terms, which depend on three independent momenta, the total number of coefficients grows as $\mathcal{O}(N^3)$. We use a standard adaptive Runge-Kutta-Fehlberg 4(5) method to integrate the equations for systems with L varying from 6 to 16. The residual off-diagonality (ROD) is tracked to determine how far the flow has converged. The evolution of the ROD for different system sizes is shown in Figure 4.22. As expected, the ROD decreases exponentially for $\ell \to \infty$ indicating a converging flow. The integration terminates when the ROD drops below $10^{-6}J$.
For the step size we impose a control tolerance of $\epsilon = 10^{-6}J$. Eventually, we expect the total numerical error to be in the order of $\delta \approx 10^{-6}J$.

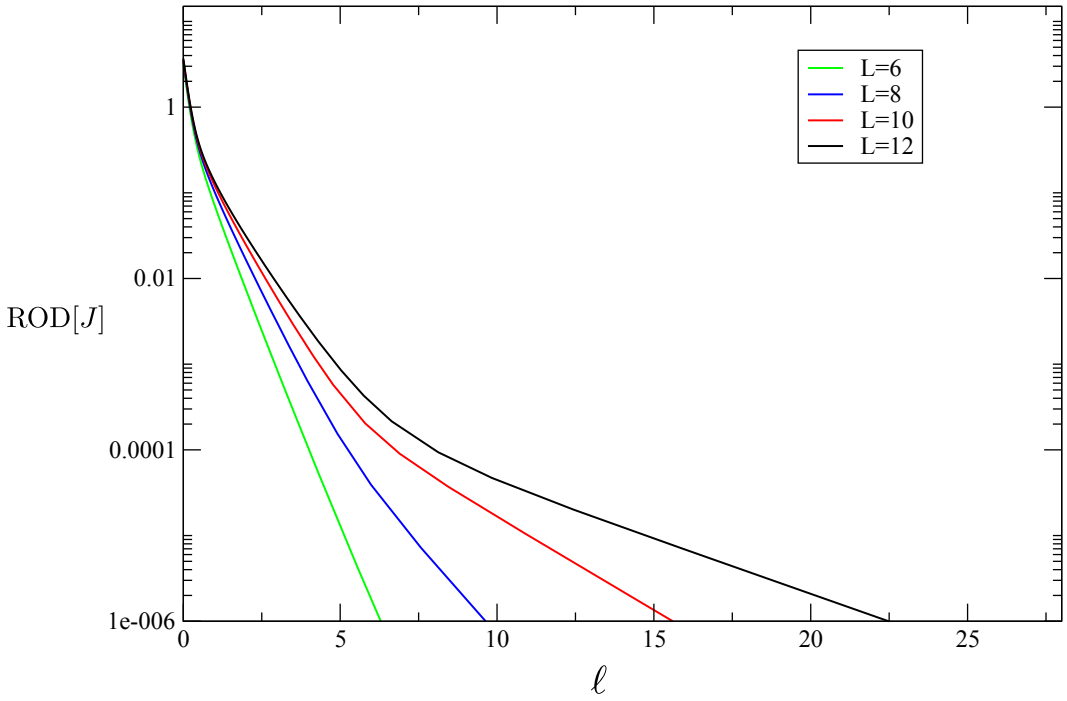

Figure 4.22: The residual off-diagonality (ROD) is shown for different systems of size L.

4.3.3 Evaluation of spectral densities

The effective Hamiltonian H_{eff} allows us to study the dynamic structure factors in independent n-magnon subspaces which considerably simplifies the evaluation of the spectral densities. In the following, the evaluation of the longitudinal and transverse dynamic structure factors is discussed.

Longitudinal channel

The longitudinal dynamic structure factor for the effective system is given by

$$S^{zz}(\omega,Q) = -\frac{1}{\pi}\text{Im}\ \langle 0|S^z_{\text{eff}}(-Q)\frac{1}{\omega-(H_{\text{eff}}-\bar{E}_0)}S^z_{\text{eff}}(Q)|0\rangle \tag{4.59a}$$

$$= -\frac{1}{\pi}\text{Im}\sum_{\mathbf{1,2}}\langle v^L_{\mathbf{2}}|\frac{1}{\omega-(H_{\text{eff}}-\bar{E}_0)}|v^R_{\mathbf{1}}\rangle \tag{4.59b}$$

$$\langle v^L_{\mathbf{2}}| := \langle 0|\alpha_{\mathbf{2}}\beta_{\mathbf{Q\text{-}2}}s^z_3(\mathbf{\text{-}Q},\mathbf{2},\mathbf{Q\text{-}2}) \tag{4.59c}$$

$$|v^R_{\mathbf{1}}\rangle := s^z_4(\mathbf{Q},\mathbf{1},\mathbf{Q\text{-}1})\alpha^\dagger_{\mathbf{1}}\beta^\dagger_{\mathbf{Q\text{-}1}}|0\rangle \tag{4.59d}$$

Thus, only the subspace of α-β magnon pairs has to be considered.
In this subspace the effective Hamiltonian reads

$$(H^0_{\text{eff}}-\bar{E}_0) = \sum_{\mathbf{k}}\omega_{\text{eff}}(\mathbf{k})(\alpha^\dagger_{\mathbf{k}}\alpha_{\mathbf{k}}+\beta^\dagger_{\mathbf{k}}\beta_{\mathbf{k}})+V^{(\alpha-\beta)}_{\text{eff}} \tag{4.60a}$$

$$V^{(\alpha-\beta)}_{\text{eff}} = \sum_{\mathbf{1,2,3,4}}C_2(\mathbf{1},\mathbf{2},\mathbf{3},\mathbf{4})\alpha^\dagger_{\mathbf{1}}\alpha_{\mathbf{2}}\beta^\dagger_{\mathbf{3}}\beta_{\mathbf{4}}\delta_G(1-2+3-4) \quad . \tag{4.60b}$$

The non-interacting case is obtained by the neglect of the terms in $V^{(\alpha-\beta)}_{\text{eff}}$.
The total weight in the spectral density for given $\mathbf{Q}$ is determined by the longitudinal static structure factor

$$W^{2\text{mag}}_{\mathbf{Q}} = \sum_{\mathbf{12}}s^z_3(\mathbf{\text{-}Q},\mathbf{1},\mathbf{Q\text{-}1})s^z_4(\mathbf{Q},\mathbf{1},\mathbf{Q\text{-}1}) \quad . \tag{4.61}$$

In order to obtain the corresponding spectral density we proceed as follows. The non-diagonal Lanczos tridiagonalization algorithm is used to determine the coefficients of the continued fraction representation of the corresponding resolvent. The information about the spectral density is encoded in the sequence in the tridiagonal matrix α_n and $b_n = \sqrt{\beta_n\gamma_n}$. In general the coefficients show a very systematic behavior [125]. In particular, the asymptotic behavior of sequence for $n\to\infty$ is related to the upper bound E_u and lower bound E_l of the continuum according to (3.35a).
In Figure 4.23 the α_n-sequence of the resolvent in the longitudinal dynamic structure factor at $(\pi/2,\pi/2)$ for various system sizes is shown. For smaller system size $L\leq 16$ we observe considerable fluctuations in the coefficient sequence which increase with larger n. This leads to deviations from the asymptotic behaviour in the thermodynamic limit.
In order to reduce these finite size effects, we enlarge the Hilbert space by appropriate interpolation schemes increasing the number of grid points in the MBZ. This in turn increases the maximum number n_{max} of Lanczos steps before the coefficients start to deviate from the

asymptotic behavior. Apparently, the fluctuations are considerably reduced for increasing system size. This feature is generally observed for the α_n as well as the b_n sequences.
For finite systems, one has to find an appropriate $n_{\max}$ before spurious effects become apparent. A continuous function for the spectral density is obtained either by an artificial broadening $\omega \to \omega + i\delta$ or by the use of square root terminators (for example see Ref. [125] or Ref. [70]). The best results are found for $n_{\max} = 15$-25 using a system size of $L = 144$-192. For $n_{\max} > 25$ spurious effects are observed which are manifested by wobbles in the spectral density. We assume that these wobbles are due to finite size effects and the limited accuracy of the interpolants which lead to spurious behavior in the continued fraction coefficients.
Note, that we are dealing with a non-hermitian problem for which truncation errors may spuriously lead to finite imaginary parts in the eigenvalue spectrum. Consequently, the coefficient sequences obtained in the non-symmetric Lanczos tridiagonalization are much more fragile than in the symmetric case.
Moreover, we have a finite discretization in momentum space with $\Delta\mathbf{k}$. Thus, any finite system exhibits a small residual gap $\delta(L) = \omega_{\text{eff}}(\Delta\mathbf{k})$ which decreases with $\delta \propto 1/L$. The finite residual gap is taken into account in the square root terminator by defining the lower edge of the continuum as $E_l^{(L)}(\mathbf{Q}) = E_l^{(\infty)}(\mathbf{Q}) + \delta(L)$ where $E_l^{(\infty)}(\mathbf{Q}) = \omega_{\text{eff}}(\mathbf{Q})$. This agrees well with the obtained coefficient sequences as shown in Figure 4.23.
The interaction is either interpolated by a direct or an indirect nearest-neighbour interpolation scheme using the information about the initial coefficient function (see 3.4.4 for technical details). In order to assess the effects of the direct and indirect interpolation method, we compare the longitudinal dynamic structure factors obtained for a both schemes as shown in Figure 4.24.
The interaction leads to a considerable shift of spectral weight to the lower edge of the continuum and the formation of a resonance which indicates a strong attractive interaction between pairs of magnons. For the indirectly interpolated interaction this resonance is directly adjacent to the lower edge of the continuum. By contrast, the resonance is shifted to higher energies and slightly squeezed if we use of a piecewise constant interaction. We assume that this is a spurious effect because the nearest neighbor interpolant does not capture the correct behavior of the interaction at small momenta.
We conclude that the indirectly interpolated interaction provides more accurate results because the bare nearest neighbor interpolant is a piecewise constant function, which may lead to larger deviations especially for small momenta. The values of the interaction at small momenta are particularly important for the correct description of the spectral density at the lower edge of the continuum.
A comprehensive presentation and discussion of the results for the longitudinal dynamic structure factor is given in section 4.4.2.

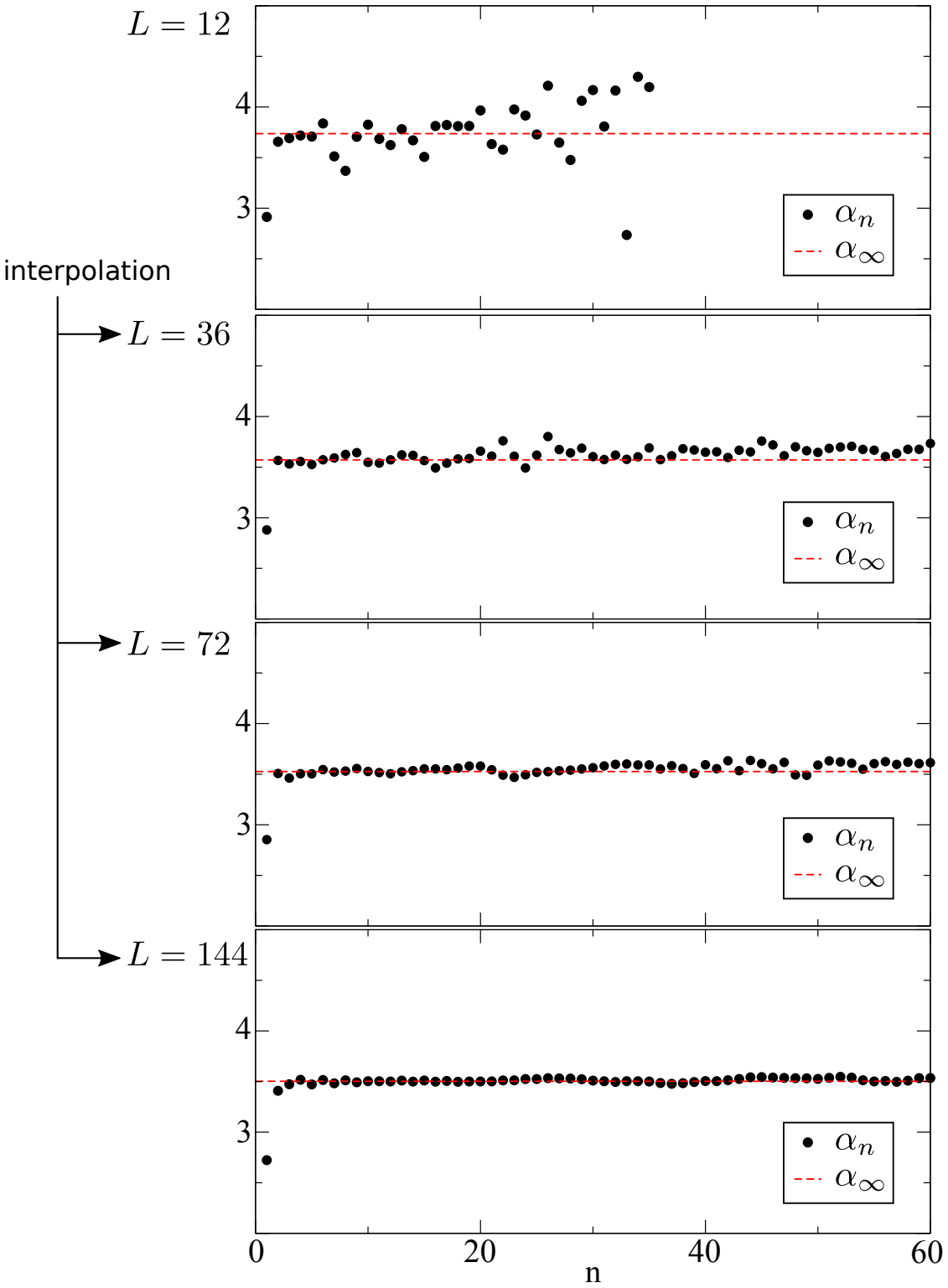

Figure 4.23: The behaviour of the diagonal continued fraction coefficients a_n with increasing system size is depicted. Larger system sizes are obtained by an interpolation of the effective coefficients in the Hamiltonian.

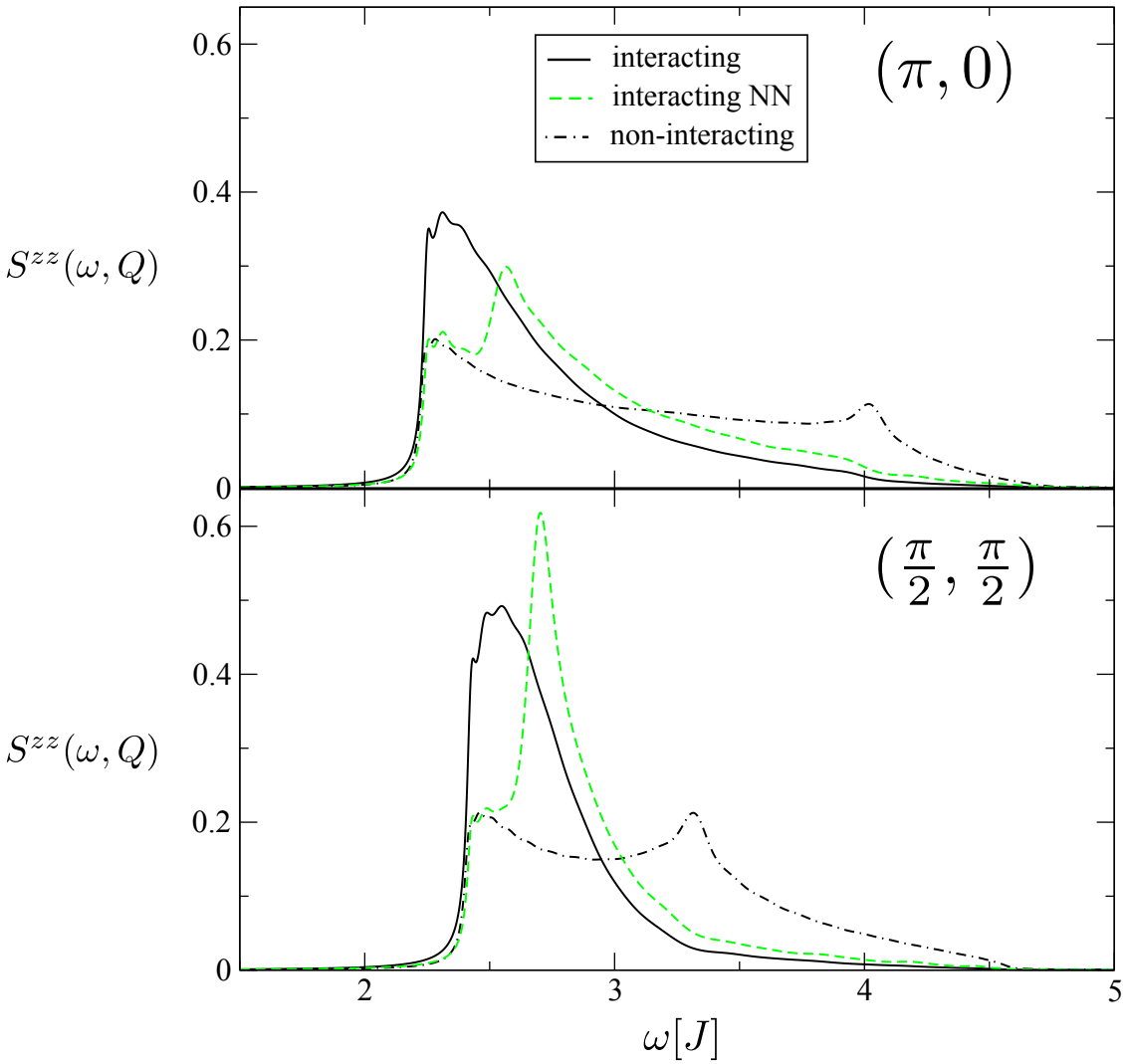

Figure 4.24: The longitudinal dynamic structure factor for $\mathbf{Q} = (\pi, 0)$ and $\mathbf{Q} = (\frac{\pi}{2}, \frac{\pi}{2})$ for the interacting and non-interacting system is shown. The effective interaction is either obtained by a nearest neighbour interpolation (NN) or by an indirect nearest neighbour interpolation which is more accurate.

Transverse channel

The transverse dynamic structure factor in the effective description is given by

$$S^{xx+yy}(\omega,Q) = -\frac{1}{\pi}\mathrm{Im}\left(\langle 0|\, S^-_{\mathrm{eff}}(-Q)\frac{1}{\omega-(H_{\mathrm{eff}}-\bar{E}_0)}S^+_{\mathrm{eff}}(Q)\,|0\rangle\right) \tag{4.62a}$$

It splits into a one-magnon contribution

$$\begin{aligned} S^{xx+yy}(\omega,Q)\big|_{1\mathrm{mag}} &= -\frac{1}{\pi}\mathrm{Im}\left(\langle 0|\, s_2^-(\mathbf{-Q})\,\beta_{\mathbf{Q}}\frac{1}{\omega-(H_{\mathrm{eff}}-\bar{E}_0)}s_2^+(\mathbf{Q})\,\beta^\dagger_{\mathbf{Q}}\,|0\rangle\right) && (4.63a)\\ &= s_2^-(\mathbf{-Q})\,s_2^+(\mathbf{Q})\,\delta(\omega-\omega(Q)) && (4.63b)\end{aligned}$$

where

$$W^{1\mathrm{mag}}_{\mathbf{Q}} := s_2^-(\mathbf{-Q})\,s_2^+(\mathbf{Q}) \tag{4.64}$$

defines the one-magnon spectral weight, and a three-magnon contribution

$$\begin{aligned} S^{xx+yy}(\omega,Q)\big|_{3\mathrm{mag}} &= \sum_{\mathbf{1,2,3,4}}\langle v^L_{\mathbf{12}}|\,\frac{1}{\omega-(H_{\mathrm{eff}}-\bar{E}_0)}\,|v^R_{\mathbf{34}}\rangle && (4.65a)\\ \langle v^L_{\mathbf{12}}| &:= \langle 0|\,\alpha_{\mathbf{1}}\beta_{\mathbf{2}}\beta_{\mathbf{Q\text{-}1\text{-}2}}s_8^-(\mathbf{Q},\mathbf{1},\mathbf{2},\mathbf{Q\text{-}1\text{-}2}) && (4.65b)\\ |v^R_{\mathbf{34}}\rangle &:= s_5^+(\mathbf{-Q},\mathbf{3},\mathbf{4},\mathbf{Q\text{-}3\text{-}4})\,\alpha^\dagger_{\mathbf{3}}\beta^\dagger_{\mathbf{4}}\beta^\dagger_{\mathbf{Q\text{-}3\text{-}4}}\,|0\rangle && (4.65c)\end{aligned}$$

which constitutes the incoherent part of the spectral density. The transverse static structure factor in the three-magnon subspace

$$W^{3\mathrm{mag}}_{\mathbf{Q}} := \sum_{\mathbf{1}} s^z_3(\mathbf{-Q},\mathbf{1},\mathbf{Q\text{-}1})\,s^z_4(\mathbf{Q},\mathbf{1},\mathbf{Q\text{-}1}) \tag{4.66}$$

provides the total weight in the spectral density.
In the transverse channel the effective Hamiltonian reads

$$\begin{aligned} (H^0_{\mathrm{eff}}-\bar{E}_0) &= \sum_{\mathbf{k}}\omega_{\mathrm{eff}}(\mathbf{k})(\alpha^\dagger_{\mathbf{k}}\alpha_{\mathbf{k}}+\beta^\dagger_{\mathbf{k}}\beta_{\mathbf{k}})+V^{(\alpha-\beta)}_{\mathrm{eff}}+V^{(\alpha-\alpha)}_{\mathrm{eff}}+V^{(\beta-\beta)}_{\mathrm{eff}} && (4.67a)\\ V^{(\alpha-\beta)}_{\mathrm{eff}} &= \sum_{\mathbf{1,2,3,4}} C_2(\mathbf{1},\mathbf{2},\mathbf{3},\mathbf{4})\,\alpha^\dagger_{\mathbf{1}}\alpha_{\mathbf{2}}\beta^\dagger_{\mathbf{3}}\beta_{\mathbf{4}}\delta_G(1-2+3-4) && (4.67b)\\ V^{(\beta-\beta)}_{\mathrm{eff}} &= \sum_{\mathbf{1,2,3,4}} C_3(\mathbf{1},\mathbf{2},\mathbf{3},\mathbf{4})\,\beta^\dagger_{\mathbf{1}}\beta^\dagger_{\mathbf{2}}\beta_{\mathbf{3}}\beta_{\mathbf{4}}\delta_G(1+2-3-4)\quad . && (4.67c)\end{aligned}$$

The Hilbert space of three magnons grows as $\mathcal{O}(N^2)$ for given total momentum, in contrast to the longitudinal channel which grows as $\mathcal{O}(N)$. Thus, the system size can be only increased up to $L = 24$–32.
Moreover, the indirect interpolation scheme for the effective observable cannot be used because the initial functions in (4.56) are zero.
As a consequence, the evaluation of the spectral density by means of the continued fraction representation is complicated due to instabilities in the Lanczos algorithm which occur for

Lanczos steps $n > 15$. These instabilities are manifestations of finite size effects and the limited accuracy of the interpolants.
Based on our methodical tools it is not possible to extract enough information to determine fine structures in the spectral density of the transverse DSF.
However, even finite systems provide important information about the distribution of spectral weight. In fact, this is sufficient for a comparison with experimental data which exhibit a finite resolution.
As an alternative to the calculation of the continued fraction representation we determine the spectrum and the eigenstates of the effective Hamiltonian in (4.67a) by means of an exact diagonalization method. The spectral density is then defined by (3.34b).
As we want to reproduce the finite resolution in the experiment, we are replacing the δ-peaks by Gaussian distribution functions with the corresponding weight W_i and an artificial broadening σ which fits the resolution of the experimental data

$$\sum_i W_i \delta(\omega - \omega_i) \to I(\omega) = \sum_i W_i \frac{1}{\sqrt{2\sigma^2\pi}} \mathrm{e}^{\frac{1}{2}\left(\frac{\omega-\omega_i}{\sigma}\right)^2} \quad . \tag{4.68}$$

The non-hermitian Hamiltonian exhibits isolated eigenvalues with small imaginary part ($\mathrm{Im}\,\omega_i \approx 10^{-3}\mathrm{Re}\,\omega_i$) which can be ascribed to truncation errors of the CST. In the evaluation of (4.68) we project these eigenvalues onto the real axis.
Moreover, eigenstates which have a negative overlap with the inital states $S^+_{\mathrm{eff}}(Q)|0\rangle$ and $\langle 0|S^-_{\mathrm{eff}}(-Q)$ are discarded.
Eventually, we normalize the resulting spectral functions by $(\sum_i W_i)^{-1} I(\omega)$ and rescale them by the associated static structure factors in the thermodynamic limit.
For finite broadening both approaches, the continued fraction representation and the exactly diagonalized system, provide very similar results.
The data for the transverse DSFs are discussed in section 4.4.4.

Interpolation schemes

In the folowing, we summarize the interpolation schemes used to enlarge the Hilbert space of the effective model.

For the dispersion $\omega(\mathbf{k})$ we are apply a Lanczos resampling method [128] which is suitable for the interpolation of periodic functions. In order to avoid the kink at $\mathbf{k} = 0$ where the dispersion has a linear cusp we are interpolating the function $f(\mathbf{k}) = \omega(\mathbf{k})^2$ instead, taking the square root afterwards.

The coefficient functions in the longitudinal Observable depend on a two dimensional argument (as the dispersion). However, these functions exhibit poles at certain momenta which makes it more complicated to interpolate them directly. In order to overcome this problem, we interpolate the function $f(\mathbf{k}) = \frac{\bar{s}(\mathbf{k})+c}{s(\mathbf{k})+c}$ where $\bar{s}(\mathbf{k})$ is the function transformed by the CST and $s(\mathbf{k})$ denotes the corresponding function before the CST, which is known analytically. As the renormalization of the CST does not shift or alter the pole in $\bar{s}(\mathbf{k})$ the function $f(\mathbf{k})$ is finite and smooth. The constant shift c is introduced to avoid zeroes in the denominator. This also requires to track sign changes in $s(\mathbf{k})$ due to umklapp processes induced by the corresponding factors $\Gamma(\mathbf{K})$. Typically, we set the shift to $c = \alpha \cdot \min(s(\mathbf{k}))$ with $\alpha \approx 1.5$

The coefficient functions in the three-magnon contribution of the transverse observable are

directly interpolated using a quadrilinear interpolation scheme. Note, that the interpolation scheme used in the longitudinal part cannot be applied here as the initial functions in (4.56) are zero. However, the interpolation for the three-magnon contributions does not need to be as sophisticated as for the two-magnon contribution because the required number of intermediate grid points is much smaller compared to the longitudinal case.

The vertex functions with the six-dimensional arguments are interpolated by direct and indirect nearest neighbor interpolation schemes. The arguments of the vertex functions $C_i(\mathbf{k}_1, \mathbf{k}_2, \mathbf{k}_3, \mathbf{k}_4)$ are momenta defined in the 1$^{\text{st}}$ MBZ. Thus, the reciprocal vector $\mathbf{G} = \sum_i \mathbf{k}_i$ determined by the total momentum conservation might switch inside the 1$^{\text{st}}$ MBZ leading to a sign change in the coefficients. In order to avoid such jumps we track sign changes in the interpolation scheme.

We normalize each spectral function $I(\omega, \mathbf{Q})$ and rescale it by the total weight which is defined by the corresponding static structure factor in the thermodynamic limit. By this way, we avoid any influence of the different interpolation schemes on the total weights of the spectral densities. The static structure factors are calculated for non-interpolated systems of finite size L. The value in the thermodynamic limit is then obtained by a finite size scaling in $1/L$.

4.4 Results and Discussion

In this section the main results of the effective spin wave description are presented and discussed.
The first part addresses the low-energy properties of the system such as the ground state energy and the spin wave velocity which is an important characteristic of long wavelength spin waves.
In the second part we discuss the dynamic properties of single magnons focusing on the high-energy part at short wavelengths.
Then the results for the static and dynamic correlations between spin waves are presented. Moreover, we point out the relevance of attractive spin wave interactions at short wavelengths. The results are interpreted and illustrated by means of a diagrammatic visualization.
In the last section, we compare our results to recent experimental data and provide a concluding discussion.

4.4.1 Low-energy properties

In order to fulfill the requirements of a comprehensive spin wave description the effective model must yield quantitative results for both, high and low energies, i.e., at short and long wavelengths. In the following we present the results for the ground state energy and the spin wave velocity which are characteristic quantities of the low-energy part.

Ground state energy

The CST results for the ground state energy per spin $e_0 = E_0/2N$ for different system size $L = \sqrt{N}$ are displayed in Figure 4.25. We compare our data to second and third order spin wave calculations [194], quantum Monte Carlo simulations (QMC) [168] and high order series expansions from the Ising limit (series) [202].
The value in the thermodynamic limit is estimated by a finite size scaling in $1/L$ using a linear fit, as well as a quadratic fit to account for the finite curvature in the data. Both fits agree reasonably well with the series and QMC results within the margin of error. The quadratic fit yields a value of $e_0 = -0.669419(6)J$ which is in excellent agreement with the QMC value of $e_0^{\mathrm{QMC}} = 0.669437(5)J$. Note, that the perturbative correction from second to third order spin wave theory is a magnitude larger.
The consistency between the various data indicates that our results for the ground state energy are indeed well converged.

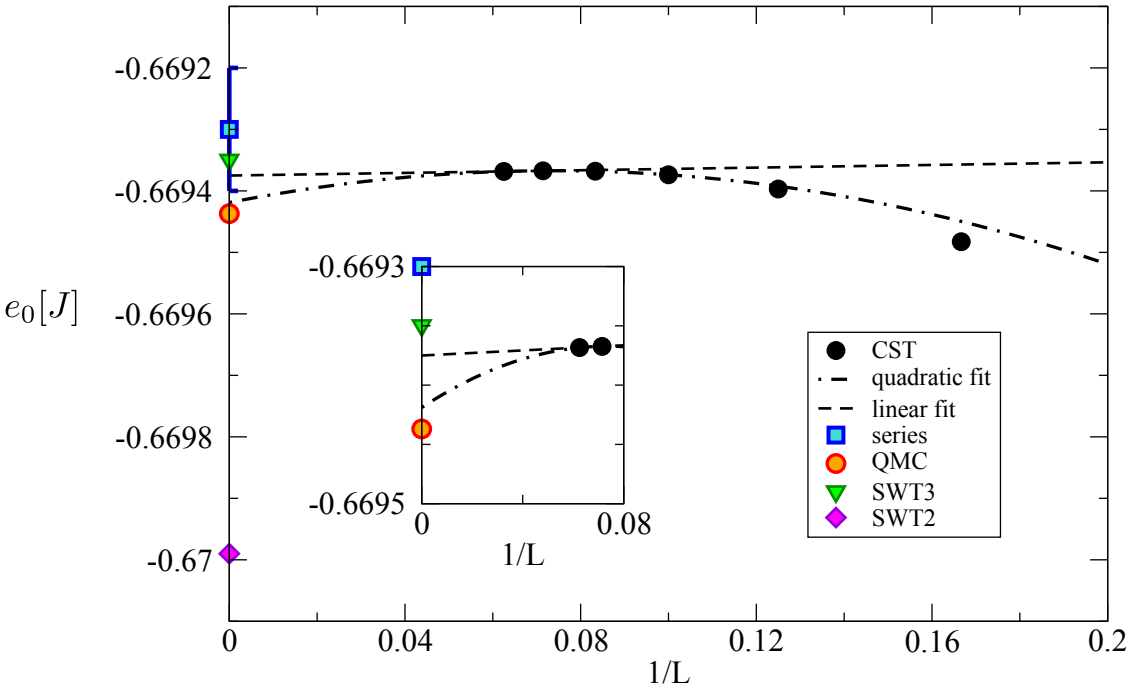

Figure 4.25: The CST data for the ground state energy per spin are compared to analytical results from perturbative spin wave expansions ($1/S^2$ and $1/S^3$) and to numerical results obtained in quantum Monte Carlo simulations [168] and high order series expansions from the Ising limit [202].

Spin wave velocity

The spin wave velocity v_c is defined as the slope of the magnon dispersion in the limit of long wavelengths [99] given by

$$v_c = |\nabla_{\mathbf{k}} \omega(\mathbf{k})|_{\mathbf{k}=0} \,. \tag{4.69}$$

In order to obtain an estimate of the spin wave velocity from discretized systems we are fitting the effective dispersion $\omega_{\text{eff}}(\mathbf{k})$ by a function of the form

$$f(|\mathbf{k}|) = a \cdot \sin(b\mathbf{k}) \tag{4.70}$$

in two distinct directions $v_1 = (k,k)$ and $v_2 = (k,0)$. We take only small momenta $\mathbf{k}_i$ into account, i.e., only the first two or three data points are considered depending on the actual system size. In addition, we require the function (4.70) to be periodic in the MBZ which fixes the parameter b. The concrete value of b depends on the considered direction.
The results are depicted in Figure 4.26. We fit the data by a third order polynomial in $1/L$ to estimate the spin wave velocity in the thermodynamic limit. In the thermodynamic limit the dispersion is expected to be isotropic in the limit of long wavelengths $\omega(\mathbf{k}) = v_c\,|\mathbf{k}|$. Indeed, for both directions we find that the spin wave velocity approaches a value of $v_c[v_1] = 1.667(2)J$ and $v_c[v_2] = 1.669(7)J$ which is in excellent agreement with series and QMC results [26, 168]. Note, that the function in (4.70) essentially resembles the dispersion of the next-leading order spin wave theory in both directions. Thus, the larger deviations of the fit in v_2 direction are due to the fact, that the renormalization of the dispersion along this direction is larger than

for the dispersion in v_1 direction which, on the contrary, is very well approximated by (4.70) along the whole MBZ.

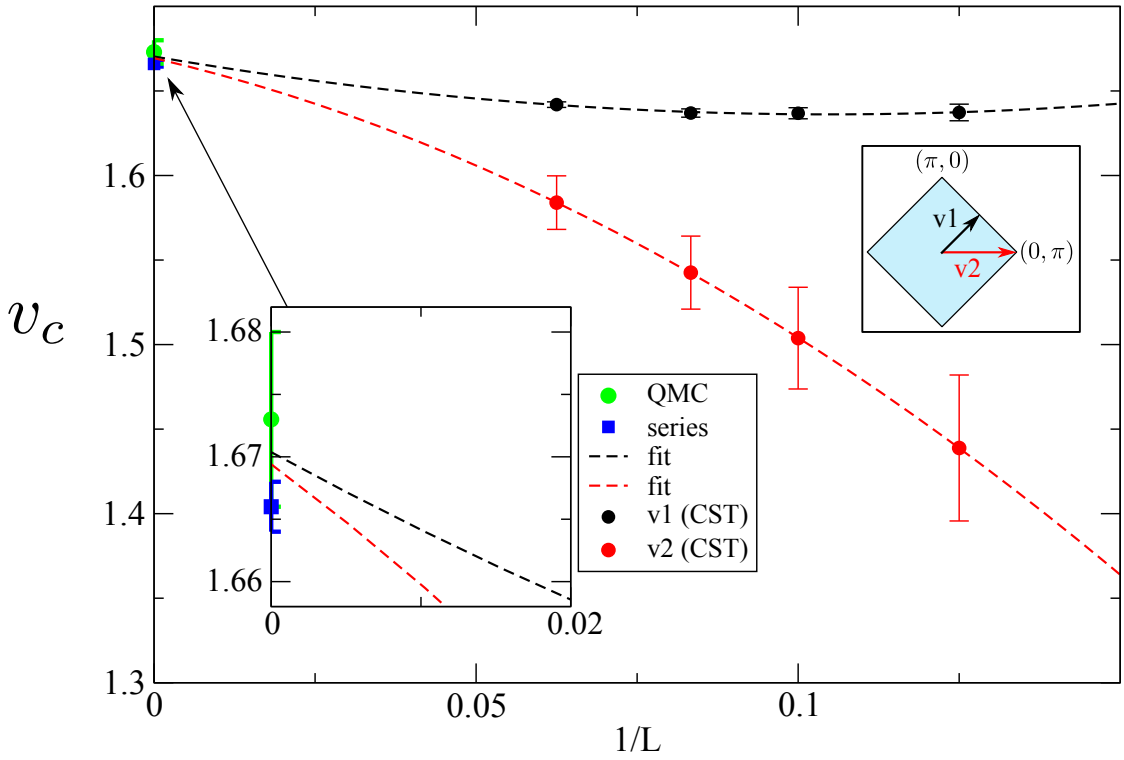

Figure 4.26: The spin wave velocity obtained by a fit of the CST data using (4.70) for two distinct directions v_1 and v_2. The data are compared to quantum Monte Carlo simulations (QMC) [168] and series expansions about the Ising limit [26].

4.4.2 High-energy properties

In this section the high-energy properties are addressed. The main focus is on high-energy magnons at the zone boundary of the MBZ where an anomalous dispersion is observed in numerical studies [25, 26] and experiments [27, 28, 190]. The data discussed in the following are partly published in Ref. [97].

Magnon dispersion

The anomalous dispersion at the zone boundary is quantified by the energy dip between $\mathbf{k}_{\text{min}} = (\pi, 0)$ and $\mathbf{k}_{\text{max}} = (\pi/2, \pi/2)$ as defined in (4.47).
The results for the effective one-magnon dispersion are shown in Figure 4.27. For $L = 16$ the dispersion exhibits an energy dip of $\delta_{\text{dip}} = 6.2\%$ which is a considerable improvement compared to the results of the conventional $1/S$-expansion. Extrapolating the values of the dispersion at momenta $(\pi/2, \pi/2)$ and $(\pi, 0)$ in $1/L$ yields a dip of $\delta_{\text{dip}} = 7.5\%$ which is in agreement with series and QMC results taking into account uncertainties of all methods.

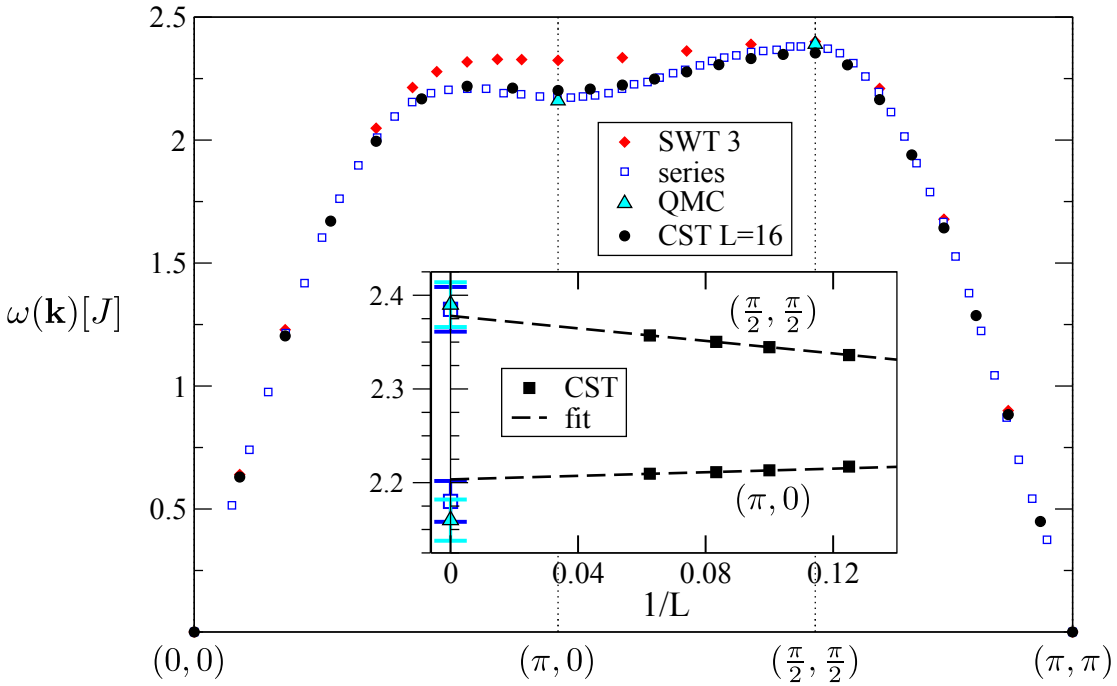

Figure 4.27: One-magnon dispersion along high symmetric paths in the magnetic Brilluoin zone obtained by the CST for $L = 16$ is depicted. The data are compared to quantum Monte Carlo simulations (QMC) [25] and series expansions about the Ising limit (series) [26] which were both extrapolated to the thermodynamic limit. Moreover, the dispersion of third order spin wave theory is displayed. The inset shows the extrapolation of the dispersion at momenta $\mathbf{k} = (\frac{\pi}{2}, \frac{\pi}{2})$ and $\mathbf{k} = (\pi, 0)$. This is a slightly modified version of FIG. 1 published in Ref. [97].[7]

Note, that the local minimum of the dispersion at $\mathbf{k} = (\pi, 0)$ is further depressed with increasing system size. This effect is neither observed in the $1/S$-expansions nor in the deepCST extrapolations which indicates that the relevant physical processes are indeed captured by the scaling dimension approach.

In the following, we examine the relevant ingredients from a technical point of view. To this end, we compare the respective flow equation systems of both approaches (see (4.3.2), section B.2 and Appendix B.1). After that, we provide a physical interpretation.

In fact, the comparison between both equation systems shows a noticeable difference besides the presence of hexatic terms in the deepCST which has a small effect anyway (see also section 4.2.3). In the scaling dimension approach the two-magnon interaction terms C_1, C_2 and C_3 are renormalized during the flow whereas the deepCST exhibits $\partial_\ell C_1 = \partial_\ell C_2 = \partial_\ell C_3 = 0$ which means that only the bare interactions are included. The coefficients C_1 and C_3 describe the interaction between two α or two β magnons and the coefficient C_2 corresponds to the α-β interaction (see also the diagrams in Figure 4.8). In order to highlight the relevance of the renormalized interaction, we evaluate the flow equations for different settings, switching off the corresponding flow of the $\alpha - \alpha/\beta - \beta$ interactions or the $\alpha - \beta$ interactions. The results are shown in Figure 4.28.

It can clearly be seen that the dip is considerably diminished if we neglect the renormalization of the α-β interaction (bare α-β). Moreover, the local minimum at $\mathbf{k} = (\pi, 0)$ increases for larger system size L. By contrast, switching off the α-α interaction (bare α-α) does not alter

[7] © 2015 American Physical Society

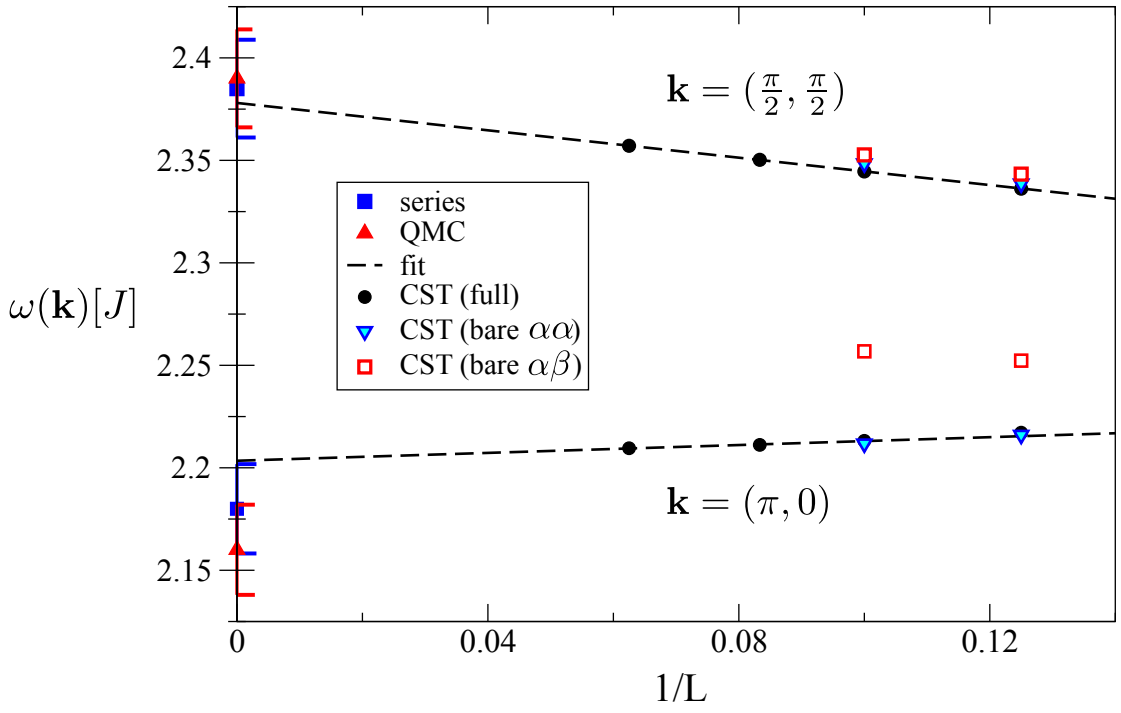

Figure 4.28: Results for the effective one-magnon dispersion at $\mathbf{k} = (\pi, 0)$ and $\mathbf{k} = (\frac{\pi}{2}, \frac{\pi}{2})$ obtained by sCSTs for which the flow of the α-α or α-β interaction is artificially switched off. This implies that only the corresponding bare interaction is taken into account (bare α-α or bare α-β).

the results significantly.
It can therefore be concluded that the interaction between $\alpha - \beta$ magnons plays a major role in the anomalous dipsersion at the zone boundary. At firs glance, this might be surprising because particle conserving interactions do not directly influence the flow of the dispersion, i.e., they do not appear on the right hand side of the flow equation in ∂_ℓ. However, in the isotropic HAF one-magnon states are linked with three-magnon states which in turn are affected by two-magnon interactions.
Note, that the impact of two-magnon interactions on the effective dispersion is mediated by the flow of C_6, and C_4 which describe the decay from one into three-magnon states and vice versa [203].[8] The relevant processes and their renormalization during the flow are illustrated in Figure 4.29. Regarding the energy dip at $(\pi, 0)$ the results suggest the following scenario.
Attractive magnon-magnon interactions shift spectral weight in the three-magnon continuum to lower energies pressing down the energy of single magnon states. The increased spectral weight at the lower edge of the continuum can lead to enhanced decay channels [51, 52] giving rise to a significant hybridization between one- and three-magnon states. Apparently, this effect is only captured correctly if the proper renormalization of the magnon-magnon interaction is taken into account. The influence of higher quasi-particle continua on the single quasi-particle dispersion is also observed in spin ladders [68].
In order to provide direct evidence for this interpretation, the multi-magnon continua have to be examined. In the following we analyze the two-magnon continuum, which is addressed by the longitudinal dynamic structure.

[8] Here the decay processes of the α magnons are considered. The corresponding processes for the β magnons are C_5 and C_7.

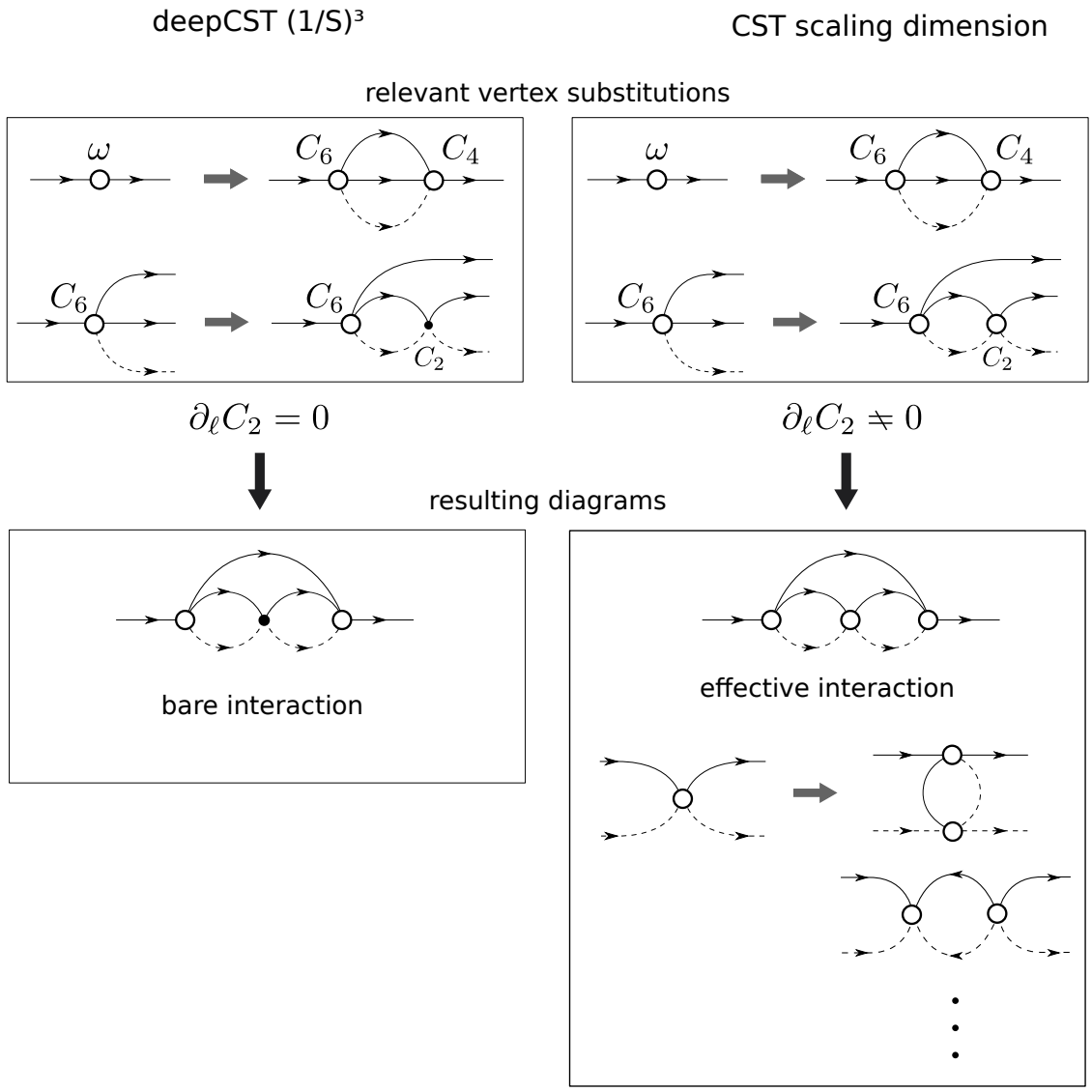

Figure 4.29: The diagrammatic representation of the dispersion renormalization induced by virtual fluctuations into three-magnon states is depicted. Diagrammatic from the deepCST in order $(1/S^3)$ and sCST for scaling dimension $d = 2$ are compared. The black circles represent bare vertices. Empty circles denote effective vertices. The corresponding diagrammatic contributions can be obtained by a successive substitution of the effective vertices based on the substitution rules defined in the flow equation (for details see section 2.4.2). In the deepCST only the bare α-β interaction C_2 is taken into account.

Longitudinal dynamic structure factor

The spectral density of the longitudinal dynamic structure factor defined in (4.59a) provides information about the two-magnon continuum.
The results of the longitudinal dynamic structure factor along symmetric paths in the MBZ are shown in Figure 4.30. In addition, the corresponding spectral density at $(\pi, 0)$ and $(\frac{\pi}{2}, \frac{\pi}{2})$ is depicted in Figure 4.31. The line shapes in Figure 4.31 are well converged except for slight wobbles at the lower edge of the continuum due to finite size effects. A higher resolution requires the inclusion of further coefficients in the continued fraction representation.
We compare the line shapes of the interacting case and the non-interacting case. The results clearly show that the α-β interaction gives rise to a considerable shift of spectral weight to the lower edge of the continuum. This is an indication for a considerable attraction between α-β magnons on short length scales. Calculations based on a $S = 0$ singlon approach for the two dimensional Heisenberg antiferromagnet support our observation [191].
Note, that the effects of interactions are not captured by conventional perturbative approaches in $1/S$ [201]. The line shapes of the non-interacting case, however, are very similar to those obtained in Ref. [201].
The $\alpha-\beta$ pairs are longitudinal $S^z_{\text{tot}} = 0$ states, also referred to as longitudinal magnons [204–206]. The shift of spectral weight in this channel leads to the formation of a resonance which is located at the lower edge of the continuum. This resonance can be interpreted as a longitudinal mode with finite lifetime. In the literature the longitudinal mode is also referred to as the amplitude or Higgs mode of the continuously broken SU(2) symmetry [206].
The occurrence of Higgs modes in condensed matter is a fascinating topic which is subject of current research [206, 207]. For instance a Higgs mode was observed via neutron scattering in the antiferromagnetically ordered phase of $TlCuCl_3$ by applying high pressure [205]. The presence of a Higgs mode is also predicted by the effective field theory of Raman scattering for the two dimensional quantum antiferromagnet [208]. The corresponding observable couples only to the $\mathbf{Q} = 0$ modes. By contrast, our results provide information about momentum resolved spectral properties. The existence of a Higgs mode in the two dimensional quantum antiferromagnet is also supported by numerical studies [209].
According to our discussion in the previous section, the significant increase of spectral weight at the lower edge of the two-magnon continuum can have a relevant impact on the one-magnon dispersion. Single magnons decay into three-magnon states which are essentially a magnon and a Higgs resonance as illustrated in Figure 4.32. As the energy of the Higgs resonance is lowered at $\mathbf{Q} = (\pi, 0)$ the corresponding magnon-Higgs continuum is pressing down the energy of the single magnon state by means of quantum level repulsion. Such effects are well studied within CUTs for various gapped systems [51, 52]. Based on this view, we can take the roton minimum as an indication for magnon-Higgs scattering [97].

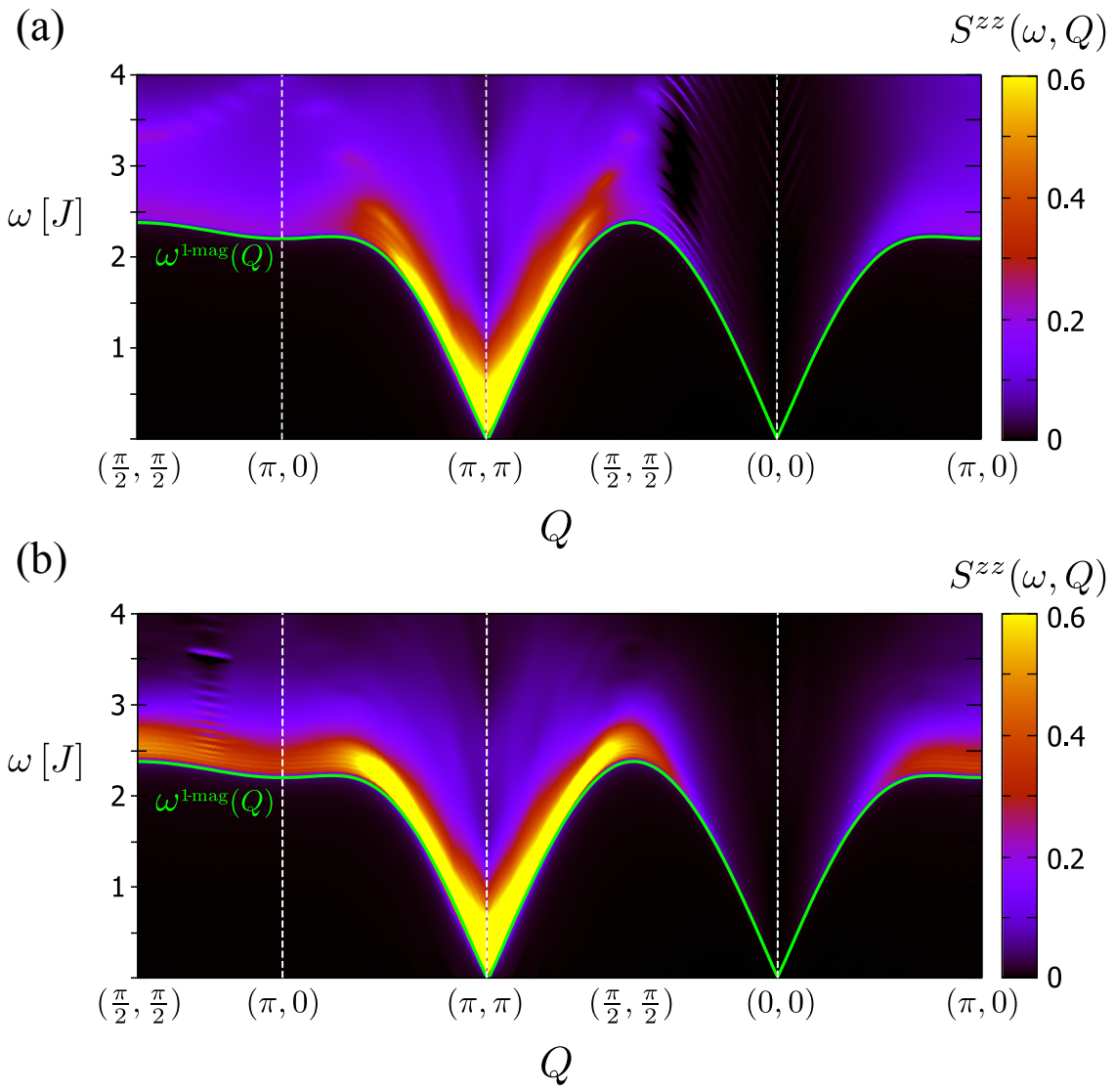

Figure 4.30: A contour plot of the longitudinal dynamic structure factor along symmetric paths in the MBZ is shown. The line shapes are obtained from the $L = 144$ system using a finite broadening $\delta = 0.02J$ in the corresponding continued fraction representation. The upper panel (a) depicts the non-interacting case. In (b) the α-β interaction is taken into account. The green line shows the one-magnon dispersion which defines the lower edge of the continuum.

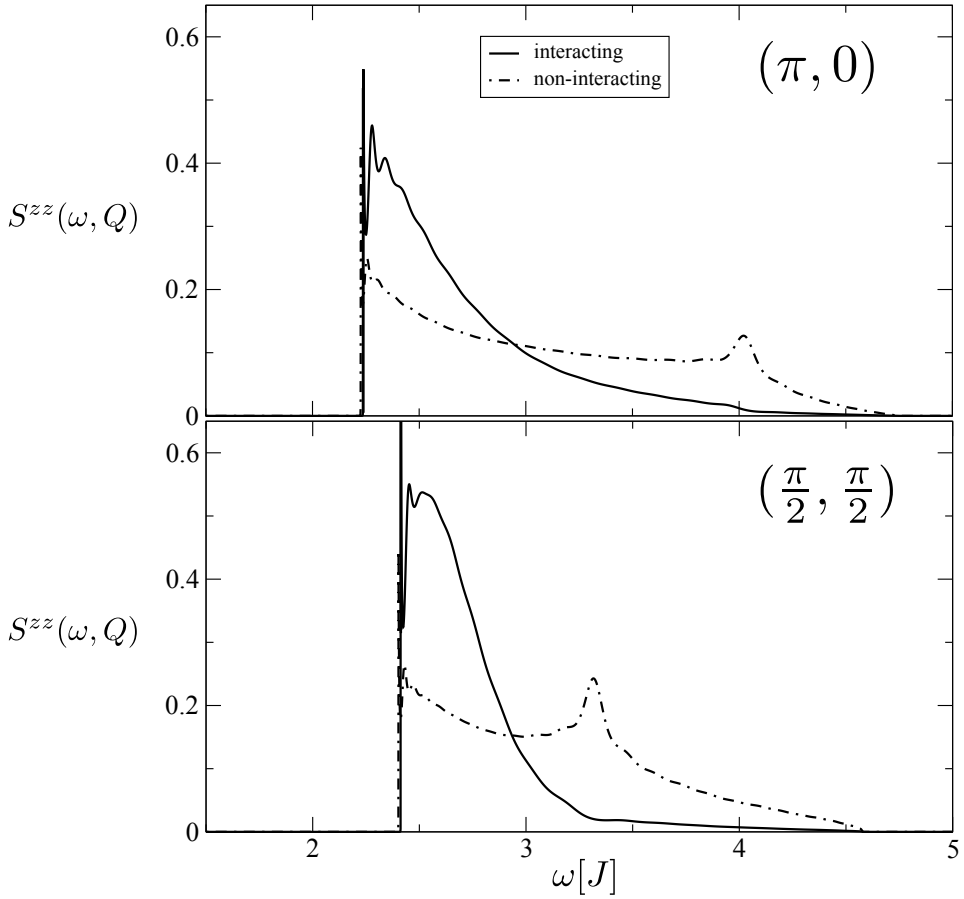

Figure 4.31: Longitudinal dynamic structure factors at $\mathbf{Q} = (\pi, 0)$ and $\mathbf{Q} = (\frac{\pi}{2}, \frac{\pi}{2})$ for the interacting and non-interacting case are displayed. The continuous line shapes are determined for a system with $L = 192$ using a square root terminator for the continued fraction coefficients at $n > 21$.

Comparing the line shapes at $\mathbf{Q} = (\pi, 0)$ and $\mathbf{Q} = (\frac{\pi}{2}, \frac{\pi}{2})$ we see a different qualitative behavior at the lower edge of the two-magnon continuum. Apart from slight wobbles due to finite size effects, the continuum at $\mathbf{Q} = (\pi, 0)$ increases in form of a ramp which may be a precursor for the formation of a bound state. Indeed, this feature is reminiscent of the the build-up of a bound-state observed in the antiferromagnetic two leg ladder [13]. We may infer that the Higgs resonance is very close in energy or even degenerate with the one-magnon dipsersion at $\mathbf{Q} = (\pi, 0)$. By contrast, the resonance at $\mathbf{Q} = (\frac{\pi}{2}, \frac{\pi}{2})$ is higher in energy and the line shape seems to flatten above the lower edge of the continuum suggesting that the impact of two-magnon attraction is weaker at this wavelength. However, we stress that the finite size wobbles at the lower edge preclude a precise and definitive assessment of sharp features at the lower edge.

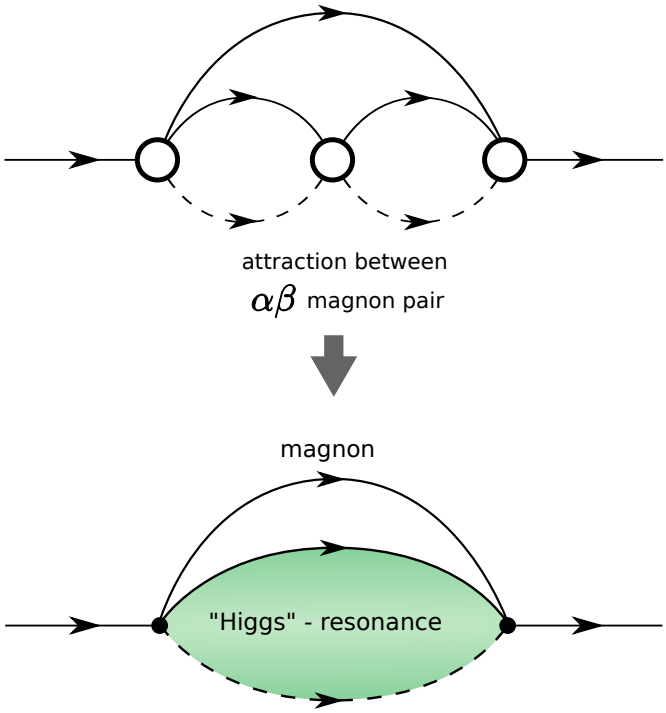

Figure 4.32: The diagrammatic representation of magnon Higgs scattering in the renormalization of the effective one-magnon dispersion is depicted. In order to capture this effect quantitatively, a proper renormalization of two-magnon interactions is required.

In the next sections we provide a comprehensive analysis of the single magnon weights and multi-magnon continua. In this context, we also address the three-magnon continuum which constitutes the incoherent part of the transverse dynamic structure factor. First, the static structure factors, i.e., the spectral weights, are examined and compared with numerical data. After that, we compare the dynamic structure factors with experimental data.

4.4.3 Static structure factors

In the following we compare our results for the static structure factors with numerical data obtained by quantum Monte Carlo simulations(QMC) [25] and series expansions about the Ising limit [26].
First, we check if the sum rules in the longitudinal and transverse channel defined by

$$S_{\mathrm{l}}^{\mathrm{tot}} = \int_{BZ} d\mathbf{Q} \int d\omega S^{zz}(\mathbf{Q},\omega) \quad = S^2 \tag{4.71a}$$

$$S_{\mathrm{t}}^{\mathrm{tot}} = \frac{1}{2}\int_{BZ} d\mathbf{Q} \int d\omega S^{xx+yy}(\mathbf{Q},\omega) \; = S \tag{4.71b}$$

[26] are retained in the CST. Note, that we do not track the constant term in the longitudinal observable which is given by a δ-peak at $\mathbf{Q} = (\pi,\pi)$. Without this term the integrated effective structure factor corresponds to the reduced value $\tilde{S}_{\mathrm{l}}^{\mathrm{tot}} = S^2 - M^2$ where M is the magnetization of the system. We evaluate the sums for $L = 8$ up to $L = 12$ and extrapolate the results in $1/L$ to obtain the corresponding value in the thermodynamic limit. For the total transverse weight we find $S_{\mathrm{t}}^{\mathrm{tot}} \approx 0.495 = 0.99S$. Moreover, we obtain $\tilde{S}_{\mathrm{l}}^{\mathrm{tot}} \approx 0.1461$ or $S_{\mathrm{l}}^{\mathrm{tot}} \approx 0.2403 = 0.96S^2$ if we assume a magnetization of $M = 0.307$ [25, 168, 193]. The small deviations of 1-4% can be ascribed to truncation errors of the CST as well as finite size errors. Note, that the longitudinal and transverse structure factor diverge as they approach the ordering wave vector $\mathbf{Q} = (\pi,\pi)$ leading to larger deviations for finite discretizations of the Brillouin zone. Taking into account these uncertainties we may infer that the sum rules are indeed retained in the CST.
In addition, in Figure 4.33 the CST results for the static structure factors are compared to the data from series expansions [26]. The plot shows CST data for $L \to \infty$ which are obtained by an linear extrapolation in $1/L$. The overall agreement is convincing.

Next, we consider the single-magnon fraction of the total transverse weight which is defined by

$$\frac{W_1(\mathbf{Q})}{W_{1+3}(\mathbf{Q})} = \frac{W^{1\mathrm{mag}}}{W^{1\mathrm{mag}} + W^{3\mathrm{mag}}} \quad . \tag{4.72}$$

It quantifies the hybridization between the one-magnon state at $\mathbf{k} = \mathbf{Q}$ with the corresponding three-magnon continuum. Lower values of $\frac{W_1(\mathbf{Q})}{W_{1+3}(\mathbf{Q})}$ indicate larger hybridization effects, i.e., more spectral weight is shifted to the three-magnon continuum.
A comparison between the corresponding CST and QMC data is shown in Figure 4.34. At $\mathbf{Q} = (\pi, 0)$ the one-magnon state comprises only 58% of the total weight which agrees very well with the QMC data. For finite system size the CST and QMC results match reasonably well at $\mathbf{Q} = (\frac{\pi}{2}, \frac{\pi}{2})$. The linear extrapolation $1/L$ yields $\frac{W_1(\mathbf{Q})}{W_{1+3}(\mathbf{Q})} \approx 82\%$ which is marginally lower than the QMC prediction of $85 \pm 1\%$. At $\mathbf{Q} = (\frac{\pi}{2}, \frac{\pi}{2})$ the three-magnon continuum holds a significant amount of the total transverse weight. By contrast, there is only 18% in the three-magnon continuum at $\mathbf{Q} = (\frac{\pi}{2}, \frac{\pi}{2})$.
The results clearly support our view that the roton minimum is caused by hybridization effects between one- and three-magnon states. This picture is also consistent with experimental observations for various cuprates [28, 29, 190, 210].

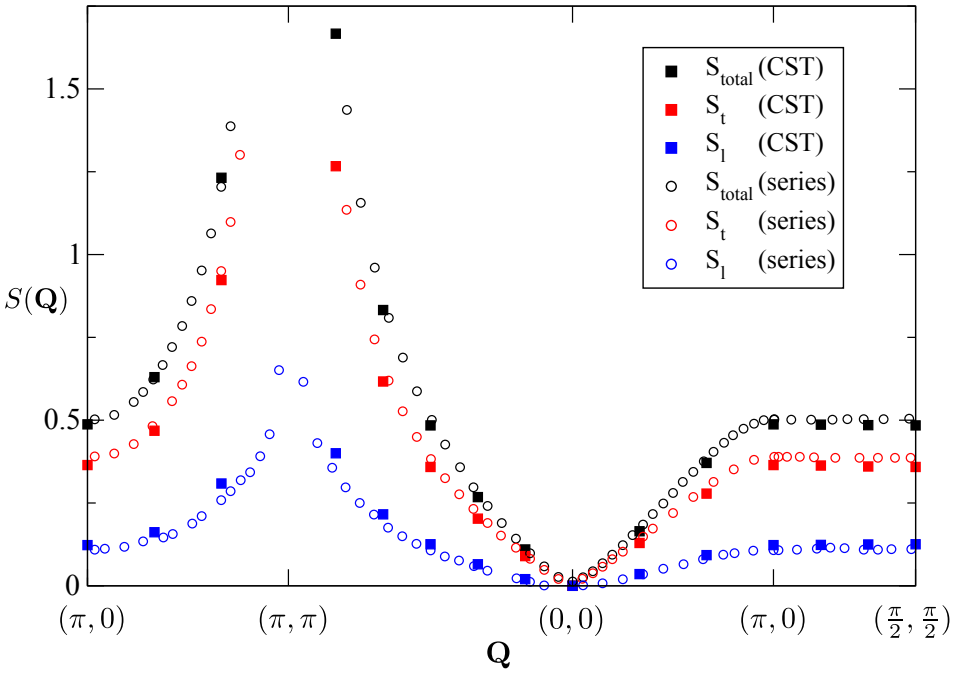

Figure 4.33: Results for the effective longitudinal, transverse and total static structure factor are compared with data obtained by series expansion about the Ising limit [26]. The series data are extracted from the corresponding figures in Ref.[26] using the Web Plot Digitizer [211]

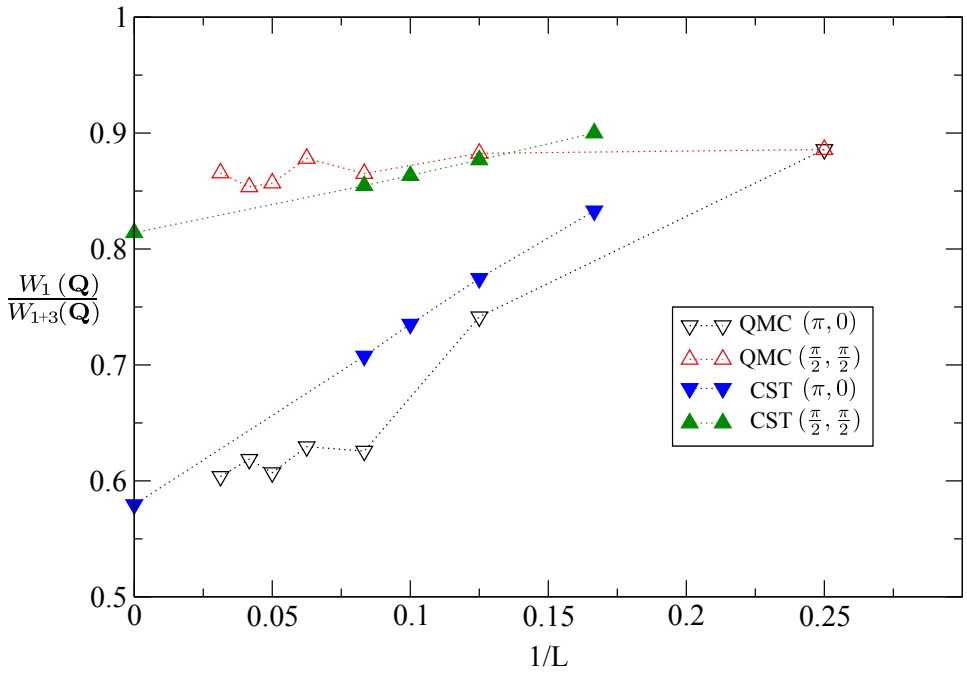

Figure 4.34: Single-magnon fraction of the total transverse weight is compared with data obtained by quantum Monte Carlo simulations [25]. The QMC data are extracted from the corresponding figures in Ref.[25] using the Web Plot Digitizer [211]

Next, we compare the spectral weights for both, transverse and longitudinal magnons. To this end, we consider the ratio between the longitudinal and transverse static structure factor $2S_l(\mathbf{Q})/S_t(\mathbf{Q})$ as defined in Ref. [25] and Ref. [26]. The results are displayed in Figure 4.35. Although there is a qualitative agreement between the results of QMC and series expansions, both methods yield different absolute values. We stress that both results are supposed to represent the thermodynamic limit. The authors in Ref. [26] suggest that finite size effects in the QMC simulations may account for this discrepancy. Surprisingly, the CTS data for $L = 12$ match the series expansion results, whereas the extrapolated CST data for $L \to \infty$ comply with the QMC results. The origin of these deviations is not clear which precludes a conclusive judgment. Nevertheless, we may infer that the effective spin wave description provides very consistent results since the overall agreement with the numerical data is very convincing.
The static structure factors examined in this section provide information about the static correlations in the system. In order to understand the dynamic properties, we also address the dynamic structure factors in the following.

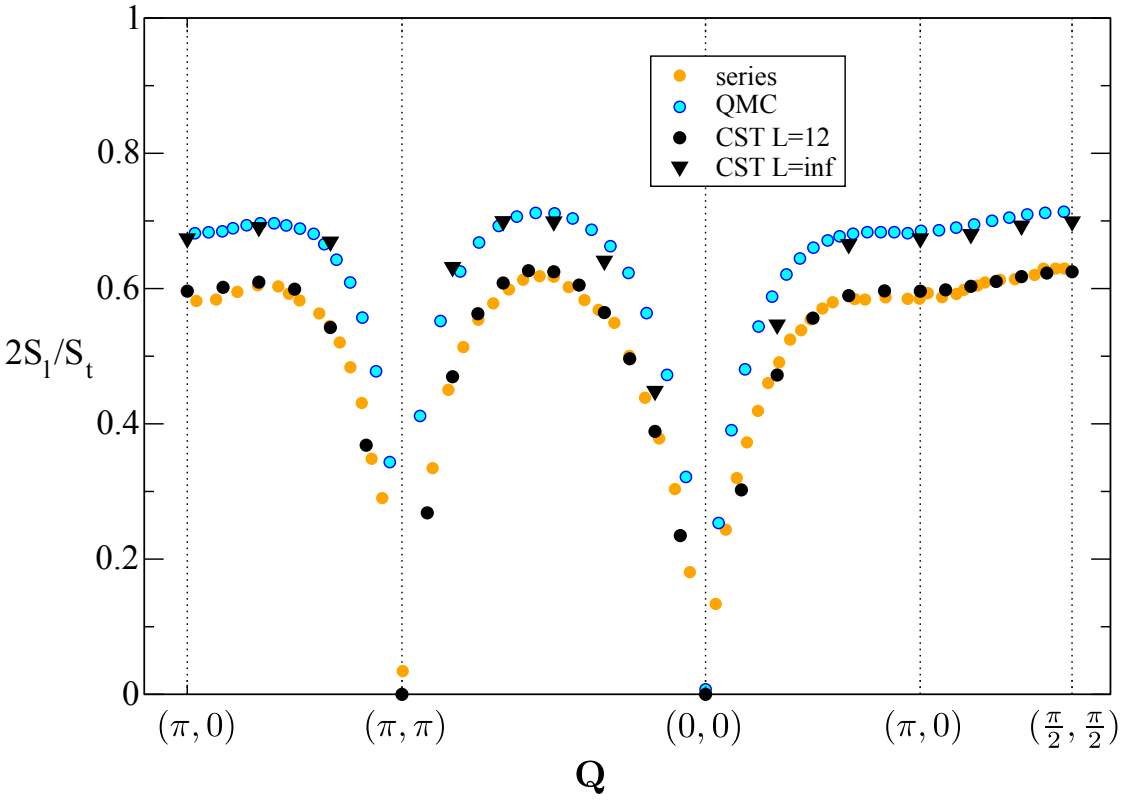

Figure 4.35: Ratio of longitudinal and transverse static structure factors is compared with series expansion about the Ising limit (series) and quantum Monte Carlo simulations (QMC). The QMC and series data are extracted from FIG. 5 in Ref.[26] using the Web Plot Digitizer [211]

4.4.4 Comparison with the experiment

In this section the results of the effective spin wave model are compared to experimental data obtained in inelastic neutron scattering of CFTD (copper formiate tetrahydrate deuterated) [28]. CFTD is known as a very good realization of the quantum antiferromagnet on the square lattice [179, 180, 212]. The experiment in Ref. [28] provides measurements which allow the distinction between the dynamic correlations of longitudinal and transverse excitations by means of the polarization of the neutrons. The experimental data was kindly provided by N. B. Christensen and H. M. Rønnow. The presented theoretical data are published in [213].
For a comparison between the theoretical results and the experimental data further information is required. One has to identify the concrete value of the exchange coupling J which defines the experimental energy scale as well as the proportionality constant between the DSFs and the measured counting rate. Both values are obtained from a fit of the theoretical results to the experimental data. Moreover, the line shapes depend on the broadening σ which is supposed to resemble the finite resolution in the experiment. Thus, the broadening is considered as an additional fit parameter. We distinguish between the broadening in the transverse channel σ_t and the longitudinal channel σ_l. Technical details concerning the calculation of the DSFs are explained in Appendix C.

The main results for the DSFs are depicted in Figure 4.36.
To fit the theoretical curves to the experimental data we proceed as follows. The experimentally measured intensities in the transverse channel at $\mathbf{Q} = (\pi, 0)$ and $\mathbf{k} = (\frac{\pi}{2}, \frac{\pi}{2})$ (see (c) and (d) in Figure 4.36) exhibit pronounced peaks which we identify as the one-magnon peaks. We use these resolution limited peaks to fit the corresponding one-magnon energies at $\mathbf{k} = (\pi, 0)$ and $\mathbf{k} = (\frac{\pi}{2}, \frac{\pi}{2})$ which sets the energy scale to $J = 6.11(2)$ meV. The consistency of the determined energy scale can be assessed by a comparison of the theoretical and experimental one-magnon spectrum. The resulting curve of the effective dispersion agrees very well with the experimental data as shown in Figure 4.36.
After that, the broadening and overall height of the line shapes is fitted to match the resolution of the experiment and the measured intensity. The broadening is set to $\sigma_t = 0.58(2)$ meV for the transverse channel and $\sigma_l = 1.41(5)$ meV for the longitudinal channel. We stress, that the units of the energy axis and y-axis are fixed globally for both, the transverse and longitudinal channel.
The good overall agreement between the theoretical curves and the experimental data in Figure 4.37 is convincing. First, we address the total DSF which is obtained by the sum of the transverse and longitudinal DSFs. The position and the height of the pronounced one-magnon peaks as well as the continuum tail are captured by the theoretical line shapes in a quantitatively correct way. The slight wobbles in the continuum are due to the finite discretization of the Brillouin zone.
In the transverse channel we distinguish between the one-magnon contribution which is given by a Gaussian distribution function (dashed magenta line) and the three-magnon continuum which is highlighted in blue. A noticeable feature observed in the experiment is the pronounced continuum tail at $\mathbf{Q} = (\pi, 0)$. By contrast, there is only a marginal amount of spectral weight in the continuum at $\mathbf{Q} = (\frac{\pi}{2}, \frac{\pi}{2})$. Both aspects, are captured with remarkable accuracy by the theoretical line shapes.
To emphasize the crucial relevance of the two-magnon interaction, we determine the three-magnon continuum for the non-interacting case which is represented by the green curve. The difference between the magnon continuum for the interacting and non-interacting case at

$\mathbf{Q} = (\pi, 0)$ is striking. If we neglect the two-magnon interaction the spectral weight is shifted to higher energies leading to a clear mismatch with the experimental findings. Thus, we infer that the enhanced continuum tail observed in the experiment is a direct consequence of attractive two-magnon interactions.
A similar observation applies to the longitudinal channel. The CST results agree very well with the experimental data. This clear match is obviously spoiled by the omission of the magnon interaction. Consequently, the pronounced signals in the measured intensities can be directly identified as the longitudinal resonance or Higgs resonance.
Figure 4.38 shows a qualitative comparison between the total dynamic structure factor obtained by the CST and the experimental results for a representative cut through the Brillouin zone. It is supposed to underline the consistency of the CST data for all wavelengths. Characteristic low and high-energy features of the magnons are equally well described by our theoretical results.

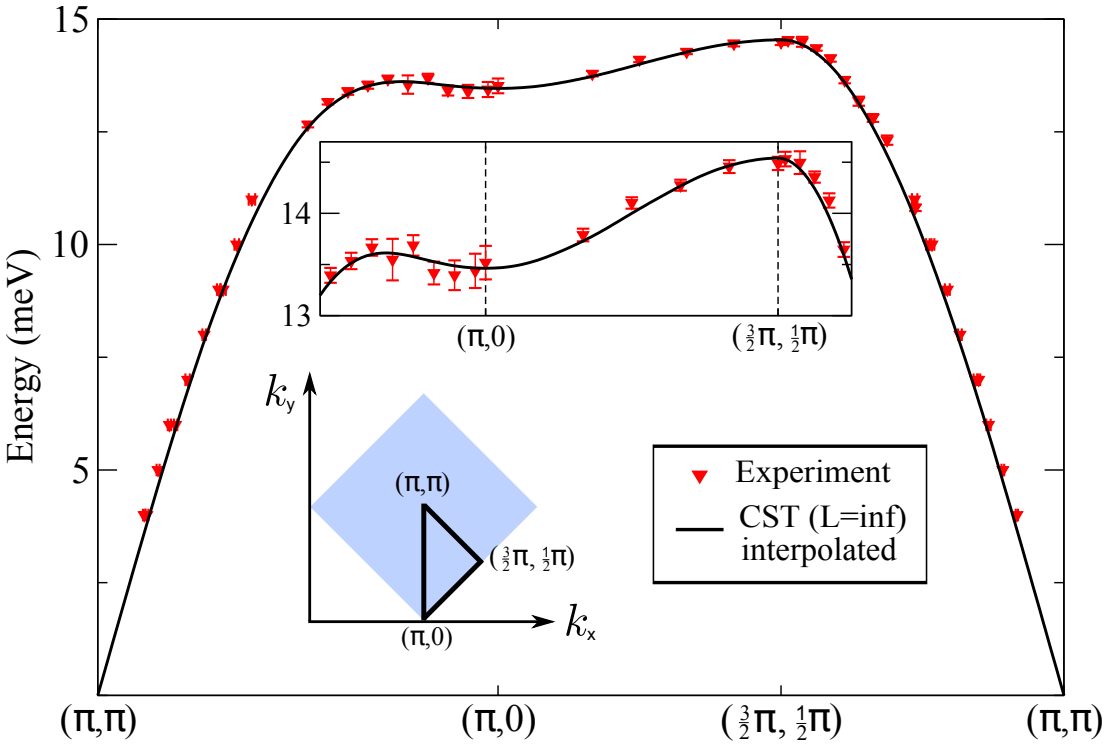

Figure 4.36: The effective one-magnon dispersion and the corresponding experimental data from Ref. [28] are shown for a representative path in the magnetic Brillouin zone (lower inset). The solid line of the dispersion is obtained by an extrapolation of the CST data on a finite mesh of momenta and a subsequent Lanczos interpolation. The energy scale is set to $J = 6.11(2) meV$. The figure is taken from Ref. [213]

.

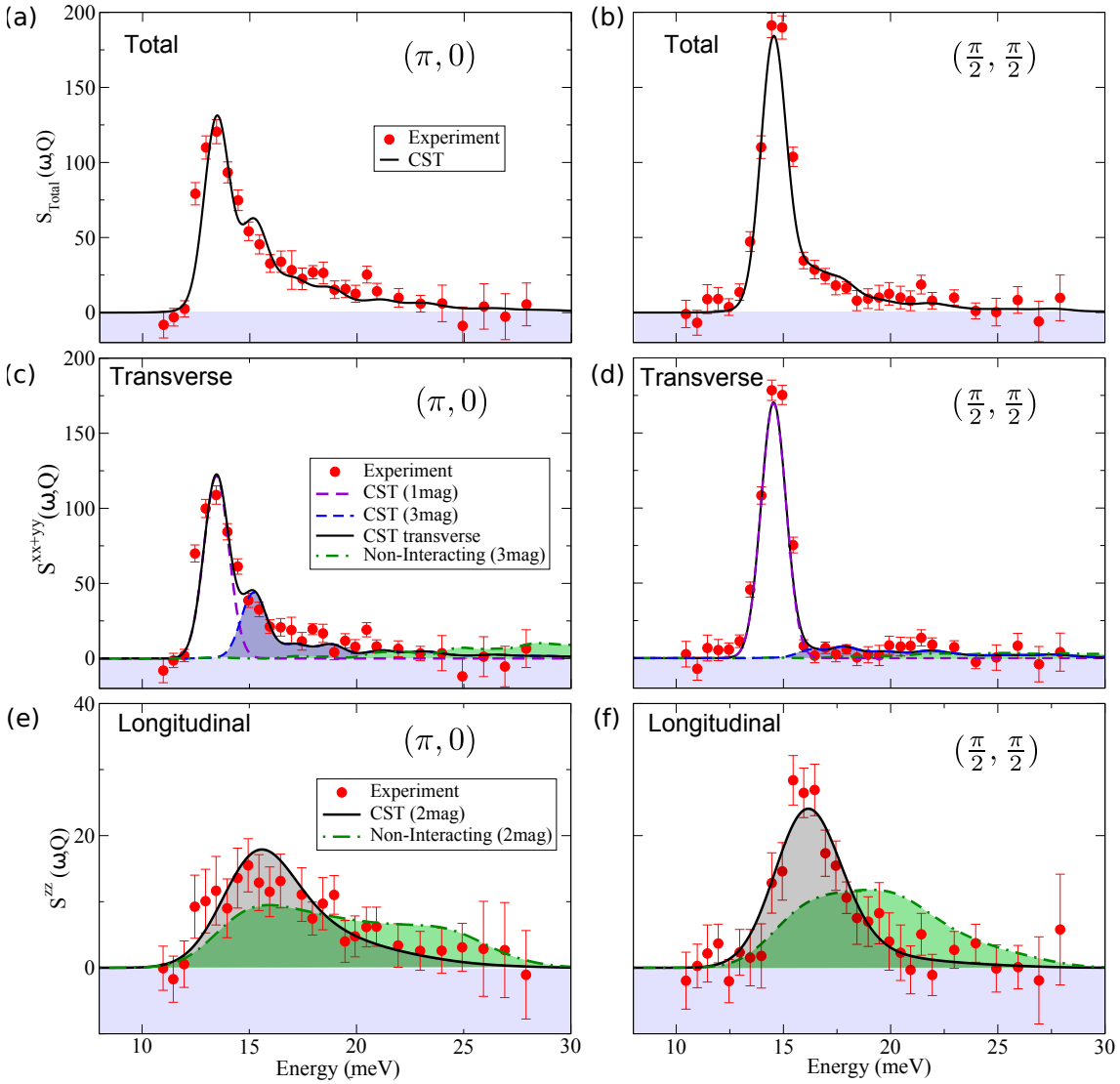

Figure 4.37: Comparison between the dynamic structure factors measured in Ref.[28] and the corresponding line shapes obtained from the continuous similarity transformation. The energy scale is fitted to $J = 6.11(2)$ meV for all curves. (a) and (b) show the total structure factor at momenta $\mathbf{Q} = (\pi, 0)$ and $\mathbf{Q} = (\frac{\pi}{2}, \frac{\pi}{2})$. The corresponding transverse channel of the dynamic structure factor is shown in (c) and (d). The broadening is set to $\sigma_t = 0.58(2)$ meV. The magenta dashed line shows the resolution limited one-magnon peak. The blue and the green line show the three-magnon continuum for the interacting and non-interacting case. For better visibility the area enclosed by the corresponding curves is highlighted in blue or green, respectively. The black solid curve represents the sum of the one- and interacting three-magnon contribution. The two-magnon continuum in the longitudinal channel is displayed in (e) and (f). Here the broadening is set to $\sigma_l = 1.41(5)$ meV. The interacting case is emphasized by a grey shade. The green line represents the non-interacting case. The figure is taken from Ref. [213].

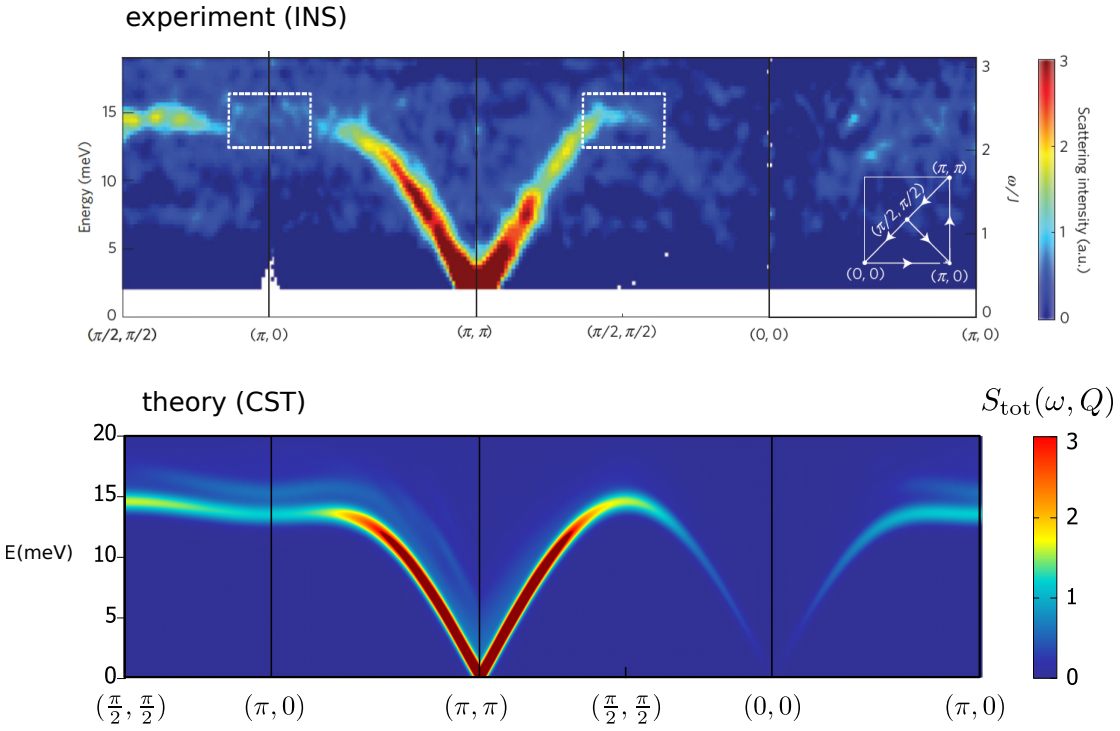

Figure 4.38: Qualitative comparison of the total dynamic structure factor for a representative path in the Brillouin zone. The upper panel depicts the experimental findings from Ref. [28]. The lower panel represents the CST data. The color code and the corresponding scale are fitted to match the experimental data. The energy scale is set to $J = 6.11(2)$ meV. The figure in the upper panel is extracted from Figure 1 in Ref. [28].[9]

4.4.5 Concluding discussion

In the following we give a brief resumé about the results obtained in this final section. We have shown that the effective magnon model obtained by the continous similarity transformation (CST) for scaling dimension $d = 2$ yields quantitatively correct results for magnons in the two dimensional quantum antiferromagnet. The comparison of the low- and high-energy properties of magnons and their static correlations with various numerical studies exhibits a considerable overall agreement. Moreover, the CST results account for various features observed in the experiment [28, 29] showing a very convincing agreement for the dynamic structure factors. In particular, our approach provides quantitatively correct results for the roton mininum and the pronounced continuum tail in the transverse dynamic structure factor at $\mathbf{k} = (\pi, 0)$. This is indeed an important finding, because previously these features were interpreted as evidence of a fractionalization of magnons into spinons [28].
By contrast, our results show that all these aspects can be understood by means of a comprehensive magnon description. The crucial point is the proper incorporation of attractive magnon interactions which lead to the formation of a resonance in the longitudinal channel. This resonance can be interpreted as the amplitude or Higgs mode with finite lifetime. Based on this picture the roton minimum and the significant continuum tail at $\mathbf{k} = (\pi, 0)$ in the transverse channel can be attributed to a hybridization between one- and three-magnon states which is mediated by magnon-Higgs scattering [97]. Thus, the nature of high-energy magnons is finally clarified.

CHAPTER 5

Concluding summary

This chapter gives a concluding summary of the main methodical advancements and scientific results achieved in this thesis. After that we give a brief outlook pointing out the relevance of our advancements for possible future applications and developments.

5.1 Summary

In the first part of this thesis the method of continuous unitary transformations is introduced. This method provides a powerful tool to derive effective low energy models for many body systems based on a quasi-particle description. In particular, the method leads to an effective model where the number of quasi-particles is conserved providing a considerable simplification of intricate many body problems.
An important part of this thesis is the development of a CUT method for gapless quasi-particles in systems with long range order. For practical evaluations of CUTs physically justified truncation schemes are required. Conventional CUT approaches are truncated in real space which limits their application to systems with finite correlation length, i.e. with finite energy gap.
Therefore, the CUT method is extended to its use in momentum space. This representation circumvents generic problems of real space approaches and gives rise to new kinds of truncation schemes. In particular, the scaling dimension of operator terms is identified as an appropriate truncation criterion for gapless quasi-particles.
Moreover, a diagrammatic representation of momentum space operators is introduced which simplifies the derivation of flow equations in momentum space and visualizes intricate renormalization effects which arise in perturbative and non-perturbative momentum space CUTs.

In the second part of the thesis the developed approach is applied to a concrete physical problem. The aim is a comprehensive and quantitative description of gapless magnons in the antiferromagnetic spin-1/2 Heisenberg model on the square lattice. This model is a canonical example of long range ordered quantum magnets. Furthermore, it is of major relevance for the understanding of high-T_c superconductors because it describes a large class of undoped cuprates [17].
Although the excitations at long wavelengths are very well understood in terms of spin wave theory their nature at short wave lengths (high energies) is not clarified, yet. Numerical and

experimental data indicate an energy dip at $\mathbf{k} = (\pi, 0)$ which is also referred to as a roton minimum [30]. This phenomenon is not captured by conventional spin wave calculations [30, 31]. As a consequence of this seeming failure, a fractionalization of magnons into spinons is debated [28, 29].

The working hypothesis of this thesis is that spin wave theory does account for the roton minimum if the interaction between spin waves is taken into account properly. Technically, this is achieved by means of the momentum space CUT developed in the first part.

The initial point of the CUT approach is the antiferromagnetic Heisenberg Hamiltonian in the Dyson-Maleev representation [192, 195]. An important advantage of the Dyson-Maleev representation is that the spin wave interactions are expressed exactly on a quartic level in boson operators. However, the corresponding Hamiltonian is superficially non-hermitian and, thus, the CUT has to be generalized to a continuous similarity transformation (CST).

The resulting flow equations are truncated by means of the scaling dimension of operator terms. At scaling dimension $d = 1$ the quartic terms are neglected which corresponds to next leading order spin wave theory. For the effective spin wave description we additionally incorporate the quartic operator terms performing a self similar CST (sCST) for scaling dimension $d = 2$.

The coefficients of the effective Hamiltonian are calculated for finite discretizations of the magnetic Brilluoin zone (MBZ). Their values in the thermodynamic limit are obtained by extrapolations in the inverse system length $1/L$. In addition, we transform the observables of the longitudinal and transverse dynamic structure factors which are required for a direct comparison with experimental data of inelastic neutron scattering.

The resulting effective model indeed provides a comprehensive picture of spin waves for all lengths scales. It captures both aspects in a quantitative fashion, the gapless nature of spin waves at long wavelengths, as well as the roton minimum of high-energy magnons at short wavelengths. For the analysis of the low energy regime the ground state energy per spin e_0 and the spin wave velocity v_c are determined. The effective model exhibits $e_0 = -0.669419(6)J$ and $v_c = 1.667(2)J$ which is in excellent agreement with the literature [25, 26, 168, 194].

The resulting effective one-magnon dispersion in the thermodynamic limit exhibits an energy dip of $\delta \approx 7,5\%$. This is a considerable improvement compared to conventional spin wave approaches which yield only values of $\delta = 1\% - 3\%$ [30, 31]. Most importantly, the results are in agreement with experimental and numerical data which suggest an energy dip of $\delta = 7\% - 9\%$ [25–28, 190].

A key step of our approach is the proper renormalization of the magnon interaction. Thus, we also examine the spectral properties of the multi-magnon continuum by means of the longitudinal and transverse dynamic structure factors. In particular, a strong attraction between spin waves at short wave lengths is observed. This attraction leads to a resonance of magnon pairs in the longitudinal channel which can be interpreted as the amplitude or Higgs mode of the continuously broken SU(2) symmetry with finite lifetime [97, 206].

Based on the effective model the origin of the roton minum dip can be understood as follows. In the initial Hamiltonian single magnons decay into three magnon-states which are essentially a magnon and a Higgs resonance. At $(\pi, 0)$ the scattering between magnons and the longitudinal resonance leads to strong hybridization of one and three-magnon states which in turn becomes manifest in a significant three-magnon continuum. Thereby, the single-magnon energy is reduced giving rise to the roton minimum at $(\pi, 0)$. Moreover, the weight of the single-magnon peak at $(\pi, 0)$ holds only 58% of the total weight giving rise to a significant three-magnon continuum tail. By contrast, at $(\frac{\pi}{2}, \frac{\pi}{2})$ only a marginal hybridization with the

three-magnon continuum is observed. These results are in quantitative agreement with experimental findings obtained by inelastic neutron scattering of CFTD [28, 29] which is an almost ideal realization of the square lattice quantum antiferromagnet [177, 179]. Furthermore, the CST results for the static structure factors are consistent with quantum Monte Carlo simulations [25] and series expansions about the Ising limit [26].
The good agreement with numerical data and the fact that the effective model accounts for relevant features observed in experiments [28, 29] strongly suggest that spin wave theory is indeed a valid description of the elementary excitations in the whole MBZ, i.e., at all length scales. The long standing problem of high-energy spin waves in a large class of undoped cuprates is therefore solved.

5.2 Outlook

The method developed in this thesis opens up new possibilities for the theoretical description of gapless excitations in a multitude of systems with long range order. A fascinating field of current research are quantum phase transitions between magnetically ordered phases and magnetically disordered quantum systems which are induced by geometric frustration [214]. A canonical example for this scenario is the J_1-J_2 model defined by the Heisenberg antiferromagnet with next nearest neighbour exchange J_2 which induces geometric frustration between spin orientations [215].
It is known that this frustrated Heisenberg model exhibits collinear long range order for large values of (J_2/J_1), long range Néel order for small values of (J_2/J_1) and a non-magnetic phase for intermediate values which are dominated by frustration effects [216]. The existence of such an intermediate phase attracted a huge amount of attention in the search for resonating valence bond states [188, 215–217]. In particular, a spin liquid phase is expected in the presence of large frustration [218, 219]. However, the nature of the intermediate phase in the J_1-J_2 model is still subject of intense debate [220–223].
The developed CUT approach can be directly applied to the J_1-J_2 model for both limits, $(J_2/J_1) \ll 1$ and $(J_2/J_1) \gg 1$, by adjusting the initial conditions of the flow equations.
First interesting results were achieved by Jonas Haarz in his Master thesis [224] where he calculated the ground state energy and the magnetization by means of the $\eta^{0:n}$-generator scheme [51] studying the break down of the magnetic long range order. Interestingly, divergences are encountered for the full quasi-particle generator precluding the analysis of the excitations even before the long range order breaks down. These divergences may be indications for a decay of magnons at high energies since the roton minimum is enhanced by an increasing frustration.
Further extensions of the CST approach are required to study the fate of the high energy-magnons, as well as the possible occurrence of bound states and their relevance in the break down of the long range order.
In fact, the CUT method in momentum space provides a very suitable alternative for the treatment of quasi-particle decay. It exhibits important advantages compared to previous real space approaches [51–53]. Due to the conservation of total momentum it is possible to decouple quasi-particle states only for certain momenta just where no quasi-particle decay is expected. In other words, one defines the generator such that the resulting effective model is quasi-particle conserving only for restricted values of total momentum. In this procedure one retains decay processes for areas where the quasi-particle states become deficient. In the resulting

effective model the remaining processes can be treated with perturbative or variational methods [51, 70]. This approach may be suitable for the description of magnons in the Néel ordered phase of the frustrated Heisenbergmodel.
The results in this thesis provide an important understanding of the excitations in undoped copper oxide layers. In order to understand high-T_c superconductors, however, one has to consider cuprates with finite doping. This requires the introduction of holes which are fermionic degrees of freedom. Theoretically, such a system is described in terms of the $t-J$ model [15, 150, 151]. In general, the hopping of a single hole induces spin flips thereby reducing the magnetic order [225].
The CUT approach can be used to decouple the spin degrees of freedom from a single hole within a momentum space representation. The resulting effective Hamiltonian would provide information about the effects of the antiferromagnetic background on the dynamic properties of a single effective hole. Similar problems were already tackled in spin-(1/2) two-leg ladders by means of a sCUT approach in real space [47]. Moreover, one can also attempt to derive effective descriptions for two holes. This enables the study of effective hole interactions which are of crucial importance for the understanding of d-wave Cooper pair formation in cuprate superconductors [149, 154].
This task is technically very challenging because additional degrees of freedom give rise to operator terms which are numerically expensive. Therefore, additional truncation may be required in order to perform a CUT. Nevertheless, the CUT approach in momentum space has the potential to provide new insights into the mechanisms of high-T_c superconductors.

APPENDIX A

Spectral density of non-interacting hard-core bosons

In the following we use the Dyson-Maleev representation to study the spectral density of two non-interacting hardcore bosons in one and two dimensions. Results for the one dimensional case are given in Ref. [226].
We consider a Hamiltonian of non-interacting hardcore bosons

$$H = t \sum_{\langle i,j \rangle} b_i^\dagger b_j + \text{h.c.} \tag{A.1}$$

where the sum runs over all nearest neighbors. The hardcore property [197] can be expressed by the following commutation relation

$$\left[b_i, b_j^\dagger \right] = \delta_{ij}(1 - 2 b_i^\dagger b_i) \quad . \tag{A.2}$$

Typical approaches treat the hardcore property by means of an infinite on-site repulsion $U \to \infty$ [57] which may become problematic in numerical evaluations. The Dyson-Maleev representation [195] provides a useful alternative where the hardcore bosons $b_i^\dagger$ are mapped on bosons $a_i^\dagger$

$$b_i = a_i \qquad b_i^\dagger = a_i^\dagger (1 - a_i^\dagger a_i) \quad . \tag{A.3}$$

This mapping leads to a non-hermitian Hamiltonian. However, the infinite on-site repulsion is transformed into a finite quartic interaction term.
The resulting Hamiltonian in momentum space reads

$$H = t \sum_{\mathbf{k}} \gamma(\mathbf{k}) a_{\mathbf{k}}^\dagger a_{\mathbf{k}} - \frac{t}{2} \sum_{\mathbf{1,2,q}} \left(\gamma(\mathbf{1-q}) + \gamma(\mathbf{2+q}) \right) a_{\mathbf{1}}^\dagger a_{\mathbf{2}}^\dagger a_{\mathbf{1-q}} a_{\mathbf{2+q}} \tag{A.4}$$

where $\gamma(\mathbf{k}) = \sum_\delta e^{i\mathbf{k}\delta}$ and the sum runs over all primitive lattice vectors δ. In this representation hardcore bosons can be viewed as normal bosons with an additional non-hermitian interaction. Accordingly, we obtain non-interacting bosons by the neglect of the quartic term. In the following, we show that this interaction term indeed accounts for the correct spectral properties of hardcore bosons. To this end, we reproduce the analytical results for the one

dimensional chain given in Ref. [226] by means of a non-symmetric Lanczos algorithm (see section 3.3 for details). After that, we apply this scheme for a square lattice. We compare the reults for hardcore and normal bosons.
According to Ref. [226] the spectral density of two hardcore bosons in one dimension is obtained with respect to the following initial state

$$|d,\mathbf{K}\rangle = \frac{1}{\sqrt{N}} \sum_{\mathbf{r}} e^{i\mathbf{K}\mathbf{r}} |\mathbf{r},\mathbf{r}+\mathbf{d}\rangle \tag{A.5}$$

where $|\mathbf{r},\mathbf{r}+\mathbf{d}\rangle$ denotes a state with bosons on sites $\mathbf{r}$ and $\mathbf{r}+\mathbf{d}$.
The Hamiltonian of the non-interacting bosons is diagonal in momentum space. Thus, we identify the uniform superposition of all basis states, i.e. two-boson states with total momentum $\mathbf{K}$, as the corresponding initial vector

$$|\mathbf{K}\rangle_u = \frac{1}{\sqrt{N}} \sum_{\mathbf{q}} |\mathbf{K}+\mathbf{q},-\mathbf{q}\rangle \quad . \tag{A.6}$$

The spectral density of two neighboring hardcore bosons with total momentum $\mathbf{K}=0$ in one dimension reads

$$S^{\mathrm{hb}}(\mathbf{K}=0,\omega) = \frac{1}{2\pi t}\sqrt{1-(\omega/4t)^2} \quad \text{for } -4t<\omega<4t. \tag{A.7}$$

The spectral density for normal bosons in one dimension is given by

$$S^{\mathrm{b}}(\mathbf{K}=0,\omega) = \frac{1}{2\pi t}\frac{1}{\sqrt{1-(\omega/4t)^2}} \quad \text{for } -4t<\omega<4t. \tag{A.8}$$

Both functions are derived in Ref. [226].
We determine the line shapes by means of a continued fraction representation and the use of squareroot terminators [125]. To this end, we use a non-symmetric Lanczos algorithm with $|d,\mathbf{K}\rangle$ and $\langle d,\mathbf{K}|$ as initial states. Similarly, we apply the Lanczos algorithm for the Hamiltonian of the normal bosons using $|\mathbf{K}\rangle_u$ and $\langle\mathbf{K}|_u$ as initial states. The corresponding results for the one dimensional chain are shown in Figure A.1. We see that the non-symmetric Lanczos approach reproduces the theoretical predictions correctly.
Figure A.2 shows the results obtained for the square lattice. Note, that we exclusively used the uniform state $|\mathbf{K}\rangle_u$ in the two dimensional case. The comparison shows that the hardcore repulsion has a considerable impact on the corresponding spectral properties. In particular, considerable weight is shifted away from the upper and lower edge due to the hardcore constraint.
Interestingly, the non-hermitian approach based on the Dyson-Maleev representation does account for the spectral features of hardcore bosons without the use of infinitely large interaction terms. It provides a very suitable tool to treat hardcore bosonic systems with additional interactions. In fact, the Heisenberg antiferromagnet studied in this thesis is an excellent example.

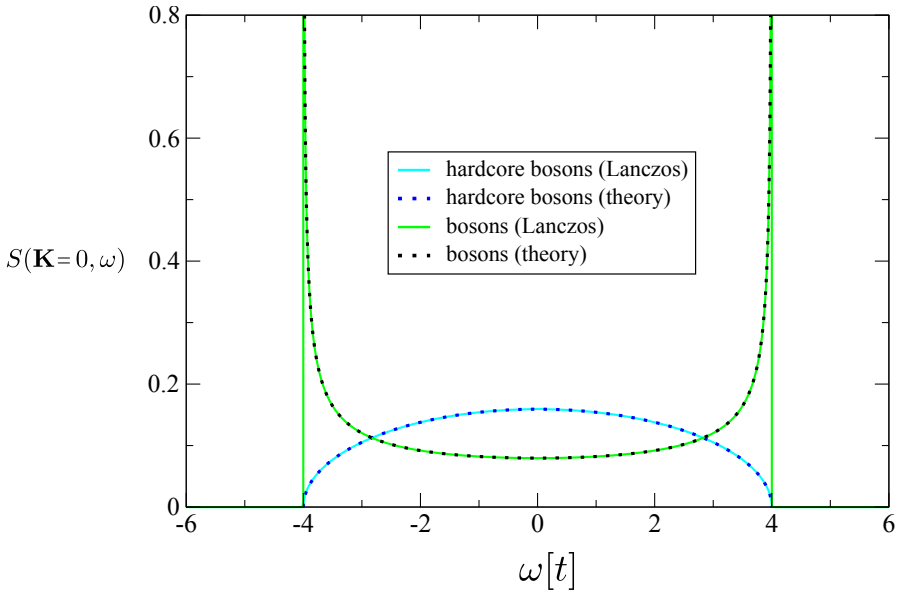

Figure A.1: Spectral density of non-interacting bosons and hardcore bosons on a one dimensional chain for zero total momentum $\mathbf{K} = 0$. Results obtained by a non-symmetric Lanczos algorithm are compared to the theoretical curves derived in Ref. [226].

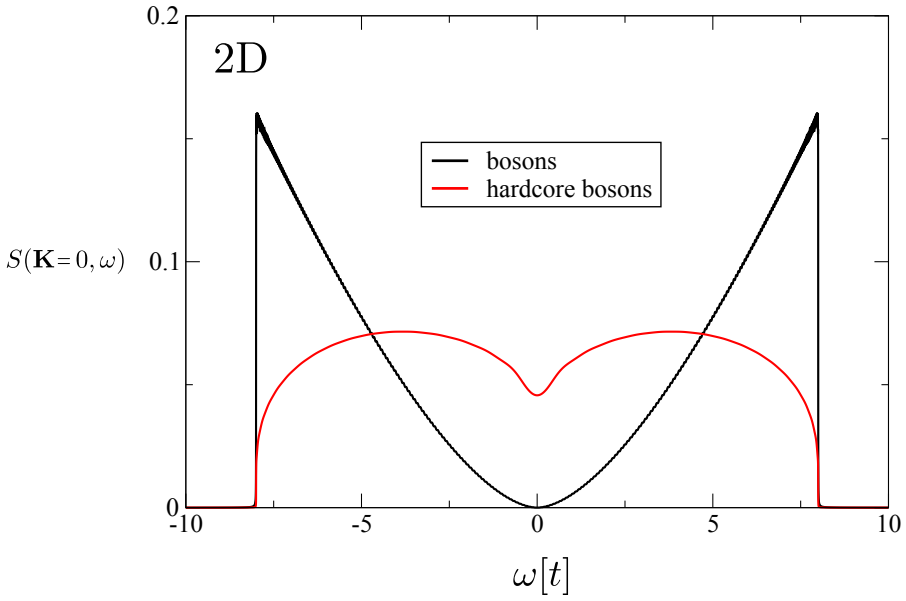

Figure A.2: Spectral density of the two-particle continuum for non-interacting bosons and hardcore bosons on a square lattice. The curves are obtained by a non-symmetric Lanczos algorithm for total momentum $\mathbf{K} = 0$.

APPENDIX B

Flow equations

In the first section the flow equations of the perturbative epCST approach in $(1/S)^2$ and $(1/S)^3$ are shown. In the subsequent section the flow equations of the sCST approach for scaling dimension $d = 2$ are given in standard notation. The last section provides the corresponding flow equations of the effective observables required for the longitudinal and transverse dynamic structure factor.

B.1 epCUT

$$\partial_\ell E_0^{(2)} = \sum_{\mathbf{1,2,3,4}} (-8)\, C_8^{(1)}(\mathbf{1,2,3,4})\, C_9^{(1)}(\mathbf{1,2,3,4})\, \delta_G(1+2+3+4) \tag{B.1}$$

$$\begin{aligned}\partial_\ell E_0^{(3)} = \sum_{\mathbf{1,2,3,4}} & (-8)\, C_8^{(1)}(\mathbf{1,2,3,4})\, C_9^{(2)}(\mathbf{1,2,3,4})\, \delta_G(1+2+3+4) + \\ & (-8)\, C_8^{(2)}(\mathbf{1,2,3,4})\, C_9^{(1)}(\mathbf{1,2,3,4})\, \delta_G(1+2+3+4)\end{aligned} \tag{B.2}$$

$$\begin{aligned}\partial_\ell \omega^{(2)}(\mathbf{1}) = \sum_{\mathbf{3,4}} \Big\{ & (-4)\, C_4^{(1)}(\mathbf{3,4,1,5})\, C_6^{(1)}(\mathbf{1,3,4,5})\, \delta_G(3+4-1+5) + \\ & (-16)\, C_8^{(1)}(\mathbf{1,3,4,5})\, C_9^{(1)}(\mathbf{1,3,4,5})\, \delta_G(3+4+1+5) \Big\}\end{aligned} \tag{B.3}$$

$$\begin{aligned}\partial_\ell \omega^{(3)}(\mathbf{1}) = & \sum_{\mathbf{3,4}} \Big\{ (-4)\, C_4^{(1)}(\mathbf{3,4,1,5})\, C_6^{(2)}(\mathbf{1,3,4,5})\, \delta_G(3+4-1+5) \\ & (-4)\, C_4^{(2)}(\mathbf{3,4,1,5})\, C_6^{(1)}(\mathbf{1,3,4,5})\, \delta_G(3+4-1+5) + \\ & (-16)\, C_8^{(1)}(\mathbf{1,3,4,5})\, C_9^{(2)}(\mathbf{1,3,4,5})\, \delta_G(3+4+1+5) + \\ & (-16)\, C_8^{(2)}(\mathbf{1,3,4,5})\, C_9^{(1)}(\mathbf{1,3,4,5})\, \delta_G(3+4+1+5) \Big\} \\ & \sum_{\mathbf{3}} \Big\{ (-4)\, C_8^{(1)}(\mathbf{1,3,1,-3})\, \Gamma^{(2)}(\mathbf{3}) - 4 C_6^{(1)}(\mathbf{1,1,3,-3})\, \Gamma^{(2)}(\mathbf{3}) \\ & \sum_{\mathbf{3,4,5,6}} (-24)\, C_8^{(1)}(\mathbf{3,4,5,6})\, \tilde{C}_{11}^{(2)}(\mathbf{1,3,4,5,6})\, \delta_G(3+4+5+6) \\ & \sum_{\mathbf{3,4,5,6}} (-24)\, C_9^{(1)}(\mathbf{3,4,5,6})\, \tilde{C}_{10}^{(2)}(\mathbf{1,3,4,5,6})\, \delta_G(3+4+5+6) \Big\}\end{aligned}$$

$$\begin{aligned}\partial_\ell \Gamma^{(2)}(\mathbf{1}) = & (-2)\, \Gamma^{(2)}(\mathbf{1})\, \omega^{(0)}(\mathbf{1}) + \\ & \sum_{\mathbf{3,4,5}} \Big\{ (-8)\, C_4^{(1)}(\mathbf{3,4,1,5})\, C_9^{(1)}(\mathbf{3,4,-1,5})\, \delta_G(-1+3+4+5) + \\ & (-8)\, C_5^{(1)}(\mathbf{3,4,5,-1})\, C_9^{(1)}(\mathbf{1,3,4,5})\, \delta_G(1+3+4+5) \Big\}\end{aligned} \tag{B.4}$$

$$\partial_\ell C_1(\mathbf{1},\mathbf{2},\mathbf{3},\mathbf{4}) = 0 \tag{B.5}$$

$$\partial_\ell C_2^{(1)}(\mathbf{1},\mathbf{2},\mathbf{3},\mathbf{4}) = 0 \tag{B.6}$$

$$\partial_\ell C_3^{(1)}(\mathbf{1},\mathbf{2},\mathbf{3},\mathbf{4}) = 0 \tag{B.7}$$

$$\begin{aligned}\partial_\ell C_4^{(2)}(\mathbf{1},\mathbf{2},\mathbf{3},\mathbf{4}) &= \delta_G(1+2-3+4)\Big\{ \\ &\quad \left(\omega^{(0)}(\mathbf{3})-\omega^{(0)}(\mathbf{1})-\omega^{(0)}(\mathbf{2})-\omega^{(0)}(\mathbf{4})\right) C_4^{(1)}(\mathbf{1},\mathbf{2},\mathbf{3},\mathbf{4})\Big\}\end{aligned} \tag{B.8}$$

$$\begin{aligned}\partial_\ell C_4^{(2)}(\mathbf{1},\mathbf{2},\mathbf{3},\mathbf{4}) = \;& \delta_G(1+2-3+4)\Big\{ \\ & \left(\omega^{(0)}(\mathbf{3})-\omega(\mathbf{1})0-\omega^{(0)}(\mathbf{2})-\omega^{(0)}(\mathbf{4})\right) C_4^{(2)}(\mathbf{1},\mathbf{2},\mathbf{3},\mathbf{4})+ \\ & \left(\omega^{(1)}(\mathbf{3})-\omega(\mathbf{1})1-\omega^{(1)}(\mathbf{2})-\omega^{(1)}(\mathbf{4})\right) C_4^{(1)}(\mathbf{1},\mathbf{2},\mathbf{3},\mathbf{4})+ \\ & \sum_{\mathbf{5},\mathbf{6}} (-2)\, C_1^{(1)}(\mathbf{1},\mathbf{2},\mathbf{5},\mathbf{6})\, C_4^{(1)}(\mathbf{5},\mathbf{6},\mathbf{3},\mathbf{4})\, \delta_G(1+2-5-6)+ \\ & (-1)\, C_2^{(1)}(\mathbf{2},\mathbf{5},\mathbf{4},\mathbf{6})\, C_4^{(1)}(\mathbf{1},\mathbf{5},\mathbf{3},\mathbf{6})\, \delta_G(2-5+4-6)+ \\ & (-1)\, C_2^{(1)}(\mathbf{1},\mathbf{5},\mathbf{4},\mathbf{6})\, C_4^{(1)}(\mathbf{2},\mathbf{5},\mathbf{3},\mathbf{6})\, \delta_G(1-5+4-6)+ \\ & (-8)\, C_6^{(1)}(\mathbf{2},\mathbf{3},\mathbf{5},\mathbf{6})\, C_8^{(1)}(\mathbf{1},\mathbf{5},\mathbf{4},\mathbf{6})\, \delta_G(2-3-5-6)+ \\ & (-8)\, C_6^{(1)}(\mathbf{1},\mathbf{3},\mathbf{5},\mathbf{6})\, C_8^{(1)}(\mathbf{2},\mathbf{5},\mathbf{4},\mathbf{6})\, \delta_G(1-3-5-6)+ \\ & (-4)\, C_7^{(1)}(\mathbf{3},\mathbf{4},\mathbf{5},\mathbf{6})\, C_8^{(1)}(\mathbf{1},\mathbf{2},\mathbf{5},\mathbf{6})\, \delta_G(3-4+5+6)\Big\}\end{aligned} \tag{B.9}$$

$$\begin{aligned}\partial_\ell C_5^{(1)}(\mathbf{1},\mathbf{2},\mathbf{3},\mathbf{4}) &= \delta_G(1+2+3-4)\Big\{ \\ &\quad \left(-\omega^{(0)}(\mathbf{1})-\omega^{(0)}(\mathbf{2})-\omega^{(0)}(\mathbf{3})+\omega^{(0)}(\mathbf{4})\right) C_5^{(1)}(\mathbf{1},\mathbf{2},\mathbf{3},\mathbf{4})\Big\}\end{aligned} \tag{B.10}$$

$$\partial_\ell C_6^{(1)}(\mathbf{1},\mathbf{2},\mathbf{3},\mathbf{4}) = \delta_G(1-2-3-4)\Big\{ \Big(\omega^{(0)}(\mathbf{1})-\omega^{(0)}(\mathbf{2})-\omega^{(0)}(\mathbf{3})+\omega^{(0)}(\mathbf{4})\Big) C_6^{(1)}(\mathbf{1},\mathbf{2},\mathbf{3},\mathbf{4})\Big\} \tag{B.11}$$

$$\begin{aligned}\partial_\ell C_6^{(2)}(\mathbf{1},\mathbf{2},\mathbf{3},\mathbf{4}) = \\ &\delta_G(1-2-3-4)\Big\{ \\ &\Big(\omega^{(0)}(\mathbf{1})-\omega^{(0)}(\mathbf{2})-\omega^{(0)}(\mathbf{3})+\omega^{(0)}(\mathbf{4})\Big) C_6^{(2)}(\mathbf{1},\mathbf{2},\mathbf{3},\mathbf{4}) \\ &\Big(\omega^{(1)}(\mathbf{1})-\omega^{(1)}(\mathbf{2})-\omega^{(1)}(\mathbf{3})+\omega^{(1)}(\mathbf{4})\Big) C_6^{(1)}(\mathbf{1},\mathbf{2},\mathbf{3},\mathbf{4}) + \\ &\sum_{\mathbf{5},\mathbf{6}} (-2) C_1^{(p)}(\mathbf{5},\mathbf{6},\mathbf{2},\mathbf{3}) C_6^{(1)}(\mathbf{1},\mathbf{5},\mathbf{6},\mathbf{4}) \delta_G(5+6-2-3) + \\ &(-1) C_2^{(1)}(\mathbf{5},\mathbf{3},\mathbf{6},\mathbf{4}) C_6^{(1)}(\mathbf{1},\mathbf{2},\mathbf{5},\mathbf{6}) \delta_G(5-3+6-4) + \\ &(-1) C_2^{(1)}(\mathbf{5},\mathbf{2},\mathbf{6},\mathbf{4}) C_6^{(1)}(\mathbf{1},\mathbf{3},\mathbf{5},\mathbf{6}) \delta_G(5-2+6-4) + \\ &(-8) C_4^{(1)}(\mathbf{1},\mathbf{5},\mathbf{3},\mathbf{6}) C_9^{(1)}(\mathbf{2},\mathbf{5},\mathbf{4},\mathbf{6}) \delta_G(1+5-3+6) + \\ &(-8) C_4^{(1)}(\mathbf{1},\mathbf{5},\mathbf{2},\mathbf{6}) C_9^{(1)}(\mathbf{3},\mathbf{5},\mathbf{4},\mathbf{6}) \delta_G(1+5-2+6) + \\ &(-4) C_5^{(1)}(\mathbf{1},\mathbf{5},\mathbf{6},\mathbf{4}) C_9^{(1)}(\mathbf{2},\mathbf{3},\mathbf{5},\mathbf{6}) \delta_G(1+5+6-4)\Big\}\end{aligned} \tag{B.12}$$

$$\partial_\ell C_7^{(1)}(\mathbf{1},\mathbf{2},\mathbf{3},\mathbf{4}) = \delta_G(1-2+3+4)\Big\{ \Big(-\omega^{(0)}(\mathbf{1})+\omega^{(0)}(\mathbf{2})-\omega^{(0)}(\mathbf{3})-\omega^{(0)}(\mathbf{4})\Big) C_7^{(1)}(\mathbf{1},\mathbf{2},\mathbf{3},\mathbf{4}) \tag{B.13}$$

$$\partial_\ell C_8^{(1)}(\mathbf{1},\mathbf{2},\mathbf{3},\mathbf{4}) = \delta_G(1+2+3+4)\Big\{ \Big(-\omega^{(0)}(\mathbf{1})-\omega^{(0)}(\mathbf{2})-\omega^{(0)}(\mathbf{3})-\omega^{(0)}(\mathbf{4})\Big) C_8^{(1)}(\mathbf{1},\mathbf{2},\mathbf{3},\mathbf{4}) \tag{B.14}$$

$$
\begin{aligned}
\partial_\ell C_8^{(2)}(\mathbf{1},\mathbf{2},\mathbf{3},\mathbf{4}\,) \;=\; & \delta_G(1+2+3+4)\Big\{ \\
& \left(-\omega^{(0)}(\mathbf{1})-\omega^{(0)}(\mathbf{2})-\omega^{(0)}(\mathbf{3})-\omega^{(0)}(\mathbf{4})\right) C_8^{(2)}(\mathbf{1},\mathbf{2},\mathbf{3},\mathbf{4}\,)+ \\
& \left(-\omega^{(1)}(\mathbf{1})-\omega^{(1)}(\mathbf{2})-\omega^{(1)}(\mathbf{3})-\omega^{(1)}(\mathbf{4})\right) C_8^{(1)}(\mathbf{1},\mathbf{2},\mathbf{3},\mathbf{4}\,)+ \\
& \sum_{5,6} (-2)\, C_1^{(1)}(\mathbf{1},\mathbf{2},\mathbf{5},\mathbf{6}\,)\, C_8^{(1)}(\mathbf{5},\mathbf{6},\mathbf{3},\mathbf{4}\,)\, \delta_G(1+2-5-6)+ \\
& (-1)\, C_2^{(1)}(\mathbf{2},\mathbf{5},\mathbf{4},\mathbf{6}\,)\, C_8^{(1)}(\mathbf{1},\mathbf{5},\mathbf{3},\mathbf{6}\,)\, \delta_G(2-5+4-6)+ \\
& (-1)\, C_2^{(1)}(\mathbf{1},\mathbf{5},\mathbf{4},\mathbf{6}\,)\, C_8^{(1)}(\mathbf{2},\mathbf{5},\mathbf{3},\mathbf{6}\,)\, \delta_G(1-5+4-6)+ \\
& (-1)\, C_2^{(1)}(\mathbf{2},\mathbf{5},\mathbf{3},\mathbf{6}\,)\, C_8^{(1)}(\mathbf{1},\mathbf{5},\mathbf{4},\mathbf{6}\,)\, \delta_G(2-5+3-6)+ \\
& (-1)\, C_2^{(1)}(\mathbf{1},\mathbf{5},\mathbf{3},\mathbf{6}\,)\, C_8^{(1)}(\mathbf{2},\mathbf{5},\mathbf{4},\mathbf{6}\,)\, \delta_G(1-5+3-6)+ \\
& (-2)\, C_3^{(1)}(\mathbf{3},\mathbf{4},\mathbf{5}\,,\mathbf{6}\,)\, C_8^{(1)}(\mathbf{1},\mathbf{2},\mathbf{5},\mathbf{6}\,)\, \delta_G(3+4-5-6)\Big\}
\end{aligned}
\tag{B.15}
$$

$$
\begin{aligned}
\partial_\ell C_9^{(1)}(\mathbf{1},\mathbf{2},\mathbf{3},\mathbf{4}\,) \;=\; & \delta_G(1+2+3+4)\Big\{ \\
& \left(-\omega^{(0)}(\mathbf{1})-\omega^{(0)}(\mathbf{2})-\omega^{(0)}(\mathbf{3})-\omega^{(0)}(\mathbf{4})\right) C_9^{(1)}(\mathbf{1},\mathbf{2},\mathbf{3},\mathbf{4}\,)
\end{aligned}
\tag{B.16}
$$

$$
\begin{aligned}
\partial_\ell C_9^{(2)}(\mathbf{1},\mathbf{2},\mathbf{3},\mathbf{4}\,) \;=\; & \delta_G(1+2+3+4)\Big\{ \\
& \left(-\omega^{(0)}(\mathbf{1})-\omega^{(0)}(\mathbf{2})-\omega^{(0)}(\mathbf{3})-\omega^{(0)}(\mathbf{4})\right) C_9^{(2)}(\mathbf{1},\mathbf{2},\mathbf{3},\mathbf{4}\,)+ \\
& \sum_{\mathbf{5},\mathbf{6}} (-2)\, C_1^{(1)}(\mathbf{5},\mathbf{6},\mathbf{1},\mathbf{2}\,)\, C_9^{(1)}(\mathbf{5},\mathbf{6},\mathbf{3},\mathbf{4}\,)\, \delta_G(5+6-1-2)+ \\
& (-1)\, C_2^{(1)}(\mathbf{5},\mathbf{2},\mathbf{6},\mathbf{4}\,)\, C_9^{(1)}(\mathbf{1},\mathbf{5},\mathbf{3},\mathbf{6}\,)\, \delta_G(5-2+6-4)+ \\
& (-1)\, C_2^{(1)}(\mathbf{5},\mathbf{1},\mathbf{6},\mathbf{4}\,)\, C_9^{(1)}(\mathbf{2},\mathbf{5},\mathbf{3},\mathbf{6}\,)\, \delta_G(5-1+6-4)+ \\
& (-1)\, C_2^{(1)}(\mathbf{5},\mathbf{2},\mathbf{6},\mathbf{3}\,)\, C_9^{(1)}(\mathbf{1},\mathbf{5},\mathbf{4},\mathbf{6}\,)\, \delta_G(5-2+6-3)+ \\
& (-1)\, C_2^{(1)}(\mathbf{5},\mathbf{1},\mathbf{6},\mathbf{3}\,)\, C_9^{(1)}(\mathbf{2},\mathbf{5},\mathbf{4},\mathbf{6}\,)\, \delta_G(5-1+6-3)+ \\
& (-2)\, C_3^{(1)}(\mathbf{5},\mathbf{6},\mathbf{3},\mathbf{4}\,)\, C_9^{(1)}(\mathbf{1},\mathbf{2},\mathbf{5},\mathbf{6}\,)\, \delta_G(3+4-5-6)\Big\}
\end{aligned}
\tag{B.17}
$$

$$
\begin{aligned}
\partial_\ell \tilde{C}_{10}^{(2)}(\mathbf{1},\mathbf{2},\mathbf{3},\mathbf{4},\mathbf{5}) \;=\;& \delta_G(2+3+4+5)\Big\{ \\
& \left(-\omega^{(0)}(\mathbf{2})-\omega^{(0)}(\mathbf{3})-\omega^{(0)}(\mathbf{4})-\omega^{(0)}(\mathbf{5})\right)\tilde{C}_{10}^{(2)}(\mathbf{1},\mathbf{2},\mathbf{3},\mathbf{4},\mathbf{5}) + \\
& \sum_{\mathbf{6}} (-\tfrac{4}{3})\, C_1^{(1)}(\mathbf{2},\mathbf{3},\mathbf{1},\mathbf{6})\, C_8^{(1)}(\mathbf{1},\mathbf{6},\mathbf{4},\mathbf{5})\,\delta_G(2+6+4+5) + \\
& (-\tfrac{4}{3})\, C_1^{(1)}(\mathbf{1},\mathbf{3},\mathbf{1},\mathbf{6})\, C_8^{(1)}(\mathbf{2},\mathbf{6},\mathbf{4},\mathbf{5})\,\delta_G(2+6+4+5) + \\
& (-\tfrac{4}{3})\, C_1^{(1)}(\mathbf{1},\mathbf{2},\mathbf{1},\mathbf{6})\, C_8^{(1)}(\mathbf{3},\mathbf{6},\mathbf{4},\mathbf{5})\,\delta_G(2+6+4+5) + \\
& (-\tfrac{1}{3})\, C_2^{(1)}(\mathbf{3},\mathbf{1},\mathbf{5},\mathbf{6})\, C_8^{(1)}(\mathbf{1},\mathbf{2},\mathbf{4},\mathbf{6})\,\delta_G(2+6+4+5) + \\
& (-\tfrac{1}{3})\, C_2^{(1)}(\mathbf{2},\mathbf{1},\mathbf{5},\mathbf{6})\, C_8^{(1)}(\mathbf{1},\mathbf{3},\mathbf{4},\mathbf{6})\,\delta_G(2+6+4+5) + \\
& (-\tfrac{1}{3})\, C_2^{(1)}(\mathbf{1},\mathbf{1},\mathbf{5},\mathbf{6})\, C_8^{(1)}(\mathbf{2},\mathbf{3},\mathbf{4},\mathbf{6})\,\delta_G(2+6+4+5) + \\
& (-\tfrac{1}{3})\, C_2^{(1)}(\mathbf{3},\mathbf{1},\mathbf{4},\mathbf{6})\, C_8^{(1)}(\mathbf{1},\mathbf{2},\mathbf{5},\mathbf{6})\,\delta_G(2+6+4+5) + \\
& (-\tfrac{1}{3})\, C_2^{(1)}(\mathbf{2},\mathbf{1},\mathbf{4},\mathbf{6})\, C_8^{(1)}(\mathbf{1},\mathbf{3},\mathbf{5},\mathbf{6})\,\delta_G(2+6+4+5) + \\
& (-\tfrac{1}{3})\, C_2^{(1)}(\mathbf{1},\mathbf{1},\mathbf{4},\mathbf{6})\, C_8^{(1)}(\mathbf{2},\mathbf{3},\mathbf{5},\mathbf{6})\,\delta_G(2+6+4+5) \qquad \text{(B.18)}
\end{aligned}
$$

$$
\begin{aligned}
\partial_\ell \tilde{C}^{(2)}_{11}(\mathbf{1},\mathbf{2},\mathbf{3},\mathbf{4},\mathbf{5}) \;=\;& \delta_G(2+3+4+5)\Big\{ \\
& \big(-\omega^{(0)}(\mathbf{2})-\omega^{(0)}(\mathbf{3})-\omega^{(0)}(\mathbf{4})-\omega^{(0)}(\mathbf{5})\big)\,\tilde{C}^{(2)}_{10}(\mathbf{1},\mathbf{2},\mathbf{3},\mathbf{4},\mathbf{5}) + \\
& \sum_{\mathbf{6}} (-\tfrac{4}{3})\,C^{(1)}_1(\mathbf{1},\mathbf{6},\mathbf{3},\mathbf{1})\,C^{(1)}_9(\mathbf{2},\mathbf{6},\mathbf{4},\mathbf{5})\,\delta_G(2+6+4+5) + \\
& (-\tfrac{4}{3})\,C^{(1)}_1(\mathbf{1},\mathbf{6},\mathbf{1},\mathbf{2})\,C^{(1)}_9(\mathbf{3},\mathbf{6},\mathbf{4},\mathbf{5})\,\delta_G(3+6+4+5) + \\
& (-\tfrac{4}{3})\,C^{(1)}_1(\mathbf{1},\mathbf{6},\mathbf{2},\mathbf{3})\,C^{(1)}_9(\mathbf{1},\mathbf{6},\mathbf{4},\mathbf{5})\,\delta_G(1+6+4+5) + \\
& (-\tfrac{1}{3})\,C^{(1)}_2(\mathbf{1},\mathbf{1},\mathbf{6},\mathbf{5})\,C^{(1)}_9(\mathbf{2},\mathbf{3},\mathbf{4},\mathbf{6})\,\delta_G(2+3+4+6) + \\
& (-\tfrac{1}{3})\,C^{(1)}_2(\mathbf{1},\mathbf{3},\mathbf{6},\mathbf{5})\,C^{(1)}_9(\mathbf{2},\mathbf{1},\mathbf{4},\mathbf{6})\,\delta_G(2+1+4+6) + \\
& (-\tfrac{1}{3})\,C^{(1)}_2(\mathbf{1},\mathbf{2},\mathbf{6},\mathbf{5})\,C^{(1)}_9(\mathbf{3},\mathbf{1},\mathbf{4},\mathbf{6})\,\delta_G(3+1+4+6) + \\
& (-\tfrac{1}{3})\,C^{(1)}_2(\mathbf{1},\mathbf{1},\mathbf{6},\mathbf{4})\,C^{(1)}_9(\mathbf{2},\mathbf{3},\mathbf{5},\mathbf{6})\,\delta_G(2+3+5+6) + \\
& (-\tfrac{1}{3})\,C^{(1)}_2(\mathbf{1},\mathbf{3},\mathbf{6},\mathbf{4})\,C^{(1)}_9(\mathbf{2},\mathbf{1},\mathbf{5},\mathbf{6})\,\delta_G(2+1+5+6) + \\
& (-\tfrac{1}{3})\,C^{(1)}_2(\mathbf{1},\mathbf{2},\mathbf{6},\mathbf{4})\,C^{(1)}_9(\mathbf{3},\mathbf{1},\mathbf{5},\mathbf{6})\,\delta_G(3+1+5+6) \qquad \text{(B.19)}
\end{aligned}
$$

B.2 Flow equations: scaling dimension

$$\begin{aligned}
\partial_\ell E_0 = & \sum_{1,2,3,4} (-8)\, C_8(\mathbf{1},\mathbf{2},\mathbf{3},\mathbf{4}\,)\, C_9(\mathbf{1},\mathbf{2},\mathbf{3},\mathbf{4})\, \delta_G(1+2+3+4) + \\
& \sum_{1} (-2)\, \Gamma(\mathbf{1})\, \Gamma(\mathbf{1}) \qquad \text{(B.20)}
\end{aligned}$$

$$\begin{aligned}
\partial_\ell \omega(\mathbf{1}) = & \quad (-2)\, \Gamma(\mathbf{1})\, \Gamma(\mathbf{1}) + \\
& \sum_{3,4} \Big\{ (-4)\, C_4(\mathbf{3},\mathbf{4},\mathbf{1},\mathbf{5})\, C_6(\mathbf{1},\mathbf{3},\mathbf{4},\mathbf{5})\, \delta_G(3+4-1+5) \\
& \qquad (-16)\, C_8(\mathbf{1},\mathbf{3},\mathbf{4},\mathbf{5}\,)\, C_9(\mathbf{1},\mathbf{3},\mathbf{4},\mathbf{5}\,)\, \delta_G(3+4+1+5) \Big\} \\
& \sum_{3} \Big\{ (-4)\, C_8(\mathbf{1},\mathbf{3},\mathbf{1},\text{-}\mathbf{3})\, \Gamma(\mathbf{3}) - 4 C_6(\mathbf{1},\mathbf{1},\mathbf{3},\text{-}\mathbf{3})\, \Gamma(\mathbf{3}) \Big\} \qquad \text{(B.21)}
\end{aligned}$$

$$\begin{aligned}
\partial_\ell \Gamma(\mathbf{1}) = & \quad (-2)\, \Gamma(\mathbf{1})\, \omega(\mathbf{1}) + \\
& \sum_{3,4,5} \Big\{ (-8)\, C_4(\mathbf{3},\mathbf{4},\mathbf{1},\mathbf{5})\, C_9(\mathbf{3},\mathbf{4},\text{-}\mathbf{1},\mathbf{5})\, \delta_G(-1+3+4+5) \\
& \qquad (-8)\, C_5(\mathbf{3},\mathbf{4},\mathbf{5},\text{-}\mathbf{1})\, C_9(\mathbf{1},\mathbf{3},\mathbf{4},\mathbf{5})\, \delta_G(1+3+4+5) \Big\} \\
& \sum_{3} \Big\{ (-1)\, C_2(\mathbf{1},\mathbf{3},\text{-}\mathbf{1},\text{-}\mathbf{3})\, \Gamma(\mathbf{3}) + (-8) C_8(\mathbf{1},\mathbf{3},\text{-}\mathbf{1},\text{-}\mathbf{3})\, \Gamma(\mathbf{3}) \Big\} \qquad \text{(B.22)}
\end{aligned}$$

$$\begin{aligned}
\partial_\ell C_1(\mathbf{1},\mathbf{2},\mathbf{3},\mathbf{4}\,) = & \quad \delta_G(1+2-3-4) \Big\{ \\
& (-1)\, C_4(\mathbf{1},\mathbf{2},\mathbf{4},\text{-}\mathbf{3}\,)\, \Gamma(\mathbf{3}) + \\
& (-1)\, C_4(\mathbf{1},\mathbf{2},\mathbf{3},\text{-}\mathbf{4}\,)\, \Gamma(\mathbf{4}) + \\
& (-1)\, C_6(\mathbf{2},\mathbf{3},\mathbf{4},\text{-}\mathbf{1}\,)\, \Gamma(\mathbf{1}) + \\
& (-1)\, C_6(\mathbf{1},\mathbf{3},\mathbf{4},\text{-}\mathbf{2}\,)\, \Gamma(\mathbf{2}) + \\
& \sum_{5,6} (-2)\, C_4(\mathbf{2},\mathbf{5},\mathbf{4},\mathbf{6}\,)\, C_6(\mathbf{1},\mathbf{3},\mathbf{5},\mathbf{6}\,)\, \delta_G(2+5-4+6) + \\
& \qquad (-2)\, C_4(\mathbf{1},\mathbf{5},\mathbf{3},\mathbf{6}\,)\, C_6(\mathbf{2},\mathbf{4},\mathbf{5},\mathbf{6}\,)\, \delta_G(1+5-3+6) + \\
& \qquad (-2)\, C_4(\mathbf{2},\mathbf{5},\mathbf{3},\mathbf{6}\,)\, C_6(\mathbf{1},\mathbf{4},\mathbf{5},\mathbf{6}\,)\, \delta_G(1+5-3+6) + \\
& \qquad (-2)\, C_4(\mathbf{1},\mathbf{5},\mathbf{4},\mathbf{6}\,)\, C_6(\mathbf{2},\mathbf{3},\mathbf{5},\mathbf{6}\,)\, \delta_G(1+5-3+6) + \\
& \qquad (-4)\, C_8(\mathbf{1},\mathbf{2},\mathbf{5},\mathbf{6}\,)\, C_9(\mathbf{3},\mathbf{4},\mathbf{5},\mathbf{6}\,)\, \delta_G(1+2+5+6) \Big\}
\end{aligned} \qquad \text{(B.23)}$$

$$
\begin{aligned}
\partial_\ell C_2(\mathbf{1},\mathbf{2},\mathbf{3},\mathbf{4}) \;=\; & \delta_G(1-2+3-4)\Big\{ \\
& (-4)\,C_4(\mathbf{1},\text{-}\mathbf{4},\mathbf{2},\mathbf{3})\,\Gamma(\text{-}\mathbf{4}) + \\
& (-4)\,C_5(\mathbf{1},\mathbf{3},\text{-}\mathbf{2},\mathbf{4})\,\Gamma(\mathbf{2}) + \\
& (-4)\,C_6(\mathbf{1},\mathbf{2},\text{-}\mathbf{3},\mathbf{4})\,\Gamma(\text{-}\mathbf{3}) + \\
& (-4)\,C_7(\mathbf{2},\mathbf{3},\mathbf{4},\text{-}\mathbf{1})\,\Gamma(\mathbf{1}) + \\
\sum_{\mathbf{5},\mathbf{6}} & (-4)\,C_4(\mathbf{5},\mathbf{6},\mathbf{2},\mathbf{3})\,C_6(\mathbf{1},\mathbf{5},\mathbf{6},\mathbf{4})\,\delta_G(5+6-2+3) + \\
& (-4)\,C_5(\mathbf{1},\mathbf{5},\mathbf{6},\mathbf{4})\,C_7(\mathbf{2},\mathbf{3},\mathbf{5},\mathbf{6})\,\delta_G(1+5+6-4) + \\
& (-8)\,C_4(\mathbf{1},\mathbf{5},\mathbf{2},\mathbf{6})\,C_7(\mathbf{5},\mathbf{3},\mathbf{4},\mathbf{6})\,\delta_G(1+5-2+6) + \\
& (-8)\,C_5(\mathbf{5},\mathbf{3},\mathbf{6},\mathbf{4})\,C_6(\mathbf{1},\mathbf{2},\mathbf{5},\mathbf{6})\,\delta_G(5+3+6-4) + \\
& (-32)\,C_8(\mathbf{1},\mathbf{5},\mathbf{3},\mathbf{6})\,C_9(\mathbf{2},\mathbf{5},\mathbf{4},\mathbf{6})\,\delta_G(1+5+3+6)\Big\}
\end{aligned}
\tag{B.24}
$$

$$
\begin{aligned}
\partial_\ell C_3(\mathbf{1},\mathbf{2},\mathbf{3},\mathbf{4}) \;=\; & \delta_G(1+2-3-4)\Big\{ \\
& (-1)\,C_5(\text{-}\mathbf{3},\mathbf{1},\mathbf{2},\mathbf{4})\,\Gamma(\text{-}\mathbf{3}) + \\
& (-1)\,C_5(\text{-}\mathbf{4},\mathbf{1},\mathbf{2},\mathbf{3})\,\Gamma(\text{-}\mathbf{4}) + \\
& (-1)\,C_7(\text{-}\mathbf{2},\mathbf{1},\mathbf{3},\mathbf{4})\,\Gamma(\text{-}\mathbf{2}) + \\
& (-1)\,C_7(\text{-}\mathbf{1},\mathbf{2},\mathbf{3},\mathbf{4})\,\Gamma(\text{-}\mathbf{1}) + \\
\sum_{\mathbf{5}} & (-4)\,C_5(\mathbf{5},\mathbf{2},\mathbf{6},\mathbf{4})\,C_7(\mathbf{5},\mathbf{1},\mathbf{3},\mathbf{6})\,\delta_G(5+1+6-4) + \\
& (-4)\,C_5(\mathbf{5},\mathbf{1},\mathbf{6},\mathbf{3})\,C_7(\mathbf{5},\mathbf{2},\mathbf{4},\mathbf{6})\,\delta_G(5+1+6-3) + \\
\sum_{\mathbf{5}} & (-4)\,C_5(\mathbf{5},\mathbf{2},\mathbf{6},\mathbf{3})\,C_7(\mathbf{5},\mathbf{1},\mathbf{4},\mathbf{6})\,\delta_G(5+1+6-4) + \\
& (-4)\,C_5(\mathbf{5},\mathbf{1},\mathbf{6},\mathbf{4})\,C_7(\mathbf{5},\mathbf{2},\mathbf{3},\mathbf{6})\,\delta_G(5+1+6-3) + \\
& (-4)\,C_8(\mathbf{5},\mathbf{6},\mathbf{1},\mathbf{2})\,C_9(\mathbf{5},\mathbf{6},\mathbf{3},\mathbf{4})\,\delta_G(5+6+1+2)\Big\}
\end{aligned}
\tag{B.25}
$$

$$
\begin{aligned}
\partial_\ell C_4(\mathbf{1},\mathbf{2},\mathbf{3},\mathbf{4}) \;=\;& \delta_G(1+2-3+4)\Big\{ \\
& (\omega(\mathbf{3})-\omega(\mathbf{1})-\omega(\mathbf{2})-\omega(\mathbf{4}))\, C_4(\mathbf{1},\mathbf{2},\mathbf{3},\mathbf{4}) + \\
& (-2)\, C_1(\mathbf{1},\mathbf{2},\mathbf{3},\text{-}\mathbf{4})\,\Gamma(\text{-}\mathbf{4}) + \\
& \left(-\frac{1}{2}\right)\left(C_2(\mathbf{2},\mathbf{3},\mathbf{4},\text{-}\mathbf{1})\,\Gamma(\mathbf{1}) + C_2(\mathbf{1},\mathbf{3},\mathbf{4},\text{-}\mathbf{2})\,\Gamma(\mathbf{2})\right) + \\
& (-4)\, C_8(\mathbf{1},\mathbf{2},\mathbf{4},\text{-}\mathbf{3})\,\Gamma(\mathbf{3}) + \\
& \sum_{\mathbf{5,6}} (-2)\, C_1(\mathbf{1},\mathbf{2},\mathbf{5},\mathbf{6})\, C_4(\mathbf{5},\mathbf{6},\mathbf{3},\mathbf{4})\,\delta_G(1+2-5-6) + \\
& (-1)\, C_2(\mathbf{2},\mathbf{5},\mathbf{4},\mathbf{6})\, C_4(\mathbf{1},\mathbf{5},\mathbf{3},\mathbf{6})\,\delta_G(2-5+4-6) + \\
& (-1)\, C_2(\mathbf{1},\mathbf{5},\mathbf{4},\mathbf{6})\, C_4(\mathbf{2},\mathbf{5},\mathbf{3},\mathbf{6})\,\delta_G(1-5+4-6) + \\
& (-8)\, C_6(\mathbf{2},\mathbf{3},\mathbf{5},\mathbf{6})\, C_8(\mathbf{1},\mathbf{5},\mathbf{4},\mathbf{6})\,\delta_G(2-3-5-6) + \\
& (-8)\, C_6(\mathbf{1},\mathbf{3},\mathbf{5},\mathbf{6})\, C_8(\mathbf{2},\mathbf{5},\mathbf{4},\mathbf{6})\,\delta_G(1-3-5-6) + \\
& (-4)\, C_7(\mathbf{3},\mathbf{4},\mathbf{5},\mathbf{6})\, C_8(\mathbf{1},\mathbf{2},\mathbf{5},\mathbf{6})\,\delta_G(3-4+5+6)\Big\}
\end{aligned}
\tag{B.26}
$$

$$
\begin{aligned}
\partial_\ell C_5(\mathbf{1},\mathbf{2},\mathbf{3},\mathbf{4}) \;=\;& \delta_G(1+2+3-4)\Big\{ \\
& (-\omega(\mathbf{1})-\omega(\mathbf{2})-\omega(\mathbf{3})+\omega(\mathbf{4}))\, C_5(\mathbf{1},\mathbf{2},\mathbf{3},\mathbf{4}) + \\
& (-2)\, C_3(\mathbf{2},\mathbf{3},\mathbf{4},\text{-}\mathbf{1})\,\Gamma(\mathbf{1}) + \\
& \left(-\frac{1}{2}\right)(C_2(\mathbf{1},\text{-}\mathbf{2},\mathbf{3},\mathbf{4})\,\Gamma(\text{-}\mathbf{2}) + C_2(\mathbf{1},\text{-}\mathbf{3},\mathbf{2},\mathbf{4})\,\Gamma(\text{-}\mathbf{3})) + \\
& (-4)\, C_8(\mathbf{1},\text{-}\mathbf{4},\mathbf{2},\mathbf{3})\,\Gamma(\text{-}\mathbf{4}) + \\
& \sum_{\mathbf{5,6}} (-2)\, C_3(\mathbf{2},\mathbf{3},\mathbf{5},\mathbf{6})\, C_5(\mathbf{1},\mathbf{5},\mathbf{6},\mathbf{4})\,\delta_G(2+3-5-6) + \\
& (-1)\, C_2(\mathbf{1},\mathbf{5},\mathbf{3},\mathbf{6})\, C_5(\mathbf{5},\mathbf{2},\mathbf{6},\mathbf{4})\,\delta_G(1-5+3-6) + \\
& (-1)\, C_2(\mathbf{1},\mathbf{5},\mathbf{2},\mathbf{6})\, C_5(\mathbf{5},\mathbf{3},\mathbf{6},\mathbf{4})\,\delta_G(1-5+2-6) + \\
& (-8)\, C_7(\mathbf{5},\mathbf{3},\mathbf{4},\mathbf{6})\, C_8(\mathbf{1},\mathbf{5},\mathbf{2},\mathbf{6})\,\delta_G(5-3+4+6) + \\
& (-8)\, C_7(\mathbf{5},\mathbf{2},\mathbf{4},\mathbf{6})\, C_8(\mathbf{1},\mathbf{5},\mathbf{3},\mathbf{6})\,\delta_G(5-2+4+6) + \\
& (-4)\, C_6(\mathbf{1},\mathbf{5},\mathbf{6},\mathbf{4})\, C_8(\mathbf{5},\mathbf{6},\mathbf{2},\mathbf{3})\,\delta_G(1-5-6-4)\Big\}
\end{aligned}
\tag{B.27}
$$

$$
\begin{aligned}
\partial_\ell C_6(\mathbf{1},\mathbf{2},\mathbf{3},\mathbf{4}) \;=\; & \\
& \delta_G(1-2-3-4)\Big\{ \\
& (\omega(\mathbf{1})-\omega(\mathbf{2})-\omega(\mathbf{3})-\omega(\mathbf{4}))\, C_6(\mathbf{1},\mathbf{2},\mathbf{3},\mathbf{4}) + \\
& (-2)\, C_1(\mathbf{1},\text{-}\mathbf{4},\mathbf{2},\mathbf{3})\,\Gamma(\text{-}\mathbf{4}) + \\
& \left(-\frac{1}{2}\right)\left(C_2(\mathbf{1},\mathbf{3},\text{-}\mathbf{2},\mathbf{4})\,\Gamma(\mathbf{2}) + C_2(\mathbf{1},\mathbf{2},\text{-}\mathbf{3},\mathbf{4})\,\Gamma(\mathbf{3})\right) + \\
& (-4)\, C_9(\mathbf{2},\mathbf{3},\mathbf{4},\text{-}\mathbf{1})\,\Gamma(\mathbf{1}) + \\
& \sum_{\mathbf{5,6}} (-2)\, C_1(\mathbf{5},\mathbf{6},\mathbf{2},\mathbf{3})\, C_6(\mathbf{1},\mathbf{5},\mathbf{6},\mathbf{4})\,\delta_G(5+6-2-3) + \\
& (-1)\, C_2(\mathbf{5},\mathbf{3},\mathbf{6},\mathbf{4})\, C_6(\mathbf{1},\mathbf{2},\mathbf{5},\mathbf{6})\,\delta_G(5-3+6-4) + \\
& (-1)\, C_2(\mathbf{5},\mathbf{2},\mathbf{6},\mathbf{4})\, C_6(\mathbf{1},\mathbf{3},\mathbf{5},\mathbf{6})\,\delta_G(5-2+6-4) + \\
& (-8)\, C_4(\mathbf{1},\mathbf{5},\mathbf{3},\mathbf{6})\, C_9(\mathbf{2},\mathbf{5},\mathbf{4},\mathbf{6})\,\delta_G(1+5-3+6) + \\
& (-8)\, C_4(\mathbf{1},\mathbf{5},\mathbf{2},\mathbf{6})\, C_9(\mathbf{3},\mathbf{5},\mathbf{4},\mathbf{6})\,\delta_G(1+5-2+6) + \\
& (-4)\, C_5(\mathbf{1},\mathbf{5},\mathbf{6},\mathbf{4})\, C_9(\mathbf{2},\mathbf{3},\mathbf{5},\mathbf{6})\,\delta_G(1+5+6-4)\Big\}
\end{aligned}
\tag{B.28}
$$

$$
\begin{aligned}
\partial_\ell C_7(\mathbf{1},\mathbf{2},\mathbf{3},\mathbf{4}) \;=\; & \delta_G(1-2+3+4)\Big\{ \\
& (-\omega(\mathbf{1})+\omega(\mathbf{2})-\omega(\mathbf{3})-\omega(\mathbf{4}))\, C_7(\mathbf{1},\mathbf{2},\mathbf{3},\mathbf{4}) + \\
& (-2)\, C_3(\text{-}\mathbf{1},\mathbf{2},\mathbf{3},\mathbf{4})\,\Gamma(\mathbf{1}) + \\
& \left(-\frac{1}{2}\right)\left(C_2(\text{-}\mathbf{4},\mathbf{1},\mathbf{2},\mathbf{3})\,\Gamma(\mathbf{4}) + C_2(\text{-}\mathbf{3},\mathbf{1},\mathbf{2},\mathbf{4})\,\Gamma(\mathbf{3})\right) + \\
& (-4)\, C_9(\mathbf{1},\text{-}\mathbf{2},\mathbf{3},\mathbf{4})\,\Gamma(\mathbf{2}) + \\
& \sum_{\mathbf{5,6}} (-2)\, C_3(\mathbf{5},\mathbf{6},\mathbf{3},\mathbf{4})\, C_7(\mathbf{1},\mathbf{2},\mathbf{5},\mathbf{6})\,\delta_G(5+6-3-4) + \\
& (-1)\, C_2(\mathbf{5},\mathbf{1},\mathbf{6},\mathbf{4})\, C_7(\mathbf{5},\mathbf{2},\mathbf{3},\mathbf{6})\,\delta_G(5-1+6-4) + \\
& (-1)\, C_2(\mathbf{5},\mathbf{1},\mathbf{6},\mathbf{3})\, C_7(\mathbf{5},\mathbf{2},\mathbf{4},\mathbf{6})\,\delta_G(5-1+6-3) + \\
& (-8)\, C_5(\mathbf{5},\mathbf{2},\mathbf{6},\mathbf{4})\, C_9(\mathbf{1},\mathbf{5},\mathbf{3},\mathbf{6})\,\delta_G(5+2+6-4) + \\
& (-8)\, C_5(\mathbf{5},\mathbf{2},\mathbf{6},\mathbf{3})\, C_9(\mathbf{1},\mathbf{5},\mathbf{4},\mathbf{6})\,\delta_G(5+2+6-3) + \\
& (-4)\, C_4(\mathbf{5},\mathbf{6},\mathbf{1},\mathbf{2})\, C_9(\mathbf{5},\mathbf{6},\mathbf{3},\mathbf{4})\,\delta_G(5+6-1+2)\Big\}
\end{aligned}
\tag{B.29}
$$

$$
\begin{aligned}
\partial_\ell C_8(\mathbf{1},\mathbf{2},\mathbf{3},\mathbf{4}) \;=\;& \delta_G(1+2+3+4)\Big\{ \\
& (-\omega(\mathbf{1})-\omega(\mathbf{2})-\omega(\mathbf{3})-\omega(\mathbf{4}))\, C_8(\mathbf{1},\mathbf{2},\mathbf{3},\mathbf{4}) + \\
& \sum_{5,6} (-2)\, C_1(\mathbf{1},\mathbf{2},\mathbf{5},\mathbf{6})\, C_8(\mathbf{5},\mathbf{6},\mathbf{3},\mathbf{4})\, \delta_G(1+2-5-6) + \\
& (-1)\, C_2(\mathbf{2},\mathbf{5},\mathbf{4},\mathbf{6})\, C_8(\mathbf{1},\mathbf{5},\mathbf{3},\mathbf{6})\, \delta_G(2-5+4-6) + \\
& (-1)\, C_2(\mathbf{1},\mathbf{5},\mathbf{4},\mathbf{6})\, C_8(\mathbf{2},\mathbf{5},\mathbf{3},\mathbf{6})\, \delta_G(1-5+4-6) + \\
& (-1)\, C_2(\mathbf{2},\mathbf{5},\mathbf{3},\mathbf{6})\, C_8(\mathbf{1},\mathbf{5},\mathbf{4},\mathbf{6})\, \delta_G(2-5+3-6) + \\
& (-1)\, C_2(\mathbf{1},\mathbf{5},\mathbf{3},\mathbf{6})\, C_8(\mathbf{2},\mathbf{5},\mathbf{4},\mathbf{6})\, \delta_G(1-5+3-6) + \\
& (-2)\, C_3(\mathbf{3},\mathbf{4},\mathbf{5},\mathbf{6})\, C_8(\mathbf{1},\mathbf{2},\mathbf{5},\mathbf{6})\, \delta_G(3+4-5-6)\Big\}
\end{aligned}
\tag{B.30}
$$

$$
\begin{aligned}
\partial_\ell C_9(\mathbf{1},\mathbf{2},\mathbf{3},\mathbf{4}) \;=\;& \delta_G(1+2+3+4)\Big\{ \\
& (-\omega(\mathbf{1})-\omega(\mathbf{2})-\omega(\mathbf{3})-\omega(\mathbf{4}))\, C_9(\mathbf{1},\mathbf{2},\mathbf{3},\mathbf{4}) + \\
& \sum_{5,6} (-2)\, C_1(\mathbf{5},\mathbf{6},\mathbf{1},\mathbf{2})\, C_9(\mathbf{5},\mathbf{6},\mathbf{3},\mathbf{4})\, \delta_G(5+6-1-2) + \\
& (-1)\, C_2(\mathbf{5},\mathbf{2},\mathbf{6},\mathbf{4})\, C_9(\mathbf{1},\mathbf{5},\mathbf{3},\mathbf{6})\, \delta_G(5-2+6-4) + \\
& (-1)\, C_2(\mathbf{5},\mathbf{1},\mathbf{6},\mathbf{4})\, C_9(\mathbf{2},\mathbf{5},\mathbf{3},\mathbf{6})\, \delta_G(5-1+6-4) + \\
& (-1)\, C_2(\mathbf{5},\mathbf{2},\mathbf{6},\mathbf{3})\, C_9(\mathbf{1},\mathbf{5},\mathbf{4},\mathbf{6})\, \delta_G(5-2+6-3) + \\
& (-1)\, C_2(\mathbf{5},\mathbf{1},\mathbf{6},\mathbf{3})\, C_9(\mathbf{2},\mathbf{5},\mathbf{4},\mathbf{6})\, \delta_G(5-1+6-3) + \\
& (-2)\, C_3(\mathbf{5},\mathbf{6},\mathbf{3},\mathbf{4})\, C_9(\mathbf{1},\mathbf{2},\mathbf{5},\mathbf{6})\, \delta_G(3+4-5-6)\Big\}
\end{aligned}
\tag{B.31}
$$

B.3 Observables

$$
\begin{aligned}
\partial_\ell s_1^z(\mathbf{Q},\mathbf{1},\mathbf{2}) \;=\;& \delta_G(Q+1-2)\Big\{ \\
& (-1)\Gamma(\mathbf{1})\, s_3^z(\mathbf{Q},\mathbf{2},\text{-}\mathbf{1}) + \\
& (-1)\Gamma(\mathbf{2})\, s_4^z(\mathbf{Q},\mathbf{1},\text{-}\mathbf{2}) + \\
& \sum_{3,4} (-2) C_4(\mathbf{1},\mathbf{3},\mathbf{2},\mathbf{4})\, s_3^z(\mathbf{Q},\mathbf{3},\mathbf{4})\, \delta_G(1+3-2+4) + \\
& (-2) C_6(\mathbf{1},\mathbf{2},\mathbf{3},\mathbf{4})\, s_4^z(\mathbf{Q},\mathbf{3},\mathbf{4})\, \delta_G(1-2-3-4)\Big\}
\end{aligned}
\tag{B.32}
$$

$$\begin{aligned}\partial_\ell s_2^z(\mathbf{Q},\mathbf{1},\mathbf{2}\,) = \delta_G(Q+1-2)\Big\{ & \\ & (-1)\Gamma(\mathbf{1})s_4^z(\mathbf{Q},\text{-}\mathbf{2},\mathbf{1})+ \\ & (-1)\Gamma(\mathbf{2})s_3^z(\mathbf{Q},\text{-}\mathbf{1},\mathbf{2})+ \\ \sum_{3,4} \quad & (-2)C_5(\mathbf{3},\mathbf{1},\mathbf{4},\mathbf{2}\,)s_3^z(\mathbf{Q},\mathbf{3},\mathbf{4})\,\delta_G(3+1+4-2)+ \\ & (-2)C_7(\mathbf{3},\mathbf{1},\mathbf{2},\mathbf{4}\,)s_4^z(\mathbf{Q},\mathbf{3},\mathbf{4})\,\delta_G(3-1+2+4)+\Big\}\end{aligned} \tag{B.33}$$

$$\begin{aligned}\partial_\ell s_3^z(\mathbf{Q},\mathbf{1},\mathbf{2}\,) = \delta_G(Q-1-2)\Big\{ & \\ & (-1)\Gamma(\text{-}\mathbf{2})s_1^z(\mathbf{Q},\text{-}\mathbf{2},\mathbf{1})+ \\ & (-1)\Gamma(\mathbf{1})s_2^z(\mathbf{Q},\text{-}\mathbf{1},\mathbf{2})+ \\ \sum_{3,4} \quad & (-4)C_9(\mathbf{1},\mathbf{3},\mathbf{2},\mathbf{4}\,)s_4^z(\mathbf{Q},\mathbf{3},\mathbf{4})\,\delta_G(1+3+2+4)\Big\}\end{aligned} \tag{B.34}$$

$$\begin{aligned}\partial_\ell s_4^z(\mathbf{Q},\mathbf{1},\mathbf{2}\,) = \delta_G(Q+1+2)\Big\{ & \\ & (-1)\Gamma(\text{-}\mathbf{2})s_1^z(\mathbf{Q},\mathbf{1},\text{-}\mathbf{2})+ \\ & (-1)\Gamma(\mathbf{1})s_2^z(\mathbf{Q},\mathbf{2},\text{-}\mathbf{1})+ \\ \sum_{3,4} \quad & (-4)C_8(\mathbf{1},\mathbf{3},\mathbf{2},\mathbf{4}\,)s_4^z(\mathbf{Q},\mathbf{3},\mathbf{4})\,\delta_G(1+3+2+4)\Big\}\end{aligned} \tag{B.35}$$

$$\begin{aligned}\partial_\ell s_1^+(\mathbf{Q}) = \; & (-1)\Gamma(\mathbf{Q})s_2^+(\text{-}\mathbf{Q})+ \\ \sum_{2} \quad & \Big\{(-1)\Gamma(\mathbf{2})s_7^+(\mathbf{Q},\mathbf{2},\mathbf{Q},\text{-}\mathbf{2})+ \\ & (-2)\Gamma(\mathbf{2})s_8^+(\mathbf{Q},\mathbf{Q},\mathbf{2},\text{-}\mathbf{2})+\Big\} \\ \sum_{2,3,4} \quad & \Big\{(-2)C_4(\mathbf{2},\mathbf{3},\mathbf{Q},\mathbf{4}\,)s_8^+(\mathbf{Q},\mathbf{2},\mathbf{3},\mathbf{4})\,\delta_G(2+3-Q+4)+ \\ & (-4)C_9(\mathbf{Q},\mathbf{2},\mathbf{3},\mathbf{4}\,)s_5^+(\mathbf{Q},\mathbf{2},\mathbf{3},\mathbf{4})+\delta_G(Q+2+3+4)\Big\}\end{aligned} \tag{B.36}$$

$$
\begin{aligned}
\partial_\ell s_2^+(\mathbf{Q}) \;=\;& (-1)\Gamma(\text{-}\mathbf{Q})\, s_1^+(\text{-}\mathbf{Q}) + \\
& \sum_{2} \Big\{(-2)\Gamma(\mathbf{2})\, s_5^+(\text{-},\mathbf{Q},\mathbf{2},\mathbf{Q})\text{-}2 + \\
& \qquad (-1)\Gamma(\mathbf{2})\, s_6^+(\text{-}\mathbf{Q},\mathbf{2},\mathbf{Q},\text{-}\mathbf{2})\Big\} + \\
& \sum_{2,3,4} \Big\{(-2)C_7(\mathbf{2},\mathbf{Q},\mathbf{3},\mathbf{4}\,)\, s_5^+(\text{-}\mathbf{Q},\mathbf{2},\mathbf{3},\mathbf{4})\,\delta_G(2-Q+3+4) + \\
& \qquad (-4)C_8(\mathbf{2},\mathbf{3},\mathbf{Q},\mathbf{4}\,)\, s_8^+(\text{-}\mathbf{Q},\mathbf{2},\mathbf{3},\mathbf{4})\,\delta_G(Q+2+3+4)\Big\}
\end{aligned}
\tag{B.37}
$$

$$
\begin{aligned}
\partial_\ell s_3^+(\mathbf{Q},\mathbf{1},\mathbf{2},\mathbf{3}) \;=\;& \delta_G(Q+1+2-3)\Big\{ \\
& (-1)C_5(\mathbf{Q},\mathbf{1},\mathbf{2},\mathbf{3})\, s_1^+(\mathbf{Q}) + \\
& (-1)\Gamma(\text{-}\mathbf{3})\, s_5^+(\text{-}\mathbf{Q},\text{-}\mathbf{3},\mathbf{1},\mathbf{2}) + \\
& \left(-\frac{1}{2}\right)\Gamma(\text{-}\mathbf{1})\, s_6^+(\mathbf{Q},\text{-}\mathbf{1},\mathbf{2},\mathbf{3}) + \\
& \left(-\frac{1}{2}\right)\Gamma(\text{-}\mathbf{2})\, s_6^+(\,\mathbf{Q},\text{-}\mathbf{2},\mathbf{1},\mathbf{3}) + \\
& \sum_{4,5} (-2)C_7(\mathbf{4},\mathbf{1},\mathbf{3},\mathbf{5}\,)\, s_5^+(\mathbf{Q},\mathbf{4},\mathbf{2},\mathbf{5})\,\delta_G(4-1+3-5) + \\
& \qquad (-2)C_7(\mathbf{4},\mathbf{1},\mathbf{2},\mathbf{5}\,)\, s_5^+(\mathbf{Q},\mathbf{4},\mathbf{3},\mathbf{5})\,\delta_G(4-1+2-5) + \\
& \qquad (-1)C_5(\mathbf{4},\mathbf{1},\mathbf{5},\mathbf{3}\,)\, s_6^+(\mathbf{Q},\mathbf{4},\mathbf{1},\mathbf{5})\,\delta_G(4+1+5-3) + \\
& \qquad (-1)C_5(\mathbf{4},\mathbf{2},\mathbf{5},\mathbf{3}\,)\, s_6^+(\mathbf{Q},\mathbf{4},\mathbf{2},\mathbf{5})\,\delta_G(4+2+5-3) + \\
& \qquad (-2)C_8(\mathbf{4},\mathbf{5},\mathbf{1},\mathbf{2}\,)\, s_8^+(\mathbf{Q},\mathbf{4},\mathbf{5},\mathbf{3})\,\delta_G(4+5+1+2)\Big\}
\end{aligned}
\tag{B.38}
$$

$$
\begin{aligned}
\partial_\ell s_4^+(\mathbf{Q},\mathbf{1},\mathbf{2},\mathbf{3}) \;=\; & \delta_G(Q+1-2-3)\Big\{ \\
& (-1)C_6(\mathbf{1},\mathbf{2},\mathbf{3},\text{-}\mathbf{Q})\, s_2^+(\text{-}\mathbf{Q}) + \\
& \left(-\frac{1}{2}\right)\Gamma(\mathbf{2})\, s_7^+(\mathbf{Q},\mathbf{1},\mathbf{3},\text{-}\mathbf{2}) + \\
& \left(-\frac{1}{2}\right)\Gamma(\mathbf{3})\, s_7^+(\mathbf{Q},\mathbf{1},\mathbf{2},\text{-}\mathbf{3}) + \\
& (-1)\Gamma(\mathbf{1})\, s_8^+(\mathbf{Q},\mathbf{2},\mathbf{3},\text{-}\mathbf{1}) + \\
\sum_{4,5} \quad & (-2)C_4(\mathbf{1},\mathbf{4},\mathbf{2},\mathbf{5})\, s_8^+(\mathbf{Q},\mathbf{3},\mathbf{4},\mathbf{5})\, \delta_G(1+4-2+5) + \\
& (-2)C_4(\mathbf{1},\mathbf{4},\mathbf{3},\mathbf{5})\, s_8^+(\mathbf{Q},\mathbf{2},\mathbf{4},\mathbf{5})\, \delta_G(1+4-3+5) + \\
& (-2)C_9(\mathbf{2},\mathbf{3},\mathbf{4},\mathbf{5})\, s_5^+(\mathbf{Q},\mathbf{1},\mathbf{4},\mathbf{5})\, \delta_G(2+3+4+5) + \\
& (-1)C_6(\mathbf{1},\mathbf{2},\mathbf{4},\mathbf{5})\, s_7^+(\mathbf{Q},\mathbf{4},\mathbf{3},\mathbf{5})\, \delta_G(1-2-4-5) + \\
& (-1)C_6(\mathbf{1},\mathbf{3},\mathbf{4},\mathbf{5})\, s_7^+(\mathbf{Q},\mathbf{4},\mathbf{2},\mathbf{5})\, \delta_G(1-3-4-5)\Big\}
\end{aligned}
\tag{B.39}
$$

$$
\begin{aligned}
\partial_\ell s_5^+(\mathbf{Q},\mathbf{1},\mathbf{2},\mathbf{3}) \;=\; & \delta_G(Q+1+2+3)\Big\{ \\
& (+1)C_5(\mathbf{1},\mathbf{2},\mathbf{3},\text{-}\mathbf{Q})\, s_2^+(\text{-}\mathbf{Q}) + \\
& (-2)C_8(\mathbf{1},\mathbf{Q},\mathbf{2},\mathbf{3})\, s_1^+(\mathbf{Q})\, 13 + \\
& (-1)\Gamma(\mathbf{1})\, s_3^+(\,\mathbf{Q},\mathbf{2},\mathbf{3},\text{-}\mathbf{1}) + \\
& \left(-\frac{1}{2}\right)\Gamma(\text{-}\mathbf{2})\, s_7^+(\mathbf{Q},\mathbf{1},\text{-}\mathbf{2},\mathbf{3}) + \\
& \left(-\frac{1}{2}\right)\Gamma(\text{-}\mathbf{3})\, s_7^+(\mathbf{Q},\mathbf{1},\text{-}\mathbf{3},\mathbf{2}) + \\
\sum_{4,5} \quad & (-2)C_8(\mathbf{4},\mathbf{5},\mathbf{2},\mathbf{3})\, s_4^+(\mathbf{Q},\mathbf{1},\mathbf{4},\mathbf{5})\, \delta_G(4+5+2+3) + \\
& (-2)C_8(\mathbf{1},\mathbf{4},\mathbf{2},\mathbf{5})\, s_6^+(\mathbf{Q},\mathbf{4},\mathbf{3},\mathbf{5})\, \delta_G(1+4+2+5) + \\
& (-2)C_8(\mathbf{1},\mathbf{4},\mathbf{3},\mathbf{5})\, s_6^+(\mathbf{Q},\mathbf{4},\mathbf{2},\mathbf{5})\, \delta_G(1+4+3+5)\Big\}
\end{aligned}
\tag{B.40}
$$

$$
\begin{aligned}
\partial_\ell s_6^+(\mathbf{Q},\mathbf{1},\mathbf{2},\mathbf{3}) \;=\; & \delta_G(Q-1+2-3)\Big\{ \\
& (-2)C_7(\mathbf{1},\mathbf{2},\mathbf{3},\text{-}\mathbf{Q})\, s_2^+(\text{-}\mathbf{Q}) + \\
& (-2)\Gamma(\text{-}\mathbf{2})\, s_8^+(\mathbf{Q},\mathbf{1},\text{-}\mathbf{2},\mathbf{3}) + \\
& (-2)\Gamma(\mathbf{1})\, s_3^+(\mathbf{Q},\mathbf{2},\text{-}\mathbf{1},\mathbf{3}) + \\
& (-1)\Gamma(\text{-}\mathbf{3})\, s_7^+(\mathbf{Q},\text{-}\mathbf{3},\mathbf{1},\mathbf{2}) + \\
\sum_{4,5} \quad & (-8)C_9(\mathbf{1},\mathbf{4},\mathbf{3},\mathbf{5})\, s_5^+(\mathbf{Q},\mathbf{4},\mathbf{2},\mathbf{5})\, \delta_G(1+4+3+5) + \\
& (-4)C_5(\mathbf{1},\mathbf{4},\mathbf{2},\mathbf{5})\, s_8^+(\mathbf{Q},\mathbf{1},\mathbf{4},\mathbf{5})\, \delta_G(1+4+2-5) + \\
& (-2)C_7(\mathbf{1},\mathbf{2},\mathbf{4},\mathbf{5})\, s_3^+(\mathbf{Q},\mathbf{4},\mathbf{5},\mathbf{3})\, \delta_G(1-2+4+5) + \\
& (-2)C_7(\mathbf{4},\mathbf{2},\mathbf{3},\mathbf{5})\, s_7^+(\mathbf{Q},\mathbf{4},\mathbf{1},\mathbf{5})\, \delta_G(4-2+3+5) + \\
& (-2)C_4(\mathbf{4},\mathbf{5},\mathbf{1},\mathbf{2})\, s_8^+(\mathbf{Q},\mathbf{4},\mathbf{5},\mathbf{3})\, \delta_G(4+5-1+2)\Big\}
\end{aligned}
\tag{B.41}
$$

$$
\begin{aligned}
\partial_\ell s_7^+(\mathbf{Q},\mathbf{1},\mathbf{2},\mathbf{3}) \;=\; & \delta_G(Q+1-2+3)\Big\{ \\
& (-2)C_4(\mathbf{1},\mathbf{Q},\mathbf{2},\mathbf{3})\, s_1^+(\mathbf{Q}) + \\
& (-2)\Gamma(\text{-}\mathbf{3})\, s_4^+(\mathbf{Q},\mathbf{1},\mathbf{2},\text{-}\mathbf{3}) + \\
& (-2)\Gamma(\mathbf{2})\, s_5^+(\mathbf{Q},\mathbf{1},\mathbf{3},\text{-}\mathbf{2}) + \\
& (-1)\Gamma(\mathbf{1})\, s_6^+(\mathbf{Q},\mathbf{2},\mathbf{3},\text{-}\mathbf{1}) + \\
\sum_{4,5} \quad & (-8)C_8(\mathbf{1},\mathbf{4},\mathbf{3},\mathbf{5})\, s_8^+(\mathbf{Q},\mathbf{2},\mathbf{4},\mathbf{5})\, \delta_G(1+4+3+5) + \\
& (-4)C_6(\mathbf{1},\mathbf{2},\mathbf{4},\mathbf{5})\, s_5^+(\mathbf{Q},\mathbf{4},\mathbf{3},\mathbf{5})\, \delta_G(1-2-4-5) + \\
& (-2)C_4(\mathbf{4},\mathbf{5},\mathbf{3},\mathbf{3})\, s_4^+(\mathbf{Q},\mathbf{1},\mathbf{4},\mathbf{5})\, \delta_G(4+5-3+3) + \\
& (-2)C_7(\mathbf{2},\mathbf{3},\mathbf{4},\mathbf{5})\, s_5^+(\mathbf{Q},\mathbf{1},\mathbf{4},\mathbf{5})\, \delta_G(2-3+4+5) + \\
& (-2)C_4(\mathbf{1},\mathbf{4},\mathbf{2},\mathbf{5})\, s_6^+(\mathbf{Q},\mathbf{4},\mathbf{3},\mathbf{5})\, \delta_G(1+4-2+5)\Big\}
\end{aligned}
\tag{B.42}
$$

$$
\begin{aligned}
\partial_\ell s_8^+(\mathbf{Q},\mathbf{1},\mathbf{2},\mathbf{3}) \;=\; & \delta_G(Q-1-2-3)\Big\{ \\
& (+1)C_6(\mathbf{Q},\mathbf{1},\mathbf{2},\mathbf{3})\,s_1^+(\mathbf{Q}) + \\
& (-2)C_9(\mathbf{1},\mathbf{2},\mathbf{3},\text{-}\mathbf{Q})\,s_2^+(\text{-}\mathbf{Q}) + \\
& (-1)\Gamma(\text{-}\mathbf{3})\,s_4^+(\mathbf{Q},\text{-}\mathbf{3},\mathbf{1},\mathbf{2}) + \\
& \left(-\frac{1}{2}\right)\Gamma(\mathbf{1})\,s_6^+(\mathbf{Q},\mathbf{2},\text{-}\mathbf{1},\mathbf{3}) + \\
& \left(-\frac{1}{2}\right)\Gamma(\mathbf{2})\,s_6^+(\mathbf{Q},\mathbf{1},\text{-}\mathbf{2},\mathbf{3}) + \\
\sum_{4,5} \quad & (-2)C_9(\mathbf{1},\mathbf{2},\mathbf{4},\mathbf{5})\,s_3^+(\mathbf{Q},\mathbf{4},\mathbf{5},\mathbf{3})\,\delta_G(1+2+4+5) + \\
& (-2)C_9(\mathbf{1},\mathbf{4},\mathbf{3},\mathbf{5})\,s_7^+(\mathbf{Q},\mathbf{4},\mathbf{2},\mathbf{5})\,\delta_G(1+4+3+5) + \\
& (-2)C_9(\mathbf{2},\mathbf{4},\mathbf{3},\mathbf{5})\,s_7^+(\mathbf{Q},\mathbf{4},\mathbf{1},\mathbf{5})\,\delta_G(2+4+3+5)\Big\}
\end{aligned}
\tag{B.43}
$$

$$
\begin{aligned}
\partial_\ell s_1^-(\mathbf{Q}) \;=\; & (-1)\Gamma(\mathbf{Q})\,s_2^-(\text{-}\mathbf{Q}) + \\
\sum_{2} \quad & \Big\{(-1)\Gamma(\mathbf{2})\,s_6^-(\text{-}\mathbf{Q},\mathbf{Q},\mathbf{2},\text{-}\mathbf{2}) + \\
& (-2)\Gamma(\mathbf{2})\,s_3^-(\text{-}\mathbf{Q},\mathbf{Q},\mathbf{2},\text{-}\mathbf{2})\Big\} + \\
\sum_{2,3,4} \quad & \Big\{(-2)C_6(\mathbf{Q}\;\mathbf{2}\;\mathbf{3}\;\mathbf{4})\,s_3^-(\text{-}\mathbf{Q},\mathbf{2},\mathbf{3},\mathbf{4})\,\delta_G(Q-2-3-4) + \\
& (-4)C_8(\mathbf{Q}\;\mathbf{2}\;\mathbf{3}\;\mathbf{4})\,s_8^-(\mathbf{Q},\mathbf{2},\mathbf{3},\mathbf{4})\,\delta_G(Q-2+3+4)\Big\}
\end{aligned}
\tag{B.44}
$$

$$
\begin{aligned}
\partial_\ell s_2^-(\mathbf{Q}) \;=\; & (-1)\Gamma(\mathbf{Q})\,s_1^-(\mathbf{Q}) + \\
\sum_{2} \quad & \Big\{(-2)\Gamma(\mathbf{2})\,s_8^-(\mathbf{Q},\mathbf{2},\mathbf{Q},\text{-}\mathbf{2}) + \\
& (-1)\Gamma(\mathbf{2})\,s_5^-(\;\mathbf{Q},\mathbf{2},\text{-}\mathbf{2},\mathbf{Q})\Big\} + \\
\sum_{2,3,4} \quad & \Big\{(-2)C_5(\mathbf{2}\;\mathbf{3}\;\mathbf{4}\;\mathbf{Q})\,s_8^-(\mathbf{Q},\mathbf{2},\mathbf{3},\mathbf{4})\,\delta_G(2+3+4-Q) + \\
& (-4)C_9(\mathbf{2}\;\mathbf{3}\;\mathbf{Q}\;\mathbf{4})\,s_3^-(\mathbf{Q},\mathbf{2},\mathbf{3},\mathbf{4})\,\delta_G(Q+2+3+4)\Big\}
\end{aligned}
\tag{B.45}
$$

$$
\begin{aligned}
\partial_\ell s_3^-(\mathbf{Q},\mathbf{1},\mathbf{2},\mathbf{3}) \;=\; & \delta_G(Q+1+2+3)\Big\{ \\
& (+1)C_4(\mathbf{1},\mathbf{2},\text{-}\mathbf{Q},\mathbf{3})\,s_1^-(\text{-}\mathbf{Q}) + \\
& (-1)\Gamma(\text{-}\mathbf{3})\,s_4^-(\mathbf{Q},\mathbf{1},\mathbf{2},\mathbf{Q}) + \\
& \left(-\frac{1}{2}\right)\Gamma(\mathbf{1})\,s_5^-(\mathbf{Q},\mathbf{2},\mathbf{3},\text{-}\mathbf{1}) + \\
& \left(-\frac{1}{2}\right)\Gamma(\mathbf{2})\,s_5^-(\,\mathbf{Q},\mathbf{1},\mathbf{3},\text{-}\mathbf{2}) + \\
& (-2)C_8(\mathbf{1},\mathbf{2},\mathbf{3},\mathbf{Q})\,s_2^-(\mathbf{Q}) + \\
\sum_{4,5} \quad & (-2)C_8(\mathbf{1},\mathbf{2},\mathbf{4},\mathbf{5})\,s_7^-(\mathbf{Q},\mathbf{3},\mathbf{4},\mathbf{5})\,\delta_G(1+2+4+5) + \\
& (-2)C_8(\mathbf{1},\mathbf{4},\mathbf{3},\mathbf{5})\,s_6^-(\mathbf{Q},\mathbf{2},\mathbf{4},\mathbf{5})\,\delta_G(1+3+4+5) + \\
& (-2)C_8(\mathbf{2},\mathbf{4},\mathbf{3},\mathbf{5})\,s_6^-(\mathbf{Q},\mathbf{1},\mathbf{4},\mathbf{5})\,\delta_G(2+3+4+5)\Big\}
\end{aligned}
\tag{B.46}
$$

$$
\begin{aligned}
\partial_\ell s_4^-(\mathbf{Q},\mathbf{1},\mathbf{2},\mathbf{3}) \;=\; & \delta_G(Q+1+2-3)\Big\{ \\
& (-1)C_5(\mathbf{1},\mathbf{2},\mathbf{3},\mathbf{Q})\,s_2^-(\mathbf{Q}) + \\
& \left(-\frac{1}{2}\right)\Gamma(\mathbf{1})\,s_6^-(\mathbf{Q},\mathbf{2},\mathbf{3},\text{-}\mathbf{1}) + \\
& \left(-\frac{1}{2}\right)\Gamma(\mathbf{2})\,s_6^-(\,\mathbf{Q},\mathbf{1},\mathbf{3},\text{-}\mathbf{2}) + \\
& (-1)\Gamma(\mathbf{3})\,s_3^-(\,\mathbf{Q}\,,\mathbf{1},\mathbf{2},\text{-}\mathbf{3}) + \\
\sum_{4,5} \quad & (-1)C_4(\mathbf{1},\mathbf{4},\mathbf{3},\mathbf{5})\,s_6^-(\mathbf{Q},\mathbf{2},\mathbf{4},\mathbf{5})\,\delta_G(1+4-3+5) + \\
& (-1)C_4(\mathbf{2},\mathbf{4},\mathbf{3},\mathbf{5})\,s_6^-(\mathbf{Q},\mathbf{1},\mathbf{4},\mathbf{5})\,\delta_G(2+4-3+5) + \\
& (-2)C_6(\mathbf{1},\mathbf{3},\mathbf{4},\mathbf{5})\,s_3^-(\mathbf{Q},\mathbf{2},\mathbf{4}\,,\mathbf{5})\,\delta_G(1-3-4-5) + \\
& (-2)C_6(\mathbf{2},\mathbf{3},\mathbf{4},\mathbf{5}\,)\,s_3^-(\mathbf{Q}\,,\mathbf{1},\mathbf{4},\mathbf{5})\,\delta_G(2-3-4-5) + \\
& (-2)C_8(\mathbf{1},\mathbf{2},\mathbf{4},\mathbf{5})\,s_8^-(\mathbf{Q}\,,\mathbf{3},\mathbf{4},\mathbf{5})\,\delta_G(1+2+4+5)\Big\}
\end{aligned}
\tag{B.47}
$$

$$
\begin{aligned}
\partial_\ell s_5^-(\mathbf{Q},\mathbf{1},\mathbf{2},\mathbf{3}) \;=\; & \delta_G(Q+1+2-3)\Big\{ \\
& (-2)C_5(\mathbf{1},\mathbf{2},\mathbf{Q},\mathbf{3})\, s_2^-(\mathbf{Q}) + \\
& (-2)\Gamma(\text{-}\mathbf{3})\, s_3^-(\mathbf{Q},\mathbf{1},\text{-}\mathbf{3},\mathbf{2}) + \\
& (-1)\Gamma(\text{-}\mathbf{2})\, s_6^-(\mathbf{Q},\mathbf{1},\text{-}\mathbf{2},\mathbf{3}) + \\
& (-2)\Gamma(\mathbf{1})\, s_7^-(\,\mathbf{Q},\mathbf{2},\mathbf{3},\text{-}\mathbf{1}) + \\
\sum_{4,5} \quad & (-2)C_6(\mathbf{1},\mathbf{4},\mathbf{5},\mathbf{3})\, s_3^-(\mathbf{Q},\mathbf{4},\mathbf{5},\mathbf{2})\,\delta_G(1-4-5-3) + \\
& (-4)C_7(\mathbf{4},\mathbf{2},\mathbf{3},\mathbf{5})\, s_3^-(\mathbf{Q},\mathbf{1},\mathbf{4},\mathbf{5})\,\delta_G(-4+2-3-5) + \\
& (-2)C_5(\mathbf{4},\mathbf{2},\mathbf{5},\mathbf{3})\, s_6^-(\mathbf{Q},\mathbf{1},\mathbf{4},\mathbf{5})\,\delta_G(4+2+5-3) + \\
& (-2)C_5(\mathbf{1},\mathbf{4},\mathbf{5},\mathbf{3})\, s_7^-(\mathbf{Q},\mathbf{2},\mathbf{4},\mathbf{5})\,\delta_G(1+4+5-3) + \\
& (-8)C_8(\mathbf{1},\mathbf{4},\mathbf{2},\mathbf{5})\, s_8^-(\mathbf{Q},\mathbf{4},\mathbf{3},\mathbf{5})\,\delta_G(1+4+2+5)\Big\}
\end{aligned}
\tag{B.48}
$$

$$
\begin{aligned}
\partial_\ell s_6^-(\mathbf{Q},\mathbf{1},\mathbf{2},\mathbf{3}) \;=\; & \delta_G(Q+1+2-3)\Big\{ \\
& (-2)C_6(\mathbf{1},\mathbf{2},\text{-}\mathbf{Q},\mathbf{3})\, s_1^-(\text{-}\mathbf{Q}) + \\
& (-2)\Gamma(\text{-}\mathbf{3})\, s_4^-(\,\mathbf{Q},\mathbf{1},\text{-}\mathbf{3},\mathbf{2}) + \\
& (-2)\Gamma(\mathbf{1})\, s_8^-(\,\mathbf{Q},\mathbf{2},\mathbf{3},\text{-}\mathbf{1}) + \\
& (-1)\Gamma(\mathbf{2})\, s_5^-(\,\mathbf{Q},\mathbf{1},\text{-}\mathbf{2},\mathbf{3}) + \\
\sum_{4,5} \quad & (-2)C_6(\mathbf{1},\mathbf{4},\mathbf{5},\mathbf{3})\, s_4^-(\mathbf{Q},\mathbf{4},\mathbf{5},\mathbf{2})\,\delta_G(1-4-5-3) + \\
& (-2)C_6(\mathbf{1},\mathbf{2},\mathbf{4},\mathbf{5})\, s_5^-(\mathbf{Q},\mathbf{4},\mathbf{5},\mathbf{3})\,\delta_G(1-2-4-5) + \\
& (-2)C_5(\mathbf{1},\mathbf{4},\mathbf{5},\mathbf{3})\, s_8^-(\mathbf{Q},\mathbf{2},\mathbf{4},\mathbf{5})\,\delta_G(1+4+5-3) + \\
& (-4)C_4(\mathbf{1},\mathbf{4},\mathbf{2},\mathbf{5})\, s_8^-(\mathbf{Q},\mathbf{4},\mathbf{3},\mathbf{5})\,\delta_G(1+4-2+5) + \\
& (-8)C_9(\mathbf{2},\mathbf{4},\mathbf{3},\mathbf{5})\, s_3^-(\mathbf{Q},\mathbf{1},\mathbf{4},\mathbf{5})\,\delta_G(2+4+3+5)\Big\}
\end{aligned}
\tag{B.49}
$$

$$
\begin{aligned}
\partial_\ell s_7^-(\mathbf{Q},\mathbf{1},\mathbf{2},\mathbf{3}) \;=\; & \delta_G(Q+1-2-3)\Big\{ \\
& (-1)C_8(\text{-}\mathbf{Q},\mathbf{1},\mathbf{2},\mathbf{3})\, s_1^-(\text{-}\mathbf{Q}) + \\
& (-1)\Gamma(\text{-}\mathbf{1})\, s_8^-(\,\mathbf{Q},\text{-}\mathbf{1},\mathbf{2},\mathbf{3}) + \\
& \left(-\frac{1}{2}\right)\Gamma(\text{-}\mathbf{2})\, s_5^-(\,\mathbf{Q},\text{-}\mathbf{2},\mathbf{1},\mathbf{3}) + \\
& \left(-\frac{1}{2}\right)\Gamma(\text{-}\mathbf{3})\, s_5^-(\,\mathbf{Q},\text{-}\mathbf{3},\mathbf{1},\mathbf{2}) + \\
\sum_{4,5} \quad & (-1)C_7(\mathbf{4},\mathbf{1},\mathbf{2},\mathbf{5})\, s_5^-(\mathbf{Q},\mathbf{4},\mathbf{5},\mathbf{3})\,\delta_G(4-1+2+5) + \\
& (-1)C_7(\mathbf{4},\mathbf{1},\mathbf{3},\mathbf{5})\, s_5^-(\mathbf{Q},\mathbf{4},\mathbf{5},\mathbf{2})\,\delta_G(4-1+3+5) + \\
& (-2)C_5(\mathbf{4},\mathbf{1},\mathbf{5},\mathbf{2})\, s_8^-(\mathbf{Q},\mathbf{4},\mathbf{3},\mathbf{5})\,\delta_G(4+1-5+2) + \\
& (-2)C_5(\mathbf{4},\mathbf{1},\mathbf{5},\mathbf{3})\, s_8^-(\mathbf{Q},\mathbf{4},\mathbf{2},\mathbf{5})\,\delta_G(4+1-5+3) + \\
& (-2)C_9(\mathbf{4},\mathbf{5},\mathbf{2},\mathbf{3})\, s_3^-(\mathbf{Q},\mathbf{4},\mathbf{5},\mathbf{1})\,\delta_G(2+4+3+5)\Big\}
\end{aligned}
\tag{B.50}
$$

$$
\begin{aligned}
\partial_\ell s_8^-(\mathbf{Q},\mathbf{1},\mathbf{2},\mathbf{3}) \;=\; & \delta_G(Q-1-2-3)\Big\{ \\
& (+1)C_7(\mathbf{1},\mathbf{Q},\mathbf{2},\mathbf{3})\, s_2^-(\mathbf{Q}) + \\
& (-2)C_9(\mathbf{1},\text{-}\mathbf{Q},\mathbf{2},\mathbf{3})\, s_1^-(\text{-}\mathbf{Q}) + \\
& (-1)\Gamma(\mathbf{1})\, s_7^-(\mathbf{Q},\text{-}\mathbf{1},\mathbf{2},\mathbf{3}) + \\
& \left(-\frac{1}{2}\right)\Gamma(\text{-}\mathbf{2})\, s_6^-(\mathbf{Q},\text{-}\mathbf{2},\mathbf{1},\mathbf{3}) + \\
& \left(-\frac{1}{2}\right)\Gamma(\text{-}\mathbf{3})\, s_6^-(\mathbf{Q},\text{-}\mathbf{3},\mathbf{1},\mathbf{2}) + \\
\sum_{4,5} \quad & (-2)C_9(\mathbf{4},\mathbf{5},\mathbf{2},\mathbf{3})\, s_4^-(\mathbf{Q},\mathbf{4},\mathbf{5},\mathbf{1})\,\delta_G(2+4+3+5) + \\
& (-2)C_9(\mathbf{1},\mathbf{4},\mathbf{2},\mathbf{5})\, s_5^-(\mathbf{Q},\mathbf{4},\mathbf{5},\mathbf{3})\,\delta_G(1+4+2+5) + \\
& (-2)C_9(\mathbf{1},\mathbf{4},\mathbf{3},\mathbf{5})\, s_5^-(\mathbf{Q},\mathbf{4},\mathbf{5},\mathbf{2})\,\delta_G(1+4+3+5)\Big\} \quad .
\end{aligned}
\tag{B.51}
$$

APPENDIX C

Technical details

In the following we summarize the main steps which were taken to determine the theoretical line shapes which are compared with the experimental results in Figure 4.37.
First, we perform a linear extrapolation of the effective coefficients for $L = 8$ and $L = 16$ in $\frac{1}{L}$. We obtain an effective model in the thermodynamic limit defined for $N = 8 \times 8$ grid points in the 1. MBZ. The same extrapolation scheme is applied to the static structure factors yielding the total weights of the two- and three-magnon contributions.
We interpolate the effective coefficients in order to increase the Hilbert space for the subsequent recursion analysis. For the longitudinal part the system size is enhanced from $L = 8$ to $L = 192$. For the transverse part, we are using a system size of $L = 16$.
The continued fraction representation of the longitudinal DSF is determined by a non-symmetric Lanczos algorithm. The list of continued fraction coefficients is extended by additional constant coefficients known from the asymptotic limit (3.35a).
In order to obtain the three-magnon contribution to the transverse DSF the interpolated effective system with $L = 16$ is diagonalized. The resulting spectrum and eigenstates are used to determine the spectral density according to section 3.3.2.
All resulting spectral densities are normalized and rescaled by the total weight obtained from the corresponding static structure factor in the thermodynamic limit. Finally, we approximate the normalized spectral densities by a sum of Gaussian distribution functions with uniform broadening σ as defined in (4.68). Accordingly, the theoretical one-magnon δ-peak at $\mathbf{Q}$ is replaced by a single Gaussian distribution function of finite width exhibiting a total weight of $W = W^{1\mathrm{mag}(\mathbf{Q})}$.

Bibliography

[1] Philip W Anderson et al. More is different. *Science*, 177(4047):393–396, 1972.

[2] Robert B Laughlin and David Pines. The theory of everything. *Proceedings of the National Academy of Sciences of the United States of America*, pages 28–31, 2000.

[3] Paul W Humphreys. More is different...sometimes: Ising models, emergence, and undecidability. In *Why More Is Different*, pages 137–152. Springer, 2015.

[4] Michael E Peskin, Daniel V Schroeder, and Emil Martinec. An introduction to quantum field theory, 1996.

[5] GV Skorniakov and KA Ter-Martirosian. Three body problem for short range forces. i. scattering of low energy neutrons by deuterons. *Soviet Phys. JETP*, 4, 1957.

[6] Gerald D Mahan. *Many-particle physics*. Springer Science & Business Media, 2013.

[7] John Cardy. *Scaling and renormalization in statistical physics*, volume 5. Cambridge university press, 1996.

[8] LD Landau. ZhETF (USSR), 30 (1956). *JETP (Sov. Phys.)*, 3:920, 1956.

[9] AA Abrikosov and IM Khalatnikov. The theory of a Fermi liquid (the properties of liquid ^{3}He at low temperatures). *Reports on Progress in Physics*, 22(1):329, 1959.

[10] Liesbeth Venema, Bart Verberck, Iulia Georgescu, Giacomo Prando, Elsa Couderc, Silvia Milana, Maria Maragkou, Lina Persechini, Giulia Pacchioni, and Luke Fleet. The quasiparticle zoo. *Nature Physics*, 12(12):1085–1089, 2016.

[11] Gyaneshwar P Srivastava. *The physics of phonons*. CRC press, 1990.

[12] WY Liang. Excitons. *Physics Education*, 5(4):226, 1970.

[13] C Knetter, KP Schmidt, M Grüninger, and GS Uhrig. Fractional and integer excitations in quantum antiferromagnetic spin 1/2 ladders. *Physical Review Letters*, 87(16):167204, 2001.

[14] Kai P Schmidt and Götz S Uhrig. Excitations in one-dimensional $S = 1/2$ quantum antiferromagnets. *Physical Review Letters*, 90(22):227204, 2003.

[15] A Brooks Harris and Robert V Lange. Single-particle excitations in narrow energy bands. *Physical Review*, 157(2):295, 1967.

[16] Daniel C Mattis. *The theory of magnetism I: Statics and Dynamics*, volume 17. Springer Science & Business Media, 2012.

[17] Efstratios Manousakis. The spin-1/2 Heisenberg antiferromagnet on a square lattice and its application to the cuprous oxides. *Reviews of Modern Physics*, 63(1):1, 1991.

[18] E Jordao Neves and J Fernando Perez. Long range order in the ground state of two-dimensional antiferromagnets. *Physics Letters A*, 114(6):331–333, 1986.

[19] Tomáš Brauner. Spontaneous symmetry breaking and Nambu-Goldstone bosons in quantum many-body systems. *Symmetry*, 2(2):609–657, 2010.

[20] T Barnes. The 2D Heisenberg antiferromagnet in high-T_c superconductivity: A review of numerical techniques and results. *International Journal of Modern Physics C*, 2(02): 659–709, 1991.

[21] Philip W Anderson. An approximate quantum theory of the antiferromagnetic ground state. *Physical Review*, 86(5):694, 1952.

[22] Ryogo Kubo. The spin-wave theory of antiferromagnetics. *Physical Review*, 87(4):568, 1952.

[23] Yoichiro Nambu. Quasi-particles and gauge invariance in the theory of superconductivity. *Physical Review*, 117(3):648, 1960.

[24] Jeffrey Goldstone, Abdus Salam, and Steven Weinberg. Broken symmetries. *Physical Review*, 127(3):965, 1962.

[25] Anders W Sandvik and Rajiv RP Singh. High-energy magnon dispersion and multimagnon continuum in the two-dimensional Heisenberg antiferromagnet. *Physical Review Letters*, 86(3):528, 2001.

[26] Weihong Zheng, J Oitmaa, and CJ Hamer. Series studies of the spin-1/2 Heisenberg antiferromagnet at $T = 0$: Magnon dispersion and structure factors. *Physical Review B*, 71(18):184440, 2005.

[27] NB Christensen, DF McMorrow, HM Rønnow, A Harrison, TG Perring, and R Coldea. Deviations from linear spin wave theory in the 2D $S = 1/2$ Heisenberg antiferromagnet CFTD. *Journal of magnetism and magnetic materials*, 272:896–897, 2004.

[28] B Dalla Piazza, M Mourigal, Niels Bech Christensen, GJ Nilsen, P Tregenna-Piggott, TG Perring, Mechtild Enderle, Desmond Francis McMorrow, DA Ivanov, and Henrik Moodysson Rønnow. Fractional excitations in the square-lattice quantum antiferromagnet. *Nature physics*, 11(1):62–68, 2015.

[29] Niels Bech Christensen, Henrik Moodysson Rønnow, Desmond Francis McMorrow, A Harrison, TG Perring, Mechtild Enderle, R Coldea, LP Regnault, and G Aeppli. Quantum dynamics and entanglement of spins on a square lattice. *Proceedings of the National Academy of Sciences*, 104(39):15264–15269, 2007.

[30] Götz S Uhrig and Kingshuk Majumdar. Varied perturbation theory for the dispersion dip in the two-dimensional Heisenberg quantum antiferromagnet. *The European Physical Journal B*, 86(6):1–8, 2013.

[31] AV Syromyatnikov. Spectrum of short-wavelength magnons in a two-dimensional quantum Heisenberg antiferromagnet on a square lattice: third-order expansion in $1/S$. *Journal of Physics: Condensed Matter*, 22(21):216003, 2010.

[32] Franz Wegner. Flow-equations for Hamiltonians. *Annalen der physik*, 506(2):77–91, 1994.

[33] Stanisław D Głazek and Kenneth G Wilson. Renormalization of Hamiltonians. *Physical Review D*, 48(12):5863, 1993.

[34] HY Yang and KP Schmidt. Effective models for gapped phases of strongly correlated quantum lattice models. *EPL (Europhysics Letters)*, 94(1):17004, 2011.

[35] Marc Daniel Schulz, Sébastien Dusuel, Kai Phillip Schmidt, and Julien Vidal. Topological phase transitions in the golden string-net model. *Physical Review Letters*, 110(14): 147203, 2013.

[36] Subir Sachdev. Quantum magnetism and criticality. *Nature Physics*, 4(3):173–185, 2008.

[37] Stefan Kehrein. Flow equation solution for the weak-to strong-coupling crossover in the sine-Gordon model. *Physical Review Letters*, 83(24):4914, 1999.

[38] Götz S Uhrig. Nonadiabatic approach to spin-Peierls transitions via flow equations. *Physical Review B*, 57(22):R14004, 1998.

[39] Jürgen Stein. Flow equations and extended Bogoliubov transformation for the Heisenberg antiferromagnet near the classical limit. *The European Physical Journal B-Condensed Matter and Complex Systems*, 5(2):193–201, 1998.

[40] Christian Knetter, Alexander Bühler, Erwin Müller-Hartmann, and Götz S Uhrig. Dispersion and symmetry of bound states in the Shastry-Sutherland model. *Physical Review Letters*, 85(18):3958, 2000.

[41] Christian Knetter and Goetz S Uhrig. Perturbation theory by flow equations: dimerized and frustrated $S = 1/2$ chain. *The European Physical Journal B-Condensed Matter and Complex Systems*, 13(2):209–225, 2000.

[42] Christian Knetter, Kai P Schmidt, and Götz S Uhrig. The structure of operators in effective particle-conserving models. *Journal of Physics A: Mathematical and General*, 36 (29):7889, 2003.

[43] Christian Knetter, Kai P Schmidt, and Götz S Uhrig. High order perturbation theory for spectral densities of multi-particle excitations:$S = 1/2$ two-leg Heisenberg ladder. *The European Physical Journal B-Condensed Matter and Complex Systems*, 36(4):525–544, 2003.

[44] H Krull, NA Drescher, and GS Uhrig. Enhanced perturbative continuous unitary transformations. *Physical Review B*, 86(12):125113, 2012.

[45] Sébastien Dusuel and Götz S Uhrig. The quartic oscillator: a non-perturbative study by continuous unitary transformations. *Journal of Physics A: Mathematical and General*, 37 (39):9275, 2004.

[46] Johannes Nicolaas Kriel, AY Morozov, and FG Scholtz. Non-perturbative flow equations from continuous unitary transformations. *Journal of Physics A: Mathematical and General*, 38(1):205, 2004.

[47] S Duffe and GS Uhrig. Hole dispersions for antiferromagnetic spin-$\frac{1}{2}$ two-leg ladders by self-similar continuous unitary transformations. *The European Physical Journal B*, 84 (3):475–490, 2011.

[48] K Coester, S Clever, F Herbst, Sylvain Capponi, and KP Schmidt. A generalized perspective on non-perturbative linked-cluster expansions. *EPL (Europhysics Letters)*, 110(2): 20006, 2015.

[49] K Coester and KP Schmidt. Optimizing linked-cluster expansions by white graphs. *Physical Review E*, 92(2):022118, 2015.

[50] Dominik Ixert, Tobias Tischler, and Kai P Schmidt. Nonperturbative linked-cluster expansions for the trimerized ground state of the spin-one kagome Heisenberg model. *Physical Review B*, 92(17):174422, 2015.

[51] Tim Fischer, Sebastian Duffe, and Götz S Uhrig. Adapted continuous unitary transformation to treat systems with quasi-particles of finite lifetime. *New Journal of Physics*, 12(3):033048, 2010.

[52] Tim Fischer, Sebastian Duffe, and Götz S Uhrig. Microscopic model for Bose-Einstein condensation and quasiparticle decay. *EPL (Europhysics Letters)*, 96(4):47001, 2011.

[53] Kris Coester. *Quasiparticle pictures and graphs-from perturbative to non-perturbative linked-cluster expansions*. PhD thesis, Technische Universität Dortmund, 2015.

[54] Hong-Yu Yang, Andreas M Läuchli, Frédéric Mila, and Kai Phillip Schmidt. Effective spin model for the spin-liquid phase of the Hubbard model on the triangular lattice. *Physical Review Letters*, 105(26):267204, 2010.

[55] Sébastien Dusuel, Michael Kamfor, Román Orús, Kai Phillip Schmidt, and Julien Vidal. Robustness of a perturbed topological phase. *Physical Review Letters*, 106(10):107203, 2011.

[56] M Powalski, K Coester, R Moessner, and KP Schmidt. Disorder by disorder and flat bands in the kagome transverse field Ising model. *Physical Review B*, 87(5):054404, 2013.

[57] Kai P Schmidt and Götz S Uhrig. Hard-core magnons in the $S = 1/2$ Heisenberg model on the square lattice. *Physical Review B*, 73(17):172407, 2006.

[58] Dominik Ixert and Kai Phillip Schmidt. Non-perturbative linked-cluster expansions in long-range ordered quantum systems. *arXiv preprint arXiv:1608.05618*, 2016.

[59] Stefan Kehrein. *The flow equation approach to many-particle systems*, volume 217. Springer, 2007.

[60] Stefan K Kehrein and Andreas Mielke. Low temperature equilibrium correlation functions in dissipative quantum systems. *Annalen der Physik*, 509(2):90–135, 1997.

[61] Nils A Drescher, Tim Fischer, and Götz S Uhrig. Truncation errors in self-similar continuous unitary transformations. *The European Physical Journal B*, 79(2):225–240, 2011.

[62] Jonathan E Moussa. Approximate diagonalization method for many-fermion Hamiltonians. *arXiv preprint arXiv:1003.2596*, 2010.

[63] Andreas Mielke. Flow equations for band-matrices. *The European Physical Journal B-Condensed Matter and Complex Systems*, 5(3):605–611, 1998.

[64] Caspar P Heidbrink and Götz S Uhrig. Renormalization by continuous unitary transformations: one-dimensional spinless fermions. *The European Physical Journal B-Condensed Matter and Complex Systems*, 30(4):443–459, 2002.

[65] Matthew B Stone, Igor A Zaliznyak, Tao Hong, Collin L Broholm, and Daniel H Reich. Quasiparticle breakdown in a quantum spin liquid. *Nature*, 440(7081):187–190, 2006.

[66] ME Zhitomirsky. Decay of quasiparticles in quantum spin liquids. *Physical Review B*, 73 (10):100404, 2006.

[67] Alexander Reischl, Erwin Müller-Hartmann, and Götz S Uhrig. Systematic mapping of the Hubbard model to the generalized $t-j$ model. *Physical Review B*, 70(24):245124, 2004.

[68] Kai P Schmidt and Götz S Uhrig. Spectral properties of magnetic excitations in cuprate two-leg ladder systems. *Modern Physics Letters B*, 19(24):1179–1205, 2005.

[69] Sébastien Dusuel, Michael Kamfor, Kai Phillip Schmidt, Ronny Thomale, and Julien Vidal. Bound states in two-dimensional spin systems near the Ising limit: A quantum finite-lattice study. *Physical Review B*, 81(6):064412, 2010.

[70] Tim Fischer. *Description of quasiparticle decay by continuous unitary transformations*. PhD thesis, Technische Universität Dortmund, 2011.

[71] Nils A Drescher. *Variational and perturbative extensions of continuous unitary transformations for low-dimensional spin systems*. PhD thesis, Technische Universität Dortmund, 2014.

[72] Simone A Hamerla, Sebastian Duffe, and Götz S Uhrig. Derivation of the $t-j$ model for finite doping. *Physical Review B*, 82(23):235117, 2010.

[73] Kai Phillip Schmidt, Sébastien Dusuel, and Julien Vidal. Emergent fermions and anyons in the Kitaev model. *Physical Review Letters*, 100(5):057208, 2008.

[74] Mohsen Hafez-Torbati, Nils A Drescher, and Götz S Uhrig. From gapped excitons to gapless triplons in one dimension. *The European Physical Journal B*, 88(2):1–17, 2015.

[75] Gian-Carlo Wick. The evaluation of the collision matrix. *Physical Review*, 80(2):268, 1950.

[76] Peter Lenz and Franz Wegner. Flow equations for electron-phonon interactions. *Nuclear Physics B*, 482(3):693–712, 1996.

[77] Stefan Kehrein and Andreas Mielke. On the spin-boson model with a sub-ohmic bath. *Physics Letters A*, 219(5-6):313–318, 1996.

[78] C Brezinski. Extrapolation algorithms and Padé approximations: a historical survey. *Applied numerical mathematics*, 20(3):299–318, 1996.

[79] Cyril Domb. *Phase transitions and critical phenomena*, volume 19. Academic Press, 2000.

[80] Jeffrey Goldstone. Field theories with «superconductor» solutions. *Il Nuovo Cimento (1955-1965)*, 19(1):154–164, 1961.

[81] Subir Sachdev. Quantum phase transitions. *Physics World*, 12(4):33, 1999.

[82] Robert Yaris. Linked-cluster theorem and unitarity. *The Journal of Chemical Physics*, 41 (8):2419–2421, 1964.

[83] Baird H Brandow. Linked-cluster expansions for the nuclear many-body problem. *Reviews of Modern Physics*, 39(4):771, 1967.

[84] Ingvar Lindgren. The Rayleigh-Schrodinger perturbation and the linked-diagram theorem for a multi-configurational model space. *Journal of Physics B: Atomic and Molecular Physics*, 7(18):2441, 1974.

[85] Martin P Gelfand. Series expansions for excited states of quantum lattice models. *Solid state communications*, 98(1):11–14, 1996.

[86] Jaan Oitmaa, Chris Hamer, and Weihong Zheng. *Series expansion methods for strongly interacting lattice models*. Cambridge University Press, 2006.

[87] Yakov Il'ich FRENKEL. *Wave Mechanics. Elementary Theory...* London, 1936.

[88] Herbert Wagner. Long-wavelength excitations and the Goldstone theorem in many-particle systems with broken symmetries. *Zeitschrift für Physik*, 195(3):273–299, 1966.

[89] John A Hertz. Quantum critical phenomena. *Physical Review B*, 14(3):1165, 1976.

[90] Felix Bloch. Über die Quantenmechanik der Elektronen in Kristallgittern. *Zeitschrift für Physik*, 52(7-8):555–600, 1929.

[91] LD Faddeev and LA Takhtajan. What is the spin of a spin wave? *Physics Letters A*, 85 (6-7):375–377, 1981.

[92] DA Tennant, TG Perring, RA Cowley, and SE Nagler. Unbound spinons in the $S = 1/2$ antiferromagnetic chain $KCuF_3$. *Physical Review Letters*, 70(25):4003, 1993.

[93] B Thielemann, Ch Rüegg, HM Rønnow, AM Läuchli, J-S Caux, B Normand, D Biner, KW Krämer, H-U Güdel, J Stahn, et al. Direct observation of magnon fractionalization in the quantum spin ladder. *Physical Review Letters*, 102(10):107204, 2009.

[94] Götz S Uhrig and HJ Schulz. Magnetic excitation spectrum of dimerized antiferromagnetic chains. *Physical Review B*, 54(14):R9624, 1996.

[95] RB Laughlin. Evidence for quasiparticle decay in photoemission from underdoped cuprates. *Physical Review Letters*, 79(9):1726, 1997.

[96] Markus Grüninger, D van der Marel, A Damascelli, A Erb, T Nunner, and T Kopp. Mid-infrared absorption in $YBa_2Cu_3O_6$: Evidence for a failure of spin-wave theory for spin 1 2 in two dimensions. *Physical Review B*, 62(18):12422, 2000.

[97] M Powalski, GS Uhrig, and KP Schmidt. Roton minimum as a fingerprint of magnon-higgs scattering in ordered quantum antiferromagnets. *Physical Review Letters*, 115(20): 207202, 2015.

[98] T Holstein and Hl Primakoff. Field dependence of the intrinsic domain magnetization of a ferromagnet. *Physical Review*, 58(12):1098, 1940.

[99] Assa Auerbach. *Interacting electrons and quantum magnetism*. Springer Science & Business Media, 2012.

[100] Richard P Feynman. The theory of positrons. *Physical Review*, 76(6):749, 1949.

[101] Daniel Friedan, Zongan Qiu, and Stephen Shenker. Conformal invariance, unitarity, and critical exponents in two dimensions. *Physical Review Letters*, 52(18):1575, 1984.

[102] Stefan Kehrein. Flow equation approach to the sine-Gordon model. *Nuclear Physics B*, 592(3):512–562, 2001.

[103] Antoine Georges, Gabriel Kotliar, Werner Krauth, and Marcelo J. Rozenberg. Dynamical mean-field theory of strongly correlated fermion systems and the limit of infinite dimensions. *Rev. Mod. Phys.*, 68:13–125, Jan 1996.

[104] Leonid Mirsky. *An introduction to linear algebra*. Courier Corporation, 2012.

[105] Johann v Neumann. *Mathematische Grundlagen der Quantenmechanik*, volume 38. Springer-Verlag, 2013.

[106] Michael Sh Birman and Mikhail Zakharovich Solomjak. *Spectral theory of self-adjoint operators in Hilbert space*, volume 5. Springer Science & Business Media, 2012.

[107] John Von Neumann. Mathematische Begründung der Quantenmechanik. *Nachrichten von der Gesellschaft der Wissenschaften zu Göttingen, Mathematisch-Physikalische Klasse*, 1927:1–57, 1927.

[108] David Hilbert, J v Neumann, and Lothar Nordheim. Über die Grundlagen der Quantenmechanik. *Mathematische Annalen*, 98(1):1–30, 1928.

[109] Garrett Birkhoff and John Von Neumann. The logic of quantum mechanics. *Annals of Mathematics*, pages 823–843, 1936.

[110] Rainer W Hasse. Microscopic derivation of a frictional Schrödinger equation. *Physics Letters B*, 85(2-3):197–200, 1979.

[111] L Fonda, GC Ghirardi, and A Rimini. Decay theory of unstable quantum systems. *Reports on Progress in Physics*, 41(4):587, 1978.

[112] Léon van Hove. Von Neumann's contributions to quantum theory. *Bull. Amer. Math. Soc.*, 64:95–99, 05 1958. URL http://projecteuclid.org/euclid.bams/1183522374.

[113] J v Neumann. Allgemeine Eigenwerttheorie hermitescher Funktionaloperatoren. *Mathematische Annalen*, 102(1):49–131, 1930.

[114] François Gieres. Mathematical surprises and Dirac's formalism in quantum mechanics. *Reports on Progress in Physics*, 63(12):1893, 2000.

[115] Carl M Bender and Stefan Boettcher. Real spectra in non-hermitian Hamiltonians having PT symmetry. *Physical Review Letters*, 80(24):5243, 1998.

[116] Carl M Bender. Making sense of non-hermitian Hamiltonians. *Reports on Progress in Physics*, 70(6):947, 2007.

[117] Katherine Jones-Smith and Harsh Mathur. Non-hermitian quantum Hamiltonians with PT symmetry. *Physical Review A*, 82(4):042101, 2010.

[118] Katherine Jones-Smith. A 'Dysonization' scheme for identifying quasi-particles using non-hermitian quantum mechanics. *Philosophical Transactions of the Royal Society of London A: Mathematical, Physical and Engineering Sciences*, 371(1989):20120056, 2013.

[119] Erwin Fehlberg. Low-order classical Runge-Kutta formulas with stepsize control and their application to some heat transfer problems. 1969.

[120] Erwin Fehlberg. Klassische Runge-Kutta-formeln vierter und niedrigerer Ordnung mit Schrittweiten-Kontrolle und ihre Anwendung auf Waermeleitungsprobleme. *Computing*, 6(1-2):61–71, 1970.

[121] Ernst Hairer, Syvert Paul Nrsett, and Gerhard Wanner. *Solving Ordinary Differential Equations: Nonstiff problems. v. 2: Stiff and differential-algebraic problems*. Springer Verlag, 2010.

[122] http://pauli.uni-muenster.de/tp/fileadmin/lehre/NumMethoden/SoSe10/Skript/RKM.pdf.

[123] VS Viswanath and Gerhard Müller. *The Recursion Method: Application to Many Body Dynamics*, volume 23. Springer Science & Business Media, 1994.

[124] C Rajakumar and CR Rogers. The Lanczos algorithm applied to unsymmetric generalized eigenvalue problem. *International Journal for Numerical Methods in Engineering*, 32(5):1009–1026, 1991.

[125] David G Pettifor and Denis L Weaire. *The Recursion Method and Its Applications: Proceedings of the Conference, Imperial College, London, England September 13–14, 1984*, volume 58. Springer Science & Business Media, 2012.

[126] Ken Turkowski. Filters for common resampling tasks. In *Graphics gems*, pages 147–165. Academic Press Professional, Inc., 1990.

[127] BN Madhukar and R Narendra. Lanczos resampling for the digital processing of remotely sensed images. In *Proceedings of International Conference on VLSI, Communication, Advanced Devices, Signals & Systems and Networking (VCASAN-2013)*, pages 403–411. Springer, 2013.

[128] Cornelius Lanczos. Trigonometric interpolation of empirical and analytical functions. *Journal of Mathematics and Physics*, 17(1):123–199, 1938.

[129] Paul AM Dirac. On the theory of quantum mechanics. In *Proceedings of the Royal Society of London A: Mathematical, Physical and Engineering Sciences*, volume 112, pages 661–677. The Royal Society, 1926.

[130] Werner Heisenberg. Zur Theorie des Ferromagnetismus. *Zeitschrift für Physik*, 49(9-10): 619–636, 1928.

[131] PW Anderson. Antiferromagnetism. Theory of superexchange interaction. *Physical Review*, 79(2):350, 1950.

[132] Philip W Anderson. New approach to the theory of superexchange interactions. *Physical Review*, 115(1):2, 1959.

[133] Samuel Frederick Edwards and Phil W Anderson. Theory of spin glasses. *Journal of Physics F: Metal Physics*, 5(5):965, 1975.

[134] Philip W Anderson. The resonating valence bond state in La_2CuO_4 and superconductivity. *Science*, 235(4793):1196–1198, 1987.

[135] PHILIP W Anderson. Resonating valence bonds: A new kind of insulator? *Materials Research Bulletin*, 8(2):153–160, 1973.

[136] Leon Balents. Spin liquids in frustrated magnets. *Nature*, 464(7286):199–208, 2010.

[137] Simeng Yan, David A Huse, and Steven R White. Spin-liquid ground state of the $S = 1/2$ kagome Heisenberg antiferromagnet. *Science*, 332(6034):1173–1176, 2011.

[138] J George Bednorz and K Alex Müller. Possible high T_c superconductivity in the Ba-La-Cu-O system. In *Ten Years of Superconductivity: 1980–1990*, pages 267–271. Springer, 1986.

[139] A Harrison, SJ Clarke, TE Mason, and D Visser. Dispersion of spin-waves in the $S = 1/2$ square Heisenberg antiferromagnet $Cu(DCO_2)_2{\cdot}4D_2O$. *Journal of Magnetism and Magnetic Materials*, 104:557–558, 1992.

[140] SJ Clarke, A Harrison, TE Mason, GJ McIntyre, and D Visser. Magnetic ordering and fluctuations in the $S = 1/2$ square Heisenberg antiferromagnet $Cu(DCO_2)_2{\cdot}4D_2O$. *Journal of Physics: Condensed Matter*, 4(4):L71, 1992.

[141] VJ Emery. Theory of high-T_c superconductivity in oxides. *Physical Review Letters*, 58 (26):2794, 1987.

[142] Hiroshi Kamimura, Hideki Ushio, Shunichi Matsuno, and Tsuyoshi Hamada. *Theory of copper oxide superconductors*. Springer Science & Business Media, 2005.

[143] JE Hirsch. Antiferromagnetism, localization, and pairing in a two-dimensional model for CuO_2. *Physical Review Letters*, 59(2):228, 1987.

[144] JM Tranquada, BJ Sternlieb, JD Axe, Y Nakamura, and S Uchida. Evidence for stripe correlations of spins and holes in copper oxide superconductors. *Nature*, 375(6532): 561–563, 1995.

[145] Hadi Ebrahimnejad, George A Sawatzky, and Mona Berciu. The dynamics of a doped hole in a cuprate is not controlled by spin fluctuations. *Nature Physics*, 10(12):951–955, 2014.

[146] Heshan Yu, Ge He, Ziquan Lin, Jie Yuan, Beiyi Zhu, Yi-feng Yang, Tao Xiang, Feo V Kusmartsev, Liang Li, Junfeng Wang, et al. A close look at antiferromagnetic phase boundary in multidimensional phase diagram of electron-doped copper oxide. In *APS March Meeting Abstracts*, 2016.

[147] Chandra M Varma. Quantum-critical fluctuations in 2D metals: strange metals and superconductivity in antiferromagnets and in cuprates. *Reports on Progress in Physics*, 79(8):082501, 2016. URL http://stacks.iop.org/0034-4885/79/i=8/a=082501.

[148] Viktor V Struzhkin and Xiao-Jia Chen. Magnon-phonon coupling and implications for charge-density wave states and superconductivity in cuprates. *Low Temperature Physics*, 42(10):884–890, 2016.

[149] Douglas J Scalapino. A common thread: The pairing interaction for unconventional superconductors. *Reviews of Modern Physics*, 84(4):1383, 2012.

[150] FC Zhang and TM Rice. Effective Hamiltonian for the superconducting Cu oxides. *Physical Review B*, 37(7):3759, 1988.

[151] Masao Ogata and Hidetoshi Fukuyama. The $t - j$ model for the oxide high-T_c superconductors. *Reports on Progress in Physics*, 71(3):036501, 2008.

[152] B Vignolle, SM Hayden, DF McMorrow, HM Rønnow, B Lake, CD Frost, and TG Perring. Two energy scales in the spin excitations of the high-temperature superconductor $La_{2-x}Sr_xCuO_4$. *Nature Physics*, 3(3):163–167, 2007.

[153] OJ Lipscombe, SM Hayden, B Vignolle, DF McMorrow, and TG Perring. Persistence of high-frequency spin fluctuations in overdoped superconducting $La_{2-x}Sr_xCuO_4 (x = 0.22)$. *Physical Review Letters*, 99(6):067002, 2007.

[154] Thomas Dahm, V Hinkov, SV Borisenko, AA Kordyuk, VB Zabolotnyy, J Fink, B Büchner, DJ Scalapino, W Hanke, and B Keimer. Strength of the spin-fluctuation-mediated pairing interaction in a high-temperature superconductor. *Nature Physics*, 5(3):217–221, 2009.

[155] Mathieu Le Tacon, G Ghiringhelli, Jiří Chaloupka, M Moretti Sala, V Hinkov, MW Haverkort, M Minola, M Bakr, KJ Zhou, S Blanco-Canosa, et al. Intense paramagnon excitations in a large family of high-temperature superconductors. *Nature Physics*, 7(9): 725–730, 2011.

[156] Ian Affleck, Z Zou, T Hsu, and PW Anderson. SU(2) gauge symmetry of the large-U limit of the Hubbard model. *Physical Review B*, 38(1):745, 1988.

[157] Elliott Lieb, Theodore Schultz, and Daniel Mattis. Two soluble models of an antiferromagnetic chain. *Annals of Physics*, 16(3):407–466, 1961.

[158] Ian Affleck and Elliott H Lieb. A proof of part of Haldane's conjecture on spin chains. In *Condensed Matter Physics and Exactly Soluble Models*, pages 235–247. Springer, 1986.

[159] Matthew B Hastings. Lieb-Schultz-Mattis in higher dimensions. *Physical Review B*, 69 (10):104431, 2004.

[160] D Vaknin, SK Sinha, DE Moncton, DC Johnston, JM Newsam, CR Safinya, and HE King Jr. Antiferromagnetism in La_2CuO_{4-y}. *Physical Review Letters*, 58(26):2802, 1987.

[161] M Greven, RJ Birgeneau, Y Endoh, MA Kastner, M Matsuda, and G Shirane. Neutron scattering study of the two-dimensional spins= 1/2 square-lattice Heisenberg antiferromagnet $Sr_2CuO_2Cl_2$. *Zeitschrift für Physik B Condensed Matter*, 96(4):465–477, 1995.

[162] J Oitmaa and DD Betts. The ground state of two quantum models of magnetism. *Canadian Journal of Physics*, 56(7):897–901, 1978.

[163] JD Reger and AP Young. Monte Carlo simulations of the spin−1/2 Heisenberg antiferromagnet on a square lattice. *Physical Review B*, 37(10):5978, 1988.

[164] Efstratios Manousakis and Román Salvador. Long-range correlations in the two-dimensional spin-1/2 antiferromagnetic Heisenberg model: A quantum Monte Carlo study. *Physical Review Letters*, 60(9):840, 1988.

[165] Efstratios Manousakis and Román Salvador. Monte Carlo study of the two-dimensional spin−1/2 quantum Heisenberg model: Spin correlations in La_2CuO_4. *Physical Review B*, 39(1):575, 1989.

[166] G Gomez-Santos, JD Joannopoulos, and JW Negele. Monte carlo study of the quantum spin-1/2 Heisenberg antiferromagnet on the square lattice. *Physical Review B*, 39(7): 4435, 1989.

[167] Miloje S Makivić and Hong-Qiang Ding. Two-dimensional spin−1/2 Heisenberg antiferromagnet: A quantum Monte Carlo study. *Physical Review B*, 43(4):3562, 1991.

[168] Anders W Sandvik. Finite-size scaling of the ground-state parameters of the two-dimensional Heisenberg model. *Physical Review B*, 56(18):11678, 1997.

[169] Rajiv RP Singh. Thermodynamic parameters of the $T = 0$, spin−1/2 square-lattice Heisenberg antiferromagnet. *Physical Review B*, 39(13):9760, 1989.

[170] Sudip Chakravarty, Bertrand I Halperin, and David R Nelson. Two-dimensional quantum Heisenberg antiferromagnet at low temperatures. *Physical Review B*, 39(4):2344, 1989.

[171] Luca Capriotti, Adolfo E Trumper, and Sandro Sorella. Long-range Néel order in the triangular Heisenberg model. *Physical Review Letters*, 82(19):3899, 1999.

[172] N David Mermin and Ho Wagner. Absence of ferromagnetism or antiferromagnetism in one-or two-dimensional isotropic Heisenberg models. *Physical Review Letters*, 17(22): 1133, 1966.

[173] Minoru Takahashi. Modified spin-wave theory of a square-lattice antiferromagnet. *Physical Review B*, 40(4):2494, 1989.

[174] Rajiv RP Singh and Martin P Gelfand. Spin-wave excitation spectra and spectral weights in square lattice antiferromagnets. *Physical Review B*, 52(22):R15695, 1995.

[175] G Aeppli, SM Hayden, HA Mook, Z Fisk, S-W Cheong, D Rytz, JP Remeika, GP Espinosa, and AS Cooper. Magnetic dynamics of La_2CuO_4 and $La_{2-x}Ba_xCuO_4$. *Physical Review Letters*, 62(17):2052, 1989.

[176] SM Hayden, G Aeppli, R Osborn, AD Taylor, TG Perring, SW Cheong, and Z Fisk. High-energy spin waves in La_2CuO_4. *Physical Review Letters*, 67(25):3622, 1991.

[177] SJ Clarke, A Harrison, TE Mason, and D Visser. Characterisation of spin-waves in copper (ii) deuteroformate tetradeuterate: a square $S = 1/2$ Heisenberg antiferromagnet. *Solid state communications*, 112(10):561–564, 1999.

[178] G Aeppli, SM Hayden, P Dai, HA Mook, RD Hunt, TG Perring, and F Dogan. The weights of various features in the magnetic spectra of cuprates. *Physica Status Solidi (B)*, 215 (1):519–522, 1999.

[179] HM Rønnow, DF McMorrow, R Coldea, A Harrison, ID Youngson, TG Perring, G Aeppli, O Syljuåsen, Kim Lefmann, and Christian Rischel. Spin dynamics of the 2D spin-1/2 quantum antiferromagnet copper deuteroformate tetradeuterate (CFTD). *Physical Review Letters*, 87(3):037202, 2001.

[180] HM Rønnow, DF McMorrow, A Harrison, ID Youngson, R Coldea, TG Perring, G Aeppli, and O Syljuåsen. Correlations and fluctuations in the 2D Heisenberg antiferromagnet. *Journal of Magnetism and Magnetic Materials*, 236(1):4–5, 2001.

[181] PWAP Fazekas and PW Anderson. On the ground state properties of the anisotropic triangular antiferromagnet. *Philosophical Magazine*, 30(2):423–440, 1974.

[182] Hans Bethe. Zur Theorie der Metalle. *Zeitschrift für Physik*, 71(3-4):205–226, 1931.

[183] G Shirane, Y Endoh, RJ Birgeneau, MA Kastner, Y Hidaka, M Oda, M Suzuki, and T Murakami. Two-dimensional antiferromagnetic quantum spin-fluid state in La_2CuO_4. *Physical Review Letters*, 59(14):1613, 1987.

[184] Elbio Dagotto and TM Rice. Surprises on the way from 1D to 2D quantum magnets: the novel ladder materials. *arXiv preprint cond-mat/9509181*, 1995.

[185] Radu Coldea, DA Tennant, AM Tsvelik, and Z Tylczynski. Experimental realization of a 2D fractional quantum spin liquid. *Physical Review Letters*, 86(7):1335, 2001.

[186] Michael Hermele, T Senthil, Matthew PA Fisher, Patrick A Lee, Naoto Nagaosa, and Xiao-Gang Wen. Stability of U(1) spin liquids in two dimensions. *Physical Review B*, 70 (21):214437, 2004.

[187] Tian-Heng Han, Joel S Helton, Shaoyan Chu, Daniel G Nocera, Jose A Rodriguez-Rivera, Collin Broholm, and Young S Lee. Fractionalized excitations in the spin-liquid state of a kagome-lattice antiferromagnet. *Nature*, 492(7429):406–410, 2012.

[188] S Liang, B Doucot, and PW Anderson. Some new variational resonating-valence-bond-type wave functions for the spin-1/2 antiferromagnetic Heisenberg model on a square lattice. *Physical Review Letters*, 61(3):365, 1988.

[189] Chang-Ming Ho, VN Muthukumar, Masao Ogata, and PW Anderson. Nature of spin excitations in two-dimensional Mott insulators: Undoped cuprates and other materials. *Physical Review Letters*, 86(8):1626, 2001.

[190] NS Headings, SM Hayden, R Coldea, and TG Perring. Anomalous high-energy spin excitations in the high-T_c superconductor-parent antiferromagnet La_2CuO_4. *Physical Review Letters*, 105(24):247001, 2010.

[191] A Yu Aktersky and AV Syromyatnikov. Low-energy singlet excitations in spin-Heisenberg antiferromagnet on square lattice. *Journal of Magnetism and Magnetic Materials*, 405: 42–47, 2016.

[192] Takehiko Oguchi. Theory of spin-wave interactions in ferro-and antiferromagnetism. *Physical Review*, 117(1):117, 1960.

[193] CJ Hamer, Zheng Weihong, and Peter Arndt. Third-order spin-wave theory for the Heisenberg antiferromagnet. *Physical Review B*, 46(10):6276, 1992.

[194] Zheng Weihong and CJ Hamer. Spin-wave theory and finite-size scaling for the Heisenberg antiferromagnet. *Physical Review B*, 47(13):7961, 1993.

[195] Freeman J Dyson. General theory of spin-wave interactions. *Physical Review*, 102(5): 1217, 1956.

[196] SV Maleev. Scattering of slow neutrons in ferromagnets. *Sov. Phys.-JETP*, 6:776, 1958.

[197] K Bernardet, GG Batrouni, J-L Meunier, Guido Schmid, Matthias Troyer, and A Dorneich. Analytical and numerical study of hardcore bosons in two dimensions. *Physical Review B*, 65(10):104519, 2002.

[198] SV Maleev. Scattering of slow neutrons in ferromagnetics. *Zhur. Eksptl'. i Teoret. Fiz.*, 33, 1957.

[199] SV Maleev. Multimagnon processes in the scattering of slow neutrons in ferro-magnets. *Soviet Physics JETP*, 34(7), 1958.

[200] Walter Marshall and Stephen W Lovesey. *Theory of thermal neutron scattering: the use of neutrons for the investigation of condensed matter*. Clarendon Press, 1971.

[201] CM Canali and Mats Wallin. Spin-spin correlation functions for the square-lattice Heisenberg antiferromagnet at zero temperature. *Physical Review B*, 48(5):3264, 1993.

[202] Zheng Weihong, J Oitmaa, and CJ Hamer. Square-lattice Heisenberg antiferromagnet at t= 0. *Physical Review B*, 43(10):8321, 1991.

[203] ME Zhitomirsky and AL Chernyshev. Colloquium: Spontaneous magnon decays. *Reviews of Modern Physics*, 85(1):219, 2013.

[204] B Lake, DA Tennant, and SE Nagler. Novel longitudinal mode in the coupled quantum chain compound $KCuF_3$. *Physical Review Letters*, 85(4):832, 2000.

[205] Ch Rüegg, Bruce Normand, M Matsumoto, A Furrer, DF McMorrow, KW Krämer, H-U Güdel, SN Gvasaliya, H Mutka, and M Boehm. Quantum magnets under pressure: controlling elementary excitations in $TlCuCl_3$. *Physical Review Letters*, 100(20):205701, 2008.

[206] David Pekker and C.M. Varma. Amplitude/Higgs modes in condensed matter physics. *Annual Review of Condensed Matter Physics*, 6(1):269–297, 2015.

[207] P Merchant, B Normand, KW Krämer, M Boehm, DF McMorrow, and Ch Rüegg. Quantum and classical criticality in a dimerized quantum antiferromagnet. *Nature Physics*, 10(5):373–379, 2014.

[208] Simon Adrian Weidinger and Wilhelm Zwerger. Higgs mode and magnon interactions in 2D quantum antiferromagnets from Raman scattering. *The European Physical Journal B*, 88(9):1–12, 2015.

[209] Tomo Munehisa. Numerical study of the Higgs mode in the Heisenberg antiferromagnet on the square lattice. *World Journal of Condensed Matter Physics*, 5(04):261, 2015.

[210] KW Plumb, Andrei T Savici, Garrett E Granroth, FC Chou, and Young-June Kim. High-energy continuum of magnetic excitations in the two-dimensional quantum antiferromagnet $Sr_2CuO_2Cl_2$. *Physical Review B*, 89(18):180410, 2014.

[211] WebPlotDigitizer by Ankit Rohatgi. URL http://arohatgi.info/WebPlotDigitizer/.

[212] N Burger, H Fuess, and P Burlet. Neutron diffraction study of the antiferromagnetic phase of copper formate tetradeuterate. *Solid State Communications*, 34(11):883–886, 1980.

[213] M Powalski, KP Schmidt, and GS Uhrig. Mutually attracting spin waves in the square-lattice quantum antiferromagnet. *arXiv preprint arXiv:1701.04730*, 2017.

[214] AP Ramirez. Strongly geometrically frustrated magnets. *Annual Review of Materials Science*, 24(1):453–480, 1994.

[215] P Chandra and B Doucot. Possible spin-liquid state at large s for the frustrated square Heisenberg lattice. *Physical Review B*, 38(13):9335, 1988.

[216] Elbio Dagotto and Adriana Moreo. Phase diagram of the frustrated spin−1/2 Heisenberg antiferromagnet in 2 dimensions. *Physical Review Letters*, 63(19):2148, 1989.

[217] Luca Capriotti, Federico Becca, Alberto Parola, and Sandro Sorella. Resonating valence bond wave functions for strongly frustrated spin systems. *Physical Review Letters*, 87 (9):097201, 2001.

[218] Hong-Chen Jiang, Hong Yao, and Leon Balents. Spin liquid ground state of the spin−1/2 square $J_1 - J_2$ Heisenberg model. *Physical Review B*, 86(2):024424, 2012.

[219] Ling Wang, Didier Poilblanc, Zheng-Cheng Gu, Xiao-Gang Wen, and Frank Verstraete. Constructing a gapless spin-liquid state for the spin-1/2 $J_1 - J_2$ Heisenberg model on a square lattice. *Physical Review Letters*, 111(3):037202, 2013.

[220] Luca Capriotti and Sandro Sorella. Spontaneous plaquette dimerization in the $J_1 - J_2$ Heisenberg model. *Physical Review Letters*, 84(14):3173, 2000.

[221] R Darradi, O Derzhko, R Zinke, J Schulenburg, SE Krüger, and J Richter. Ground state phases of the spin-1/2 $J_1 - J_2$ Heisenberg antiferromagnet on the square lattice: A high-order coupled cluster treatment. *Physical Review B*, 78(21):214415, 2008.

[222] Valentin Murg, Frank Verstraete, and J Ignacio Cirac. Exploring frustrated spin systems using projected entangled pair states. *Physical Review B*, 79(19):195119, 2009.

[223] Shou-Shu Gong, Wei Zhu, DN Sheng, Olexei I Motrunich, and Matthew PA Fisher. Plaquette ordered phase and quantum phase diagram in the spin-1/2 J_1−J_2 square Heisenberg model. *Physical Review Letters*, 113(2):027201, 2014.

[224] Jonas Haarz. Quantum critical breakdown of a gapless frustrated antiferromagnet. Master's thesis, Technische Universität Dortmund, 2016.

[225] Assa Auerbach and BE Larson. Doped antiferromagnet: The instability of homogeneous magnetic phases. *Physical Review B*, 43(10):7800, 1991.

[226] Sebastian Kirschner. Multi-particle spectral densities. Master's thesis, Universität zu Köln, 2004.

List of publications

- M Powalski, GS Uhrig, and KP Schmidt.
  Roton minimum as a fingerprint of magnon-Higgs scattering
  in ordered quantum antiferromagnets.
  Physical Review Letters, 115(20):207202, 2015.

Preprints

- M Powalski, KP Schmidt, and GS Uhrig.
  Mutually attracting spin waves in the square-lattice quantum antiferromagnet.
  arXiv preprint arXiv:1701.04730, 2017.

Danksagung

An erster Stelle möchte ich mich ganz herzlich bei Prof Dr. Götz S. Uhrig
und Prof Dr. Kai. P. Schmidt für die ausgezeichnete Betreuung dieser Arbeit bedanken. Die spannenden Diskussionen und die tolle Zusammenarbeit haben mir neben dem Verständnis für die Physik vor allem viel Freude bereitet. Stets konnte ich mich auf ihren Rat und ihre Unterstützung verlassen.
Ein großes Dankeschön geht auch an alle Kollegen und Freunde an den Lehrstühlen T1 und T2 für die vielen anregenden Gespräche und die freundschaftliche Atmosphäre. Die Zeit mit euch wird mir immer positiv in Erinnerung bleiben.
Meinen Eltern möchte ich ganz besonders danken, da sie mich stets gefördert und in meinen Entscheidungen unterstützt haben.
Mein größter Dank gilt Kathrin Spindler, die all die Jahre in jeder Hinsicht für mich da ist.